CHEMISTRY JOURNAL OF MOLDOVA. General, Industrial and Ecological Chemistry. 2020, 15(1), 8-20
ISSN (p) 1857-1727 ISSN (e) 2345-1688
http://cjm.asm.md
http://dx.doi.org/10.19261/cjm.2020.669

SIMULTANEOUS QUANTITATIVE ESTIMATION OF LISINOPRIL AND HYDROCHLOROTHIAZIDE RESIDUES USING HPLC FOR CLEANING VALIDATION

Imeda Rubashvili [a,b*], Natela Karukhnishvili [b], Khatuna Makharadze [b]

[a]*Petre Melikishvili Institute of Physical and Organic Chemistry, Ivane Javakhishvili Tbilisi State University, 31, Politkovskaya str., Tbilisi 0179, Georgia*
[b]*Quality Control Laboratory, „Aversi-Rational" Ltd, 14, Chirnakhuli str., Tbilisi 0198, Georgia*
[*]*e-mail: rubashvili@yahoo.fr; phone: (+995) 593 56 02 45*

Abstract. The aim of this study was to develop and validate direct - swab and indirect - rinse sampling procedures and a high performance liquid chromatography (HPLC) method for simultaneous quantitative estimation of residues of active pharmaceutical ingredients (API) – lisinopril and hydrochlorothiazide (HCT) in cleaning control samples collected from pharmaceutical manufacturing equipment surfaces after manufacturing of lisinopril/hydrochlorothiazide 20/25 mg uncoated tablets. The swab and rinse sampling procedures were developed and validated in order to obtain a suitable and good recovery (>80%). The acceptance limits of the above-mentioned APIs on the manufacturing equipment surfaces have been established based on pharmacological and toxicological criteria. The new, rapid, specific and selective, developed HPLC method for simultaneous quantitative determination of lisinopril and HCT residues was validated with respect to robustness, system suitability test, specificity, linearity-range, precision, limits of detection and quantitation. The stability of APIs solutions and membrane filter compatibility were studied as well. The method validation was carried out according to ICH Q2 guideline and United States Pharamcopeia requirements. The limit of detection and the limit of quantitation for lisinopril were 0.039 μg/mL and 0.155 μg/mL and for HCT - 0.012 μg/mL and 0.025 μg/mL, respectively.

Keywords: lisinopril, hydrochlorthiazide, swab sampling, rinse sampling, HPLC, validation.

Received: 23 March 2020/ Revised final: 08 May 2020/ Accepted: 12 May 2020

Introduction

Cleaning validation should be performed in order to confirm the effectiveness of any cleaning procedure for all products contacting pharmaceutical manufacturing equipment. This activity is required by FDA (Food and Drug Administration) and GMP (Good Manufacturing Practice) in pharmaceutical industry and establishes documented evidence with a high degree of assurance that the cleaning procedure effectively removes chemical (the previous product's active pharmaceutical ingredient or cleaning/disinfectant agent) or microbial residues from the manufacturing equipment and facilities below the scientifically predetermined acceptable level. Drug manufacturers must demonstrate that cleaning processes are capable and effective in removing contaminants from the product contact surfaces to the above-mentioned limits. From both regulatory and industry standpoint, cleaning validation is a critical analytical responsibility of the quality assurance system and an important activity which establishes that cross-contamination of the next batch of different pharmaceutical products is under control to ensure the quality of the finished product and patient safety [1-3].

The developed cleaning procedure used in the manufacturing process of a new pharmaceutical product – uncoated tablets of lisinopril/hydrochlorothiazide 20/25 mg must have been inspected and experimentally proven in accordance with the GMP requirements to be suitable and efficient for removal of APIs residues of the above-mentioned product to ensure proper quality and prevent cross-contamination of the subsequent drug product. The need to carry out the cleaning validation was due to the fact that this product is the worst case for the cleaning procedure regarding the solubility of the product's active pharmaceutical ingredients. In order to perform cleaning validation, it was necessary to find a sensitive and specific analytical method combined with appropriate sampling procedures for simultaneous determination of lisinopril and

hydrochlorthiazide (HCT) residues on the manufacturing equipment surfaces.

Lisinopril, (2*S*)-1-[(2*S*)-6-amino-2-{[(1*S*)-1-carboxy-3-phenylpropyl]amino}hexanoyl] pyrrolidine-2-carboxylic acid, is an active pharmaceutical ingredient, which is a potent and competitive inhibitor of angiotensin-converting enzyme (ACE) and is used to treat hypertension and symptomatic congestive heart failure [4]. Hydrochlorthiazide (HCT), 3,4-dihydro-2*H*-1,2,4-benzothiadiazine 1,1-dioxide, is an active pharmaceutical ingredient as well, which is a diuretic medication often used to treat high blood pressure and swelling caused by fluid build-up [5]. Lisinopril can be used alone or in combination dosage form with HCT. The chemical structures of these compounds are shown in Figure 1.

The compendial analytical high performance liquid chromatography (HPLC) procedures for quantitative determination of lisinopril and HCT are described in the monographs of these active substances of the current version of United States Pharamcopeia, respectively. Various HPLC methods for estimation of HCT along with other compounds have been reported in several papers, which described the analysis of HCT, angiotensin-converting enzyme (ACE)-inhibitors and indapamide [6], simultaneous quantification of olmesartan and HCT [7], the analysis of HCT and candesartan cilextil [8], determination of HCT with the major degradation products [9,10]. Analysis of lisinopril along with other components by HPLC has been reported previously [11-13]. Moreover, other methods utilizing HPLC for simultaneous determination of HCT and lisinopril have also been reported [14-16]. A review of the HPLC methods available in the literature revealed that the methods were not appropriate for our analytical purposes. None of the articles discussed the use of HPLC method combined with the sampling procedures in support of cleaning validation. Therefore, a new HPLC method for simultaneous quantitative determination and sampling procedures of the above-mentioned APIs residues on pharmaceutical manufacturing equipment surfaces after manufacturing of dual drug finished product - lisinopril/hydrochlorothiazide 20/25 mg uncoated tablets should be developed and validated.

The aim of this study was to develop and validate swab and rinse sampling procedures with respect to very high recovery rate and a new, selective, specific and rapid HPLC method for simultaneous quantitative determination of lisinopril and HCT in cleaning control samples collected from manufacturing equipment surfaces in order to demonstrate the efficiency and removability of the used cleaning procedure. The novelty of the present research is that the HPLC method combined with sampling procedures suitable for cleaning validation has been developed and validated, of which analogue does not exist in the literature and fully responds to the complex analytical tasks for conducting cleaning validation on drug dosage forms such as lisinopril/hydrochlorothiazide uncoated tablets.

Experimental

Materials

The certified analytical standards of lisinopril dihydrate and HCT were supplied by USP (the United States Pharamcopeia) reference standards. The HPLC grade methanol, potassium dihydrogen phosphate, orthophosphoric acid were purchased from Sigma-Aldrich (Germany).

The HPLC grade purified water was prepared using Milli Q Adventage A10 purification system (France). Polyester microswabs (3×2.5×10 mm), teflon template holder, screw cap vials for sampling were purchased from ITW Texwipe (USA). Three stainless steel, anodized aluminium, plastic plates were used as the representative surfaces and durapore polyvinylidene difluoride (PVDF) membrane filters were used in this study. The cleaning procedure was performed using Microbac Forte 1% solution as a disinfectant and cleaning agent, which was purchased from Bode-Chemie (Germany).

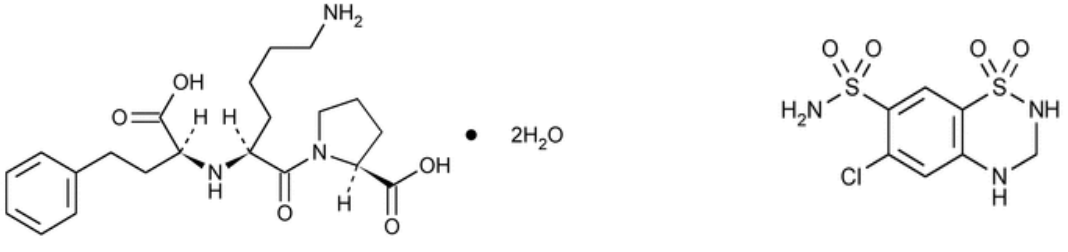

(a) ***(b)***

Figure 1. Chemical structures of lisinopril dihydrate *(a)* and HCT *(b)*.

Instrumentation

The HPLC analysis was performed using an Ag 1260 Infinity system and the output signal was monitored and processed using the Chemstation software (USA). SONOREX™ Digital 102P ultrasonic bath DK 102 (Germany), Vortex-Genie™ 2 (USA), shaker 3056 IKA SH 501 DIGITAL Werke (Germany), semi-micro analytical balance CPA 232S Sartorius (Germany), GFL water bath (Germany) were used for sample preparation. All the measuring equipment were appropriately calibrated and qualified. The experiment was carried out in a controlled laboratory area (temperature, t= 22±3°C, relative humidity, RH= 45±15%).

Chromatographic system conditions

The method was developed using the following columns - BDS Hypersil C8(2) 250×4.6 mm, 5 µm (Thermo Scientific) and LiChrospher® RP-8 250×4.6 mm, 5 µm (Merk-Millipore) with an isocratic elution of mobile phase containing a mixture of buffer solution pH 3.0 and methanol (60/40 v/v) filtered through PVDF 0.45 µm membrane filters and degassed; the flow rate of mobile phase was 0.7 mL/min; the UV detection was performed at different wavelengths - 215 nm for lisinopril and 272 nm for HCT; the injected volume was 10 µL; the column temperature was maintained at 40°C.

Validation of analytical HPLC method

The developed HPLC method was validated with respect to robustness - standard solution stability, membrane filter compatibility test, chromatographic critical factors study using design of experiments (DoE), system suitability test (SST), specificity, linearity-range, precision, limits of detection (LOD) and quantitation (LOQ) according to ICH (International Conference on Harmonisation) guideline and Microsoft Excel 2010 was used for statistical assessment and graphical analysis [17].

Sample preparation and sampling procedure

Lisinopril and HCT reference standards diluted in a mixture of methanol and water 90/10 v/v were used as a standard solution at the concentration of 10/20 µg/mL and 12.5/25 µg/mL, respectively.

Rinsing and swabbing are two sampling procedures available to demonstrate cleaning validation; the both sampling procedures were used in this study. The swabbing is a subjective manual procedure, which involves physical interaction between the swab and the equipment surface and varies from sampler to sampler. The surface was successively wiped with one swab moistened with extraction solution (diluent – a mixture of methanol and water 90/10 v/v). The scheme of swabbing procedure is shown in Figure 2*(a)*. The swabs were placed in the 5 mL screw-cap test tubes containing 1 mL of the selected diluent. Subsequently, the tubes were placed in an ultrasonic bath for 2 minutes and the solutions were analyzed by HPLC. The rinse samples from uneven surfaces (*i.e.* plastic brush) were collected by rinsing with the fixed volume of the diluent.

Due to the nature of material of the manufacturing equipment surfaces, the three types of material - stainless steel, anodized aluminium and plastic were selected, which were previously cleaned by using disinfectant/detergent and dried before the experiment. The sampling points (hard to clean) were determined based on risk assessment using HACCP (hazard analysis and critical control points).

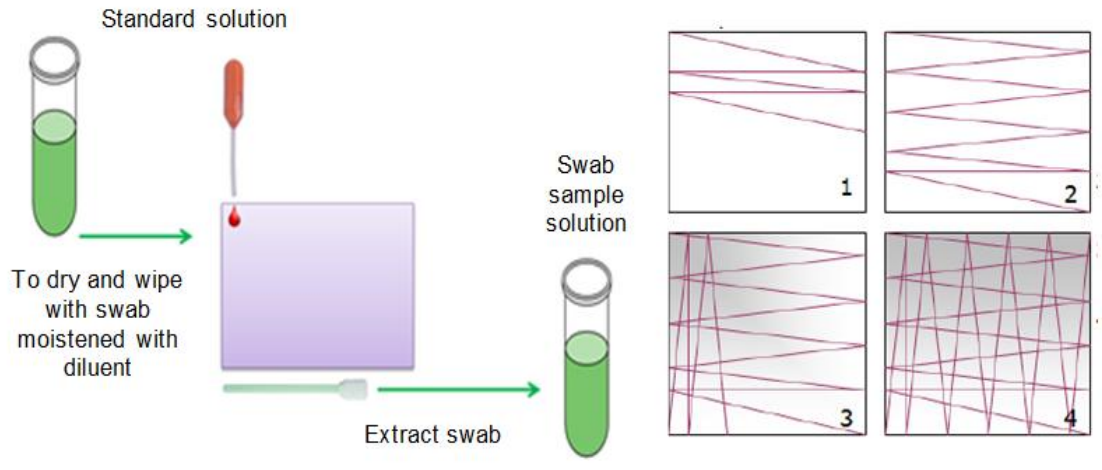

(a) ***(b)***

Figure 2. The scheme of swabbing procedure *(a)* and sequence (steps 1-4) of swab wiping *(b)*.

The usual standardized swab sampling procedure (procedure I) involved moistening swabs with solvent and swabbing the area to be sampled in an overlapping zigzag pattern – first the surface area was wiped horizontally from one side to the other (back and forth) (1, 2 in Figure 2*(b)*), then, after rotating the swab, vertically (up and down) (3, 4 in Figure 2*(b)*). Fresh surface was exposed and repeatedly wiped to extract the maximum residue. Finally, the swab was stored in a closed and labelled container for estimation. Two other variants - the procedures II and III differ from the procedure I only in the swabbing direction and were only used for the robustness study. According to the procedure II, first the surface area was wiped horizontally from one side to the other and then, after rotating the swab, again horizontally. According to the procedure III, first the surface area was wiped diagonally upwards and downwards, after rotating the swab, again diagonally in the same manner [3,18,19].

Design of experiments

For the robustness test of the developed swab sampling procedure and analytical HPLC method, both quantitative and qualitative factors, selected based on experience were considered. The five factors with their levels for swabbing procedure and HPLC method are summarized in Tables 1 and 2. The percentage recovery rate of each API from the surface and system suitability test parameters – the column efficiency (theoretical plates – *N*), the tailing factor (USP symmetry - A_s), the relative standard deviation *(RSD)* of peak areas *(RSD_A)* and the *RSD* of retention times *(RSD_{RT})* (*n*= 6) and the resolution factor between HCT and lisinopril at 215 nm *(R_s)* obtained from standard solution were used as the response variable for the swab sampling procedure and analytical HPLC method, respectively. The experiment was conducted in 2^{5-2}= 8 runs for five two-level factors.

Validation of sampling procedure

Validation parameters - robustness and accuracy of sampling procedure were studied using the DoE technique. Both developed sampling procedures were checked and the percentage recovery rate (two individual determinations) was determined. The selected surface area of the plates was sprayed with 100 µL (for swabbing) and 5 mL (rinsing) of standard stock solution (lisinopril and HCT at concentration – 100/200 mg/mL and 125/250 µg/mL, respectively) using a micropipette and the solvent was allowed to evaporate. Then swab sampling was performed according to swab wipe standardized procedure as described in sample solution preparation. The swab samples were diluted with the same diluent to 1 mL. For rinse sampling, the surface area was rinsed with approximately 100 mL of diluent and then diluted to a volume with the same diluent to 100 mL, and mixed well. Then it was filtered through a 0.45 µm membrane filter.

The percentage recovery rate was calculated by Eq.(1):

$$Rec(\%) = \frac{A_{rec}}{A_{sp}} \times 100 \quad (1)$$

where, A_{rec} is the peak area of lisinopril/HCT obtained from sample solution (recovered amount);

A_{sp} is the peak area of lisinopril/HCT obtained from spiked solution (amount added) [3].

Table 1

Robustness factors and design of experiments for swab sampling procedure.

No.	*Factor (Xi)*	*Unit*	*Low level (-)*	*Nominal level (0)*	*High level (+)*
1	Surface material *(X1)*	-	Anodized aluminum	Stainless steel	Plastic
2	Swabbing *(X2)*	-	II	I	III
3	Methanol percentage in diluent *(X3)*	%	80%	90%	100%
4	Sampler *(X4)*	-	I Chemist-analyst	-	II Chemist-analyst
5	Amount spiked (lisinopril)	µg	8	10	12
	Amount spiked (HCT) *(X5)*		10	12.5	15

Table 2

Robustness factors and design of experiments for analytical procedure.

No.	*Factor (Xi)*	*Unit*	*Low level (-)*	*Nominal level (0)*	*High level (+)*
1	Flow rate of mobile phase *(X1)*	mL/min	0.6	0.7	0.8
2	Buffer solution of mobile phase *(X2)*	pH	2.8	3.0	3.2
3	Methanol percentage in mobile phase *(X3)*	%	35	40	45
4	Column temperature *(X4)*	°C	35	40	45
5	DAD* wavelength for lisinopril/HCT *(X5)*	nm	213	215	217
			270	272	274

**Diode-array-detection.*

Quantitative estimation of lisinopril/HCT residues

The concentration (μg/mL) of lisinopril/HCT residues in sample solution was calculated by Eq.(2):

$$X = \frac{R_u \times W \times D \times 1000 \times P}{R_s \times 100} \quad (2)$$

where, R_u is the peak area of analyte obtained from the chromatogram of swab sample solution;
R_s is the peak area of analyte obtained from the chromatogram of standard solution;
W is the weighted mass of standard, mg;
D is the dilution factor;
P is the purity of the standard compound, (assay, %).

Methodology to establish acceptance limits

The acceptance limits for the drug residues must ensure the absence of cross-contamination for subsequent batches manufactured in the affected equipment. FDA's guidance for determining residues acceptance limits requires a logical, practical, achievable and verifiable determination practice [2]. The acceptance limits for cleaning validation were based on two pharmacological (the dosage criteria - the patient should not take more than 0.1% of the minimum therapeutic dose of the API of the previous product in the maximal daily dose of the subsequent product) and toxicological.

The maximum allowable carryover (mg) - *MAC* was calculated based on the both above-mentioned criteria [3,18,19].

The *MAC* was calculated based on the pharmacological criteria using Eq.(3):

$$MAC = \frac{TD \times SF \times BS}{LDD} \quad (3)$$

where, *TD* is the minimal therapeutic dose of the studied API of the control product (mg);
SF is a safety factor -1/1000 for solid oral dosage form;
BS is the smallest batch size of the subsequently processed product batch (mg);
LDD is the largest daily dose of the subsequently processed product's API (mg).

The *MAC* was calculated based on the toxicological criteria by Eq.(4):

$$MAC = \frac{NOEL \times SF \times BS}{LDD} = \frac{LD50 \times WA \times SF \times BS}{LDD \times 2000} \quad (4)$$

where, *NOEL* is no-observed effect level (mg/kg);
WA is human average weight calculated on 50 (kg);
2000 is an empirical constant.

The acceptance limits - *AL* for *API* residues in sample solution was calculated using Eq.(5) and Eq.(6) depending on the cleaning procedure. Thus, for sample solution obtained from swabbing:

$$AL = \frac{MAC \times 1000 \times Rec \times A_s \times F}{A_t \times V} \quad (5)$$

And, for sample solution obtained from rinsing:

$$AL = \frac{MAC \times 1000}{V} \quad (6)$$

where, A_s is the sampling area (cm^2);
Rec is the percentage recovery rate of the sampling method;
A_t is the total production line area (cm^2);
V is the volume of sample solution obtained from swabbing/rinsing (mL).

Results and discussion

Establishing acceptance limits

The smallest batch size of the subsequent product was selected for calculating the values of the *MAC*. The lowest obtained value of *MAC* of both APIs – lisinopril and HCT were used to calculate the acceptance limits, given in Table 3.

Table 3

The calculated acceptance limits (μg/mL).

Name of API	*Pharmacological criteria**		*Toxicological criteria***	
	Swabbing	*Rinsing*	*Swabbing*	*Rinsing*
Lisinopril	162.0	120.0	3.45	2.45
HCT	202.0	75.0	1.11	0.83

**Pharmacological criteria were calculated using the values of MAC obtained from Eq.(3);*
***Toxicological criteria were calculated using the values of MAC obtained from Eq.(4).*

The determined concentration of lisinopril and HCT residues in sample solutions should not exceed the established *AL*. According to the current version of good manufacturing practice guidelines (GMP EU Annex 15) the acceptance criteria should be based on a toxicological evaluation [1]. The results of the calculated acceptance limits based on the various approaches show that the strictest limit is the AL based on toxicological criteria. Therefore, this limit should be considered for estimation of the API residues.

Development and validation of sampling procedure

The sampling procedures were developed in order to obtain a suitable and good recovery of APIs residues. The surface (sampling area - 25 cm^2) was successively wiped with one micro polyester swab moistened with diluent. The swabs were spiked with different quantities of lisinopril and HCT. A mixture of methanol and water 90/10 v/v was used as diluent (easy to remove from surfaces by purified water after sampling and easy to check its residues using gas chromatography; the studied APIs residues are soluble in methanol; and the selected diluents ensure the best chromatographic characteristics of the peaks). The sonication time was set to 2-3 minutes.

The robustness of the swab sampling procedure was checked using the recovery rate (Table 4). All the recovery values obtained from the robustness test (8-run design experiment) were more than 86.36%, which approved that the developed swab sampling procedure can be considered robust and none of the examined factors had a significant effect on the swab recovery rate.

The accuracy of the combination of sampling procedure and analytical HPLC procedure was assessed by comparing the analyte amount determined versus the known amount spiked at two different concentration levels (10 and 20 µg/mL for lisinopril and, 12.5 and 25 µg/mL for HCT) with three individual determinations (*n*= 3). The accuracy is expressed as percentage of standard compound recovered from a spiked solution (placebo+standard) with a corresponding *RSD*, %. The average recovery should be within 80.0-120.0% and the *RSD* of percentage recovery rates for three individual determinations should not be more than 4.0% for each concentration level of spiked sample solution (acceptance criteria). The accuracy test results are shown in Table 5. The main recovery rates are more than 82.93% (at two different concentrations *n*= 3), which confirms that the developed sampling procedures have a good recovery.

To estimate the compatibility of the used swab material - polyester (ITW Texwipe swab, USA), the standard solution and extracted swab solution added standard of the same concentration were prepared and injected (Figure 3). This test confirms the existence of desorption of lisinopril/HCT residues from the swab material. The compatibility of swab material was evaluated quantitatively by the calculated percentage difference between peak areas obtained from standard solution and extracted swab solution added standard which should not be more than 3.0% (acceptance criteria).

Table 4

Robustness test results for the swab sampling procedure.

Experiment	*Factors*					*Mean recovery, %*	
no.	*X1*	*X2*	*X3*	*X4*	*X5*	*Lisinopril*	*HCT*
1	+	+	+	+	+	93.25	98.55
2	+	+	-	+	+	92.50	91.91
3	+	-	+	-	+	91.55	87.11
4	+	-	-	-	-	96.65	86.36
5	-	+	+	-	-	93.77	95.00
6	-	+	-	-	+	89.25	94.21
7	-	-	+	+	-	87.74	88.33
8	-	-	-	+	+	92.66	87.92

Table 5

The accuracy results.

API residue	*Spiked sample solution, µg/mL*	*Recovery rate, %*			*RSD (n= 3)*	*The main recovery rate, % (n= 3)*
		I	*II*	*III*		
			Swabbing			
Lisinopril	10	95.96	97.27	93.25	1.75	96.40
	20	96.77	98.01	97.15	0.53	
HCT	12.5	95.77	97.07	93.16	1.71	95.17
	25	94.25	93.78	96.96	1.48	
			Rinsing			
Lisinopril	10	87.58	81.53	85.23	2.94	85.70
	20	89.25	83.14	87.44	2.96	
HCT	12.5	82.88	80.59	84.99	2.17	82.93
	25	83.15	82.45	83.50	0.53	

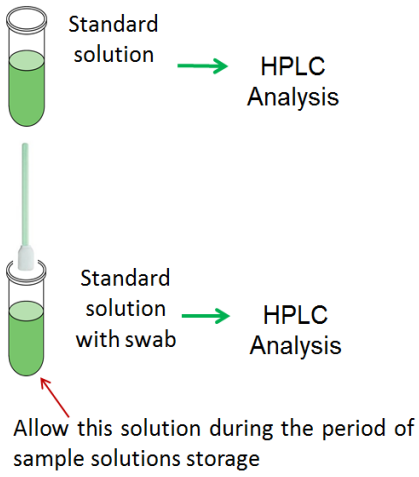

Figure 3. The scheme of compatibility testing of swab.

The calculated percentage difference is 0.43% for lisinopril and 0.25% for HCT. Hence, the lisinopril and HCT residues desorb from the swab and the swab material does not effect on the determination of the above-mentioned APIs residues.

Optimization of chromatographic system conditions and robustness study

The final chromatographic conditions were determined by optimizing the system operational parameters: wavelength for detection, composition of the mobile phase, flow rate, nature of stationary phase and checking the system suitability parameters: theoretical plates, tailing factor, peak purity, resolution, *etc*.

The calibration curve showed good linearity for the trace level quantitative estimation at 215 and 272 nm for lisinopril and HCT, respectively. Five critical factors (*X1* - flow rate of mobile phase; *X2* - buffer solution of mobile phase; *X3* - methanol percentage in mobile phase; *X4* - column temperature; *X5* - DAD wavelength for lisinopril/HCT) were selected and small variations (low and high levels) were induced in the nominal values of the method. An 8-run design experiment was performed to assess the effect of each factor in the system suitability test results. Table 6 shows the design experiments results of the robustness test for the developed HPLC method. The variability of resolution factor is 12.32% but the minimal value of the resolution factor is not bellow the acceptance criteria (>7.0).

Validation of analytical HPLC method

The specificity test was checked using the standard solution, the spiked swab and rinse sample solutions, and the blank solution. This solution was prepared in the same manner as the spike sample solution but no standard was used. The specificity test results have shown that there is no interference from the extracted blank and the diluent at the retention time (RT) of analyte peak. The lisinopril and HCT peaks were pure and the purity factor (999.988 for lisinopril and 999.995 for HCT) was more than the purity threshold (990.0). Figures 4 and 5 show the chromatograms obtained from the standard solution and the blank solution, respectively.

In order to study the linearity-range, the working solutions were prepared at eight different concentration levels (the range was 0.155-20.0 µg/mL for lisinopril and 0.025-25.0 µg/mL for HCT) and injected by six replicates (n= 6) for each concentration level. The linearity was checked by the square of correlation coefficient (acceptance criteria: >0.998), the *RSD* of peak areas (acceptance criteria: <5.0%) at all concentration levels excluding the last concentration level which should not be more than 10%, the *RSD* of retention times (acceptance criteria: <1.0%). The calibration curves were constructed by plotting the peak area against the corresponding concentration of the injected working standard solutions that indicate a perfect linearity for each compound. Figure 6*(a)* and *(b)* shows the linearity plots for lisinopril and HTC, respectively.

Table 6

Robustness results of recovery study for analytical procedure.

Experiment no.	*Factors*					*Resolution factor (Rs)*
	X1	*X2*	*X3*	*X4*	*X5*	
1	+	+	+	+	+	7.61
2	+	+	-	+	+	7.55
3	+	-	+	-	+	7.85
4	+	-	-	-	-	7.92
5	-	+	+	-	-	8.11
6	-	+	-	-	+	7.86
7	-	-	+	+	-	7.22
8	-	-	-	+	+	7.23

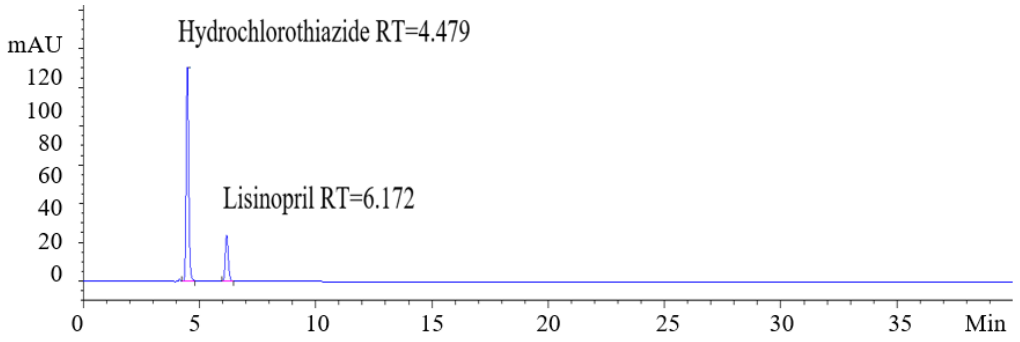

(a)

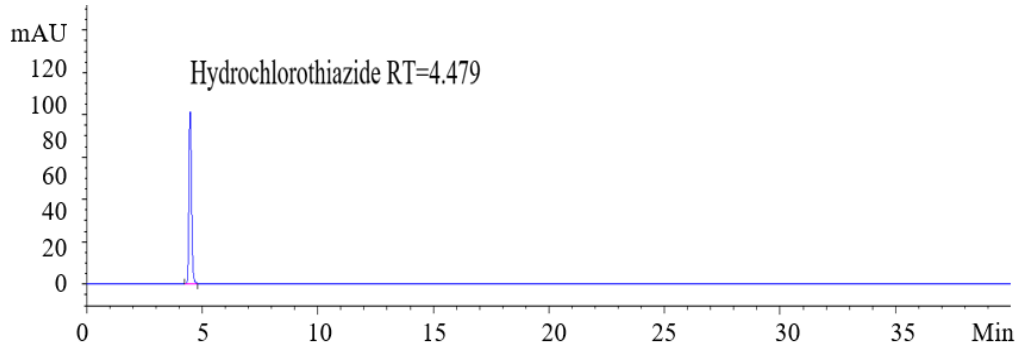

(b)

Figure 4. Chromatograms of the standard solution recorded at 215 nm *(a)* and 272 nm *(b)*.

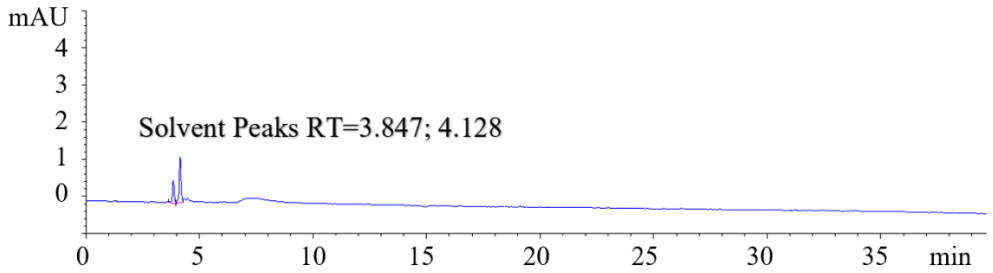

Figure 5. Chromatogram of the blank solution.

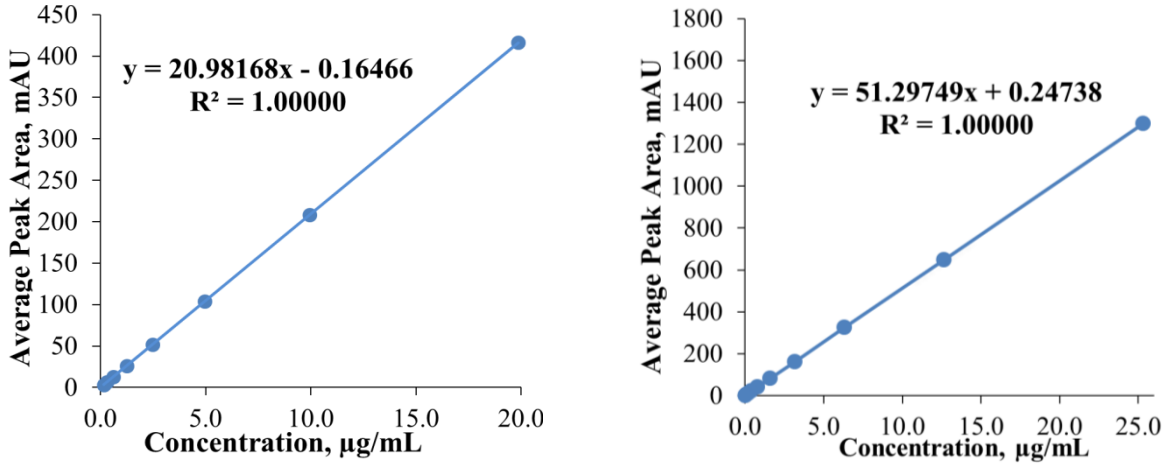

(a) ***(b)***

Figure 6. The linearity (calibration) curve for lisinopril at 215 nm *(a)* and HCT at 272 nm *(b)*.

The limit of quantitation (*LOQ*) was estimated to be ten times the s/N ratio; the limit of detection (*LOD*) was estimated to be three times of s/N ratio (acceptance criteria). The quantitation limit was achieved by injecting a series of stepwise diluted solutions and the precision was established at the specific determined level. The *RSD* of peak area should not be more than 10% (acceptance criteria). The determined limits of quantitation and detection of lisinopril and HCT by HPLC are presented in Table 7.

Table 7

The LOQ and LOD of HPLC method.

Parameter	*Value*	
	Lisinopril	*HCT*
LOQ, μg /mL	0.155	0.025
LOD, μg /mL	0.039	0.012
RSD of peak areas for LOQ (*n*= 6)	2.001	3.343
RSD of retention times for LOQ (*n*= 6)	0.050	0.073
s/N for LOQ	18.23	14.25
s/N for LOD	4.03	7.98

In order to check the chromatographic system performance, the system suitability test was performed by using six replicate injections (*n*= 6) of the standard solution at the concentrations – 10 μg/mL and 12.5 μg/mL, respectively. The following parameters - the *RSD* of peak areas, the *RSD* of the retention times, the peak tailing factor (the USP coefficient of the peak symmetry), the column efficiency - the number of theoretical plates and resolution factor between HCT and lisinopril were measured. The results are summarized in Table 8.

The precision of the analytical method was estimated by measuring repeatability (intra-day precision) and time-dependent intermediate precision (inter-day) on six replicate injections of standard solution and on six individual determinations of lisinopril and HCT in sample solution at the same concentrations (10 and 12.5 μg/mL for lisinopril and HCT, respectively).

This validation parameter was studied during the accuracy study of sampling procedures. Sample solutions were prepared according to the description in the experimental section. The intermediate precision (inter-day) was carried out on a different day. The intra-day precision was checked by the *RSD* of the determined concentrations (μg/mL) for three individual determinations of lisinopril and HCT which should not be more than 4.0%; The intermediate precision was checked by the *RSD* of six individual determinations (totally inter-day and intra-day determinations) of lisinopril and HCT which should not be more than 4.0%, the percentage difference, which should be more than 5.0% and *F*-test which should not be more than 19. The precision study results given in Tables 9, 10 and 11 are within the acceptance criteria indicating that this method has a good precision.

The standard solution stability was checked three times: initially, and after 24 h and 48 h of storage at room temperature against a freshly prepared standard solution. The stability was checked using two standard solutions and by the percentage difference between the peak areas of the standard solution stored at room temperature and the freshly prepared one which should not exceed 3.0% (acceptance criteria). The bias in terms of peak area between two standard solutions should be within 0.98-1.02 (acceptance criteria). The percentage difference between the peak areas obtained with two standard solutions, one stored at room temperature for 24 h and another prepared freshly, is 1.3% and 0.51% for lisinopril and HCT, respectively. This gives the confidence that APIs residues are stable within 48 h and the residues concentration does not change in sample solutions during cleaning validation process.

Table 8

The system suitability test parameters results.

Parameter	*Lisinopril*	*HCT*	*Acceptance criteria*
Column efficiency	>11766	>8178	>2000
RSD of peak areas (*n*= 6)	0.113%	0.127%	<2.0%
RSD of retention times (*n*= 6)	0.018%	0.024%	<1.0%
Tailing factor (USP symmetry*)	0.84	0.85	0.8÷1.2
Resolution factor between HCT and lisinopril	7.95		>7

**USP symmetry is the coefficient of the peak symmetry S= $W_{0.05}$/2f where,*
W= peak width at 5% of peak height,
f= time from width start point at 5% of peak height to RT.

Table 9

The precision repeatability results for standard solution.

Injection no.	*Lisinopril*		*HCT*	
	Peak area, mAU*	*RT**, min*	*Peak area*, mAU*	*RT**, min*
1	208.40	6.034	650.71	4.484
2	208.50	6.032	650.07	4.482
3	208.04	6.042	651.14	4.489
4	209.06	6.033	650.10	4.482
5	208.54	6.036	651.24	4.487
6	208.61	6.034	651.74	4.487
Average	208.53	6.035	650.83	4.485
RSD	0.330	0.004	0.666	0.003

** The instrument error for peak area ± 0.1 mAU;*

*** The instrument error for RT ± 0.01 min.*

Table 10

The precision results for sample obtained with swab sampling solution, µg/mL.

Sample solution no.	*Precision repeatability (intra-day)*		*Intermediate precision (inter-day)*	
	Lisinopril	*HCT*	*Lisinopril*	*HCT*
1	17.52	23.52	17.24	22.27
2	17.74	23.31	16.93	22.69
3	17.58	24.24	17.38	23.03
Average	17.61	23.69	17.18	22.66
RSD (*n*= 3)	0.115	0.488	0.230	0.381
RSD (*n*= 6)			0.286	0.685
Percentage difference			2.47	4.44
F-test			6.04	1.64

The PVDF membrane filter compatibility was evaluated using a standard solution and by calculating the percentage difference between peak areas of filtered and non-filtered standard solutions which should not be more than 0.5% (acceptance criteria). The percentage difference between peak areas of filtered and non-filtered standard solutions is 0.24% and 0.12% for lisinopril and HCT, respectively, which gives the confidence that the adsorption of each analyte does not occur on the used filter.

Estimation of lisinopril and HCT residues in samples from swabbing and rinsing

Both swabbing and rinsing procedures were performed for APIs residues sampling from manufacturing equipment surfaces. The APIs residues were expressed in µg/mL. After manufacturing of three consecutive batches of finished drug product - uncoated tablets of lisinopril/hydrochlorothiazide 20/25 mg, equipment cleaning samples were collected from different sampling points. After sampling, the equipment surfaces were rinsed with purified water for several times to remove residual methanol on surfaces. The last rinsed portions were checked using gas chromatography to detect methanol residues. Swab and rinse samples were tested immediately to estimate lisinopril and HCT residues using the validated HPLC method. The results are shown in Table 12. Figure 7 shows typical chromatograms obtained from the sample solution. The secondary peaks that appeared on the chromatograms belong to the diluent and one unknown compound (RT= 21 min) extracted from the swab material.

The determined concentrations of lisinopril and HCT residues are below the established acceptance limits for cross-contamination. The standard operating cleaning procedure established for cleaning of manufacturing equipment surfaces provides enough efficacy in order to remove the above-mentioned APIs from the cleaned surfaces and excludes the risk of cross-contamination of the subsequent finished product.

Table 11

The precision results for sample obtained with rinse sampling solution, µg/mL.

Sample solution no.	*Precision repeatability (intra-day)*		*Intermediate precision (inter-day)*	
	Lisinopril	*HCT*	*Lisinopril*	*HCT*
1	16.15	20.79	15.77	21.28
2	15.05	20.61	16.03	20.89
3	15.83	20.88	16.23	20.88
Average	15.68	20.76	16.01	21.02
RSD (*n*= 3)	0.566	0.138	0.231	0.228
RSD (*n*= 6)			0.206	0.219
Percentage difference			2.08	1.25
F-test			6.02	0.36

Table 12

The results of lisinopril and HCT residues analysis.

Sampling procedure	*Number of sampling points*	*The determined concentration range of residues, µg/mL*		*Acceptance limit, µg/mL*	
		Lisinopril	*HCT*	*Lisinopril*	*HCT*
Swabbing	10	0.19÷0.67	0.06÷0.46	3.45	1.11
Rinsing	3	0.28÷0.62	0.24÷0.69	2.45	0.83

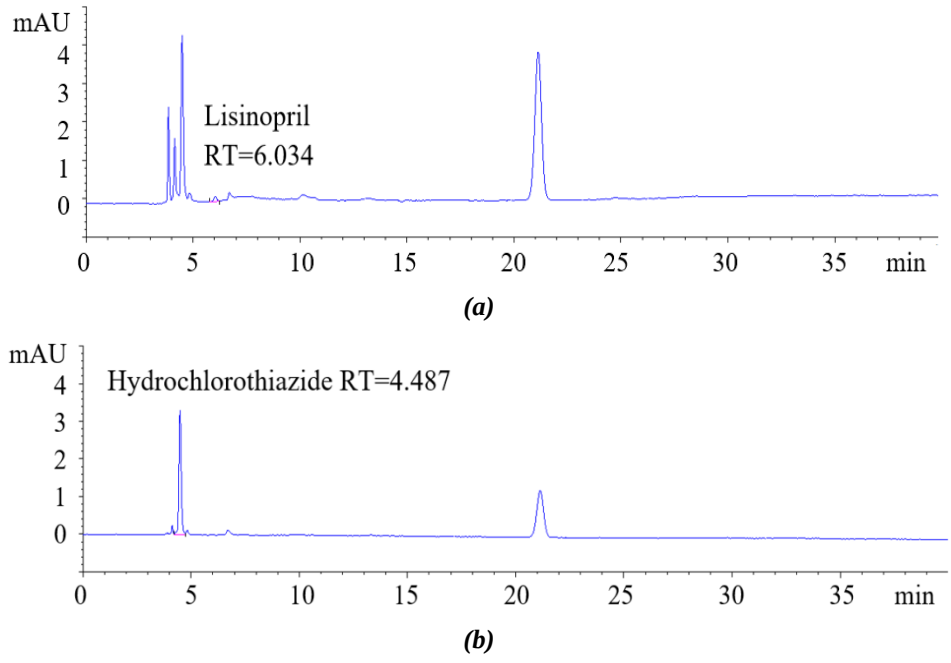

Figure 7. Chromatograms of the sample solution recorded at 215 nm *(a)* and 272 nm *(b)*.

Conclusions

An analytical HPLC method combined with swab and rinse sampling procedures was developed for simultaneous quantitative determination of lisinopril and hydrochlorthiazide (HCT) residues on surfaces of pharmaceutical equipment used in the manufacturing process. The lisinopril/hydrochlorthiazide 20/25 mg uncoated tablets were used to demonstrate cleaning validation. The analytical method was validated with respect to precision, accuracy, robustness, specificity, system suitability test and linearity-range over the concentration range from 0.155 µg/mL to 20.0 µg/mL for lisinopril and from 0.025 µg/mL to 25 µg/mL for HCT.

Both developed swab and rinse sampling procedures were found to be robust and accurate with high recovery rate (>80%). No interferences from swab/blank solutions were observed. Standard solutions of both compounds were stable

within 48 hours; therefore, the concentrations of cleaning control sample solutions did not change for a time from sampling to injecting into HPLC system. Hence, the obtained results confirm that the standard cleaning procedure is adequate and effective for removing both APIs residues from equipment surfaces. The determined concentrations of lisinopril (<3.45 µg/mL by swabbing and <2.45 µg/mL by rinsing) and HCT (<1.11 µg/mL by swabbing and <0.83 µg/mL by rinsing) in sample solutions are much lower than calculated acceptance limit of cross-contamination of the next finished product.

The validated protocol of sampling and HPLC method may be successfully used by other pharmaceutical quality control laboratories to sustain cleaning validation process for lisinopril and HCT residues after manufacturing of uncoated tablets.

References

1. EU Guidelines for good manufacturing practice for medicinal products for human and veterinary use. EudraLex, Volume 4, Annex 15: Qualification and Validation, 2015, Brussels. https://ec.europa.eu/health/documents/eudralex/vol-4_en
2. Guide to inspections validation of cleaning processes. U.S. Food and Drug Administration, Office of Regulatory Affairs, 2014, Washington. https://www.fda.gov/validation-cleaning-processes-793
3. Rubashvili, I.; Kharukhnishvili, N.; Makharadze, K. Vincamine residues analysis using HPLC and establishing limits of cross-contamination in support of cleaning validation. Revue Roumaine de Chimie, 2018, 63(3), pp. 205-215. http://revroum.lew.ro/2018/03/
4. U.S. Pharmacopeia National Formulary USP39 NF34: Volume 2. Lisinopril. The United States Pharmacopeial Convention. United Book Press: Baltimore, 2016, pp. 4580-4579. https://www.uspnf.com/official-text/proposal-statuscommentary/usp-39-nf-34
5. U.S. Pharmacopeia National Formulary USP39 NF34: Volume 2. Hydrochlorothiazide. The United States Pharmacopeial Convention. United Book Press: Baltimore, 2016. pp. 4209-4210. https://www.uspnf.com/official-text/proposal-statuscommentary/usp-39-nf-34
6. Dawud, E.R.; Shakya, A.K. HPLC-PDA analysis of ACE-inhibitors, hydrochloro thiazide and indapamide utilizing design of experiments. Arabian Journal of Chemistry, 2019, 12(5), pp. 718-728. DOI: https://doi.org/10.1016/j.arabjc.2014.10.052
7. Kumar, A.; Dwivedi, S.P.; Prasad, T. Method validation for simultaneous quantification of olmesartan and hydrochlorothiazide in human plasma using LC-MS/MS and its application through bioequivalence study in healthy volunteers. Frontiers in Pharmacology, 2019, 10, pp. 810-823. DOI: https://doi.org/10.3389/fphar.2019.00810
8. Srikalyani, V.; Madhuri, T.; Sareesh, K.; Kumar, R.M. Simultaneous estimation of hydrochlorthiazide and candesartan cilextil in bulk and pharmaceutical dosage forms by RP-HPLC PDA method. International Journal of Pharmaceutical Sciences and Research, 2018, 17, pp. 150-157. DOI: 10.13040/IJPSR.0975-8232.9(1).150-57
9. Bernardi, L.S.; Severino Júnior, P.N.; Barreto Biscaia, I.F.; Sangoi, M.S; Todeschini, V.; Mendes, C.; Segatto Silva, M.A.; Oliveira, P.R. Determination of hydrochlorothiazide and two major degradation products by stability indicating high performance liquid chromatography. Current Pharmaceutical Analysis, 2020, 16(2), pp. 176-180. DOI: 10.2174/1573412914666181017151551
10. Urupina, D.; Al-Bazi, S. Stability-indicating method development and validation for the assay of hydrochlorothiazide and determination of impurities/degradants in hydrochlorothiazide raw material and tablets using reverse-phase liquid chromatography. Austin Journal of Analytical and Pharmaceutical Chemistry, 2016, 3(3), pp. 1-7. https://austinpublishinggroup.com/analytical-pharmaceutical-chemistry/v3-i3.php
11. Arayne, M.S.; Sultana, N.; Zuberi, M.H.; Siddiqui F.A.; Haroon, U. Simultaneous determination of metformin, captopril, lisinopril, and enalapril by RP-HPLC: its applications in dosage formulations and in human serum. Medicinal Chemistry Research, 2013, 22, pp. 5717-5722. DOI: https://doi.org/10.1007/s00044-013-0501-z
12. Chandler, V.; Mohan, M.; Seth, R.; Singh, P.; Singh, R.; Gupta, S. Development and validation of RP-HPLC method for the estimation of lisinopril in tablet dosage form. Analytical Chemistry Letters, 2012, 2(5), pp. 309-313. DOI: https://doi.org/10.1080/22297928.2012.10648282
13. Chauhan, V.; Prajapati, S.T.; Patel, C.N. A validated RP-HPLC method for simultaneous estimation of amlodipine and lisinopril in pharmaceutical dosage form. International Journal of Pharmaceutical Sciences and Research, 2018, 17, pp. 1712-1715. DOI: https://dx.doi.org/10.13040/IJPSR.0975-8232.2(7).1712-15
14. Ivanović, D.; Medenica, M.; Jančić, B.; Knežević, N.; Malenović, A.; Milić, J. Validation of an analytical procedure for simultaneous determination of hydrochlorothiazide, lisinopril and their impurities. Acta Chromatographica, 2007, 18, pp. 143-156. http://acta-chromatographica.us.edu.pl/
15. Aparna, P.; Rao, S.; Thomas, K.M.; Mukkanti, K. Simultaneous determination of lisinopril and hydrochlorothiazide related impurities in lisinopril and hydrochlorothiazide combined tablet dosage forms using HPLC. Analytical Chemistry:

An Indian Journal, 2008, 7(7), pp. 454-161. https://www.tsijournals.com/journals/archive/tsac-volume-7-issue-7-year-2008.html

16. Maslarska, V.; Peikova, L.; Tsvetkova, B. RP-HPLC method for the simultaneous determination of lisinopril and NSAIDs in API, pharmaceutical formulations and human serum. American Journal of Analytical Chemistry, 2012, 3(2), pp. 147-152. DOI: https://dx.doi.org/10.4236/ajac.2012.32021
17. ICH Harmonized Tripartite Guideline: Validation of Analytical Procedures: Text and Methodology Q2 (R1). International Conference on Harmonization of Technical Requirements For Registration Of Pharmaceuticals For Human Use, Switzerland, 2005, 17 p. https://www.ich.org/
18. Rubashvili, I.; Karukhnishvili, N.; Loria, K.; Dvali, N. Validation of swab sampling and HPLC methods for determination of meloxicam residues on pharmaceutical manufacturing equipment surfaces for cleaning validation. Turkish Journal of Pharmaceutical Sciences, 2015, 12(3), pp. 287-298. http://www.turkjps.org/
19. Rubashvili, I.; Karukhnishvili, N.; Makharadze, K.; Tsitsishvili, V. Development and validation of quantitative determination and sampling methods for acetaminophen residues on pharmaceutical equipment surfaces. Bulletin of the Georgian National Academy of Sciences, 2018, 12(1), pp. 107-112. http://science.org.ge/bnas/vol-12-1.html

CHEMISTRY JOURNAL OF MOLDOVA. General, Industrial and Ecological Chemistry. 2020, 15(1), 21-30
ISSN (p) 1857-1727 ISSN (e) 2345-1688
http://cjm.asm.md
http://dx.doi.org/10.19261/cjm.2019.650

TOWARD A MULTIDISCIPLINARY STRATEGY FOR THE CLASSIFICATION AND REUSE OF IRON AND MANGANESE MINING WASTES

Daniela Guglietta [a], Girolamo Belardi [a], Giovanna Cappai [a,b], Barbara Casentini [c], Alicia Godeas [f], Stefano Milia [a], Daniele Passeri [a], Rosamaria Salvatori [d], Adalgisa Scotti [e], Vanesa Silvani [f], Emanuela Tempesta [a], Stefano Ubaldini [a], Francesca Trapasso [a*]

[a]*Institute of Environmental Geology and Geoengineering, Italian National Research Council, Research Area of Rome 1, 9, Provinciale 35d str., Monterotondo 00015, Italy*
[b]*Department of Civil-Environmental Engineering and Architecture, University of Cagliari, 2, Marengo str., Cagliari 09123, Italy*
[c]*Water Research Institute, Italian National Research Council, Research Area of Rome 1, 9, Provinciale 35d str., Monterotondo 00015, Italy*
[d]*Institute of Atmospheric Pollution Research, Italian National Research Council, Research Area of Rome 1, 9, Provinciale 35d str., Monterotondo 00015, Italy*
[e]*International Center for Earth Sciences, National Atomic Energy Commission, San Rafael M5600, Argentina*
[f]*Faculty of Exact and Natural Science, University of Buenos Aires-CONICET, Institute of Biodiversity, Experimental and Applied Biology, Ciudad Universitaria, 2160, Intendente Guiraldes str., Buenos Aires C1428EGA, Argentina*
[*]*e-mail: francesca.trapasso@igag.cnr.it; phone: (+39 06) 906 72 606; fax: (+39 06) 906 72 733*

Abstract. Mining and mineral-processing wastes have been giving a lot of concern in recent times. This paper has evaluated an integrated multidisciplinary strategy for mining wastes characterization, their possible recycling and reuse, and critical raw materials recovery. After the *in situ* sampling campaigns, mining wastes have been characterized and the acquired mineralogical, chemical and spectral information have been used to create a map of mining waste deposits by means of the new multispectral satellite Sentinel-2A classification. The use of Fe-Mn rich wastes in arsenic removal and phosphorus recovery from water was discussed. Furthermore, mycorrhizal-assisted phytoextraction of metals from contaminated soils classified as Class 1 to 4 by remote sensing showed a good potential for their possible recovery from biomass, and results indicated that the system was suitable for the uptake of several elements. Results are encouraging and the application of such approach can be important to develop a circular model for sustainable exploitation of mining wastes.

Keywords: mining waste, metal recovery, recycle, remote sensing analysis.

Received: 29 October 2019/ Revised final: 02 April 2020/ Accepted: 10 April 2020

Introduction

Resource constraints and environmental pressures are going to accelerate the transformation from a linear extraction-use-throw away model of production and consumption to a circular one. Moving towards a near-zero waste society not only has an environmental rationale, it increasingly becomes a factor of competitiveness. In fact, the technological progress and quality of life are reliant on access to a growing number of raw materials [1]. In this context mining waste not of interest for steel industry because of the low iron content and need of prior ore dressing, can find a valuable use in applications other than mining industry.

Our research has been addressed to mining wastes of one of the largest iron and manganese ore deposits in the State of Odisha (India). In particular, the materials considered not suitable for steel production are dumped in overburden dumps as waste and at the same time, the materials having higher percentage of iron are stored for future use purposes as subgrade. The wastes are particularly rich in iron, manganese and aluminium oxy-hydroxides and represent an important resource because they could be reused as adsorption filters for metals and metalloids, arsenic, as well as in phosphorus removal and recovery from treated wastewater. Iron, aluminium and manganese oxy-hydroxides are

well known adsorbents for the removal of arsenic from waters [2,3]. The possible influence of chemical, spectral and mineralogical properties for a more successful selection of suitable wastes in terms of arsenic removal efficiency has been widely discussed [4]. The potential for recovery and recycling of phosphorus is widely explored in the last decades [5]. On one side, to prevent the load of phosphate present in wastewaters onto surface water bodies with consequent impact on their ecological status [6,7]. On the other side, phosphorus availability as raw materials is critical and different technological solutions to its recovery are now pursued [8-10].

A secondary approach to transform mining wastes into valuable resources is phytoremediation, specifically phyto-mycoremediation, at greatly reduced costs and minimum side effects [11]. Roots of hyperaccumulator plant species establish mutualistic arbuscular mycorrhizal symbiosis with fungi of the phylum *Glomeromycota* [12]. The arbuscular mycorrhizal symbiosis is frequently included in the bioremediation strategies of different metal polluted soils [12-14]. Many studies have demonstrated that the arbuscular mycorrhizal association established between sunflowers (*Helianthus annuus* L.) and the fungus *Rhizophagus intraradices* is effective for the uptake and accumulation of heavy metals [12,13]. Thus, this property could be also used to recover elements from biomass by hydrometallurgical methods.

In the last years, remote sensing technologies have been used to investigate the mining areas finalized to map the spatial distribution of minerals in tailings [15]. However, it is very difficult to have, at the same time, satellite images and mineralogical and geochemical data concerning surface-outcropping materials. It would be important to create synergies between remote sensing and laboratory analysis in order to optimize resources and reduce waste. As a continuation of our research, herein we explore the possibility of classification and reuse of iron and manganese mining wastes to promote the transition to a more circular model of mining wastes sustainable exploration towards near-zero waste, as presented in Figure 1.

The aim of this paper is the identification and classification of mining wastes, the sample collection, analysis and characterization as well as phyto-mycroremediation. Thus, firstly, the capacity of satellite Sentinel-2A is used to classify mining wastes and to identify deposit areas with different percentage of iron and manganese; secondly, the field sampling campaign is conducted to collect mining wastes samples for the laboratory analyses and characterization for the potential reuse for the arsenic removal and phosphorus recovery from water; and lastly, the phyto-mycoremediation of classified mining wastes for raw materials uptake is explored.

Experimental

Samples preparation

During *in situ* sampling campaign, 37 different kinds of samples (rock as well as soil) were collected in the Joda West Iron and Manganese mine, located in village of Joda (Keonjhar district, State of Odisha, India) (Figure 2).

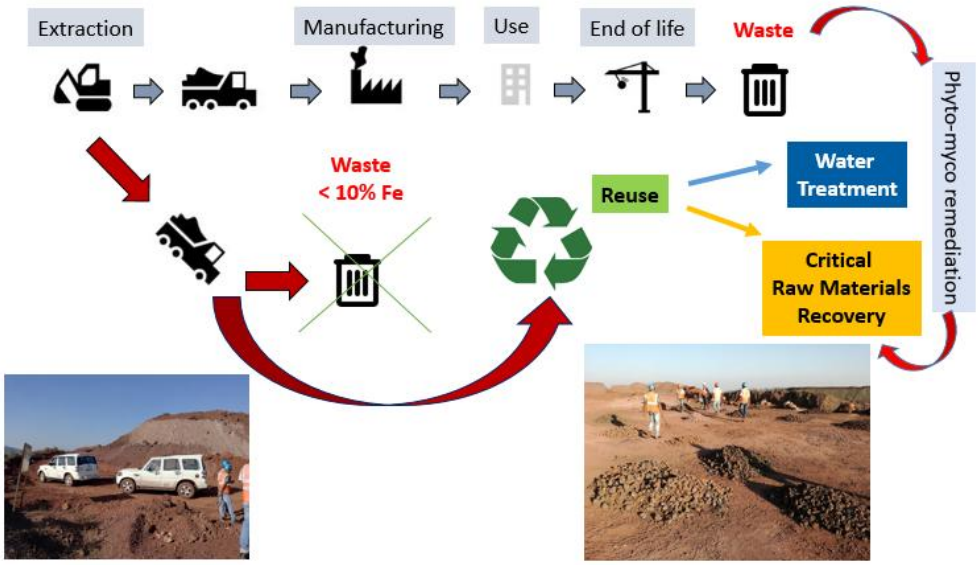

Figure 1. A scheme of the proposed multidisciplinary strategy for classification and reuse of iron and manganese mining wastes.

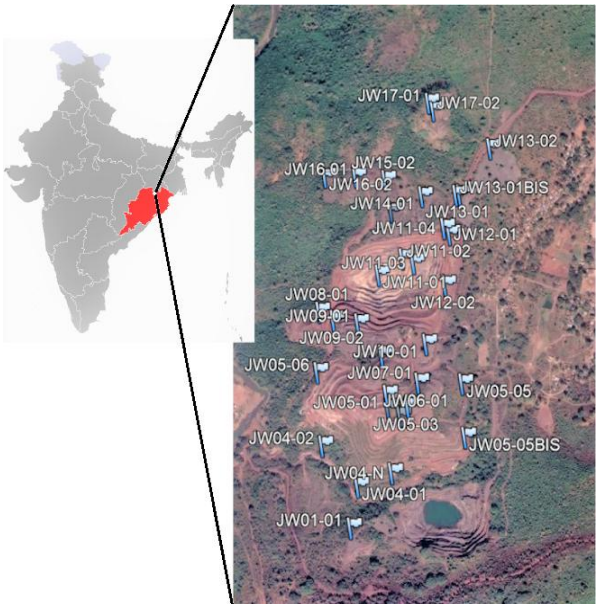

Figure 2. Location of the study area and *in situ* sampling campaign.

From 1933 onward, the mining lease was granted in favour of the TATA Steel, which offered general support during field work performed for this study. For each sample, GPS coordinates, pictures, brief description of the sampling area have been stored. Furthermore, small quantities of samples (for each sample about 200 g) have been selected to further mineralogical and physical analysis at the National Research Council in Italy.

The collected samples were micronized under 70 µ in size by a vibrating rotary cup mill (Willy Bleuler) at 900 rpm motor speed and a standard 100 mL steel crews, and used further in our studies.

Instrumentation

Physical and mineralogical characterization of the soil samples was done by X-ray powder diffraction (XRD) using a Bruker AXS D8 advance diffractometer and X-ray fluorescence (XRF) analysis using the X-ray EDS fluorescence spectrometer (XEPOS HE model).

Arsenic content in solution was determined by atomic absorption spectrometry (AAS, Perkin Elmer AAnalyst 800).

Phosphate content was determined using Hach DR2800 spectrophotometer.

Solution pH was measured using a Hach PHC101 pH-meter connected to a Hach HQ30D digital multiparametric probes reader.

Preliminary evaluation tests of Fe-Mn mining wastes reuse

Arsenic removal and phosphate ions recovery

Five samples, (*JW0504*, *JW1201*, *JW1301bis a*, *JW1301bis b*, and *JW1302*) rich in iron, aluminium and manganese, were selected for evaluation of arsenic removal from the solution.

Batch tests were performed using 50 mg of fine grained (under 70 µ) mining waste materials dispersed in 100 mL MilliQ solution spiked to a level of 1 mg/L As(V) by stock solution of 1 g/L prepared by weighing $Na_2HAsO_4 \cdot 7H_2O$ (Fluka). Samples were collected at time intervals of 0 min, 5 min, 30 min, 60 min, 120 min, 20 hours and 6 days. Samples were mildly shaken at 240 osc/min on a rotatory table throughout the test and filtered onto 0.45 µm cellulose acetate filters, afterwards the content of arsenic in solution was analysed. At the end of the experiment (after 6 days), collected samples were also analysed by inductively coupled plasma mass spectrometry (ICP-MS Agilent 7500c), prior to 0.45 µm filtration and acidification with 2% HNO_3 Suprapur (Merck) to verify possible leaching into water of other potentially toxic metals present in selected materials as evidenced by XRF measurements.

The sample with highest arsenic adsorption capacity was then evaluated for phosphate recovery. A sample portion of 1 g was placed in 50 mL flask containing 40 mL of wastewater solution of 5 mg/L of PO_4^{3-}. The kinetic of phosphate adsorption was evaluated in duplicate at different time intervals 0, 0.5, 1, 2, 4 and 24 hours. Phosphate content was determined by the spectrophotometric method at 882 nm after the formation of a blue molybdenum complex. Batch pH during the adsorption test was maintained constant at 7.0±0.5.

Mycorrhizal assisted phytoremediation

The phyto-mycoremediation system consisted of sunflowers (*Helianthus annuus* L., hybrid cultivar DK4045, Syngenta seeds) colonized by an arbuscular mycorrhizal fungal strain GA5 *Rhizophagus intraradices* (provided *in vitro* by Bank of Glomeromycota, Faculty of Exact and Natural Sciences, Buenos Aires University) grown in a substrate consisting of a homogeneous mixture of soil and volcanic ash (50:50, v/v) supplemented with $ZnSO_4$ (as catalyst).

The soil samples were collected in the Joda West Iron and Manganese mine (Keonjhar district, State of Odisha, India). Volcanic ash was provided by Pumex S.P.A. (Lipari Island, Italy). Granular pumice stone (diameter, 3-6 mm) was provided by Europomice S.R.L. (Italy). Fertile commercial topsoil was provided by Euroterriflora S.R.L. (Italy).

A substrate sample (10 g) was used to detect arbuscular mycorrhizal fungal structures;

it was wet sieved, decanted and checked for arbuscular mycorrhizal fungal spores. Non-indigenous arbuscular mycorrhizal fungal propagules were detected in soil samples. The GA5 strain was propagated as described in Silvani, V.A. *et al.* [16]. The arbuscular mycorrhizal fungus *R. intraradices* strain GA5 has been reported to promote tolerance to different abiotic stresses in several plant species and is a potential bioremediator [17,18].

The experimental design of the TRL 2 system consisted of 16 pots (height, 12 cm; diameter, 13.5 cm), as named and detailed below:

- *CS1-4*$^+$: 4 pots filled with mixed contaminated soil (*CS*) from different areas of the Indian mine and Lipari's volcanic ash (*VA*) in a 1:1 (v/v) ratio, completing to 500 mL and 125 mL granular pumice stone (*PS*; mean diameter, 3-6 mm). Considering the *CS* only, 300-500 ppm $ZnSO_4$ (as catalyst) was added. At least three *Helianthus annuus* seeds were planted and inoculated with a piece of GA5 *in vitro* culture with at least 300 spores in each pot;
- *CS1-4*$^-$: 4 pots filled with mixed *CS* and *VA* in a 1:1 (v/v) ratio, and 125 mL *PS*. Considering the *CS* only, 300-500 ppm $ZnSO_4$ was added. At least three *Helianthus annuus* seeds were planted in each pot;
- *BLS1-4*$^+$: 4 pots filled with 500 mL fertile commercial topsoil (FCT) and 125 mL *PS* by spot. At least three *Helianthus annuus* seeds were planted and inoculated with a piece of GA5 *in vitro* culture with at least 300 spores in each pot;
- *BLS1-4*$^-$: 4 pots filled with 500 mL FCT and 125 mL *PS* by spot. At least three *Helianthus annuus* seeds were planted in each pot.

As to *CS1-4*$^+$ and *CS1-4*$^-$, composition of mixed *CS* from different areas of the Indian mine is reported in Figure 3. Representative soil samples were taken from each pot on days 0 and 133 (*i.e.* the end of the experimental campaign). Samples were dried to constant weight for metals content quantification by the XRF technique.

On day 133, *Helianthus annuus* was removed from each pot, shoots and roots were separated and carefully rinsed with distilled water, dried in an oven (45°C) and analysed by XRF (Wavelength dispersive X-ray fluorescence spectrometer, Panalytical Venus 200), as well as *CS1-4*$^+$, *CS1-4*$^-$, *BLS1-4*$^+$ and *BLS1-4*$^-$. A subsample of roots was stained with trypan blue [19] and intraradical colonization by the arbuscular mycorrhizal fungus GA5 strain was checked. The frequency of mycorrhizal colonization was calculated as the percentage of root segments containing arbuscular mycorrhizal fungal structures. All measurements were performed under a Nikon light binocular microscope at 100x magnification.

The bioconcentration factors (calculated as the ratio between the concentration of metals in the plant tissue and in the soil) in aerial and radicular parts (BC_S and BC_R, respectively), and translocation factors (TF, calculated as the ratio between the concentration of metals in the aerial part and in the roots) were determined for the following metals: As, Ca, Cr, Cu, Fe, Ga, K, Mn, Ni, P, Rb, S, Sr, Ti, Zn.

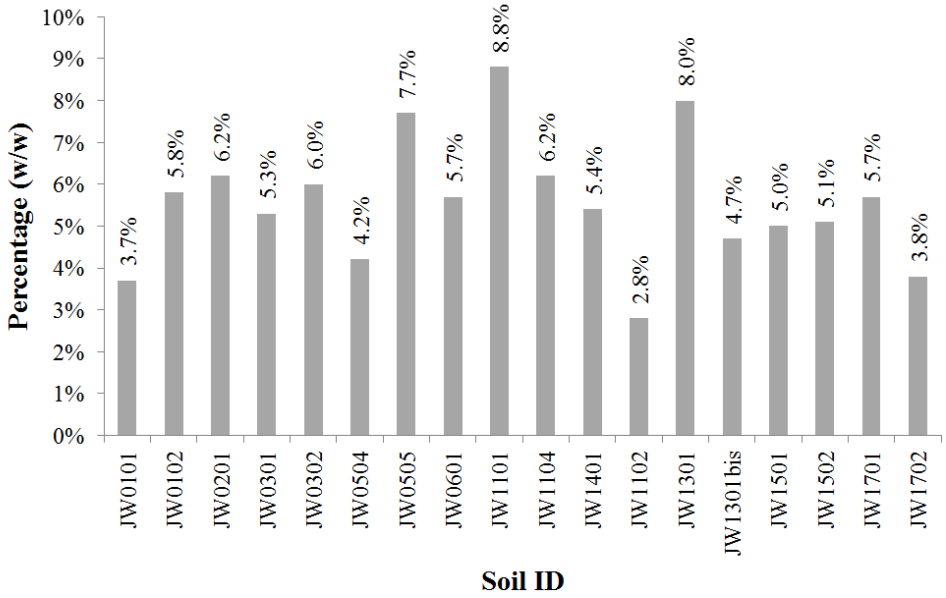

Figure 3. Composition of mixed contaminated soil used to carry out the phyto-mycoremediation experiments.

Results and discussion

Waste mining map by Sentinel-2A satellite

Evaluation of the capability of remote data in characterizing the reflectance of a specific surface is based on their ability in distinguishing one spectrum of specific surface from another, in other words, on their ability in measuring the spectral similarity between one spectrum and another.

In this research, one Sentinel-2A satellite data acquisition was carried out on the iron and manganese mining area on November 29th, 2017 and the sampling sites were recognized on the georeferenced image. For each site, the corresponding spectral signature was extracted by the image and the different spectral classes have been individuated by means of the interpretation of chemical and mineralogical analysis. Afterwards, the map of iron and manganese wastes was obtained through the spectral similarity measurements achieved by the principal supervised classifiers: the classifier used in this methodology was Spectral Angle Mapper (SAM) [20].

The results of SAM classification were represented in an iron and manganese waste mining map that highlights waste deposit areas with different mean percentage of iron and manganese (Figure 4).

In particular, the presence of vegetation in Class 1 indicates that the wastes have been accumulated over an extended period compared to Class 2, characterized by a steady accumulation of extractive wastes. Class 3 is very rich in iron and manganese but these deposits of residues are not of interest for steel industry and need prior ore dressing. Finally, in Class 4 there are wastes with lower iron and manganese content.

Image accuracy was computed matching the ground truth classes with the classification result classes. The accuracy of the classification, derived from the confusion matrix, resulted as follows:

- user's accuracy = 94.81%;
- producer's accuracy = 95.23%;
- overall accuracy = 95.88%; k= 0.806.

These results point out the capacity of Sentinel-2A to classify mining wastes but also to identify deposits with valuable materials in order to reuse for secondary applications. In particular, the deposit areas of residues rich in iron and manganese represent the potential site for further analysis (*i.e.* arsenic removal and phyto-mycoremediation application).

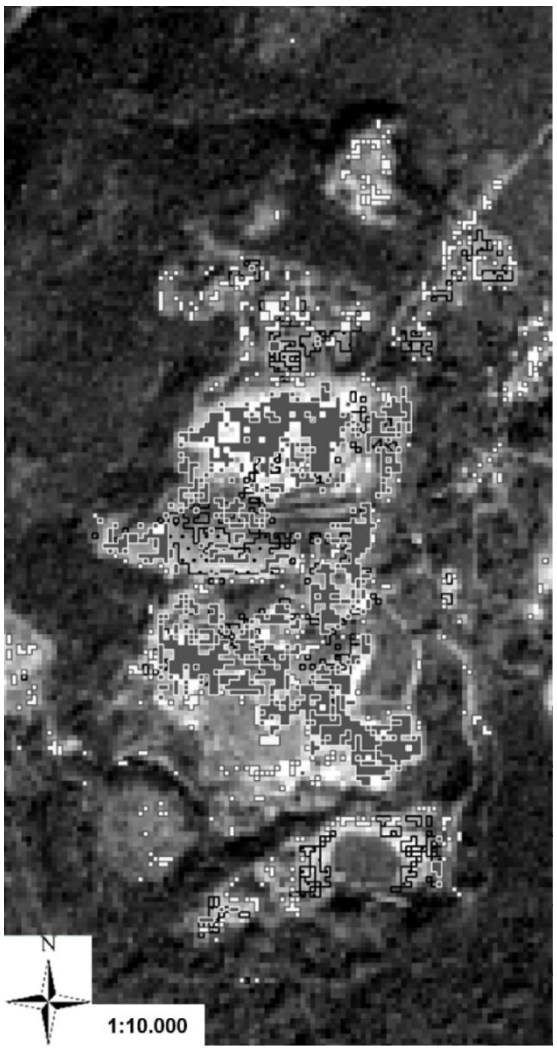

	Fe mean (%)	Mn mean (%)
Class 1	37.99	13.18
Class 2	40.34	9.6
Class 3	42.44	18.2
Class 4	22.86	1.3

Figure 4. Iron and manganese mining wastes deposits map. The four classes have been overlaid on Sentinel-2A image of the location map.

Arsenic removal efficiency

A selection of five samples was carried out among all characterized samples, based on iron, manganese and aluminium content and major mineralogical phases (Tables 1 and 2).

Among all iron oxides minerals (magnetite, lepidocrocite, maghemite, goethite, ferrihydrite, and hematite), according to XRD results (Table 1) the mostly present were iron hydroxides phases including hematite and goethite, while sample *JW0504* was selected due to its high percentage of aluminium (52.5% kaolinite). Manganese content was up to 46.9% in sample *JW1301bis b*. It should be observed that in these samples the presence of potentially toxic metals, including arsenic, was not always negligible. Chromium content was almost 400 mg/kg and lead about 300 mg/kg in sample *JW0504*. Preliminary kinetic batch adsorption tests were conducted to evaluate the efficiency in As(V) removal by selected waste materials (Figure 5).

At selected solid/water ratio (0.5 g/L), arsenic adsorption was below 30% for all samples during the first 30 min, increasing up to 41% and 53% for sample *JW0504* and *JW1301bis a*, respectively, after 6 days of contact time. Among iron hydroxides, the presence of goethite seems to promote the adsorption. If compared to commercially available materials the adsorption kinetic of these waste materials is not fast, since usually iron oxy-hydroxide used in As removal filters, such as granular ferric hydroxide (GFH) that was used in this study, are able to remove up to 90% As within first 5 min (contact time usually used in water filtration unit). Banerjee, D. *et al*. [21] found that at lower As(V) concentration (0.1 mg/L) a solution with 0.25 adsorbent to liquid ratio was able to completely remove As(V) within 2 hours. In this study, the ability of some selected materials to adsorb 30-50% of arsenic is interesting since these wastes are low cost materials largely available at Joda mining site and the efficiency in removal could be easily increased by increasing filter volume and adsorbent amount. The adsorption capacity of the studied samples ranged from 0.41 to 1.0 mg/g (As/adsorbent), while GFH had a capacity of 1.94 mg/g (As/adsorbent). Naturally occurring iron-rich materials usually show lower adsorption capacity than synthetic oxides and iron rich ore materials tested by Zhang, W. *et al*. [22], which had a maximum adsorption capacity of 0.17-0.48 mg/g (As/adsorbent).

A possible release of potentially toxic elements in solution was investigated after 6 days and results are reported in Table 3. The mobility of other toxic metals in these samples resulted to be limited and concentrations values are far below drinking water limits (EU Directive 98/83: Cr 50 μg/L, Cu 1 mg/L and Zn are not regulated).

Table 1

Selected samples for adsorption tests, their major metals content and the dominant mineralogical components (in %).

Sample Code	*Fe*	*Al*	*Mn*	*Hematite*	*Goethite*	*Muscovite*	*Kaolinite*	*Pyrolusite*
JW1201	39.1	3.6	15.6	36.9	2.4	n.d.	22.2	n.d.
JW1301bis b	16.9	1.3	46.9	19.8	6	19.8	18.1	10.8
JW1302	28.5	2	29.1	10.8	6.7	26.1	16.8	6.3
JW0504	9.8	13.8	1.8	4.4	4.2	20.3	52.5	n.d.
JW1301bis a	49.5	3.2	1.8	23.4	25.4	20.1	15.3	n.d.

n.d. = not detectable phases

Table 2

Selected samples for adsorption tests and their trace metals content (in mg/kg).

Sample Code	*As*	*Cr*	*Cu*	*Ni*	*Pb*	*Zn*
JW1201	n.d.	17.6	35.2	41.5	44	53.5
JW1301bis b	n.d.	53.1	95.6	48.2	130	48.9
JW1302	n.d.	60.7	128.6	107.6	37	92.6
JW0504	20.5	387.3	49.4	79.4	309.5	28.9
JW1301bis a	64.7	193.4	42.3	40.8	2.8	53.7

n.d. = not detectable phases

Table 3

Release into water of potentially toxic metals after 6 days contact. (Concentration is expressed as μg/L)

Sample Code	*V*	*Cr*	*Cu*	*Zn*	*Cd*	*Pb*	*U*
JW1201	< 0.05	0.11	0.07	16.3	< 0.05	< 0.05	< 0.05
JW1301bis b	< 0.05	0.29	0.08	5.6	< 0.05	< 0.05	< 0.05
JW1302	0.07	0.14	0.06	2.0	< 0.05	< 0.05	< 0.05
JW0504	0.71	0.65	0.06	1.8	< 0.05	< 0.05	< 0.05
JW1301bis a	< 0.05	0.55	0.12	11.3	< 0.05	< 0.05	< 0.05

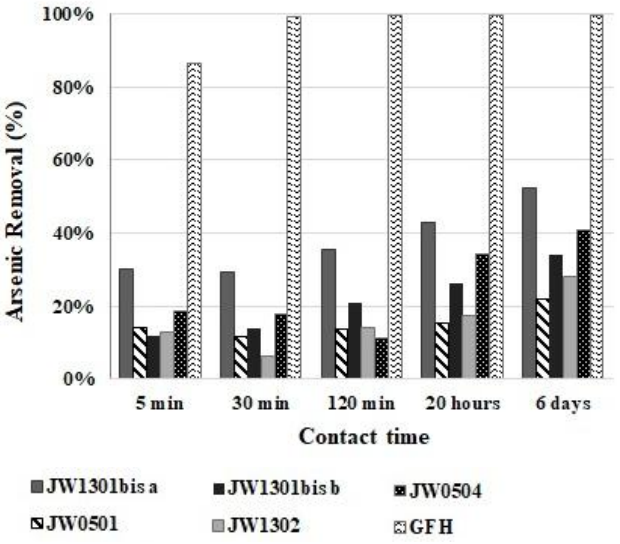

Figure 5. Batch kinetic study of As(V) removal (%) for 5 different samples (0.5 g/L) and the commercial granular ferric oxide (GFH).
Initial As(V) concentration was 1 mg/L.

Phosphate removal/recovery capacity

Sample *JW1301bis a* has shown the highest arsenic removal capacity and was further used to test also the ability to recover phosphate from a wastewater solution containing 5 mg/L of phosphate. Initial phosphate content was reduced by 95% within 30 min (Figure 6).

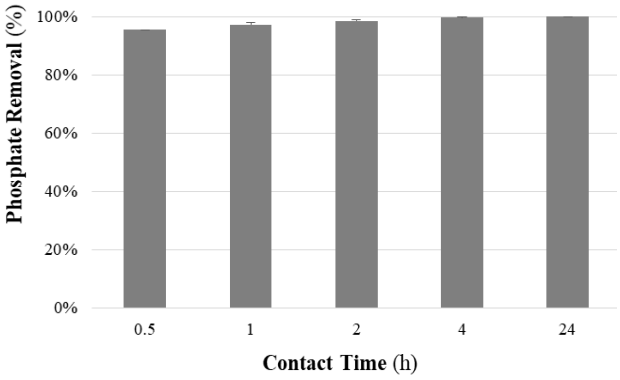

Figure 6. Phosphate removal (mean and standard deviation reported) using the sample *JW1301bis a*.

Final adsorption capacity was about 0.065 mg/g of phosphorus (the mass ratio of phosphate ions to phosphorus was 94.97/30.97 or 3.066 to 1) under neutral condition (pH= 7±0.5). Huang, W.W. *et al.* [23] tested the ability of red mud for phosphorus recovery in 1 mg/L effluent. They reported a plateau for removal after 5 hours with increasing adsorbing capacity up to 0.4 mg/g of phosphorus under acidic condition.

Phyto-mycoremediation of contaminated soil by Helianthus annuus and Rhizophagus intraradices

The concentration of elements in pots containing blank (*BLS*) and contaminated soils (*CS*), in volcanic ash (*VA*) and in granular pumice stone (*PS*) is reported in Table 1S (Supplementary material).

CS values correspond to areas classified as Class 4 by remote sensing (Figure 4) by their content (%) of Mn and Fe, 5.07±0.21 and 14.7±0.4, respectively. Although the sample extraction points correspond to areas classified by remote sensing as Class 1 and 2, the mixed proportion of the amounts of soil in each region (shown in Figure 3) and the addition of volcanic ash caused a dilution effect. *CS* values shown in Table 1S (from Supplementary material) present relevant amounts of CRMs as Ga (12.4±0.6 ppm), as well as of raw materials like Zn (1315.2±53.2 ppm), which encourage their possible recovery. Moreover, high concentrations of contaminants such as Cr (131.0±2.7 ppm) and As (11.9±0.2 ppm) are reported.

No significant difference in plant growth (*i.e.*, leaves development and length of the aerial parts) was observed among pots filled with the contaminated and the blank soils. Therefore, the presence of high contamination levels (especially of Mn and Fe) did not influence the development of *Helianthus annuus* plants. Moreover, no differences were found between mycorrhized and non-mycorrhized plants, indicating that the presence of *Rhizophagus intraradices* in roots did not influence plant growth development.

The arbuscular mycorrhizal fungus *Rhizophagus intraradices* strain GA5 colonized sunflower roots at 5±4.4% and 42±5.4% in the CS^+ and BLS^+ treatments, respectively. Typical arbuscular mycorrhizal fungal structures were observed in sunflower roots with abundant vesicles and hyphae (Figure 7*(a)*). As expected, no arbuscular mycorrhizal root colonization was observed in the BLS^- and CS^- treatments (Figure 7*(b)*).

Table 2S (Supplementary material) reports the average concentration of elements in $CS1\text{-}4^+$ and $CS1\text{-}4^-$, as well as in related biomass (shoots and roots) after the phyto-mycoremediation treatment. Preliminary results indicated that the system was suitable for the uptake of some elements: Mn, Fe, Zn, P, Cr, Cu, Ga and As. A similar result was also found by Rivelli, A.R. *et al*. [24] for uptake of Zn, Cd and Cu, and for Mn by Hajiboland, R. *et al*. [25].

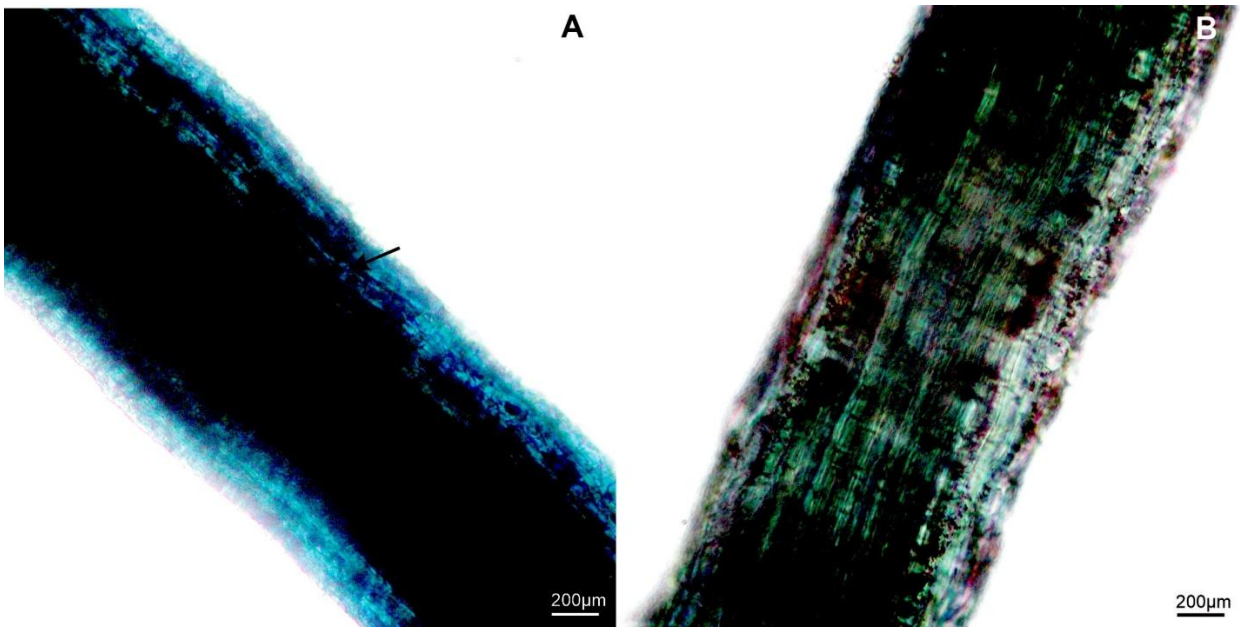

(a) ***(b)***

Figure 7. Root colonization of sunflower plant by the arbuscular mycorrhizal fungus *Rhizophagus intraradices* GA5 strain after 133 days.
***(a)* Detail of sunflower roots with intraradical hyphae, arbuscules and vesicles developed by the arbuscular mycorrhizal fungus are indicated by the arrow.**
***(b)* Uncolonized root of sunflower plant in control treatment.**

Table 4

Bioconcentration and translocation factors measured in *CS1-4*$^+$ and *CS1-4*$^-$.

	As	*Ca*	*Cr*	*Cu*	*Fe*	*Ga*	*K*	*Mn*	*P*	*Ni*	*Rb*	*S*	*Sr*	*Ti*	*Zn*
BC_S^+	0.17	2.14	0.02	0.26	0.00	1.57	3.50	0.01	5.35	0.02	1.44	5.28	3.65	0.01	0.90
BC_S^-	0.12	1.84	0.01	0.23	0.00	1.06	3.09	0.01	3.94	0.01	1.30	5.18	2.31	0.01	0.94
BC_R^+	0.28	0.94	0.26	0.27	0.10	1.27	2.11	0.08	1.73	0.53	0.16	15.01	0.70	0.17	0.79
BC_R^-	0.52	2.19	0.09	0.60	0.19	1.71	2.28	0.15	1.20	0.21	1.39	11.53	1.26	0.37	1.14
TF^+	0.62	2.28	0.09	0.94	0.02	1.23	1.66	0.11	3.10	0.05	9.28	0.35	5.19	0.02	1.14
TF^-	0.23	0.84	0.07	0.39	0.01	0.62	1.35	0.07	3.27	0.07	0.94	0.45	1.84	0.02	0.82

The mycorrhizal colonization enhanced the uptake of Cr, P and Ni in sunflower shoots and roots, of As, Ga and Sr in shoots, while S uptake was enhanced only in sunflower roots. Conversely, the uptake of Ca, Cu, Mn, Rb, Sr, Ti and Zn was reduced in mycorrhized sunflower roots, indicating that mycorrhizal fungus *Rhizophagus intraradices* GA5 strain did not have an univocal effect on elements accumulation in biomass.

Table 4 reports the accumulation coefficients measured at the end of the experimental period. As to mycorrhized systems *CS1-4*$^+$, bioconcentration factors in shoots (BC_S^+) followed the order: P(5.35)>S>Sr>K>Ca>Ga>Rb >Zn(0.9)>Cu>As>Ni>Cr>Mn(0.01)>Ti=Fe(0.00); bioconcentration factors in roots (BC_R^+) followed the order: S(15.01)>K>P>Ga>Ca(0.94)>Zn>Sr> Ni>As>Cu>Cr>Ti>Rb>Fe(0.10)>Mn(0.08); the translocation factor followed the order: Rb(9.28)>Sr>P>Ca>K>Ga>Zn>Cu(0.94)>As>S> Mn>Cr>Ni (0.05)>Fe=Ti(0.02).

As to biomass in *CS1-4*$^-$, bioconcentration factors in shoots (BC_S^-) followed the order: S(5.2)>P>K>Sr>Ca>Rb>Ga(1.06)>Zn(0.94)>Cu >As>Ni>Mn>Ti>Cr>Fe(0.003); bioconcentration factors in roots (BC_R^-) followed the order: S(11.53)>K>Ca>Ga>Rb>Sr>P>Zn(1.14)>Cu>As >Ti>Ni>Fe>Mn>Cr(0.09); the translocation factor followed the order: P(3.3)>Sr>K>Rb(0.94)>Ca>Zn>Ga>S>Cu>As> Mn>Ni>Cr>Ti>Fe (0.01).

It should be considered that the observed values of BC_S and BC_R for Mn and Fe are low due to the very high concentration of such elements in soil, rather than to a poor bioconcentration potential: in fact, low *BC* values coexisted with high concentrations of

Mn and Fe in biomass (Table 2S from Supplementary material).

Despite such promising results, it must be noticed that the overall biomass growth was not sufficient to sustain a significant recovery of elements at this stage (for instance by hydrometallurgical methods), therefore process conditions must be optimized in order to maximise biomass growth.

Conclusions

This methodology explores the advantage to employ an integrated approach to characterize and map as well as reuse mining wastes. The preliminary encouraging results highlight that the application of this approach is very useful and important to develop a circular model for sustainable exploitation of mining wastes towards near-zero waste.

The multispectral sensor such as MSI (MultiSpectral Imager) on Sentinel-2A provides the cheapest images that can be used for mineral land characterization. The resulting remotely mining waste mapping constitutes a valuable tool for optimizing *in situ* sampling strategies aimed at selecting more suitable mining waste to be reused.

Preliminary tests encourage further studies on the possible application of mining waste materials in water treatment, both for arsenic removal and phosphate removal/recovery. Arsenic removal was in the range of 40-60% and the efficiency could be enhanced by increasing the amount of solid material used to realize a filter. Phosphate adsorption was above 90%, therefore waste materials could also be successfully used to reduce phosphate load into surface water. Furthermore, in order to increase adsorption properties, mineralogical enrichment processes of higher adsorptive selected Fe minerals phases can be adopted. The possible release of toxic metals from these materials has been found negligible according to EU drinking water regulations.

As to phyto-mycoremediation tests, preliminary results show that it is possible to obtain the growth of the phyto-mycoremediation system in areas classified by remote sensing as Class 1, 2, 3 and 4. The observed bioconcentration factors and translocation factors values (>0.9-1.0), or the high concentration of certain elements in biomass, proved that such system was effective for the phytostabilization or phytoextraction of Fe, Mn, P, Rb, Ga, Cu, S, Sr, and Zn, although the experimental conditions should be optimized in order to obtain sufficient biomass quantities for metals recovery through hydrometallurgical methods.

Acknowledgments

This research was supported by Teco project. The authors are grateful to the staff of TATA Steel for providing general support during field work.

Supplementary information

Supplementary data are available free of charge at http://cjm.asm.md as PDF file.

References

1. Ubaldini, S.; Guglietta, D.; Trapasso, F.; Carloni, S.; Passeri, D.; Scotti, A. Treatment of secondary raw materials by innovative processes. Chemistry Journal of Moldova, 2019, 14(1), pp. 32-46. DOI: http://dx.doi.org/10.19261/cjm.2019.585
2. Mohan, D.; Pittman Jr., C.U. Arsenic removal from water/wastewater using adsorbents-A critical review. Journal of Hazardous Materials, 2007, 142, pp. 1-53. DOI: https://doi.org/10.1016/j.jhazmat.2007.01.006
3. Jeong, Y.; Fan, M.; Singh, S.; Chuang, C.L.; Saha, B.; van Leeuwen, J.H. Evaluation of iron oxide and aluminum oxide as potential arsenic(V) adsorbents. Chemical Engineering and Processing-Process Intensification, 2007, 46(10), pp. 1030-1039. DOI: https://doi.org/10.1016/j.cep.2007.05.004
4. Casentini, B.; Lazzazzara, M.; Amalfitano, S.; Salvatori, R.; Guglietta, D.; Passeri, D.; Belardi, G.; Trapasso, F. Mining rock wastes for water treatment: potential reuse of Fe- and Mn-rich materials for arsenic removal. Water, 2019, 11(9), pp. 1897. DOI: https://doi.org/10.3390/w11091897
5. Cordell, D.; Rosemarin, A.; Schroeder, J.J.; Smit, A.L. Towards global phosphorus security: A systems framework for phosphorus recovery and reuse options. Chemosphere, 2011, 84(6), pp. 747-758. DOI: https://doi.org/10.1016/j.chemosphere.2011.02.032
6. Carpenter, S.R.; Caraco, N.F.; Correll, D.L.; Howarth, R.W.; Sharpley, A.N.; Smith, V.H. Nonpoint pollution of surface waters with phosphorus and nitrogen. Ecological Applications, 1998, 8(3), pp. 559-568. DOI: https://doi.org/10.1890/1051-0761(1998)008[0559:NPOSWW]2.0.CO;2
7. Jarvie, H.P.; Neal, C.; Withers, P.J.A. Sewage-effluent phosphorus: a greater risk to river eutrophication than agricultural phosphorus? Science of the Total Environment, 2006, 360(1-3), pp. 246-253. DOI: https://doi.org/10.1016/j.scitotenv.2005.08.038
8. Pan, B.; Wu, J.; Pan, B.; Lv, L.; Zhang, W.; Xiao, L.; Wang, X.; Tao, X.; Zheng, S. Development of polymer-based nanosized hydrated ferric oxides (HFOs) for enhanced phosphate removal from waste effluents. Water Research, 2009, 43(17), pp. 4421-4429.

DOI: https://doi.org/10.1016/j.watres.2009.06.055
9. Blaney, L.M.; Cinar, S.; SenGupta, A.K. Hybrid anion exchanger for trace phosphate removal from water and wastewater. Water Research, 2007, 41(7), pp. 1603-1613. DOI: https://doi.org/10.1016/j.watres.2007.01.008
10. Yan, L.G; Xu, Y.Y.; Yu, H.Q.; Xin, X.D.; Wei, Q.; Du, B. Adsorption of phosphate from aqueous solution by hydroxy-aluminum, hydroxy-iron and hydroxy-iron–aluminum pillared bentonites. Journal of Hazardous Materials, 2010, 179(1-3), pp. 244-250. DOI: https://doi.org/10.1016/j.jhazmat.2010.02.086
11. Glick, B.R. Phytoremediation: synergistic use of plants and bacteria to clean up the environment. Biotechnology Advances, 2003, 21(5), pp. 383-393. DOI: https://doi.org/10.1016/S0734-9750(03)00055-7
12. Smith, S.E.; Read, D.J. Mycorrhizal Symbiosis. 3rd Edition, Academic Press: London, 2008, 800 p. https://www.elsevier.com/books/mycorrhizal-symbiosis/smith/978-0-12-370526-6
13. Ker, K; Charest, C. Nickel remediation by AM-colonized sunflower. Mycorrhiza, 2010, 20, pp. 399-406. DOI: https://doi.org/10.1007/s00572-009-0293-7
14. Yang, Y.; Liang, Y.; Han, X.; Chiu, T.Y.; Ghosh, A.; Chen, H.; Tang, M. The roles of arbuscular mycorrhizal fungi (AMF) in phytoremediation and tree-herb interactions in Pb contaminated soil. Scientific Reports, 2016, 6, pp. 20469. DOI: https://doi.org/10.1038/srep20469
15. Zabcic, N.; Rivard, B.; Ong, C.; Mueller, A. Using airborne hyperspectral data to characterize the surface pH and mineralogy of pyrite mine tailings. International Journal of Applied Earth Observation and Geoinformation, 2014, 32, pp. 152-162. DOI: https://doi.org/10.1016/j.jag.2014.04.008
16. Silvani, V.A.; Bidondo, L.F.; Bompadre, M.J.; Colombo, R.P.; Pérgola, M.; Bompadre, A.; Fracchia, S.; Godeas, A. Growth dynamics of geographically different arbuscular mycorrhizal fungal isolates belonging to the 'Rhizophagus clade' under monoxenic conditions. Mycologia, 2014, 106(5), pp. 963-975. DOI: https://doi.org/10.3852/13-118
17. Bompadre, M.J.; Silvani, V.A.; Bidondo, L.F.; Ríos de Molina, M.C.; Colombo, R.P.; Pardo, A.G.; Godeas, A.M. Arbuscular mycorrhizal fungi alleviate oxidative stress in pomegranate plants growing under different irrigation conditions. Botany, 2014, 92(3), pp. 187-193. DOI: https://doi.org/10.1139/cjb-2013-0169
18. Scotti, A.; Silvani, V.A.; Cerioni, J.; Visciglia, M.; Benavidez, M.; Godeas A. Pilot testing of a bioremediation system for water and soils contaminated with heavy metals: vegetable depuration module. International Journal of Phytoremediation, 2019, 21(9), pp. 899-907. DOI: https://doi.org/10.1080/15226514.2019.1583634
19. Phillips, J.M.; Hayman, D.S. Improved procedures for clearing roots and staining parasitic and vesicular-arbuscular mycorrhizal fungi for rapid assessment of infection. Transactions of the British Mycological Society, 1970, 55(1), pp. 158-161. DOI: https://doi.org/10.1016/S0007-1536(70)80110-3
20. Kruse, F.A.; Lefkoff, A.B.; Boardman, J.W.; Heidebrecht, K.B.; Shapiro, A.T.; Barloon, P.J.; Goetz, A.F.H. The spectral image processing system (SIPS) - Interactive visualization and analysis of imaging spectrometer data. Remote Sensing of Environment, 1993, 44(2-3), pp. 145-163. DOI: https://doi.org/10.1016/0034-4257(93)90013-N
21. Banerjee, D.; Lelandais, G.; Shukla, S.; Mukhopadhyay, G.; Jacq, C.; Devaux, F.; Prasad, R. Responses of pathogenic and nonpathogenic yeast species to steroids reveal the functioning and evolution of multidrug resistance transcriptional networks. Eukaryotic cell, 2008, 7(1), pp. 68-77. DOI: https://doi.org/10.1128/EC.00256-07
22. Zhang, W.; Singh, P.; Paling, E.; Delides, S. Arsenic removal from contaminated water by natural iron ores. Minerals Engineering, 2004, 17(4), pp. 517-524. DOI: https://doi.org/10.1016/j.mineng.2003.11.020
23. Huang, W.; Wang, S.; Zhu, Z.; Li, L.; Yao, X.; Rudolph, V.; Haghseresht, F. Phosphate removal from wastewater using red mud. Journal of Hazardous Materials, 2008, 158(1), pp. 35-42. DOI: https://doi.org/10.1016/j.jhazmat.2008.01.061
24. Rivelli, A.R.; De Maria, S.; Puschenreiter, M.; Gherbin, P. Accumulation of cadmium, zinc, and copper by *Helianthus Annuus L.*: impact on plant growth and uptake of nutritional elements. International Journal of Phytoremediation, 2012, 14(4), pp. 320-334. DOI: https://doi.org/10.1080/15226514.2011.620649
25. Hajiboland, R.; Aliasgharpour, M.; Dashtbani, F.; Movafeghi, A.; Dadpour, M.R. Localization and study of histochemical effects of excess Mn in Sunflower (*Helianthus annuus* L. cv. Azarghol) plants. Journal of Sciences, Islamic Republic of Iran, 2008, 19(4), pp. 305-315. https://jsciences.ut.ac.ir/article_31902.html

CHEMISTRY JOURNAL OF MOLDOVA. General, Industrial and Ecological Chemistry. 2020, 15(1), 31-40
ISSN (p) 1857-1727 ISSN (e) 2345-1688
http://cjm.asm.md
http://dx.doi.org/10.19261/cjm.2020.664

SYNTHESIS OF DIFFERENT STRUCTURAL TYPES OF ZEOLITES IN THE HALLOYSITE-DOLOMITE-OBSIDIAN SYSTEM

Gunel Mamedova

Institute of Natural Resources, Nakhchivan branch of the Azerbaijan National Academy of Sciences, 76, Heydar Aliyev ave., Nakhchivan AZ 7000, Azerbaijan
e-mail: gunelmamadova@mail.ru; phone: (+94 45) 036 76 948

Abstract. Gismondine, laumontite and levyne type zeolites have been synthesized based on the natural minerals of Nakhchivan and the optimal crystallization conditions have been established. The influence of temperature, alkaline solution concentration, ratio of starting components and time of processing on the synthesis process has been studied. The mineral resources of Nakhchivan − halloysite deposits of Pirigel, dolomite deposits of Negram and obsidian deposits of Zangezur served as samples. The initial components and the reaction products have been examined by X-ray diffraction, thermogravimetric and elemental analysis. The optimal conditions for the synthesis of gismondine zeolite with a 100% crystallinity are as follows: temperature of 200°C, alkaline solution of 2 N NaOH, ratio of the initial components of halloysite (H):dolomite (D):obsidian (O)= 1:1:1, processing time of 50 hours. The optimal conditions for laumontite synthesis are: temperature of 220°C, alkaline solution of NaOH of 1 N, H:D:O= 1:3:1, processing time of 75 hours. The optimal conditions for levyne are: temperature of 200°C, alkaline solution of KOH of 4 N, H:D:O= 2:1:2, processing time of 100 hours. It was found that changes in the temperature, alkalinity, ratio of starting components and time of processing of the reaction have different effects on the rate of formation of products, on their degree of crystallinity and on the phase purity of the obtained zeolite.

Keywords: hydrothermal synthesis, zeolite, gismondine, laumontite, levyne.

Received: 13 January 2020/ Revised final: 21 April 2020/ Accepted: 26 April 2020

Introduction

The synthesis of zeolites can be carried out on the basis of a wide range of starting components. The synthesis, study of physicochemical properties and applications of zeolites, as well as their implementation based on the local natural resources are currently a promising and relevant field in modern chemistry.

In the zeolites synthesis, diverse materials are used as a source of silicon and aluminum: clay [1-4], natural and synthetic glasses [5,6], diatoms [7], natural aluminosilicates [8-10], halloysite [11], including feldspars [12,13], zeolite-bearing rocks [14-16], industrial fly ash [17,18], *etc*. These starting materials mainly differ from each other in structural and chemical characteristics. As a cost-effective alternative for the synthesis of zeolites, is the use of natural mineral resources instead of chemical raw materials. In this work, halloysite deposits of Pirigel, dolomite deposits of Negram and obsidian deposits of Zangezur were used as initial local materials for the synthesis of different structural types of zeolites.

Due to their structural features, zeolites such as gismondine, laumontite and levyne are important for their use in catalysis and ion exchange. According to the literature data, gismondine was used in water purification from cations of strontium, barium, magnesium, and also, as a highly active and selective catalyst for the production of biofuels [19,20]. Laumontite was used as an adsorbent, an ion exchanger in catalytic systems, and a raw material for producing nanomaterials [21].

The gismondine framework topology consists of two sets of intersecting, doubly connected 4-membered rings linked into double crankshaft chains [22,23]. The laumontite framework exhibits two different types of four-membered rings, those where SiO_4 and AlO_4 alternate and those formed only by SiO_4 tetrahedra [24]. The crystal structure of levyne is built up of layers of single and double six-membered rings of $(Si,Al)O_4$ tetrahedra and cations are all disposed along the symmetry axis inside the levyne cage [25].

The purpose of this research work is the rational use of local natural resources of the Nakhchivan Autonomous Republic for the synthesis of gismondine, laumontite and levyne

zeolites; identification of the optimal conditions; evaluation of the influence of temperature and alkalinity on the crystallization process.

Experimental

Materials

The mineral resources of Nakhchivan Autonomous Republic − halloysite deposits of Pirigel, dolomite deposits of Negram and obsidian deposits of Zangezur served as samples.

Sodium and potassium hydroxides (flake, 99% purity, Alfa Aesar GmbH & Co KG, Germany) have been used as received without further purification.

Synthesis

Hydrothermal synthesis of gismondine, laumontite and levyne has been carried out in Morey autoclaves made of 45MNFT stainless steel. The synthesis has been studied in the temperature range from 100 to 250°C, the concentration of the alkaline solution varied from 0.5 to 5 N, the autoclaving time varied from 10 to 200 hours and the fullness degree was of 70-75%. Solid-liquid ratio was 1:10. After crystallization was completed, the final material was separated from the initial solution, washed with distilled water from excess alkali, and dried at 70–80°C. NaOH and KOH have been used as alkaline solutions.

Characterization techniques

The *X-ray diffraction* measurements were performed using the X-ray analyser 2D PHASER "Bruker" (Cu K_α radiation, 2θ= 5−50°), using of NaCl, SiO_2 (quartz) and pure zeolites in internal and external standards. Samples have been placed on a front mounted plastic sample holder. The measuring conditions have been as follows: step size of 0.15 s/step, nickel filter as incident beam, slit aperture of 0.3°.

The *thermogravimetric analysis* of the samples has been carried out on a "Derivatograph-Q 1500-D" of the Hungarian company MOM in the dynamic mode in the temperature range 20-1000°C. Shooting mode: heating rate of 20°/min; paper speed of 2.5 mm/min; the sensitivity of DTA, DTG and TG was 500 mv; ceramic crucibles with Al_2O_3 as standard.

Elemental analysis of the starting materials and their obtained products has been carried out on a Launch of Trition XL dilution refrigerator "Oxford instrument" multichannel X-ray spectrometer. Measurement mode: Pd - anode, voltage 25 kW, current strength 70 MA, exposure time 100 s, sensitivity limit of 10^{-2}. Samples have been prepared as follows: the analyte has been diluted with $Li_2B_4O_7$ flux (ratio 1:10) at a temperature of 1250°C. The resulting glass has been crushed and pressed under the pressure of 20 t/cm^2 with a holding time of 1 min.

Results and discussion

General characterization of the starting materials

An analysis of the scientific literature showed that numerous works have been done on the synthesis of gismondine [26-28], laumontite [29], levyne [30-33]. The difference of this work in relation to the above is in the use of natural mineral resources of the country, as well as in the conditions of synthesis.

The initial components and the reaction products have been examined by X-ray diffraction, thermogravimetric and elemental analysis. The chemical composition of the collected mineral resources samples is presented in Tables 1-3, showing that the local mineral resources of Nakhchivan are distinguished by phase purity, thus making possible their use as starting materials in the synthesis of zeolites.

Table 1

Chemical analysis of major elements (wt.%) of the halloysite deposit of Pirigel.

Element	*Weight*	*Amount of oxide*	*Formula*
Si	29.37	44.52	SiO_2
Al	20.54	32.78	Al_2O_3
Ca	1.17	2.33	CaO
Na	0.63	0.78	Na_2O
K	0.79	0.93	K_2O
Mg	2.23	3.15	MgO
Fe	0.98	1.47	Fe_2O_3
Fe	0.73	0.87	FeO
Ti	0.12	0.24	TiO_2
O	43.44		
		12.93	H_2O
Total	100.00		

Table 2

Chemical analysis of major elements (wt.%) of the dolomite deposit of Negram.

Element	*Weight*	*Amount of oxide*	*Formula*
Ca	26.38	31.34	CaO
Mg	17.43	23.44	MgO
Na	0.77	0.93	Na_2O
K	0.65	0.82	K_2O
Si	3.93	7.43	SiO_2
Fe	0.98	1.07	FeO
C	15.03	34.97	CO_2
O	34.83		
Total	100.00		

Table 3

Chemical analysis of major elements (wt.%) of the obsidian deposit of Zangezur.

Element	*Weight*	*Amount of oxide*	*Formula*
Si	29.37	44.42	SiO_2
Al	20.54	32.68	Al_2O_3
Ca	1.17	2.33	CaO
Na	0.63	0.78	Na_2O
K	0.79	0.93	K_2O
Mg	2.23	3.15	MgO
Fe	0.98	1.47	Fe_2O_3
Fe	0.73	0.87	FeO
Ti	0.12	0.24	TiO_2
Mg	0.10	0.20	MgO
O	43.34		
		12.93	H_2O
Total	100.00		

X-ray diffraction patterns of the initial mineral resources − halloysite and dolomite of Nakhchivan are shown in Figure 1. Since obsidian is amorphous, its diffraction pattern is not presented. The comparison of X-ray experimental data with the known literature [34] showed that the test sample is the halloysite clay mineral (Figure 1*(a)*). In the X-ray diffraction pattern, the interplanar spacing is 10.48; 9.77; 4.41; 3.62; 1.48 Å being characteristic for halloysite, which is dominant in the sample. Values of interplanar distances (*d*) are equal to 15.3; 11.5; 4.50; 3.07; 2.62 Å and suggest the presence of montmorilonite in the sample. According to the diffraction pattern, quartz is also present in the sample (*d*= 4.24; 3.34; 2.45; 2.28; 1.81 Å). In the natural mineral - dolomite, besides the main mineral (*d*= 3.70; 3.34; 2.88; 2.19; 1.78 Å), in the composition of the sample also can be detected quartz in a small amount (*d*= 4.24; 3.34; 2.45; 2.28; 1.81 Å) (Figure 1*(b)*). X-ray diffraction patterns and thermograms of the synthesized gismondine, laumontite and levyne zeolites are presented in Figures 2 and 3, respectively.

According to results presented in Figure 2, the obtained zeolites are characterized by a high degree of crystallinity demonstrated by phase purity. Comparison of the experimental values of interplanar spacings (*d*, Å) with theoretical and calculated ones has shown that the obtained diffraction patterns indicate the obtaining of phase-pure gismondine, laumontite and levyne zeolites. In the presented diffraction patterns, peaks with a relative intensity of 100% characterize the baseline of the synthesized zeolites. For gismondine, a baseline with 100% relative intensity is characterized by a value of *d*= 4.27; 3.18 Å, for laumontite of 9.57 Å and for levyne of 8.15; 4.08 Å, which is in good agreement with the literature data [34]. According to the X-ray phase analysis, gismondine crystallizes in the monoclinic crystal system $P112_1/a$ with the unit cell parameters *a*= 9.84 Å; *b*= 10.02 Å; *c*= 10.62 Å, *β*= 92°25′; laumontite in the monoclinic crystal system $C12/m1$ with *a*= 14.90 Å; *b*= 13.17 Å; *c*= 7.50 Å, *β*= 111°30'; levyne – in the rhombohedral crystal system $R\bar{3}m$ with *a*= 10.75 Å, *α*= 76°25', which also is in good agreement with the reference data [34].

Using the thermogravimetric analysis, the region of dehydration and thermostability of the synthesized zeolites has been established (Figure 3). The DTA curve presented in Figure 3*(a)*, in the case of gismondine zeolite is characterized by one endothermic and one exothermic effect.

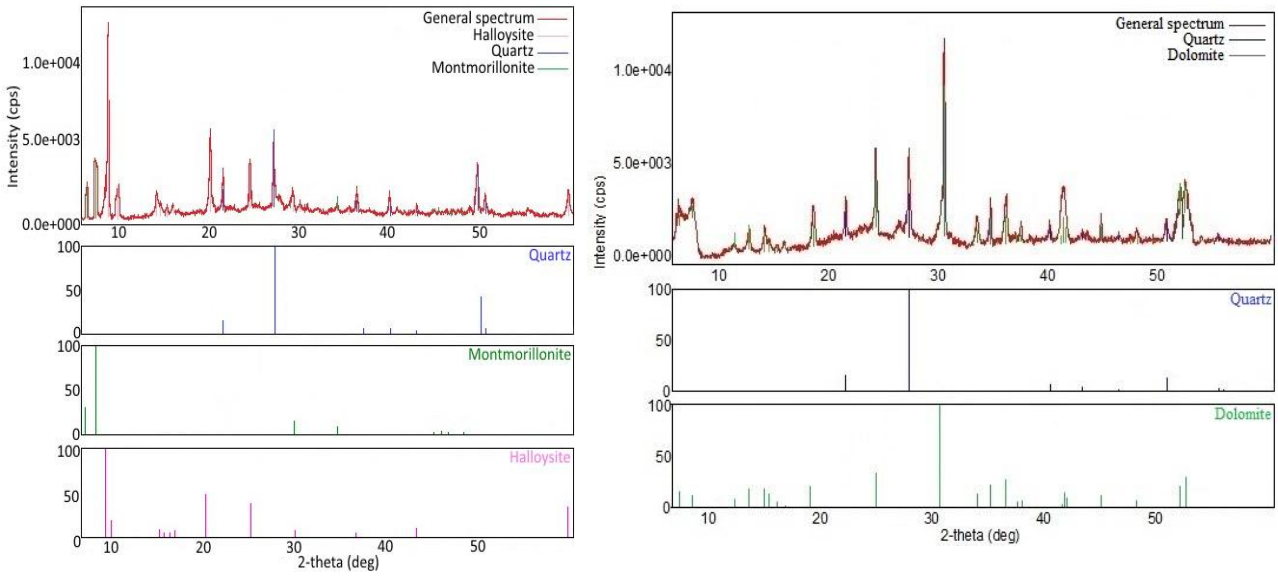

(a) ***(b)***

Figure 1. X-ray diffraction patterns of the starting components: halloysite *(a)* and dolomite *(b)*.

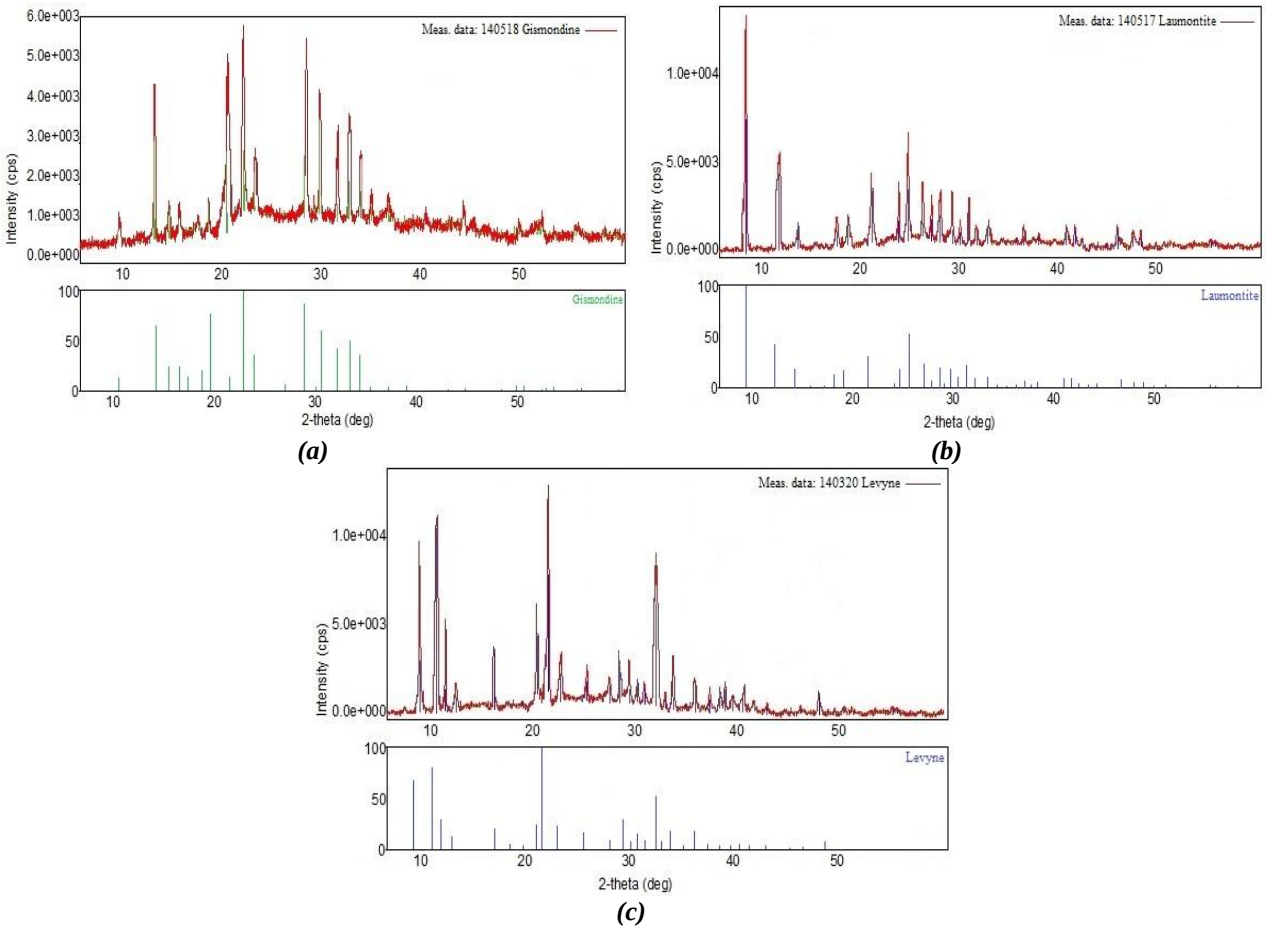

Figure 2. X-ray diffraction patterns of the synthesized zeolites obtained under optimal conditions with a 100% degree of crystallinity: gismondine *(a)*, laumontite *(b)* and levyne *(c)*.

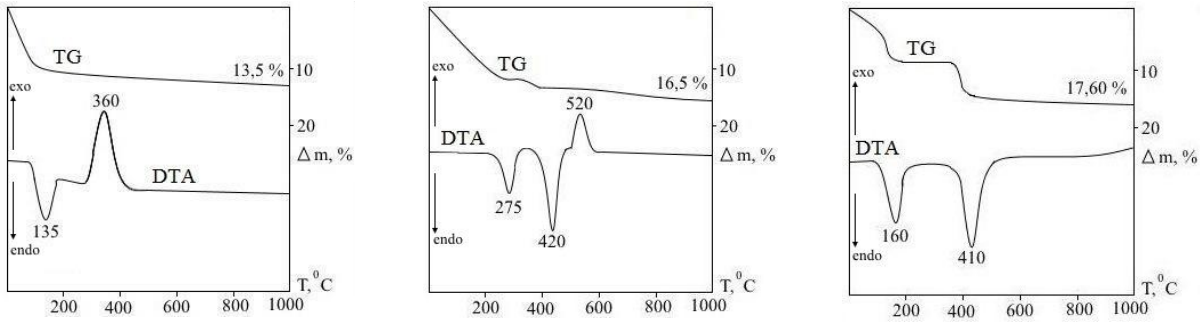

Figure 3. Thermograms of the zeolites obtained under optimal conditions: gismondine *(a)*, laumontite *(b)* and levyne *(c)*.

The endothermic effect corresponds to the dehydration of the sample with a maximum of 135°C, at which the weight loss along the TG curve is 13.5%. The exothermic effect, detected at a temperature with a maximum of 360°C, according to X-ray diffraction analysis, refers to the formation of fieldspar - anorthite. The DTA curve of laumontite (Figure 3*(b)*) is characterized by two endothermic and one exothermic effect. The first two endothermic effects relate to dehydration of the sample, which occurs in stages with maxima at 275 and 420°C, with a 16.5% weight loss along the TG curve. The exothermic effect detected at a temperature of 520°C, according to X-ray diffraction analysis, refers to the formation of anorthite. For levyne the DTA curve (Figure 3*(c)*) is characterized by two endo-effects thus the dehydration occurs in two stages in a wide temperature range from 100 (max. 160°C) to 500°C (max. 410°C) with 17.60% weight loss. As shown by X-ray diffraction analysis, the structure of levyne is stable at 1000°C.

Zeolites are very sensitive to changes in synthesis conditions, namely temperature, alkalinity and processing time [35]. The effect of temperature, alkaline solution concentration, the ratio of the starting components and processing time on the crystallization process of the synthesized zeolites has been studied. Figures 4, 6 and 8 show the kinetic curves of crystallization process of the synthesized zeolites.

Gismondine synthesis

The crystallization process of gismondine has been studied at temperatures of 180°C, 200°C and 240°C (Figure 4). Studies have shown that the optimum crystallization temperature of gismondine with a high degree of crystallinity is 200°C.

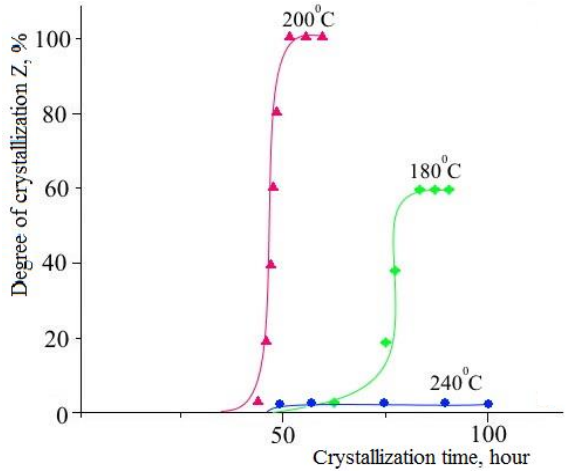

Figure 4. Kinetic curves of crystallization process of gismondine.

At a temperature of 180°C, the crystallization process is not completed, and gismondine is obtained with a low degree of crystallinity. At a temperature of 240°C, the product of synthesis is anorthite.

The studies conducted at various concentrations of alkaline solution (NaOH, 1.0–3.0 N) showed that, in addition to gismondine, quartz and anorthite are present in the reaction product at 1.0 N NaOH. At a concentration of alkaline solution of 3.0 N, the structure of gismondine is destroyed and phillipsite and anorthite crystallize. The optimal concentration of NaOH to obtain gismondine with high crystallinity is 2.0 N. The effect of the ratio of the starting components on the crystallization of gismondine has showed that, the halloysite increase leads to crystallization of phillipsite and anorthite in addition to gismondine, and an increase of dolomite to the synthesis of anorthite. The increasing of the obsidian content promotes crystallization of phillipsite and quartz. The optimal ratio of the starting components is H:D:O= 1:1:1. The optimal crystallization time of gismondine is 50 hours. Less than 50 hours of processing time (starting from 10 hours) contributes to the formation of gismondine with a low degree of crystallinity, while increasing the processing time to 100 hours promotes the transition of gismondine into phillipsite and anorthite. X-ray diffraction patterns of crystallization products in the case of gismondine are presented in Figure 5.

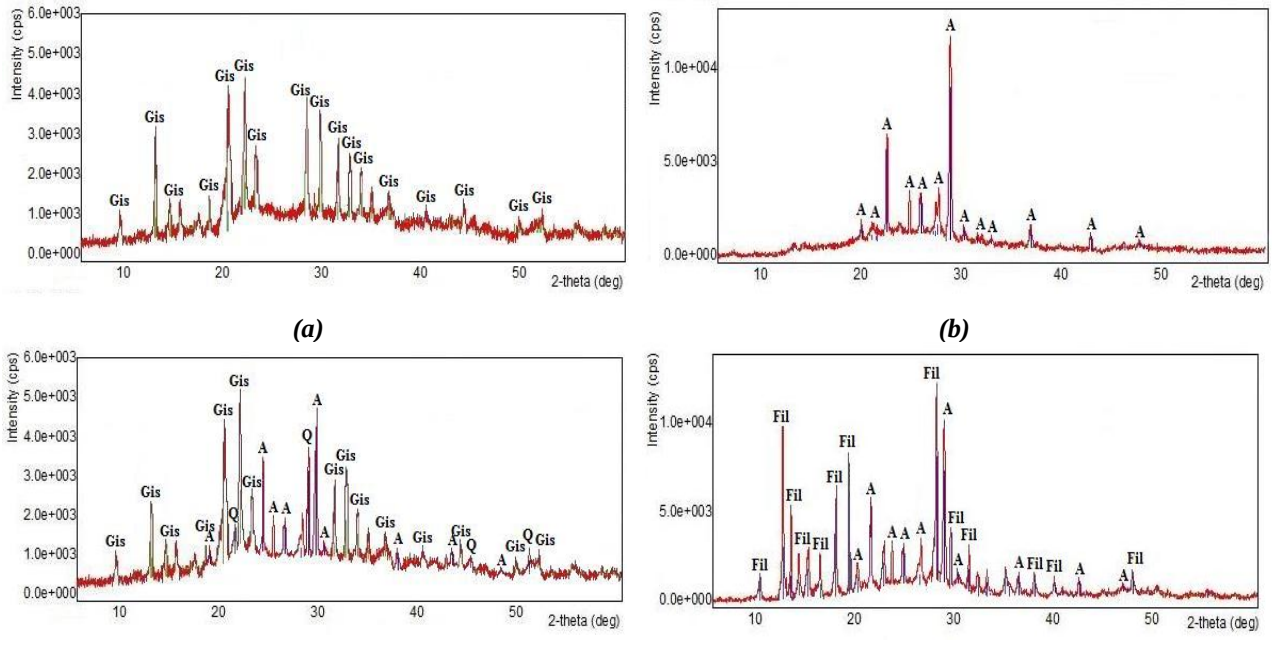

Figure 5. X-ray diffraction patterns of the products in the case of gismondine at synthesis conditions: 180°C *(a)*; 240°C *(b)*; 1.0 N NaOH *(c)*; 3.0 N NaOH *(d)* (Gis – gismondine, A – anorthite, Q – quartz, Fil – phillipsite).

Laumontite synthesis

The synthesis of laumontite has been studied at temperatures of 180°C, 200°C, 220°C and 240°C (Figure 6). A study of the temperature influence has shown that, at 180°C, clinoptilolite, quartz and anorthite have been obtained; at 200°C, clinoptilolite, laumontite with low crystallinity and quartz, and at 240°C, wairakite with a high degree of crystallinity have been obtained. The temperature of 220°C is optimal for the synthesis of laumontite with a high degree of crystallinity. The study of the influence of the concentration of NaOH solution (in the range of 0.5–2.5 N) has showed that at 0.5 N, clinoptilolite and quartz are obtained; at 2.0 N, clinoptilolite and wairakite and at 2.5 N, wairakite crystallize. The optimal NaOH concentration for the synthesis of laumontite with a high degree of crystallinity is 1.0 N.

The study of influence of the ratio of starting components has showed that, the increase of halloysite content leads to crystallization of wairakite and quartz in addition to laumontite (Figure 7). An increase of dolomite content leads to the synthesis of clinoptilolite and increase of obsidian to wairakite synthesis. The optimal ratio in obtaining highly crystallized laumontite is H:D:O= 1:3:1.

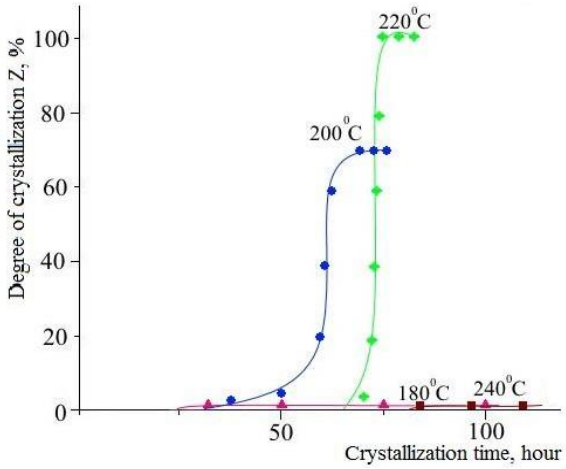

Figure 6. Kinetic curves of crystallization process of laumontite.

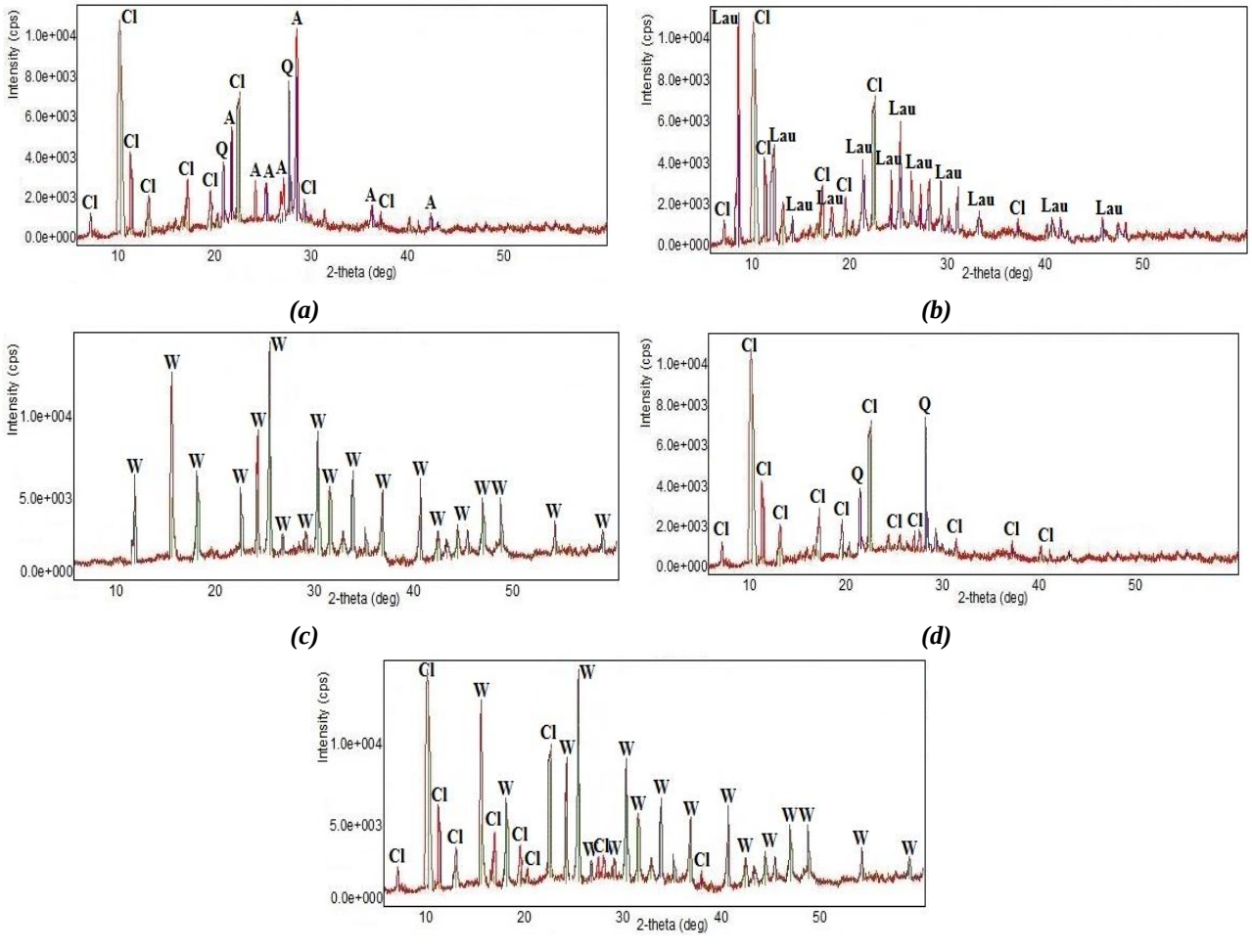

Figure 7. X-ray diffraction patterns of the products in the case of laumontite at synthesis conditions: 180°C *(a)*; 200°C *(b)*; 240°C and 2.5 N NaOH *(c)*; 0.5 N NaOH *(d)*; 2.0 N NaOH *(e)* (Cl – clinoptilolite, A – anorthite, Q – quartz, Lau – laumontite, W – wairakite).

Processing for 50 hours leads to the formation of laumontite with a low degree of crystallinity, and when the processing time is increased to 100 hours, laumontite transition into wairakite. The optimal processing time was established at 75 hours. X-ray diffraction patterns of crystallization products in the case of laumontite are presented in Figure 7.

Levyne synthesis

The crystallization kinetics of levyne zeolite has been studied at temperatures of 180°C, 200°C and 210°C (Figure 8). The obtained results (Figures 8 and 9) show that levyne zeolite does not form at 180°C, its formation occurs at 210°C, but the product with 100% degree of crystallinity is not obtained. At a temperature, above 210°C, hydrothermal crystallization changes its direction and zeolite-levyne recrystallizes into zeolite-phillipsite. The crystallization of zeolite at 200°C is very intense and the zeolite-levyne with a high degree of crystallization is obtained. Analysis of the hydrothermal reaction products has shown that crystallization reaches a maximum within 100 hours.

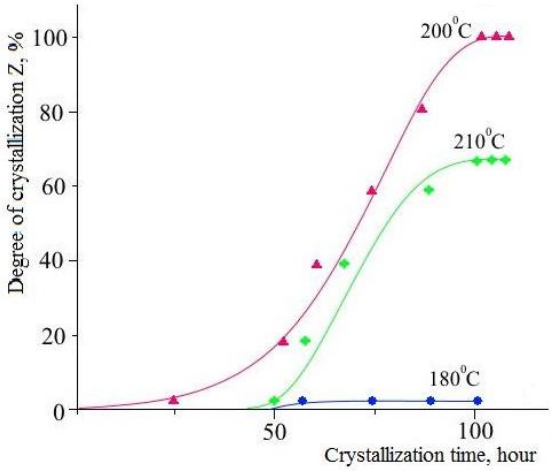

Figure 8. Kinetic curves of crystallization process of levyne.

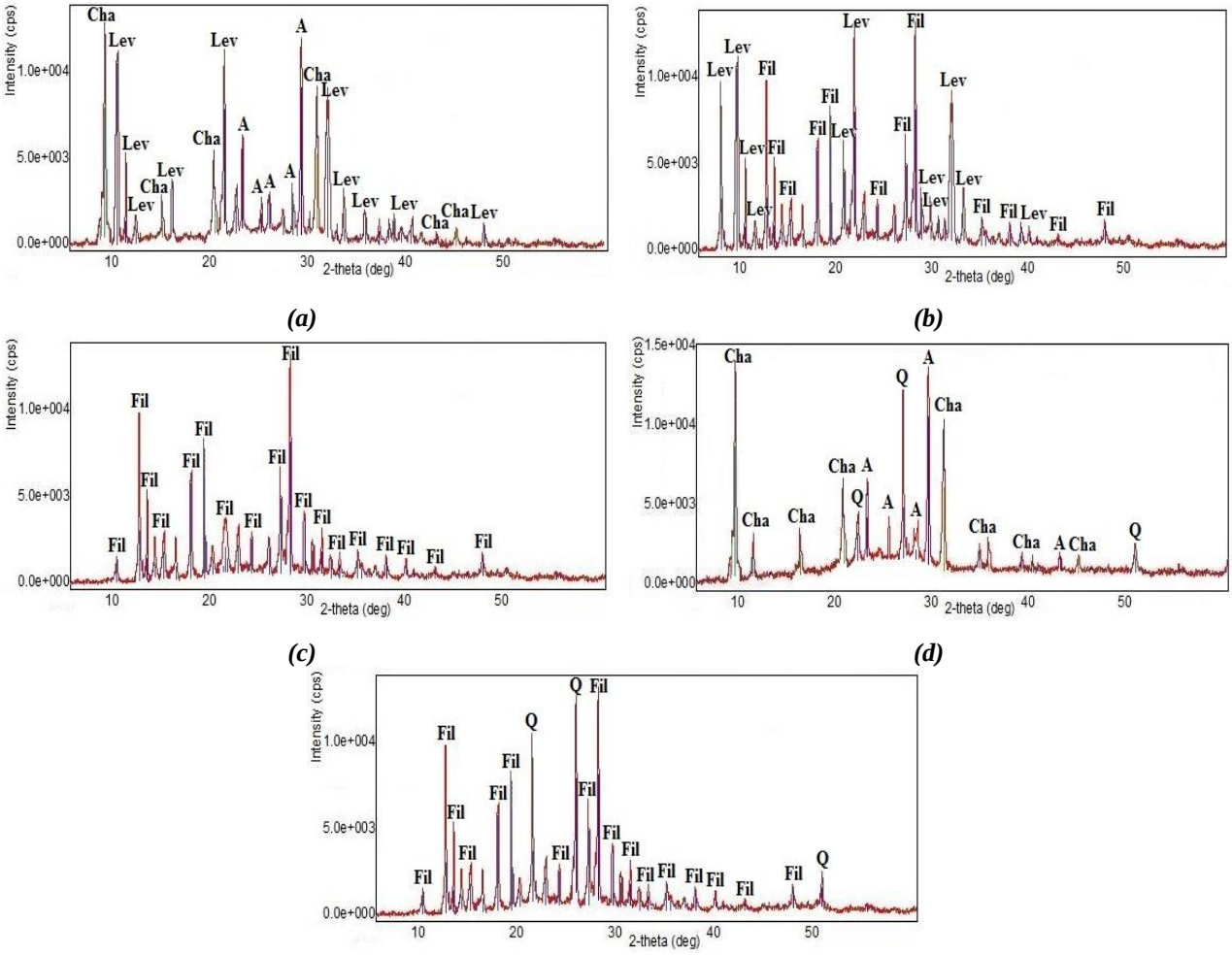

Figure 9. X-ray diffraction patterns of the products in the case of levyne at synthesis conditions: 180°C *(a)*; 210°C *(b)*; > 210°C *(c)*; 2.0-3.5 N KOH *(d)*; 4.5-5.0 N KOH *(e)* (Lev – levyne, Cha – chabazite, A – anorthite, Fil – phillipsite, Q – quartz).

The influence of the concentration of the KOH solution has been studied in the range 2.5–5.0 N. The optimal concentration of the alkaline solution for the synthesis of levyne with a high degree of crystallinity is 4.0 N. At a concentration of the alkaline solution below 4.0 N, in the range 2.0–3.5 N, chabazite, anorthite, and quartz have been identified in the crystallization products. Increasing the concentration above 4.0 N, 4.5–5.0 N, leads to crystallization of phillipsite and quartz. The optimal ratio of the starting components in the crystallization of levyne with a high degree of crystallinity is H:D:O= 2:1:2. A decrease of halloysite or obsidian in the content contributes to the formation of levyne with a low degree of crystallinity. An increase of dolomite leads crystallization of phillipsite, chabazite and quartz. Processing for 50 hours leads to the formation of chabazite with a low degree of crystallinity and quartz, and when the crystallization time is increased to 150 hours, levyne transition to phillipsite. The optimal processing time is 100 hours. X-ray diffraction patterns of crystallization products in the case of levyne are presented in Figure 9.

Optimal synthesis conditions

Gismondine, laumontite and levyne with a 100% degree of crystallinity have been obtained under the following optimal conditions: temperature of 200°C, solvent concentration of 2.0 N NaOH, ratio of the initial components of halloysite (H):dolomite (D):obsidian (O)= 1:1:1, processing time of 50 hours; temperature of 220°C, solvent concentration of NaOH of 1.0 N, H:D:O= 1:3:1, processing time of 75 hours; temperature of 200°C, solvent concentration of 4.0 N KOH, H:D:O= 2:1:2, processing time of 100 hours, respectively. A representation of the optimal synthesis process of zeolites of gismondine, laumontite and levyne with a 100% degree of crystallinity is shown in Scheme 1.

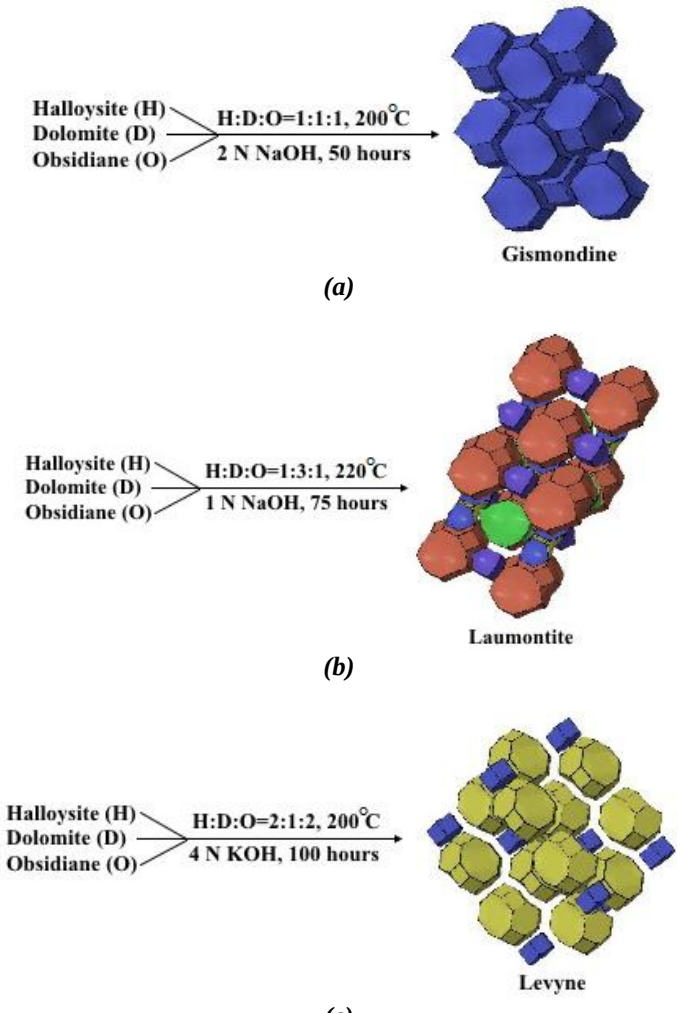

Scheme 1. The optimal conditions of the process for the synthesis of zeolites with a 100% crystallinity: gismondine *(a)*, laumontite *(b)* and levyne *(c)*.

The use of KOH, instead of NaOH, in the case of levyne, as an alkaline solution, is explained by the fact that the synthesis in KOH solutions lead to the formation of levyne with a 100% degree of crystallinity. Most likely, in the case of crystallization of levyne in a solution of NaOH, Na^+ cations interfere to obtain the product with a 100% degree of crystallinity. For this reason, KOH solutions have been used and allowed to obtain positive results.

Conclusions

The natural mineral resources of Nakhchivan have been used for the synthesis of zeolites such as gismondine, laumontite and levyne.

Crystallization kinetics and the effect of temperature, alkaline solution concentration, processing time, the ratio of the starting components on the speed, direction and crystallinity of zeolites have been studied. Gismondine with a 100% degree of crystallinity has been obtained at temperature of 200°C, alkaline solution concentration of 2 N NaOH, ratio of the initial components of halloysite (H):dolomite (D):obsidian (O)= 1:1:1, processing time of 50 hours. The optimal conditions for the synthesis of laumontite with a 100% degree of crystallinity are temperature 220°C, alkaline solution concentration of 1 N NaOH, H:D:O= 1:3:1, crystallization time of 75 hours. In the case of levyne, the optimal conditions included temperature of 200°C, alkaline solution concentration of 4 N KOH, H:D:O= 2:1:2, synthesis time of 100 hours.

According to the obtained experimental data, even small changes in the synthesis conditions lead to obtain various products. It has been found that changes in temperature, alkaline solution concentration, processing time and the ratio of the starting components differently affect the rate of formation of products, their degree of crystallinity, the phase purity of the obtained zeolite. According to X-ray phase analysis, it has been found that, under the selected optimal conditions, the synthesized zeolites are characterized by a high degree of crystallinity.

References

1. Olaremu, A.G.; Odebunmi, E.O.; Nwosu, F.O.; Adeola, A.O.; Abayomi, T.G. Synthesis of zeolite from kaolin clay from Erusu Akoko Southwestern Nigeria. Journal of Chemical Society of Nigeria, 2018, 43(3), pp. 381-386. http://journals.chemsociety.org.ng/index.php/jcsn/article/view/188
2. Li, X.-Y.; Jiang, Y.; Liu, X.-Q.; Shi, L.-Y.; Zhang, D.-Y.; Sun, L.-B. Direct synthesis of zeolites from a natural clay, attapulgite. ACS Sustainable Chemistry & Engineering, 2017, 5(7), pp. 6124-6130. DOI: https://doi.org/10.1021/acssuschemeng.7b01001
3. Gougazeh, M.; Buhl, J.-Ch. Synthesis and characterization of zeolite A by hydrothermal transformation of natural Jordanian kaolin. Journal of the Association of Arab Universities for Basic and Applied Sciences, 2014, 15(1), pp. 35-42. DOI: https://doi.org/10.1016/j.jaubas.2013.03.007
4. Moneim, M.A.; Ahmed, E.A. Synthesis of faujasite from Egyptian clays: characterizations and removal of heavy metals. Geomaterials, 2015, 5(2), pp. 68-76. DOI: 10.4236/gm.2015.52007
5. Belviso, C. EMT-type zeolite synthesized from obsidian. Microporous and Mesoporous Materials, 2016, 226, pp. 325-330. DOI: https://doi.org/10.1016/j.micromeso.2016.01.048
6. Grela, A.; Lach, M.; Bajda, T.; Mikula, J.; Hebda, M. Characterization of the products obtained from alkaline conversion of tuff and metakaolin. Journal of Thermal Analysis and Calorimetry, 2018, 133, pp. 217-226. DOI: https://doi.org/10.1007/s10973-018-6970-z
7. Anderson, M.W.; Holmes, S.M.; Mann, R.; Foran, P.; Cundy, C.S. Zeolitisation of Diatoms. Journal of Nanoscience and Nanotechnology, 2005, 5(1), pp. 92-95. DOI: https://doi.org/10.1166/jnn.2005.022
8. Faghihian, H.; Godazandeha, N. Synthesis of nano crystalline zeolite Y from bentonite. Journal of Porous Materials, 2009, 16, pp. 331-335. DOI: https://doi.org/10.1007/s10934-008-9204-0
9. Rios, C.A.; Williams, C.D. Synthesis of zeolitic materials from natural clinker: A new alternative for recycling coal combustion by-products. Fuel, 2008, 87(12), pp. 2482-2492. DOI: https://doi.org/10.1016/j.fuel.2008.03.014
10. Sandoval, M.V.; Henao, J.A.; Rios, C.A.; Williams, C.D.; Apperley, D.C. Synthesis and characterization of zeotype ANA framework by hydrothermal reaction of natural clinker. Fuel, 2009, 88(2), pp. 272-281. DOI: https://doi.org/10.1016/j.fuel.2008.08.017
11. Gualtieri, A.F. Synthesis of sodium zeolites from a natural halloysite. Physics and Chemistry of Minerals, 2001, 28, pp. 719-728. DOI: https://doi.org/10.1007/s002690100197
12. Su, S.; Ma, H.; Chuan, X. Hydrothermal synthesis of zeolite A from K-feldspar and its crystallization mechanism. Advanced Powder Technology, 2016, 27(1), pp. 139-144. DOI: https://doi.org/10.1016/j.apt.2015.11.011
13. Galbarczyk-Gasiorowska, L.; Slaby, E. Experimental investigation of the reaction: An-rich plagioclase + quartz + fluid = analcime-wairakitess. Acta Geologica Polonica, 2001, 51(2), pp. 155-162. https://geojournals.pgi.gov.pl/agp/article/view/10350
14. Sariman, S. Synthesis of Na-A zeolite from natural zeolites. Indonesian Mining Journal, 2005, 8(01),

pp. 37-51. https://jurnal.tekmira.esdm.go.id/index.php/imj/article/view/210
15. Tatlier, M.; Atalay-Oral, C. Crystallization of zeolite A coatings from natural zeolite. Materials Research, 2016, 19(6), pp. 1469-1477. DOI: http://doi.org/10.1590/1980-5373-mr-2016-0564
16. Mamedova, G.A. Modification of a Nakhchivan natural zeolite in the alkaline environment. Moscow University Chemistry Bulletin, 2019, 74, pp. 46-53. (in Russian). DOI: https://doi.org/10.3103/S0027131419010085
17. Franus, W.; Wdowin, M.; Franus, M. Synthesis and characterization of zeolites prepared from industrial fly ash. Environmental Monitoring and Assessment, 2014, 186, pp. 5721-5729. DOI: https://doi.org/10.1007/s10661-014-3815-5
18. Ojha, K.; Pradhan, N.C.; Samanta, A.N. Zeolite from fly ash: synthesis and characterization. Bulletin of Materials Science, 2004, 27(6), pp. 555-564. DOI: https://doi.org/10.1007/BF02707285
19. Allen, S.; Carr, S.; Chapple, A.; Dyer, A.; Heywood, B. Ion exchange in the synthetic gismondine, zeolite MAP. Physical Chemistry Chemical Physics, 2002, 4(11), pp. 2409-2415. DOI: https://doi.org/10.1039/B111490P
20. Al-Ani, A.; Mordvinova, N.E.; Lebedev, O.I.; Khodakov, A.Y.; Zholobenko, V. Ion-exchanged zeolite P as a nanostructured catalyst for biodiesel production. Energy Reports, 2019, 5, pp. 357-363. DOI: https://doi.org/10.1016/j.egyr.2019.03.003
21. Urotadze, S.; Tsitsishvili, V.; Osipova, N.; Kvernadze, T. Laumontite – natural zeolite mineral of Georgia. Bulletin of the Georgian National Academy of Sciences, 2016, 10(1), pp. 32-37. http://science.org.ge/bnas/vol-10-1.html
22. Kol'tsova, T.N. Structures of gismondine, cymrite, anorthite, and celsian solid solutions. Inorganic Materials, 2017, 53, pp. 820-830. DOI: https://doi.org/10.1134/S0020168517080088
23. Albert, B.R.; Cheetham, A.K.; Adams, C.J. Investigations on P zeolites: synthesis and structure of the gismondine analogue, highly crystalline low-silica CaP. Microporous and Mesoporous Materials, 1998, 21(1-3), pp. 127-132. DOI: https://doi.org/10.1016/S1387-1811(97)00058-9
24. Kol'tsova, T.N. Crystal structures of zeolites with the general formula $CaAl_2Si_4O_{12} \cdot nH_2O$. Inorganic Materials, 2007, 43, pp. 176-184. DOI: https://doi.org/10.1134/S002016850702015X
25. Merlino, S.; Galli, E.; Alberti, A. The crystal structure of levyne. Tschermaks mineralogische und petrographische Mitteilungen, 1975, 22, pp. 117-129. DOI: https://doi.org/10.1007/BF01089112
26. Ghobarkar, H.; Schäf, O. Synthesis of gismondine-type zeolites by the hydrothermal method. Materials Research Bulletin, 1999, 34(4), pp. 517-525. DOI: https://doi.org/10.1016/S0025-5408(99)00052-5
27. Chen, H.-F.; Fang, J.-N.; Lo, H.-J.; Song, S.-R.; Chung, S.-H.; Chen, Y.-L.; Lin, I-C.; Li, L.-J. Syntheses of zeolites of the gismondine group. Western Pacific Earth Sciences, 2002, 2(3), pp. 331-346. http://www.earth.sinica.edu.tw/webearth-library-en/journals/wpes
28. Kotova, O.B.; Shabalin, I.N.; Shushkov, D.A.; Kocheva, L.S. Hydrothermal synthesis of zeolites from coal fly ash. Advances in Applied Ceramics, 2016, 115(3), pp. 152-157. DOI: https://doi.org/10.1179/1743676115Y.0000000063
29. Ghobarkar, H.; Schäf, O. Hydrothermal synthesis of laumontite, a zeolite. Microporous and Mesoporous Materials, 1998, 23(1-2), pp. 55-60. DOI: https://doi.org/10.1016/S1387-1811(98)00045-6
30. Tuoto, C.V.; Regina, A.; Nagy, J.B.; Nastro, A. The synthesis of Levyne-type zeolite studied by thermal analysis of methylquinuclidine aluminosilicate gels. Journal of Thermal Analysis and Calorimetry, 1998, 54, pp. 891-899. DOI: https://doi.org/10.1023/A:1010164508871
31. Tuoto, C.V.; Nagy, J.B.; Nastro, A. Synthesis and characterization of levyne type zeolite obtained from gels with different SiO_2/Al_2O_3 ratios. Studies in Surface Science and Catalysis, 1997, 105, pp. 213-220. DOI: https://doi.org/10.1016/S0167-2991(97)80558-7
32. Zhang, H.; Yang, C.; Zhu, L.; Meng, X.; Yilmaz, B.; Müller, U.; Feyen, M.; Xiao, F.-S. Organotemplate-free and seed-directed synthesis of levyne zeolite. Microporous and Mesoporous Materials, 2012, 155, pp. 1-7. DOI: https://doi.org/10.1016/j.micromeso.2011.12.051
33. Xie, B.; Zhang, H.; Yang, C.; Liu, S.; Ren, L.; Zhang, L.; Meng, X.; Yilmaz, B.; Müller, U.; Xiao, F.-S. Seed-directed synthesis of zeolites with enhanced performance in the absence of organic templates. Chemical Communications, 2011, 47(13), pp. 3945-3947. DOI: https://doi.org/10.1039/C0CC05414C
34. Treacy, M.M.J.; Higgins, J.B. Collection of Simulated XRD Powder Patterns for Zeolites. Elsevier: New York, 2001, 388 p.
35. Baerns, M. Basic Principles in Applied Catalysis. Springer: New York, 2004, 558 p. DOI: 10.1007/978-3-662-05981-4

CHEMISTRY JOURNAL OF MOLDOVA. General, Industrial and Ecological Chemistry. 2020, 15(1), 41-50
ISSN (p) 1857-1727 ISSN (e) 2345-1688
http://cjm.asm.md
http://dx.doi.org/10.19261/cjm.2020.672

ORGANOCHLORINE PESTICIDES RESIDUES IN SOIL OF SOROCA DISTRICT, REPUBLIC OF MOLDOVA

Elena Culighin

Institute of Chemistry, 3, Academiei str., Chisinau MD-2028, Republic of Moldova
e-mail: culighin.elena@gmail.com; phone: (+373 22) 73 71 44

Abstract. The level, composition, and distribution of hexachlorocyclohexane (HCH) and dichlorodiphenyltrichloroethane (DDT) residues were determined by GC-ECD technique in soil samples from the Soroca district, Republic of Moldova. The concentrations of DDTs and HCHs were up to 1100 and 640 mg/kg, respectively. The obtained results indicated that in 77% of analysed soil samples the (DDE+DDD)/DDT ratios showed aged sources of DDT pollution, suggesting that in the studied area, the DDT residues have been transformed significantly into their degradation products. The α-HCH/γ-HCH ratios were generally high (in the range of 1-28) suggesting that technical HCH is the main source of contamination. The high concentration and the degradation rates of pesticides in soil suggest that the contaminated sites are acting as continuous sources of pollution for the environment.

Keywords: pesticide, hexachlorocyclohexane, dichlorodiphenyltrichloroethane, soil, Republic of Moldova.

Received: 02 April 2020/ Revised final: 02 June 2020/ Accepted: 06 June 2020

Introduction

Pesticides are mostly used to prevent pests and to combat various biological vectors of human and animal diseases [1]. The main fields of pesticides use are health and agriculture sectors [2]. The distribution and fate of pesticides in the environment depends on many factors, including the dispersion method, their distribution in the environment, their physico-chemical properties (partition coefficients, degradation, and deposition rates) and the characteristics of the environment itself [3]. The most lasting pesticides are termed "persistent organic pollutants" (POPs). As it comes from their name, POPs are compounds that are resistant to chemical, biological and physical degradation and tend to accumulate in tissues of living organisms and along the food chain, causing a wide range of health problems to animals, fishes, and humans [4]. These are considered endocrine disruptors; exposure to POPs could lead to reproductive and immune dysfunctions, brain and nervous system disorders, developmental disorders, and cancer [5]. The most harmful pesticides such as organochlorine pesticides (OCPs) including HCHs (isomers of hexachlorocyclohexane), DDTs (dichlorodiphenyl trichloroethane, its isomers and degradation products isomers), polycyclic aromatic hydrocarbons, and triazines are listed in the Stockholm Convention, also named by the United Nations Environmental Program as "the Dirty Dozen" [6]. Because of their persistence, OCPs are found in the environment even after 20-30 years of application to the soil and crops. To control soil pesticides pollution, regulatory guidance values are applied worldwide.

In the Republic of Moldova, the high level of the organochlorine pesticides in the soil is due to the historical intensive use in agriculture, a situation that is still maintained through the use of new generation preparations, components less stable in the environment. The application of OCPs on the territory of the Republic of Moldova has been suspended since 1970, but several decades of their use in the Moldovan agriculture has left hundreds of contaminated sites, persisting until now [7-9]. According to regulatory guidance of the Republic of Moldova for values of several organic compounds in soil, the maximum allowable concentration for DDTs, for lindane (γ-HCH) and for HCH (hexachloran) is 0.1 mg/kg [10,11].

Inventory of old pesticide warehouses performed by the Ministry of Environment of the Republic of Moldova during 2008-2010 has demonstrated that there is a great number of sites polluted with POPs [12,13]. Previous studies have shown that there are 252 POPs polluted sites in the Republic of Moldova, with the concentration higher than 50 mg/kg and the pollution spectra of the analysed sites is comprised mainly of five compound groups: DDT, HCH, chlordane,

heptachlors and toxaphene [12,14]. Studies have shown the presence of DDTs and HCHs compounds in soil, water, and biota of the Republic of Moldova [9,15-18]. According to the Dniester hydrographic district management plan, there are 12 warehouses that contain about 1045.4 tons of pesticides [19]. One of the districts with contaminated sites is Soroca with 34.4 tons of pesticides that are stored in known locations, but their fate and impact on the environmental ecosystems was not assessed.

The goal of this study was to investigate the residue level and composition of OCPs, and to identify their possible sources in soil of Soroca district, Republic of Moldova, as well as their correlation to the total OCPs pollution of soil.

Experimental

Materials

Acetone, *n*-hexane, dichloromethane, anhydrous sodium sulphate and OCPs standard solution (a mix of 14 different OCPs: *α*-HCH, *β*-HCH, *γ*-HCH, heptachlor, heptachlor epoxide, aldrine, endrine, chlordane, *o,p'*-DDE, *p,p'*-DDE, *o,p'*-DDD, *p,p'*-DDD, *o,p'*-DDT, *p,p'*-DDT) of residue analysis grade were purchased from Supelco® and Sigma Aldrich.

Standard solutions of OCPs with initial concentrations varying from 24.0 to 248.0 µg/mL were prepared by diluting the stock standard solution (Sigma Aldrich standard mix of 14 different OCPs) in methanol. The stock standard solution was diluted at 5 different concentrations: 1:1000 (1 mL of standard mix and 1000 mL solvent), 1:500 (1 mL of standard mix and 500 mL solvent), 1:200 (1 mL of standard mix and 200 mL solvent), 1:100 (1 mL of standard mix and 100 mL solvent), 1:50 (1 mL of standard mix and 50 mL solvent).

The internal standard method using decachlorobiphenyl was used for the quality control.

Soil sampling

Soil samples were collected in spring-summer of 2012, from the proximity of 56 former storage sites in 30 settlements of the Soroca district, Republic of Moldova (Figure 1).

Sampling was performed according to the method described in ISO 18400-101 [20]. One composite soil sample (2.5 kg of soil) comprising 25 samples (0.1 kg each), was collected per contaminated site. Sampling depth was 10-15 cm from the ground line; the soil samples were combined in a rigid plastic bag in the field, labelled and transported to the laboratory facility.

Pesticide residue determination

Before pesticide residue extraction and determination, the collected soil samples were air dried at room temperature (18-20°C), ground, thoroughly mixed and sieved at 250 µm particle size. The extraction procedure was made according to the United States Environmental Protection Agency method 3500B [21]. The extraction of the analytes of interest (DDTs and HCHs) was performed by the microwave assisted extraction procedure.

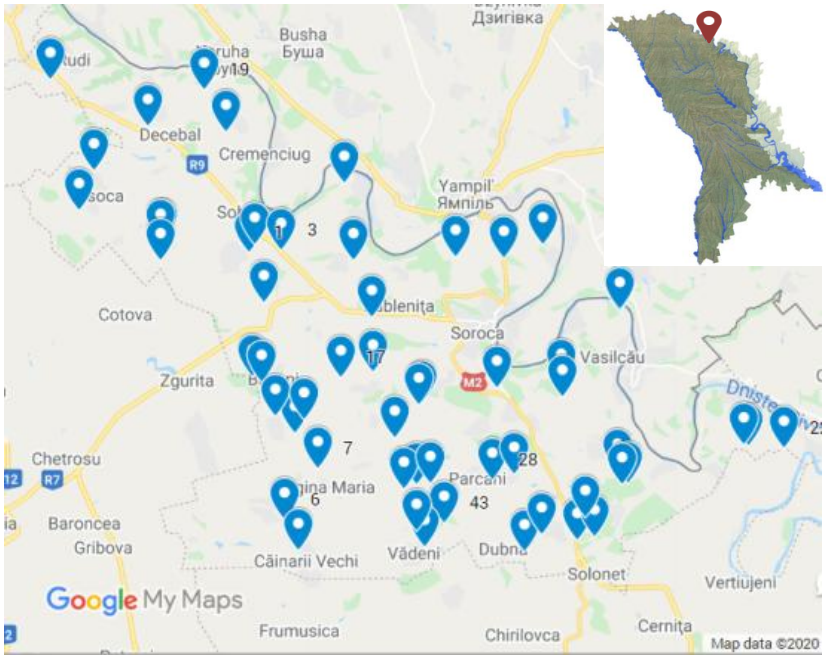

Figure 1. The map of sampling sites of the Soroca district (Republic of Moldova).

For this purpose, a portion of 10 g of sample was placed in the extraction vessel to which a volume of 20 mL of appropriate solvent (*n*-hexane/acetone, 1:2, v/v) was added. For a better extraction yield, for each sample the extraction was done twice at maximal power of microwave extraction system (140 W) for 15 min. After cooling down, the extracts were collected in the glass condenser and concentrated in *n*-hexane to a 1 mL volume. Extracts were purified on adsorption chromatography columns filled up with 1 g of silica gel previously activated for 16 h at 135°C. The column was conditioned with 5 mL of hexane. The analytes of interest were eluted from column with 5 mL of *n*-hexane, followed by 5 mL of *n*-hexane/dichloromethane mixture (1:1, v/v). The final elutes were concentrated to 1 mL under argon flow. One blank sample was prepared for each set of soil samples. The blank value was subtracted from the sample chromatogram for further calculations.

An internal standard (spike) was added to samples prior to extraction. The spiking was done by adding 1 mL of decachlorobiphenyl to each sample, to achieve a concentration of 0.05 µg/mL in the final sample.

The method used for the OCPs determination was validated within laboratory conditions and the limit of detection (LOD), limit of quantification (LOQ), precision (RSD_R), recovery and working range were calculated (Table 1). LOD and LOQ were calculated based on the standard deviation of the response and the slope by using Eq.(1) and Eq.(2), respectively:

$$\mathrm{LOD}(\mu\mathrm{g/kg}) = 3.3 \times \sigma/S \quad (1)$$

$$\mathrm{LOQ}(\mu\mathrm{g/kg}) = 10 \times \sigma/S \quad (2)$$

where σ- the standard deviation of the response, µg/kg;

S- the slope of the calibration curve [22].

The precision and recovery of the analytical procedure were tested with a reference material (CRM847, clay loam, Sigma-Aldrich, USA). The recovery was calculated as the ratio between the found concentration of analyte and the concentration stated to be present in the sample. The precision of the analytical procedure was calculated as the standard deviation of a series of measurements.

Instrumentation

Determination of OCPs was done according to the operational procedure based on SM SR ISO 10382:2008 on a gas chromatograph 6890 system of Agilent [23]. System parameters were: injector type: split/splitless; 300°C temperature; 2 µL injected volume; split 5:1; carrier gas: He, 1.4 mL/min, or average velocity 30 cm/sec, constant flow; column type: HP–5MS with length of 30 m, internal diameter 320 µm, and 0.25 µm film thickness; detector: µECD, 3200°C temperature; oven program: initial: 100°C for 1 min, 1st rate 20°C/min, isothermal: 200°C for 3 min, 2nd rate 10°C/min, isothermal: 280°C for 6 min, ChemStation, ChemStation Integrator.

Statistical Analysis

The statistical analysis of the experimental data was performed using the Analyse-It Add-in of Microsoft Excel 2016 software. The link between the OCPs concentrations was described by the Pearson correlation test, at the $p \leq 0.05$ degree of confidence [24,25]. The principal component analysis tool was used for predicting the sources of pollution by grouping the data into different interrelated modules based on their component loading [26,27].

Results and discussion

To fulfil the aim of this study, concentrations of organochlorinated pesticides such as DDTs and HCHs were assessed in soils of the Soroca district, Republic of Moldova in the proximity to the former pesticides' storages.

Table 1

Validation parameters of the SM SR ISO 10382:2008 method.

Compound	*LOD, µg/kg*	*LOQ, µg/kg*	*Concentration range, µg/kg*	*RSD_R, %*	*Recovery, %*
α-HCH	0.003	0.008	0.005-0.05	9.45	94
β-HCH	0.014	0.041	0.015-0.2	7.03	107
γ-HCH	0.004	0.012	0.005-0.05	7.36	93
o,p'-DDE	0.014	0.041	0.028-0.45	8.24	91
p,p'-DDE	0.013	0.041	0.015-0.2	8.36	92
o,p'-DDD	0.043	0.130	0.045-0.4	10.89	89
p,p'-DDD	0.025	0.077	0.025-0.38	12.89	113
o,p'-DDT	0.014	0.041	0.028-0.45	5.59	100
p,p'-DDT	0.021	0.065	0.025-0.52	16	113

Results of this study will offer a better understanding on the fate of these contaminants in the environment and the risks associated with agricultural and industrial pollution.

The chromatogram of one of the samples with composite soil extract for the study area is shown in Figure 2. The statistical results of OCPs in the soils from Soroca district, Republic of Moldova, are presented in Table 2. According to the obtained results, the overall concentration of OCPs (ΣOCPs) in surface soils of Soroca district, Republic of Moldova, ranged between 0.072 and 1953.6 mg/kg with mean concentration of 84 mg/kg. The order of overall OCPs concentration in different sites was: *γ*-HCH> *p,p'*-DDT> *α*-HCH> *o,p'*-DDT> *p,p'*-DDE> *β*-HCH> *o,p'*-DDD> *p,p'*-DDD> *o,p'*-DDE. The degree of contamination is in concordance with the study performed previously by Bogdevich, O. *et al.* [28].

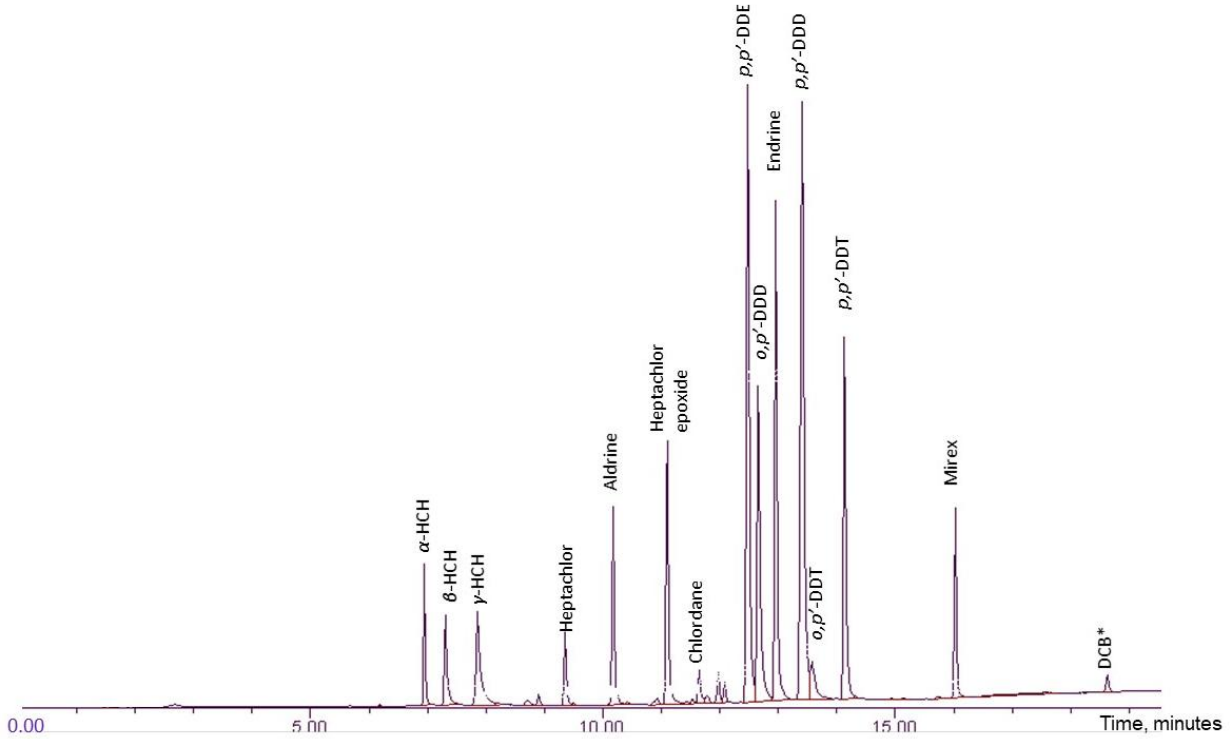

Figure 2. Chromatogram of the soil extract (DCB*-indicates the internal standard).

Table 2

Organochlorine pesticides concentration (mg/kg) in analysed soil.

Compound	*Mean*	*SD*	*Median*	*Minimum*	*Maximum*
α-HCH	11.2	51.9	0.26	ND	369
β-HCH	4.23	13.6	0.29	ND	87.7
γ-HCH	18.8	131	0.07	ND	978
ΣHCHs	34.3	160	0.77	ND	1096
o,p'-DDE	1.54	7.32	0.06	ND	53.8
p,p'-DDE	6.57	36.0	0.43	ND	270
o,p'-DDD	2.90	14	0.09	ND	101
p,p'-DDD	2.34	10.1	0.10	ND	69.8
o,p'-DDT	8.76	34.7	0.26	ND	212
p,p'-DDT	12.5	71.4	0.23	ND	531
ΣDDTs	34.6	141	1.38	ND	841
ΣOCPs	83.99	286.56	4.1	0.072	1953.6

Note: Mean, standard deviation (SD), maximum and minimum were calculated assuming that non-detected (ND) measurements were equal to zero.

Total DDT concentrations (ΣDDTs), comprised of two DDT isomers and four DDT degradation products (*o,p'*-DDT, *p,p'*-DDT and *o,p'*-DDD, *p,p'*-DDD, *o,p'*-DDE, *p,p'*-DDE), were up to 841 mg/kg dry weight. The average concentration of total DDT observed in sampling locations was 34.6 mg/kg.

The total content of HCHs (ΣHCHs) that is the sum of concentrations of *α, β* and *γ* isomers, was up to 1096 mg/kg dry weight and the overall concentration of the total HCHs was 34.3 mg/kg.

ΣDDTs concentration in most of the soil samples (57.17%) is relatively higher than the ΣHCHs concentrations (42.9%), however the mean concentrations are equal, indicating that the concentrations of DDTs and HCHs are evenly distributed among samples (Figures 3 and 4).

There are two possible reasons that might explain the high concentrations of DDTs in soil samples of Soroca district compared to HCHs concentration. The first possibility is that HCHs have less lipophilic properties, higher volatility and water solubility than DDTs [29], thus could be more easily transferred from the source point to surrounding farmland *via* surface runoff. On the other hand, it may be due to their different use and stored amount over the soviet period (during 1960-1980). There was a correlation between ΣHCHs concentration and ΣDDTs concentration (R^2> 0.42) as shown in Figure 5, suggesting that they may have similar sources and fate in this area [29].

Dichlorodiphenyltrichloroethane and its degradation products

Technical DDT generally consists of *p,p'*-DDT isomer (*approx*. 85%), with lesser amounts of *o,p'*-DDT and *o,o'*-DDT isomers [30]. Residues of DDTs in the environment include *p,p'*-DDT, its isomer *o,p'*-DDT and their degradation products (*o,p'*- and *p,p'*-dichlorodiphenyldichloroethylene (*o,p'*- and *p,p'*-DDE) and *o,p'*- and *p,p'*-dichlorodiphenyldichloroethane (*o,p'*- and *p,p'*-DDD)). In environmental ecosystems, *p,p'*-DDT degrades mainly to *p,p'*-DDE and *p,p'*-DDD as a consequence of different environmental factors [30].

The *p,p'* isomers of DDT, DDD and DDE were present in higher concentration than the associated *o,p'* compounds (Table 2). The *p,p'*-DDT residues were detected in levels≤ 531.0 mg/kg dry weight in 96% of the total soil samples. The *p,p'*-DDE isomer was detected in 98%, with levels≤ 69.8 mg/kg and *p,p'*-DDD in 77% with levels≤ 270 mg/kg.

The mean concentrations of individual compounds in soil samples were as follows: *o,p'*-DDE< *p,p'*-DDD< *o,p'*-DDD< *p,p'*-DDE< *o,p'*-DDT< *p,p'*-DDT (Table 2). Such an order could be explained by the transformation of DDT to its degradation products, DDE and DDD.

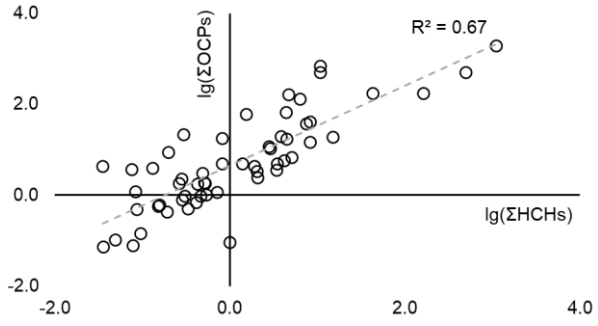

Figure 3. ΣHCHs distribution in studied soil samples.

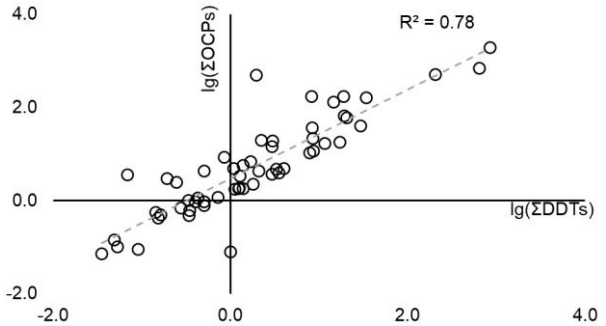

Figure 4. ΣDDTs distribution in studied soil samples.

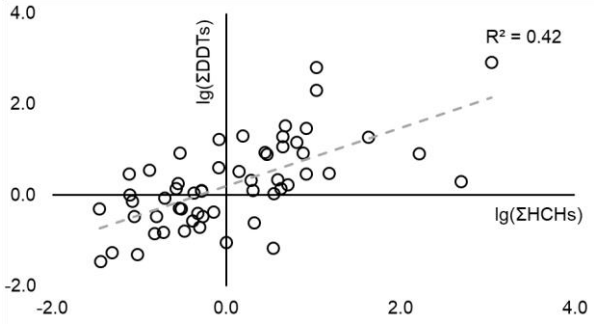

Figure 5. Correlation of ΣDDTs and ΣHCHs.

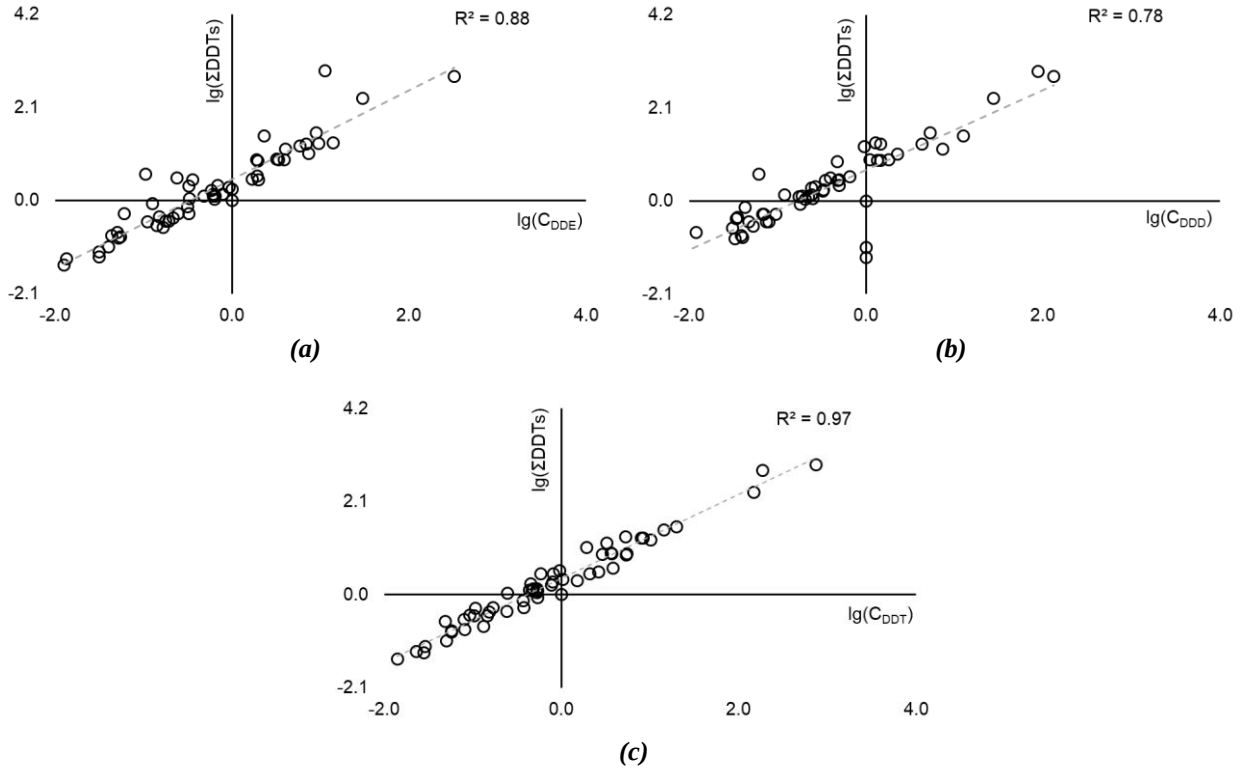

Figure 6. Distribution of DDT isomers concentration: correlation for the concentrations of DDE isomers *(a)*, DDD isomers *(b)*, DDT isomers *(c)* to the total DDT isomers concentrations (ΣDDTs).

After DDT usage, a considerable amount of DDT may be converted to *p,p'*-DDE [31]. In Figure 6, the distribution of total concentration of DDT isomers, and their degradation products (DDE and DDD) is shown, suggesting that DDT isomers are more abundant in the soils of the studied area. Thereby, sources of DDTs could be identified according to the ratios of (*p,p'*-DDE+*p,p'*-DDD)/*p,p'*-DDT or *p,p'*-DDE/*p,p'*-DDT. A ratio value >1 suggest a past input of DDT, and a ratio <1, respectively, suggest a recent input of the pollution [29,32].

The degradation status of DDT was evaluated using (DDE+DDD)/DDT ratios, which varied from 0.005 to 49.3 [33]. In 77% of analysed soil samples these ratios showed aged sources of pollution with DDT, indicating that DDT residues have significantly been transformed into their degradation products in these areas. There are strong positive correlations in the concentrations of the DTT isomers and their degradation products (R^2= 0.78-0.97, p< 0.01), indicating common sources of pollution (Figure 6).

Hexachlorocyclohexanes

The *α*-HCH residues were detected in levels up to 369.0 mg/kg dry weight in 96% of the total soil samples. The *β*-HCH isomer was detected in 98% of analysed samples, with levels up to 87.7 and *γ*-HCH isomer in 80% with levels ≤ 978 mg/kg (Table 2).

The percentage distribution of HCH isomers in total HCHs varied among soil samples (Figure 7). This may be related to the isomerization of HCH during the transformation process in soil as well as the differences in physico-chemical properties and degradation rates [34]. The *β*-HCH was the most dominant isomer in soil samples that is due to the differences in the degradation rates of the HCH isomers, *β*-HCH being the most stable and persistent in soil [34,35]. The persistence of *β*-HCH in soil is mainly due to a higher partition coefficient (K_{ow}) and a lower vapour pressure than of other HCH isomers, which enhances its adsorption into soil and hinders its evaporation. The *α*-HCH/*γ*-HCH ratios varied from 0 to 28 and both low and high ratios were found in samples, indicating both lindane and technical HCH as the sources of HCH contamination. Very high ratios may be related to old inputs and transformation of *γ*-HCH into *α*-HCH [36]. There are strong positive correlations in the concentrations of most HCH isomers (R^2= 0.48–0.90, p< 0.01) (Figure 7), indicating common pollution sources.

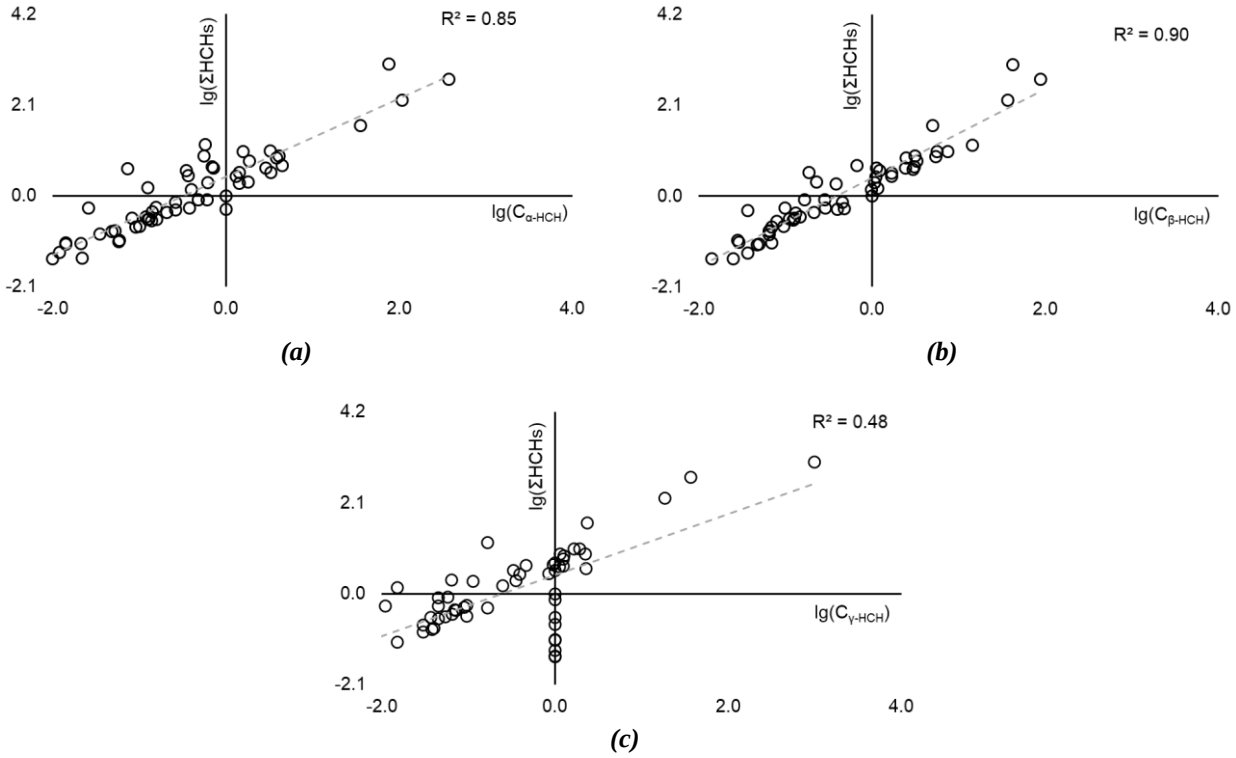

Figure 7. Distribution of HCH isomers concentration: correlation for the *α*-HCH isomer *(a)*, *β*-HCH isomer *(b)*, and *γ*-HCH isomer *(c)* to the total HCH isomers concentration (ΣHCHs).

Factor analysis

Factor loading plot showed loadings for each OCP in the principal component plane (Factor 1 that shows the largest possible variance in the data set *versus* Factor 2 which is uncorrelated with Factor 1 and accounts for the next highest variance; Figure 8).

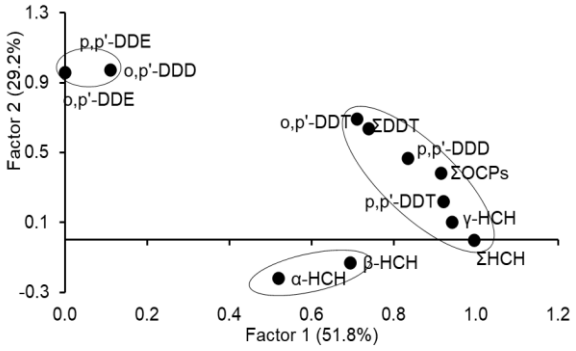

Figure 8. Loading plot of factor analysis based on concentrations of organochlorine pesticides. ΣHCHs is sum of *α*-HCH, *β*-HCH, and *γ*-HCH. ΣDDTs is sum of *p,p'*-DDE; *o,p'*-DDE; *p,p'*-DDD. *o,p'*-DDD; *o,p'*-DDT and *p,p'*-DDT. ΣOCPs is the sum of all OCPs. The circles indicate factors of high scores.

By processing, two factors were considered here, accounting for 81.0% of the total variance. Factor 1 explained 51.8% of the total variance and was mainly associated with *p,p'*-DDD (0.83), *o,p'*-DDT (0.74), *p,p'*-DDT (0.92), *γ*-HCH (0.94), which were generally high correlated with the total concentrations of OCPs (Table 3). In Factor 1, *α*-HCH (0.52) and *β*-HCH (0.69) had medium loading, meaning that the HCHs appeared to have the similar contributions to OCPs and originated from the similar source. Factor 2 was associated mainly with the *o,p'*-DDE (0.97), *p,p'*-DDE (0.96) and *o,p'*-DDD (0.97). The fact that DDT isomers were the highest loading of all the factors, suggested that they appeared to have higher contributions to OCPs than other individual OCPs.

According to the relevance to both Factor 1 and Factor 2, these components can be represented by DDT and HCHs, respectively. The DDT and HCHs accounted for the highest loading for Factor 1, whereas the DDE and DDD isomers accounted for the highest loading for Factor 2 (Table 3). This finding suggested that DDT and HCHs showed larger contributions to OCPs possibly originating from the similar source.

Summarization of the obtained results revealed that the compositions of the contaminants indicated mainly the parent compounds with low levels of degradation products at most sites. The slow degradation rates of the pesticides for most sites and their low mobility in soil suggest that the contaminated sites are acting as continuous point sources of contamination for the environment.

Table 3

Pearson correlations of OCPs identified in the analysed samples.

	o,p'-DDE	*p,p'-DDE*	*o,p'-DDD*	*p,p'-DDD*	*o,p'-DDT*	*p,p'-DDT*	*ΣDDT*	*α-HCH*	*β-HCH*	*γ-HCH*	*ΣHCH*
o,p'-DDE	1										
p,p'-DDE	0.98*	1									
o,p'-DDD	0.98**	0.97**	1								
p,p'-DDD	0.36**	0.40**	0.49**	1							
o,p'-DDT	0.55**	0.54**	0.68**	0.92**	1						
p,p'-DDT	0.097	0.11	0.26	0.94**	0.87**	1					
ΣDDTs	0.61**	0.62**	0.73**	0.94**	0.99**	0.85**	1				
α-HCH	-0.02	-0.02	0.00	0.15	0.12	0.16	0.12	1			
β-HCH	0.03	0.03	0.09	0.36**	0.33*	0.38**	0.32*	0.96**	1		
γ-HCH	-0.02	0.02	0.14	0.91**	0.79**	0.99**	0.78**	0.21	0.41**	1	
ΣHCHs	-0.02	0.01	0.12	0.82**	0.72**	0.89**	0.70**	0.58**	0.74**	0.92**	1

** ** Significant at probability P< 0.05 and P< 0.01, respectively.*

This study should be considered as a first steppingstone (as a regional study) towards a major investigation on the main sources and levels of OCPs throughout the territory of the Republic of Moldova. The study has highlighted the area of Soroca district with high concentrations of some OCPs that could pose some potential human health concerns, which need addressing urgently. Thus, remediation measures are required to reduce the levels of the contaminants.

Conclusions

The OCPs compounds concentration was determined in urban and rural soils in the immediate proximity of former pesticides storages in the Soroca district, in the north-eastern part of the Republic of Moldova. The main findings revealed that the concentration of nine OCPs were up to 1954 mg/kg (average was 84 mg/kg). The level of contamination in the analysed samples was higher than the national maximum allowable concentration in soil (0.1 mg/kg for *γ*-HCH and DDTs). The highest concentrations were found within the former pesticides' storage points.

The HCH and DDT isomers and their degradation products were the most abundant contaminants, accounting for 79.4% of the total OCPs. Diagnostic ratios of DDTs residues and of HCHs isomers clearly unveiled a dominance of historical application of these compounds in soil. The most dominant OCP species were *γ*-HCH, followed by *p,p'*-DDT and *o,p'*-DDE isomer was present in smallest amount, that confirms the high persistence and slow degradation of the studied OCPs.

The compositions of the contaminants indicated mainly the parent compounds with low levels of degradation products at most sites. The slow degradation rates of the pesticides for most sites and their low mobility in soil suggest that the contaminated sites are acting as continuous point sources of contamination for the environment.

Acknowledgements

I would like to express my gratitude to my supervisors, Acad., Prof., Dr. Hab. Tudor Lupascu and Dr. Oleg Bogdevici for their continuous guidance and kind support.

This work was supported by the financial support by GEF and FAO contract FAO1-16 and ENPI project code MIS ETC 1676.

It is greatly appreciated the effort of the management of the Institute of Chemistry for equipping the Center of Ecological Chemistry and Environment Protection for core teaching and research work where this research work was carried out.

References

1. Jayaraj, R.; Megha, P.; Sreedev, P. Organochlorine pesticides, their toxic effects on living organisms and their fate in the environment. Interdisciplinary Toxicology, 2016, 9(3–4), pp. 90-100. DOI: https://doi.org/10.1515/intox-2016-0012
2. Kaur, R.; Mavi, G.K.; Raghav, S. Pesticides classification and its impact on environment. International Journal of Current Microbiology and Applied Sciences, 2019, 8(3), pp. 1889-1897. DOI: https://doi.org/10.20546/ijcmas.2019.803.224
3. Ravichandra, N.G. Agrochemicals in plant disease management. Scientific Publishers, India, 2018, 556 p. https://www.scientificpub.com/book-details/

Agrochemicals-in-Plant-Disease-Management-HB-964.html
4. Chen, M.W.; Santos, H.M.; Que, D.E.; Gou, Y.Y.; Tayo, L.L.; Hsu, Y.C.; Chen, Y.B.; Chen, F.A.; Chao, H.R.; Huang, K.L. Association between organochlorine pesticide levels in breast milk and their effects on female reproduction in a Taiwanese population. International Journal of Environmental Research and Public Health, 2018, 15(5), pp. 931-953. DOI: https://doi.org/10.3390/ijerph15050931
5. The Concern About POPs. Persistent Organic Pollutants Toolkit, 2008. http://www.popstoolkit.com/about/concern.aspx
6. United Nations Environment Programme, Stockholm Convention on Persistent Organic Pollutants (POPs). Text and Annexes, 2009, Switzerland. https://www.wipo.int/edocs/lexdocs/treaties/en/unep-pop/trt_unep_pop_2.pdf
7. Spătaru, P.; Spînu, O.; Spătaru, T.; Povar, I. Analysis of the environment contamination sources with halogenated organic pesticides. Akademos, 2017, 1(44), pp. 42-47 (in Romanian). http://akademos.asm.md/taxview/97
8. Government Decision of the Republic of Moldova No. 1155 of 20 October 2004 for approving National Strategy on reducing and eliminating persistent organic pollutants and the National Plan for implementing the Stockholm Convention on persistent organic by pollutants. Official Monitor no. 193-198 (29.10.2004), art. no. 1347 (in Romanian).
9. Inspectorate for Environmental Protection. Environmental protection in the Republic of Moldova, Yearbook-2018, Chisinau, 2019, 358 p. (in Romanian).
10. Regulation No. 100 of 18 January 2000 of the Ministry of the Environment and Territorial Planning regarding the estimation of damages for the prejudices caused to the environment. Official Monitor no. 112-114 (05.09.2000), art. no. 317 (in Romanian).
11. Instruction no. 383 of 8 August 2004 of the Ministry of Ecology and Natural Resources on the assessment of damage caused to soil resources. Official monitor no. 189-192 (22.10.2004), art. no. 383 (in Romanian).
12. Plesca, V.; Barbarasa, I.; Cupcea, L.; Melian, R. Inventory of POP pesticides polluted areas in Moldova. International Conference Contaminated Sites, Bratislava, 2013, pp. 75-80. https://contaminated-sites.sazp.sk/node/2
13. Slobodnik, J.; Isac, A. WB/GEF Persistent Organic Pollutants (POPs) stockpiles management and destruction project. Koš, Slovak Republic, 2010, 251 p. http://www.moldovapops.md/app/includes/files/POPs%20MIS.pdf
14. Duca, Gh.; Bogdevich, O.; Cadocinicov, O.; Porubin, D. The pollution spectrum of old pesticides storages in Moldova. Chemistry Journal of Moldova, 2012, 7(1), pp. 124-128. DOI: dx.doi.org/10.19261/cjm.2012.07(1).23
15. Gliga, O. Content of organochlorine pesticide residues in environmental components. Intellectus, 2015, 2, pp. 103-112 (in Romanian).
16. Sapozhnikova, Y.; Zubcov, E.; Zubcov, N.; Schlenk, D. Occurrence of pesticides, polychlorinated biphenyls (PCBs), and heavy metals in sediments from the Dniester River, Moldova. Archives of Environmental Contamination and Toxicology, 2005, 49(4), pp. 439-448. DOI: https://doi.org/10.1007/s00244-005-8011-8
17. Ene, A.; Bogdevich, O.; Sion, A. Levels and distribution of organochlorine pesticides (OCPs) and polycyclic aromatic hydrocarbons (PAHs) in topsoils from SE Romania. Science of the Total Environment, 2012, 439, pp. 76-86. DOI: https://doi.org/10.1016/j.scitotenv.2012.09.004
18. Bogdevich, O.; Ene, A.; Cadocinicov, O.; Culighin E.; Nicolau, E.; Grigoras, M. The study of POPs contaminated sites in Danube River Basin of Republic Moldova for risk assessment and remediation actions. Contaminated Sites Conference: Bratislava, Slovakia, 2016, pp. 64-68. http://contaminated-sites.sazp.sk/node/58
19. Government Decision of the Republic of Moldova no. 814 of 17 October 2017 on approval of the Management plan of the Dniester river basin district. Official Monitor no. 371-382 (27.10.2017), art. no. 942 (in Romanian).
20. ISO 18400-101:2017 - Soil quality — Sampling — Part 101: Framework for the preparation and application of a sampling plan. The International Organization for Standardization, 2017.
21. EPA Method 3500B, Organic extraction and sample preparation. Environmental Protection Agency, 1996. https://gtanalytical.com/epa-methods/
22. Validation of analytical procedures: text and methodology Q2(R1). International Conference on Harmonization of technical requirements for registration of pharmaceuticals for human use, Step 4 version, November 2005. https://www.ich.org/page/quality-guidelines
23. ISO 10382:2002 - Soil quality — Determination of organochlorine pesticides and polychlorinated biphenyls — gas-chromatographic method with electron capture detection. The International Organization for Standardization, 2002. https://www.iso.org/standard/32422.html
24. Zhang, C.; Liu, L.; Ma, Y.; Li, F. Using isomeric and metabolic ratios of DDT to identify the sources and fate of DDT in Chinese agricultural topsoil. Environmental Science and Technology, 2018, 52(4), pp. 1990-1996. DOI: https://doi.org/10.1021/acs.est.7b05877
25. Mungai, T.M.; Wang, J. Occurrence and toxicological risk evaluation of organochlorine pesticides from suburban soils of Kenya. International Journal of Environmental Research

and Public Health, 2019, 16(16), pp. 2937-2950. DOI: https://doi.org/10.3390/ijerph16162937
26. Girones, L.; Arias, A.H.; Oliva, A.L.; Recabarren-Villalon, T.; Marcovecchio, J.E. Occurrence and spatial distribution of organochlorine pesticides in the southwest Buenos Aires using the freshwater snail *Chilina parchappii* as environmental biomonitor. Regional Studies in Marine Science, 2020, 33, p. 100898. DOI: https://doi.org/10.1016/j.rsma.2019.100898
27. Shunthirasingham, C.; Gawor, A.; Hung, H.; Brice, K.A.; Su, K.; Alexandrou, N.; Dryfhout-Clark, H.; Backus, S.; Sverko, E.; Shin, C.; Park, R.; Noronha, R. Atmospheric concentrations and loadings of organochlorine pesticides and polychlorinated biphenyls in the Canadian Great Lakes Basin (GLB): Spatial and temporal analysis (1992–2012). Environmental Pollution, 2016, 217, pp. 124-133. DOI: https://doi.org/10.1016/j.envpol.2016.01.039
28. Bogdevich, O.; Ene A.; Cadocinicov, O.; Culighin, E. The analysis of old pesticides and PAHs pollution sources in Low Danube region. Journal of International Scientific Publications: Ecology & Safety, 2013, 7(2), pp. 233-243. https://www.scientific-publications.net/en/archive/
29. Zhang, F.; He, J.; Yao, Y.; Hou, D.; Jiang, C.; Zhang, X.; Di, C.; Otgonbayar, K. Spatial and seasonal variations of pesticide contamination in agricultural soils and crops sample from an intensive horticulture area of Hohhot, North-West China. Environmental Monitoring and Assessment, 2013, 185(8), pp. 6893-6908. DOI: https://doi.org/10.1007/s10661-013-3073-y
30. Toxicological Profile for DDT, DDE, and DDD. US Department of Health and Human Services, Public Health Service, Agency For Toxic Substances And Disease Registry, Atlanta, GA, United States of America: 2002, 480 p. https://www.atsdr.cdc.gov/ToxProfiles/tp.asp?id=81&tid=20
31. Agapkina, G.I.; Brodskiy, E.S.; Shelepchikov, A.A.; Artukhova, M.B. Transformation and form of dichlorodiphenyltrichloroethane (DDT) applied to Moscow soils. Moscow University Soil Science Bulletin, 2017, 72(3), pp. 125-131. DOI: https://doi.org/10.3103/S0147687417030024
32. Ssebugere, P.; Wasswa, J.; Mbabazi, J.; Nyanzi, S.A.; Kiremire, B.T.; Marco, J.A.M. Organochlorine pesticides in soils from south-western Uganda. Chemosphere, 2010, 78(10), pp. 1250-1255. DOI: https://doi.org/10.1016/j.chemosphere.2009.12.039
33. Pinkney, A.E.; McGowan, P.C. Use of the p,p'-DDD: p,p'-DDE concentration ratio to trace contaminant migration from a hazardous waste site. Environmental Monitoring and Assessment, 2006, 120, pp. 559-574. DOI: https://doi.org/10.1007/s10661-005-9103-7
34. Toxicological profile for alpha-, beta-, gamma-, and delta-hexachlorocyclohexane. U.S. Department of Health and Human Services, Public Health Service, Agency for Toxic Substances and Disease Registry (ATSDR), Atlanta, GA, 2005, 377 p. https://www.atsdr.cdc.gov/toxprofiles/tp43.pdf
35. Becker, S.; Halsall, C.J.; Tych, W.; Kallenborn, R.; Schlabach, M.; Manø, S. Changing sources and environmental factors reduce the rates of decline of organochlorine pesticides in the Arctic atmosphere. Atmospheric Chemistry and Physics, 2012, 12(9), pp. 4033-4044. DOI: https://doi.org/10.5194/acp-12-4033-2012
36. Da, C.; Liu, G.; Sun, R.; Yuan, Z.; Tang, Q.; Liu, H. Sources and risk assessment of organochlorine pesticides in surface soils from the nature reserve of the Yellow River Delta, China. Soil Science Society of America Journal, 2014, 78(3), pp. 779-786. DOI: https://doi.org/10.2136/sssaj2013.12.0547

CHEMISTRY JOURNAL OF MOLDOVA. General, Industrial and Ecological Chemistry. 2020, 15(1), 51-57
ISSN (p) 1857-1727 ISSN (e) 2345-1688
http://cjm.asm.md
http://dx.doi.org/10.19261/cjm.2020.701

ANALYSIS OF HEAVY METAL ACCUMULATION IN FISHES FROM THE COAST OF LAUTOKA, FIJI

Syed Sauban Ghani [a*] and Aman Deo [b]

[a]*Department of General Studies, Jubail Industrial College, Jubail Industrial City 31961, Saudi Arabia*
[b]*Planning and Quality Office, University of South Pacific, Laucala Bay rd., Suva, Fiji*
[*]*e-mail: syed_sg@jic.edu.sa; phone: (+96 658) 392 02 35*

Abstract. The concentrations of the accumulated heavy metals such as cadmium, lead, copper, mercury, zinc, and chromium have been determined in the muscles, gills and liver of the fish species of *Clupea pallasii*, *Macolor niger* and *Pristipomoides filamentosus* collected from the waters of the South Pacific Ocean around Lautoka in Fiji. Results of this study show the order of metal accumulation in tissues of all fishes as follows: Zn >Cu > Cr >Cd >Pb >Hg. Overall, the contents of heavy metals in all the samples were below the permissible limits, except for chromium that is slightly higher than the limits of 0.15 mg/kg and 0.05 mg/kg set by Food and Agriculture Organization of the United Nations and World Health Organization regulations respectively. As anticipated, the muscles contain the lowest concentration of all metals. Significant variations in heavy metal concentrations were found between different tissues within each species of fish.

Keywords: heavy metal, accumulation, fish, marine environment, Pacific Ocean.

Received: 06 April 2020/ Revised final: 04 May 2020/ Accepted: 08 May 2020

Introduction

In recent decades, industrial and urban activities have contributed to the increase of heavy metal contamination in the marine environment and have directly affected coastal ecosystems [1]. For this reason, the level of contaminated substances in fish tissue is often related to those found in their surroundings. Some of the heavy metals are essential to the physiological processes of fish, while others are toxic even at low concentrations. These heavy metals can enter the fish through feeding, the respiratory tract or the skin [2]. Sources of heavy metal accumulation come from food, water and sediments. In general, higher the concentration of metals in water, the more they are accumulated and stored by the fish [3,4]. The relationship between metal concentration in fish and water has been studied in field and laboratory experiments [5]. Various fish species can store different amounts of metals from the same aquatic environment. In terms of metal accumulation, these differences between fish species may be related to their lifestyle and diet [6]. Studies on many fish have shown that these metals alter the physical activity and biochemical parameters of tissues and blood. The toxic effects of heavy metals have been reviewed, among which many researchers include their bioaccumulation [7,8].

The presence of heavy metals in fish may pose a substantial risk to fish consumers such as human beings that include serious threats like renal failure, liver damage, cardiovascular diseases and even death [9,10]. Because of the dangers associated with the consumption of heavy metals, their concentration in commercial fishes in Fiji should be periodically examined to evaluate the possible risks linked to the consumption of contaminated fish. During the last twenty to thirty years, the concentrations of heavy metals in fish have been comprehensively investigated in various parts of the globe [11-13]. Most of the studies were concentrated mainly on the heavy metals in the fish muscles *i.e*. the edible part of the fish. Furthermore, few studies reported the distribution of metals in different organs such as bone, liver, gonads, kidneys, digestive tract and the brain [14,15].

Lautoka, (17.6242° S, 177.4528° E) is the second largest city of Fiji. It is in the west of the island of Viti Levu. The South Pacific Ocean encircles almost half of Lautoka and is the main source of fisheries. No analysis has been done to date on the presence of heavy metal ions in the fish species generally found at the coast of Lautoka. Therefore, the objective of the current study is to determine the heavy metals concentration (Cd, Pb, Cu, Hg, Zn, Cr) in the

muscles, gills and liver of the three different fish species such as *Clupea pallasii, Macolor niger, Pristipomoides filamentosus* collected from the waters of the South Pacific Ocean around Lautoka in Fiji.

Experimental

Generalities

All solutions were prepared with analytical grade reagents and ultra-pure water (18 MΩ cm) generated by purified distilled water with the Milli-QTM PLUS system (Millipore, Bedford, MA, USA). High grade HNO_3 and $HClO_4$ were obtained from Merck, Germany. Standard solutions were prepared from stock standard solutions of the metals (Merck, multi-element standard, Germany) by diluting the stock solutions in mg/mL [16]. All glass and plastic items were hosed overnight with 10% (vol./vol.) nitric acid, washed with distilled water as well as deionized water and dried before use.

Fish sampling

The samples of the fish species *Clupea pallasii* (Pacific Herring), *Macolor niger* (Black Snapper), and *Pristipomoides filamentosus* (Crimson Jobfish) were purchased from the fishermen, at the key fish landing areas on the South Pacific Ocean around Lautoka in Fiji. A total of 15 fish samples, comprising 3 species and for each species five samples were collected on different dates between April to November 2018. The fishes were then classified with the help of an expert zoologist. The collected fish were instantly stored in an icebox kept in a polystyrene bag and shifted to the laboratory where they were weighed and the total length measured. They were kept in a deep freezer at around -25°C for further analysis. Lengths to nearest cm and weights to nearest g of the investigated fishes are presented in Table 1. The stated weight and length are given in the range from minimum to maximum of the three measurements taken for each species.

Preparation of samples

Before analysis, the frozen fish samples were moderately defrosted and then the fishes were dissected with a stainless steel knife to take out the muscles, liver and gills. Multiple samples of 2-5 g were used for ensuing analysis. The removed parts were kept in several Petri dishes and oven dried using a microwave digestion system (Multiwave 7000, Anton Paar GmbH, Germany) that ensures the novel pressurized digestion cavity (PDC) at temperature up to 300°C and pressure up to 199 bar, respectively. The internal temperature control was used to assist the acid digestion process to eliminate the content of water. This helps in achieving complete digestions of samples. The samples for heavy metal analysis were performed according to the method prescribed by the association of official analytical chemists [17].

Procedure: A quantity of 0.5 g of dried fish parts was placed in a 125 mL Erlenmeyer flask with glass beads and 25 mL deionized water. In this, 10 mL of 1:2 mixture of concentrated HNO_3 and $HClO_4$ were added. The sample was boiled until the solution became clear. The completely digested sample was allowed to cool to room temperature. The clear solution was transferred to a 50 mL volumetric flask to bring up to the volume with deionized water and mixed.

Determination of heavy metals

The samples were analysed for Cd, Pb, Cu, Zn, and Cr using the AA800 Perkin Elmer atomic absorption spectrophotometer (Norwalk, CT, USA) with an air/acetylene flame. The instrumental parameters were adjusted in order to achieve a maximal signal-to-noise ratio. The accuracy and precision of the analytical procedure were tested with a reference material (DORM-2, dogfish muscle, National Research Council, Canada). The mean recoveries of Cd, Cr, Cu, Zn, and Pb were 98.6, 104.3, 100.8, 89.2, and 96.5%, respectively. The instrument limit of detection (LoD) was calculated as the concentration was associated with thrice the standard deviation of the background noise recorded on seven measurements of the procedural blank [18]. The instrument limit of quantification (LoQ) was calculated as the concentration was associated with 10 times the standard deviation of the background noise [19]. The methods LoD and LoQ were calculated in a similar way by using real sample digest with concentrations of metals in the range of one to five times the instrument LoD.

Table 1

Length and weight of examined fish species.

Common name	*Scientific name*	*Length (cm)*	*Weight (g)*
Pacific Herring	*Clupea pallasii*	34—41	500—550
Black Snapper	*Macolor niger*	27—34	280—450
Crimson Jobfish	*Pristipomoides filamentosus*	26—42	400—800

The Hg was determined using the Milestone DMA-80 direct Mercury Analyzer (Milestone Srl, Italy). The sample weight required is between 0.020 and 0.006 g, with drying temperature of 300°C for 60 seconds. The samples were analysed at the Institute of Applied Sciences, University of South Pacific, Fiji.

The blank sample was analysed together with each batch of samples. All samples were analysed three times. The concentrations of heavy metals were given in mg/kg, wet weight (wet wt.) for the fish sample.

Results and discussion

The increase in human population and economic growth contributed significantly to the current global decline in water quality, including the periodic accumulation of heavy metals such as Cd, Pb, Cu, Hg, Zn, and Cr in the waters of the South Pacific, Lautoka Bay, Fiji. The non-essential metals have no metabolic function; but as a consequence of their bioaccumulation in fish, these metals may be toxic to human beings even at very small concentrations [20]. The exposure to heavy metals in water leads to the accumulation in the body of all aquatic organisms but fishes are generally more affected with respect to any other organisms [21,22]. The Food and Agriculture Organization (FAO) of the United Nations and World Health Organization (WHO) have established the allowed limits of heavy metals in fishes, these are presented in Table 2. The comparison among the three fish species in the Lautoka waters according to their metal accumulation levels in muscles, liver and gills are given in Tables 2, 3 and 4, respectively.

The accumulation of heavy metals in the tissues of the different species was found to be almost similar. Therefore, the accumulation concentration of zinc and copper were the highest in all tissues of the species, except for copper in gills of *Pristipomoides filamentosus* whereas the accumulation concentration of cadmium, lead and mercury were at the lowest levels. For example, the order of metal accumulation in muscles of *Clupea pallasii* was Zn >Cu >Cr >Cd >Pb >Hg. The similar order was also followed in the tissues of all other species.

However, the trends of the accumulation of heavy metals in all the three different species were similar but there were large differences in the amounts of heavy metal accumulation in the examined tissues of the species. This shows that the three different species of the fishes in the identical region accumulated diverse levels of heavy metals in their tissues. The results presented in Tables 2, 3 and 4 show that all the fish contain the lowest concentrations of metal in the muscles except for copper and zinc whereas almost all the species of fish have the highest concentrations of chromium in liver.

Table 2

Heavy metal concentration (mg/kg) in muscles of fish species.

	Cu	*Zn*	*Cr*	*Cd*	*Pb*	*Hg*
Clupea pallasii	0.771±0.013	12.402±0.01	0.291±0.001	0.233±0.003	0.112±0.001	0.021±0.001
Macolor niger	0.472±0.011	18.331±0.06	0.344±0.003	0.151±0.002	0.091±0.003	0.092±0.002
Pristipomoides filamentosus	0.521±0.002	15.614±0.02	0.312±0.002	0.081±0.001	0.021±0.001	0.073±0.001
WHO*	30	40	0.05	1	2	0.5
FAO**	30	30	0.15	0.5	0.5	0.5

*The maximum allowed heavy concentration established by *WHO and **FAO.*

Table 3

Heavy metal concentration (mg/kg) in gills of fish species.

	Cu	*Zn*	*Cr*	*Cd*	*Pb*	*Hg*
Clupea pallasii	0.491±0.015	7.403±0.01	0.391±0.008	0.192±0.001	0.364±0.003	0.164±0.001
Macolor niger	0.422±0.01	9.201±0.04	0.313±0.005	0.261±0.002	0.243±0.001	0.071±0.001
Pristipomoides filamentosus	0.372±0.013	9.902±0.02	0.421±0.006	0.331±0.001	0.292±0.002	0.181±0.001

Table 4

Heavy metal concentration (mg/kg) in liver of fish species.

	Cu	*Zn*	*Cr*	*Cd*	*Pb*	*Hg*
Clupea pallasii	0.683±0.007	13.702±0.02	0.441±0.004	0.332±0.001	0.181±0.001	0.061±0.001
Macolor niger	0.612±0.004	23.112±0.04	0.473±0.006	0.291±0.001	0.304±0.002	0.103±0.001
Pristipomoides filamentosus	0.451±0.003	17.803±0.02	0.401±0.004	0.223±0.002	0.251±0.002	0.142±0.001

The gills were found to have the maximum concentration of lead. The highest concentrations of mercury show a discrepancy between gill and liver in the three different species with the maximum value in the tissue of *Pristipomoides filamentosus*. Many studies have shown that active metabolic organs like gill and liver can accumulate a greater concentration of heavy metals as compared to the tissues of muscles [23]. The variations in the metal concentrations in tissues may be due to their ability to induce inter-metal binding proteins such as metallothioneins, as reported in many earlier studies [24,25]. The gill is an important site for the entry of the heavy metals and is the first target organ for exposure in fish [26]. The high concentration of metals in the gills is due to the metals complexation with the mucus. The concentration of metals in the gill reflects the level of the metals in the waters where the fish live, whereas the concentration in liver represents the storage of metals [27]. Thus, the gills in fish are more often recognized as the environmental indicator organs of water pollution than any other fish organs [28].

Copper being identified as a vital element, it is necessary for a wide variety of enzymes and other cellular components with important functions in all living beings. However, the excessive consumption of copper is harmful to human health as it leads to toxicity, and other related ailments. The current investigation shows the concentrations of copper in muscles was the highest (0.77 mg/kg) in *Clupea pallasii* whereas the species *Macolor niger* shows the lowest amount (0.47 mg/kg). The concentration of copper in gills was lower in comparison to the muscles and the minimum concentration (0.37 mg/kg) was present in *Pristipomoides filamentosus*. As far as liver is concerned, the copper accumulation was found similar to that of muscles and gills. The safe and adequate daily intake of copper is estimated at 1.5-3.0 mg for adults [8]. The mean concentration of copper in fish tissue samples ranged from 0.37-0.77 mg/kg, which is similar to 0.251-0.907 mg/kg according to the available literature [29], but for human consumption, it was not greater than the allowed level (Table 2) by FAO/WHO [30]. The high copper concentration can be attributed to oil dropping by frequent boating activities or may be due to too much fishing activities around the sampling site.

Zinc is harmful to human health if taken in excess and may cause intoxication [31]. Zinc levels found in the tissues of fish species are less than the FAO permitted limits (Table 2) of 30 mg/kg [32]. The species *Macolor niger* has the maximum amount of zinc in liver (23.1 mg/kg) as well as in muscles (18.3 mg/kg) in comparison with the other two species. In the gills, the highest concentration of zinc (9.9 mg/kg) was found in *Pristipomoides filamentosus*.

Chromium is among the common heavy metal pollutants that enters the water through the effluents from electroplating, dyeing, or printing industries. Chromium is an affective teratogenic and carcinogenic agent for human. The allowed limit established by WHO for chromium is 0.05 mg/kg [33]. The concentrations of chromium were comparatively lower for all the organs of the species. The lowest concentration (0.29 mg/kg) was in the muscles of *Clupea pallasii*, while the maximum concentration (0.47 mg/kg) was determined in the livers of *Macolor niger*. Therefore, the chromium concentration for all samples was higher than the limit (0.05 mg/kg) prescribed by WHO (Table 2).

Cadmium is not an essential element however it competes with calcium ion at the enzyme sites of the organism. Cadmium is considerably accumulated in the liver, followed by gills and muscles. According to FAO standard, the maximum admissible limit of the concentration of cadmium is 0.5 mg/kg [32]. Cadmium tends to have pronounced nephrotoxic potential and the excessive intake may lead to renal and hepatic toxic effects [34]. Since fish muscles are the main edible part, the concentration of cadmium was found to be lowest in the muscles except gills of *Clupea pallasii* of all the species investigated. Cadmium concentrations in the samples of all the species of analyzed fish were below the legal limits (Table 2).

The maximum concentration of lead detected in this investigation was in the gills of *Clupea pallasii* (0.36 mg/kg), whereas the lowest concentration (0.02 mg/kg) was determined in the muscles of *Pristipomoides filamentosus*. Henceforth, regardless of the investigated fish species, lead concentration in all the analyzed samples was lower than the level 0.5 mg/kg specified by FAO [35] given in Table 2.

The consumption of fish containing mercury above the permissible limit may badly affect the central nervous system and the endocrine system. The concentration of mercury in all the investigated samples was found to be lower than the permissible limits prescribed by FAO which is 0.5 mg/kg [36]. However, the accumulation of mercury even at very low concentrations is toxic.

Table 5

Comparative results for metal accumulation in fishes (mg/kg) from different locations.

Location	*Cu*	*Zn*	*Cr*	*Cd*	*Pb*	*Hg*	*Ref.*
Gulf of Oman, Oman	0.24-19.5	1.82-67.3	0.054-0.072	<0.005	0.011-0.005	<0.5	[38]
Hainan coastal area, South China Sea, China	0.93±0.006	9.95±0.99	1.82±0.31	0.002±0.001	0.07±0.02	-	[39]
Coastal waters of Terengganu, Malaysia	0.007±0.001	0.109±0.04	-	0.005±0.002	-	-	[40]
Bulgarian Black Sea Coast, Bulgaria	0.71±0.18	8.74±0.98	0.03±0.01	0.08±0.001	0.06±0.01	0.16±0.02	[41]
Rio de Janeiro State Coast, Brazil	2.18±0.19	4.71±0.60	-	0.02±0.008	0.2±0.1	-	[42]
The Coast of Lautoka, Fiji	0.532±0.006	12.631±0.03	0.382±0.004	0.231±0.001	0.204±0.001	0.091±0.001	Present study

The concentration of mercury is generally greater in the liver of fishes than in the muscles tissue [37]. However, the present investigation does not follow the trend and the maximum concentration of 0.18 mg/kg was determined in the gills of *Pristipomoides filamentosu*s and the minimum concentration was present in the muscles of *Clupea pallasii* (0.02 mg/kg).

The comparison of literature results for metal accumulation in fishes studied from different locations has been summarized in Table 5. The average concentration of copper in this study was approximately the same as compared to the reported values. However, the average accumulation of zinc was the highest in the current investigation compared to the other studies, except the results reported by de Mora, S. *et al*. [38]. In case of the average concentration of chromium, it was only less than that determined in fish samples from Hainan coastal area, South China Sea. The average cadmium concentrations level reported in the present study were higher than the previous studies in different locations. For the average level of lead, it was found to be higher than reported results except for the Rio de Janeiro State Coast, Brazil. The average mercury level in different parts of fish in this research was found to be below than the levels reported in the selected literature.

Conclusions

The heavy metals concentration (Cd, Pb, Cu, Hg, Zn, Cr) was determined in the muscles, gills and liver of three different fish species such as *Clupea pallasii*, *Macolor niger*, *Pristipomoides filamentosus* collected from the waters of the South Pacific Ocean around Lautoka in Fiji.

The obtained results indicate that the highest concentration was detected for zinc (23.112 mg/kg) in the liver of *Macolor niger* and the lowest concentration was found for mercury (0.021 mg/kg) in the muscles of Clupea *pallasii*. There was no single type of fish that was consistently high for all metals. The concentration range of the investigated metals including copper (0.372-0.771 mg/kg), zinc (7.403-23.112 mg/kg), cadmium (0.081-0.332 mg/kg), lead (0.021-0.364 mg/kg) and mercury (0.021-0.181 mg/kg), was within the permissible limits recommended by FAO/WHO, thus makes them available for human consumption. However, the concentration of chromium among all the three species was in the range of 0.291-0.473 mg/kg, higher than the WHO limit of 0.05 mg/kg.

The results of this study show considerable variations in the bioaccumulation in muscles, gills and livers for the specific heavy metals in the fishes from the waters of South Pacific Ocean around Lautoka in Fiji.

References

1. Fernandes, C.; Fontainhas-Fernandes, A.; Peixoto, F.; Salgado, M.A. Bioaccumulation of heavy metals in Liza saliens from the Esomriz-Paramos coastal lagoon, Portugal. Ecotoxicology and Environmental Safety, 2007, 66(3), pp. 426-431. DOI: https://doi.org/10.1016/j.ecoenv.2006.02.007
2. Tchounwou, P.B.; Yedjou, C.G.; Patlolla, A.K.; Sutton, D.J. Heavy metal toxicity and the environment. Springer: Basel, 2012, vol. 101, pp. 133-164.

DOI: https://doi.org/10.1007/978-3-7643-8340-4_6
3. Baharom, Z.S.; Ishak, M.Y. Determination of heavy metal accumulation in fish species in Galas river, Kelantan and Beranang mining pool, Selangor. Procedia Environmental Sciences, 2015, 30, pp. 320-325. DOI: https://doi.org/10.1016/j.proenv.2015.10.057
4. El-Moselhy, Kh.M.; Othman, A.I.; El-Azem, H.A.; El-Metwally, M.E.A. Bioaccumulation of heavy metals in some tissues of fish in the Red Sea, Egypt. Egyptian Journal of Basic and Applied Sciences, 2014, 1(2), pp. 97-105. DOI: https://doi.org/10.1016/j.ejbas.2014.06.001
5. Yi, Y.J.; Zhang, S.H. The relationships between fish heavy metal concentrations and fish size in the upper and middle reach of Yangtze River. Procedia Environmental Sciences, 2012, 13, pp. 1699-1707. DOI: https://doi.org/10.1016/j.proenv.2012.01.163
6. Rajeshkumar, S.; Li, X. Bioaccumulation of heavy metals in fish species from the Meiliang Bay, Taihu Lake, China. Toxicology Reports, 2018, 5, pp. 288-295. DOI: https://doi.org/10.1016/j.toxrep.2018.01.007
7. Jaishankar, M.; Tseten, T.; Anbalagan, N.; Mathew, B.B.; Beeregowda, K.N. Toxicity, mechanism and health effects of some heavy metals. Interdisciplinary Toxicology, 2014, 7(2), pp. 60-72. DOI: https://doi.org/10.2478/intox-2014-0009
8. Rehman, K.; Fatima, F.; Waheed, I.; Akash, M.S.H. Prevalence of exposure of heavy metals and their impact on health consequences. Journal of Cellular Biochemistry, 2018, 119(1), pp. 157-184. DOI: https://doi.org/10.1002/jcb.26234
9. Nkansah, M.A.; Korankye, M.; Darko, G.; Dodd, M. Heavy metal content and potential health risk of geophagic white clay from the Kumasi Metropolis in Ghana. Toxicology Reports, 2016, 3, pp. 644-651. DOI: https://doi.org/10.1016/j.toxrep.2016.08.005
10. Atique Ullah, A.K.M.; Maksud, M.A.; Khan, S.R.; Lutfa, L.N.; Quraishi, S.B. Dietary intake of heavy metals from eight highly consumed species of cultured fish and possible human health risk implications in Bangladesh. Toxicology Reports, 2017, 4, pp. 574-579. DOI: https://doi.org/10.1016/j.toxrep.2017.10.002
11. Arantes, F.P.; Savassi, L.A.; Santos, H.B.; Gomes, M.V.T.; Bazzoli, N. Bioaccumulation of mercury, cadmium, zinc, chromium, and lead in muscle, liver, and spleen tissues of a large commercially valuable catfish species from Brazil. Proceedings of the Brazilian Academy of Sciences, 2016, 88(1), pp. 137-147. DOI: http://doi.org/10.1590/0001-3765201620140434
12. Uysal, K.; Emre, Y.; Köse, E. The determination of heavy metal accumulation ratios in muscle, skin and gills of some migratory fish species by inductively coupled plasma-optical emission spectrometry (ICP-OES) in Beymelek Lagoon (Antalya/Turkey). Microchemical Journal, 2008, 90(1), pp. 67-70. DOI: https://doi.org/10.1016/j.microc.2008.03.005
13. Tuzen, M. Determination of heavy metals in fish samples of the middle Black Sea (Turkey) by graphite furnace atomic absorption spectrometry. Food Chemistry, 2003, 80(1), pp. 119-123. DOI: https://doi.org/10.1016/S0308-8146(02)00264-9
14. Al-Busaidi, M.; Yesudhason, P.; Al-Mughairi, S.; Al-Rahbi, W.A.K.; Al-Harthy, K.S.; Al-Mazrooei, N.A.; Al-Habsi, S.H. Toxic metals in commercial marine fish in Oman with reference to national and international standards. Chemosphere, 2011, 85(1), pp. 67-73. DOI: https://doi.org/10.1016/j.chemosphere.2011.05.057
15. Squadrone, S.; Prearo, M.; Brizio, P.; Gavinelli, S.; Pellegrino, M.; Scanzio, T.; Guarise, S.; Benedetto, A.; Abete, M.C. Heavy metals distribution in muscle, liver, kidney and gill of European catfish (*Silurus glanis*) from Italian Rivers. Chemosphere, 2013, 90(2), pp. 358-365. DOI: https://doi.org/10.1016/j.chemosphere.2012.07.028
16. Taweel, A.; Shuhaimi-Othman, M.; Ahmad, A.K. Assessment of heavy metals in tilapia fish (*Oreochromis niloticus*) from the Langat river and engineering lake in Bangi, Malaysia and evaluation of the health risk from tilapia consumption. Ecotoxicology and Environmental Safety, 2013, 93, pp. 45-51. DOI: https://doi.org/10.1016/j.ecoenv.2013.03.031
17. Helrich, K. Official methods of analysis of the association of official analytical chemists. 19th Ed., 2012, Washington DC, USA, 1298 p.
18. Mendil, D; Unal, O.F; Tuzen, M; Soylak, M. Determination of trace metals in different fish species and sediments from River Yesilirmak in Tokat, Turkey. Food and Chemical Toxicology, 2010, 48(5), pp. 1383-1392. DOI: https://doi.org/10.1016/j.fct.2010.03.006
19. Djedjibegovic, J; Larsen, T; Skrbo, A; Marjanovic, A.; Sober, M. Contents of cadmium, copper, mercury and lead in fish from the Neretva river (Bosnia and Herzegovina) determined by inductively coupled plasma mass spectrometry (ICP-MS). Food Chemistry, 2012, 131(2), pp. 469-476. DOI: https://doi.org/10.1016/j.foodchem.2011.09.009
20. Kamaruzzaman, B.Y.; Rina, Z.; John, B.A.; Jalal, K.C.A. Heavy metal accumulation in commercially important fishes of South West Malaysian Coast. Research Journal of Environmental Sciences, 2011, 5(6), pp. 595-602. DOI: https://doi.org/10.3923/rjes.2011.595.602
21. Lahman, S.E.; Trent, K.R.; Moore, P.A. Sublethal copper toxicity impairs chemical orientation in the crayfish, *Orconectes rusticus*. Ecotoxicology and Environmental Safety, 2015, 113, pp. 369-377. DOI: https://doi.org/10.1016/j.ecoenv.2014.12.022
22. Henry, F.; Amara, R.; Courcot, L.; Lacouture, D.; Bertho, M.-L. Heavy metals in four fish species from the French coast of the Eastern English Channel and Southern bight of the North Sea. Environment International, 2004, 30(5), pp. 675-683.

DOI: https://doi.org/10.1016/j.envint.2003.12.007
23. Dural, M.; Goksu, M.Z.L.; Ozak, A.A. Investigation of heavy metal levels in economically important fish species captured from the Tuzla lagoon. Food Chemistry, 2007, 102(1), pp. 415-421. DOI: http://doi.org/10.1016/j.foodchem.2006.03.001
24. Canli, M.; Atli, G. The relationships between heavy metal (Cd, Cr, Cu, Fe, Pb, Zn) levels and the size of six Mediterranean fish species. Environmental Pollution, 2003, 121(1), pp. 129-136. DOI: https://doi.org/10.1016/S0269-7491(02)00194-X
25. Al-Yousuf, M.H.; El-Shahawi, M.S.; Al-Ghais, S.M. Trace metals in liver, skin and muscle of *Lethrinus lentjan* fish species in relation to body length and sex. Science of the Total Environment, 2000, 256(2-3), pp. 87-94. DOI: https://doi.org/10.1016/S0048-9697(99)00363-0
26. Vinodhini, R.; Narayanan, M. Bioaccumulation of heavy metals in organs of fresh water fish *Cyprinus carpio* (Common carp). International Journal of Environmental Science and Technology, 2008, 5, pp. 179-182. DOI: https://doi.org/10.1007/BF03326011
27. Romeo, M.; Siau, Y.; Sidoumou, Z.; Gnassia-Barelli, M. Heavy metals distribution in different fish species from the Mauritania coast. Science of the Total Environment, 1999, 232(3), pp. 169-175. DOI: https://doi.org/10.1016/S0048-9697(99)00099-6
28. Joshua, I.I.; Iyi-Aguebor, E.G. Evaluations of the levels of heavy metals in river water and selected species of fish from Ogba River in Benin City, Nigeria. Journal of Applied Sciences and Environmental Management, 2017, 21(6), pp. 1093-1096. DOI: https://dx.doi.org/10.4314/jasem.v21i6.16
29. Elnabris, K.J.; Muzyed, S.K.; El-Ashgar, N.M. Heavy metal concentrations in some commercially important fishes and their contribution to heavy metals exposure in Palestinian people of Gaza Strip (Palestine). Journal of the Association of Arab Universities for Basic and Applied Sciences, 2013, 13(1), pp. 44-51. DOI: http://doi.org/10.1016/j.jaubas.2012.06.001
30. Dhanakumar, S.; Solaraj, G.; Mohanraj, R. Heavy metal partitioning in sediments and bioaccumulation in commercial fish species of three major reservoirs of river Cauvery delta region, India. Ecotoxicology and Environmental Safety, 2015, 113, pp. 145-151. DOI: https://doi.org/10.1016/j.ecoenv.2014.11.032
31. Chi, Q.Q.; Zhu, G.W.; Langdon, A. Bioaccumulation of heavy metals in fishes from Taihu Lake, China. Journal of Environmental Sciences, 2007, 19(12), pp. 1500-1504. DOI: https://doi.org/10.1016/S1001-0742(07)60244-7
32. Nauen, C.E. Compilation of legal limits for hazardous substances in fish and fishery products. FAO, 1983, Rome, 102 p. www.fao.org
33. Bakshi, A.; Panigrahi, A.K. A comprehensive review on chromium induced alterations in fresh water fishes. Toxicology Reports, 2018, 5, pp. 440-447. DOI: https://doi.org/10.1016/j.toxrep.2018.03.007
34. Orr, S.E.; Bridges, C.C. Chronic Kidney Disease and Exposure to Nephrotoxic Metals. International Journal of Molecular Sciences, 2017, 18(5), pp. 1039. DOI : https://doi.org/10.3390/ijms18051039
35. Asuquo, F.E.; Ewa-Oboho, I.; Asuquo, E.F.; Udo, P.J. Fish species used as biomarker for heavy metal and hydrocarbon contamination for Cross River, Nigeria. The Environmentalist, 2004, 24, pp. 29-37. DOI: https://doi.org/10.1023/B:ENVR.0000046344.04734.39
36. Holden, A.V. Mercury in fish and shellfish. A Review. International Journal of Food Science and Technology, 1973, 8(1), pp. 1-25. DOI: https://doi.org/10.1111/j.1365-2621.1973.tb01685.x
37. Havelkova, M.; Dusek, L.; Nemethova, D.; Poleszczuk, G.; Svobodova, Z. Comparison of mercury distribution between liver and muscle - a biomonitoring of fish from lightly and heavily contaminated localities. Sensors, 2008, 8(7), pp. 4095-4109. DOI: https://doi.org/10.3390/s8074095
38. de Mora, S.; Fowler, S.W.; Wyse, E.; Azemard, S. Distribution of heavy metals in marine bivalves, fish and coastal sediments in the Gulf and Gulf of Oman. Marine Pollution Bulletin, 2004, 49(5-6), pp. 410-424. DOI: https://doi.org/10.1016/j.marpolbul.2004.02.029
39. Liu, J.-L.; Xu, X.-R.; Ding, Z.-H.; Peng, J.-X.; Jin, M.-H.; Wang, Y.-S.; Hong, Y.-G.; Yue, W.-Z. Heavy metals in wild marine fish from South China Sea: levels, tissue- and species-specific accumulation and potential risk to humans. Ecotoxicology, 2015, 24, pp. 1583-1592. DOI: https://doi.org/10.1007/s10646-015-1451-7
40. Rosli, M.N.R.; Samat, S.B.; Yasir, M.S. Analysis of heavy metal accumulation in fish from the coastal waters of Terengganu, Malaysia. AIP Conference Proceedings, 2018, 1940(1), pp. 1-6. DOI: https://doi.org/10.1063/1.5027925
41. Stancheva, M.; Makedonski, L.; Peycheva, K. Determination of heavy metal concentrations of most consumed fish species from Bulgarian Black Sea coast. Bulgarian Chemical Communications, 2014, 46(1), pp. 195-203.
42. Medeiros, R.J.; dos Santos, L.M.G.; Freire, A.S.; Santelli, R.E.; Braga, A.M.C.B.; Krauss, T.M.; Jacob, S.C. Determination of inorganic trace elements in edible marine fish from Rio de Janeiro State, Brazil. Food Control, 2012, 23(2), pp. 535-541. DOI: https://doi.org/10.1016/j.foodcont.2011.08.027

CHEMISTRY JOURNAL OF MOLDOVA. General, Industrial and Ecological Chemistry. 2020, 15(1), 58-66
ISSN (p) 1857-1727 ISSN (e) 2345-1688
http://cjm.asm.md
http://dx.doi.org/10.19261/cjm.2020.717

EVALUATION OF THE THERMAL BEHAVIOUR OF AGRICULTURAL WASTES FOR POSSIBLE USE IN THE BIOMASS PELLETS INDUSTRY

Alexandra Marcu [a], Gabriela Lisa [a*], Ioana-Emilia Sofran [b], Ion Anghel [b], Manuel Serban [b]

[a]*Department of Chemical Engineering, Faculty of Chemical Engineering and Environmental Protection "Cristofor Simionescu", Gheorghe Asachi Technical University of Iasi, 73, Prof. Dr. docent D. Mangeron blvd., Iasi RO-700050, Romania*
[b]*Fire Officers Faculty, Police Academy "Alexandru Ioan Cuza", 3, Morarilor str., Bucharest RO-022451, Romania*
[*]*e-mail: gapreot@yahoo.com, gapreot@ch.tuiasi.ro; phone: (+40 232) 27 86 83; fax: (+40 232) 27 13 11*

Abstract. This paper tackles the potential uses of agricultural wastes (sawdust, sunflower seed shells, pumpkin seed shells, cherry pits, walnut shells, and green walnut shells) for the production of pellets. Combustion heat was determined for these wastes and their thermal decomposition in an air atmosphere was analysed. Five types of mini-pellets were made from different combinations of available wastes and their thermal behaviour was analysed by the microscale combustion calorimetry method. The results were compared with those obtained for pellets available on the market and it was concluded that the mini-pellets obtained from agricultural wastes can be used to maintain combustion in heating systems based on pellets boilers.

Keywords: waste, biomass pellet, combustion heat, thermogravimetric analysis, microscale combustion calorimetry.

Received: 04 May 2020/ Revised final: 02 June 2020/ Accepted: 05 June 2020

Glossary

CP	cherry pits
DWS	dried walnut shells
GWS	green walnut shell
PSS	pumpkin seeds shells
SSS	sunflower seed shells
S	sawdust
WF	wheat flour
Pc	pellets commercially available
HRC	heat release capacity
HRR	heat release rate
PHRR	peak heat release rate
THR	total heat release
MCC	microscale combustion calorimetry method

Introduction

The concern of the researchers to develop new ways of the use of biomass for energy purposes is continuous and is supported almost worldwide. Wood pellets are a form of biomass, however they have the disadvantage of being relatively expensive, therefore cost-effective alternatives should be proposed. Holubcik, M. *et al.* showed that woody plants such as red raspberries and black currants have similar energy properties as Norwegian spruce sawdust pellets and could be regarded as efficient replacements to wood pellets [1]. The amount of wastes originating from agriculture increases along with agricultural production. These residues could be converted to energy sources by techniques such as combustion, gasification, pyrolysis, *etc.*, however the use of these raw wastes has some disadvantages, including the low energy density, low energy efficiency, large storage capacity and problems related to transportation and distribution. In order to improve the transportation, storage and energy generation characteristics of agricultural wastes, its bulk density should be increased. Briquetting is one of the methods of increasing bulk density up to 1000-1200 kg/m^3, compared to 30-150 kg/m^3 for raw material, and the volume may be reduced by 8-10 times [2].

Increased domestic and industrial demand for biomass heat and energy production in Canada, United States, Europe and China has led, in recent decades, to a strong global pellet market and a market growth is forecast for the coming years. In the near future, agricultural wastes have great potential in the biomass pellets industry. It is, therefore, of great interest to study the characteristics of this new category of raw materials, paying special attention to the problems that they may cause in terms of both production and use. From a technical point of view, the main difference between wood pellets and agropellets is the latter's slight friability, slightly lower energy

efficiency and higher ash content [3]. With 14.8 million hectares, Romania is the second largest agricultural producer in Central and Eastern Europe, after Poland, and currently holds one of the best positions in Europe in terms of biomass [3]. Within the country, the biomass energy sector is divided. Wood production is concentrated in the Carpathians and Subcarpathians, while agricultural by-products are produced in the southern part of the country and in the region of Moldova. In order to guarantee an independent supply of energy for the rural population, concepts have been developed to produce energy and heat from agricultural by-products. Nowadays, it appears that biomass pellets production strongly competes with direct biomass burning due to higher investment costs for pellets production [3].

In the next years, agro-pellets could play a more important role in the supply of thermal energy to households and towns/cities, after overcoming the difficulties related to agro-pellets combustion in small and medium boilers [4]. Several studies have been carried out in the last two decades that examined for example the thermochemical characteristics and performance of solid olive residues suggesting that these are a promising biomass resource, which could be used for energy [5,6]. On the other hand, Brlek, T. *et al*. suggested limiting the burning of olive processing waste pellets due to their high nitrogen content [7].

Marculescu, C. and Ciuta, S. established that over 20% of each kilogram of grapes processed for wine is waste. They analysed the thermal degradation of grape marc in a laboratory oven and found that it possesses high energy efficiency (19.7 kJ/kg) [8]. Rossini, G. *et al.* have found that tomato waste may be suitable for combustion, but its relatively high nitrogen content may cause NO_x emission problems; therefore, the authors suggested the separation of tomato waste into combustion peels and seeds for vegetable oil production [9]. González, J.F. *et al.* have studied the tomato waste combustion in a wall boiler and found that tomato residues proved more efficient in the boiler than other biomass (forest residues, sorghum, almond kernels and cane) [10]. Ruiz-Celma, A. *et al.* have studied tomato seeds and peels pellets and reported a high energy value and an energy density (approaching 8 GJ/m^3) similar to that of other biomass pellets, regardless of their low bulk density values [11]. In 2017, Brunerová, A. *et al.* have analysed the use of residual biomass from oats (*Avena sativa*), wheat (*Triticum spp*.), poppy (*Papaver somniferum*) and barley (*Hordeum vulgare L*.) residues, which were chosen because these do not require additional mechanical processing, when leaving the post-harvest processing lines. The assessment of the recorded results showed a satisfactory level of chemical quality and high energy potential of all investigated materials, yet a low level of their mechanical quality [12,13].

The goal of this study was to assesses the possible uses of specific agricultural wastes, dried walnut shells (DWS), green walnut shell (GWS), cherry pits (CP), sunflower seed shells (SSS), pumpkin seeds shells (PSS) and sawdust (S), for pellets production, respectively to obtain easily reproducible products in a household or small farm.

Experimental

Materials

Selected agricultural wastes, sawdust, sunflower seed shells, pumpkin seed shells, cherry pits, walnut shells, and green walnut shells, were assessed based on their combustion heat; additives (wheat flour - WF) were used to produce mini-pellets. The initial material consisted of various types of wastes dried at room temperature (approximately 20°C). Note that pumpkin seed shells dried slower than sunflower seed shells. The green walnut shells were already dried when these were gathered after harvesting the nuts. The dried agricultural wastes were then ground in a mortar to facilitate the formation of mini-pellets.

Pellets production

The mini-pellets were obtained by pressing/compressing a mixture of properly dried and minced ingredients. In order to improve the combustion process, approximately 6% beech wood ash (A) with an installed power of 7 KW was also included in the 5 types of mini-pellets. The ash was introduced as catalyst for the combustion process of mini-pellets [14]. The obtained mini-pellets were of 15 mm in diameter and 5 mm in length. Table 1 shows their percentage mass composition by codes. The humidity present in the 5 types of mini-pellets (Table 1) was determined indirectly from the thermogravimetric analysis. The recorded results on the obtained mini-pellets were validated by analysing the thermal behaviour of the pellets commercially available, with a diameter of 6 mm, humidity of 7.7% and calorific value declared by the manufacturer of 18.2 MJ/kg.

Table 1

Information about the mass composition (%) of the obtained mini-pellets.

Pellets		WF, %	GWS, %	CP, %	DWS, %	PSS, %	SSS, %	S, %	A, %	Total mass, g	Humidity, %
P1		30.05	31.65	-	-	-	-	32.36	5.94	0.9134	6.31
P2		27.40	27.91	-	-	-	39.03	-	5.66	0.9173	6.68
P3		22.68	-	37.30	-	-	34.12	-	5.90	0.9279	5.75
P4		27.20	32.29	-	34.53	-	-	-	5.98	0.9372	7.68
P5		18.45	38.50	-	-	37.00	-	-	6.05	0.8375	5.05

Methods

The *combustion heat* of agricultural wastes was determined using a Berthelot calorimeter. The samples were compressed and burned in a platinum crucible. The used calculation ratio (Eq.(1)) [15]:

$$\Delta H^0_{C,298} = \frac{-C \cdot \Delta T - m_{Fe} \cdot \Delta H^0_{C,298}(Fe)}{m_s} \quad (1)$$

where, *C*- heat capacity of the calorimeter ($1.04 \cdot 10^4$ J/K);

ΔT- temperature difference accompanying the combustion (°C);

m_{Fe}- mass of the burned Fe thread (g);

$\Delta H^0_{C,298(Fe)}$ - iron standard enthalpy of combustion ($-6.658 \cdot 10^3$ J/g);

m_s- mass of the sample submitted to combustion (g);

$\Delta H^0_{C,298}$ - standard enthalpy of combustion of the sample submitted to thermal degradation.

Thermogravimetric analysis was performed dynamically, in air with a flow rate of 20 cm^3/min, with a heating rate of 10°C/min, within the 25-700°C temperature range and the sample weight between 3.8 and 4.3 mg. The Mettler Toledo TGA-SDTA851^e equipment was used, and the thermogravimetric (TG), derivative thermogravimetric (DTG) and differential thermal (DTA) curves were processed using Mettler Toledo's STAR software. The operating parameters were kept constant for all types of analysed wastes, in order to obtain comparable data. The main thermogravimetric and thermal characteristics considered were: T_{onset} - the temperature at which the thermal degradation starts at every stage; T_{peak} - the temperature at which the thermal degradation is maximum; T_{endset} - the temperature at which the degradation process ends for each stage; *W*- percentage weight loss and DTA characteristic (exo- or endothermal processes).

The *flammability behaviour* of the samples was tested using an FTT Micro Calorimeter with microscale combustion calorimetry (MCC) method. The weight of the analysed samples ranged between 3.64 mg and 5.15 mg, and they were heated at a rate of (1°C/s) in a nitrogen atmosphere with a flow rate of 80 cm^3/min; the resulting gases were mixed with oxygen with a flow rate of 20 cm^3/min and then fed into the combustion chamber heated to 900°C. The oxygen consumption rate was measured continuously and the heat release results were calculated as the mean of five measurements for each sample. Note that ASTM D7309-2007 (method A) was applied, which involves sample degradation in a nitrogen atmosphere; then, as specified above, the flue gases are fed into a combustion chamber where these are thermally oxidized until exhausted [16]. By applying these tests, the following parameters were measured: *HRR* (heat release rate), T_{PHRR} (peak heat release rate temperature), *PHRR* (peak heat release rate), *THR* (total heat release) and *HRC* (heat release capacity). The residue remaining after the analysis was weighed and reported as a percentage [17,18].

Results and discussion

Combustion heat determination

Heats of combustion are usually determined by burning a known amount of the material in a bomb calorimeter with an excess of oxygen, and the heat of combustion can be determined by measuring the temperature change. Table 2 compares the combustion enthalpies obtained using a Berthelot calorimeter for the analysed types of wastes and also presents values from the literature. The combustion heat was determined for the studied starting material originating from agricultural wastes, the obtained results are graphically represented in Figure 1.

According to literature data, wood combustion enthalpy ranges between 18800 and 20100 J/g [15]. The results shown in the Table 2 prove that the combustion enthalpy values recorded for pumpkin and sunflower seed shells are only slightly lower than the values for wood. The combustion heat of the analysed samples increases in the following order: green walnut shells < dried walnut shells < cherry pits < pellets available on the market < sunflower seed shells < pumpkin seed shells < sawdust.

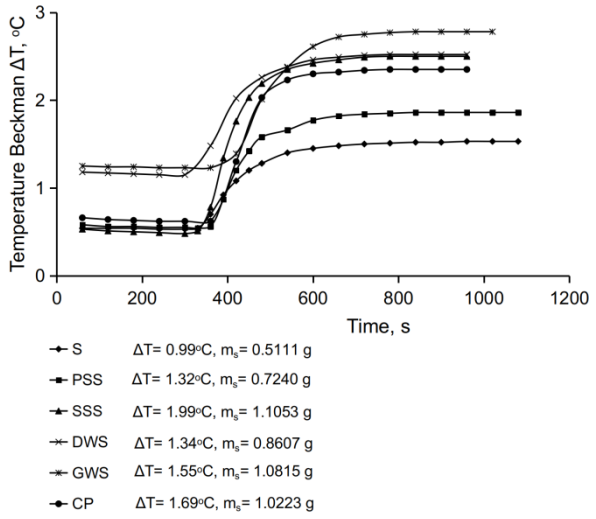

Figure 1. Temperature variation in the calorimeter for the analysed wastes.

Thermogravimetric analysis

The TG, DTG and DTA curves given comparatively in Figures 1S and 2S (Supplementary material) and Figure 2 enabled determining the main thermogravimetric characteristics of the analysed wastes presented in Table 3. According to the obtained results, in stage I, humidity is removed from wastes and varies between 4 and 11%. After humidity removal, the thermal decomposition of sawdust (S) and sunflower seed shell (SSS) samples takes place in two stages. In the case of sawdust, according to literature, the mass loss in the second stage may be associated with the total decomposition of hemicellulose and cellulose and with the partial decomposition of lignin. The last stage corresponds to the decomposition of the remaining lignin and the burning of carbon residues [24]. As expected, the main thermogravimetric characteristics obtained for commercial pellets (Pc) are close in value to those of S. The amount of residue obtained at 700°C is 9.48% for S and 6.10% for Pc. The main decomposition stage of SSS occurs within the 252-333°C temperature range and is accompanied by a 48.43% mass loss. Compared to S, the SSS thermal decomposition onset at this stage occurs earlier with a deviation of 15°C, probably due to the higher hemicellulose content, which is rich in poor etheric bonds that are thermally unstable and produce volatile combustible species, capable of homogeneous combustion in the gaseous phase [25,26].

A different behaviour was noted in the case of the thermal decomposition in air of pumpkin seed shells, which, at temperatures higher than 350°C, undergo a two-process transformation, with decomposition rate temperatures peaks at 459 and 514°C, respectively. At the end of the second stage, up to a temperature of 437°C, a series of stable intermediates are probably formed. In the case of this type of seeds (PSS), a twice higher amount of residue was obtained, compared to the other samples (S and SSS).

Table 2

Combustion enthalpy values for the analysed wastes (J/g).

Sample	*This work*	*Literature data*
Sawdust (S)	19826.93	19700 [19], 19482 [20], 9573 [21]
Sunflower seed shells (SSS)	18549.64	18674 [22]
Pumpkin seeds shells (PSS)	18780.16	-
Green walnut shells (GWS)	14785.18	-
Cherry pits (CP)	17071.47	19870 [22]
Dried walnut shells (DWS)	16157.44	17800 [23]
Pellets commercially available (Pc)	-	18200*

**value declared by the producer*

The largest amount of residue at 700°C is produced by GWS. In the last stage, this sample saw a highly exothermal thermooxidation process (Figure 2), accompanied by a considerable mass loss within the 580-630°C temperature range. At the end of the third decomposition stage, GWS also forms a stable intermediate whose decomposition starts at a temperature greater than 580°C. Both DWS and CP have comparable residual amounts, which are four times lower than those of SSS and S; however, as shown above, their caloric capacities are lower than those of the latter types of wastes. After removal of the humidity, the thermal decomposition of the DWS takes place in two stages with temperatures at which the degradation rate is maximum at 285 and 472°C respectively. The last stage of degradation is the thermooxidation process which ends at the temperature of 507°C and is accompanied (according to the DTA curve shown in Figure 2) by a highly exothermic process. Dried walnut shells were analysed by applying the TG/GC/MS (thermogravimetry/gas chromatography/mass spectrometry) technique in a helium atmosphere, within 25-900°C temperature range, by Fan, F. *et al.*, who found that in an inert atmosphere (helium) the thermal decomposition of walnut shells takes place in a single stage with a 347°C peak degradation rate temperature [27]. The TG/GC/MS technique applied on these dried walnut shells samples has helped to the identification of more than 20 different substances in pyrolysis gases, of which can be mentioned furan, furfural, benzene and long chain alkanes, *etc*. Petuhov, O. analysed the thermal decomposition of walnut shells in a nitrogen atmosphere and found that the process takes place in several stages. In the first stage, the removal of humidity and volatile substances takes place and is accompanied by a mass loss of 7.1%. In the following stages, hemicellulose, cellulose and lignin decompose [28]. In the case of wheat flour used as an additive to produce mini-pellets, thermal decomposition in an air atmosphere takes place in three stages. The first stage characterized by an endothermal process, according to the DTA curve (Figure 2), which corresponds to approximately 10% of moisture removal. Starch decomposition in disaccharides occurs during the second stage, within the 274-317°C temperature range, with a 54.34% mass loss. The process continues at temperatures higher than 420°C, with depolymerisation of amylose and amylopectin [29].

Considering the decomposition onset temperature as a thermal stability criterion, obviously disregarding humidity removal, the following thermal stability increase sequence for the analysed materials was obtained: green walnut shells < sunflower seed shells < pumpkin seed shells ≈ dried walnut shells < cherry pits < sawdust < wheat flour.

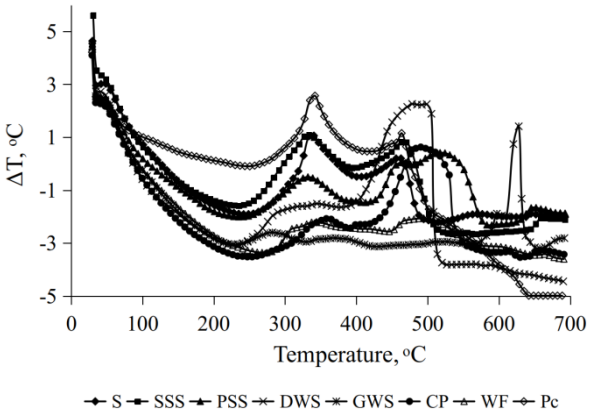

Figure 2. DTA curves of the analysed wastes.

Microscale combustion calorimetry analysis of the obtained pellets

The MCC was used to analyse the 5 mini-pellets whose composition was described in Experimental section (Table 1) and a type of wood pellets available on the market used in heating systems based on pellets boilers. The mini-pellets taken for analysis had a mass ranging between 4.11 mg and 5.15 mg and were heated at a rate of (1°C/s) in a nitrogen atmosphere with a flow rate of 80 cm^3/min; the resulting gases were mixed with oxygen at a flow rate of 20 cm^3/min, then introduced into the combustion chamber of the device heated to 900°C. The variation of the heat release rate (*HRR*) of the tested samples was calculated as a function of time shown in Figure 3. The diagrams prove that only for the mini-pellet denoted P1 the curve separates two peaks, but at much lower values of the *HRR*, compared to the other mini-pellets. The microscale combustion calorimetry was previously used by Agarwal, G. *et al.* to analyse the energetic properties of coal, biomass and mixtures. This is one of the few studies identified in the literature in which the microscale combustion calorimetry method is used to study the thermal behaviour of residues from agriculture [30]. The *HRR* peak obtained for corn biomass is 37.5 W/g, whereas the *HRR* of corn – leached biomass, in which inorganic salts were removed by washing with distilled water for two hours at 110°C and then dried under air at the same temperature, increased to 58.2 W/g [30]. According to the data shown in

Figure 3 and Table 4, the *PHRR* value, 60.78 W/g, was obtained for the mini-pellet marked P3 containing WF, CP, SSS, S and A. The mini-pellet marked P3, has the highest HRC value, and also a higher heat release rate peak temperature (Figure 3S, Supplementary material). The pellet containing 100% wood material (Pc), available on the market, obviously had a high *PHRR* value, *i.e*. 99.07 W/g, which was higher than that of mini-pellets made of different agricultural vegetable waste.

Table 3

Thermogravimetric characteristics of the analysed wastes.

Sample	*Stage*	T_{onset}, °C	T_{peak}, °C	T_{endset}, °C	*W*, %	*Residue*, %
S	I	52	69	95	4.23	9.48
	II	267	327	339	51.37	
	III	339	454	476	34.92	
SSS	I	57	78	113	4.05	8.18
	II	252	299	333	48.43	
	III	333	464	491	39.34	
PSS	I	56	76	106	5.38	17.26
	II	258	320	349	43.79	
	III	437	459	501	19.34	
	IV	501	514	561	14.23	
GWS	I	51	70	99	8.93	22.9
	II	219	278	302	30.79	
	III	302	369	450	18.00	
	IV	583	624	631	19.38	
CP	I	58	81	156	8.39	2.26
	II	262	290	320	26.08	
	III	320	344	369	27.38	
	IV	458	511	533	35.89	
DWS	I	54	84	120	8.91	2.54
	II	258	285	349	52.76	
	III	414	472	507	35.79	
WF	I	44	66	105	10.15	3.86
	II	274	301	317	54.34	
	III	428	495	542	31.65	
Pc	I	48	65	95	5.48	6.10
	II	268	331	349	56.08	
	III	410	457	498	32.34	

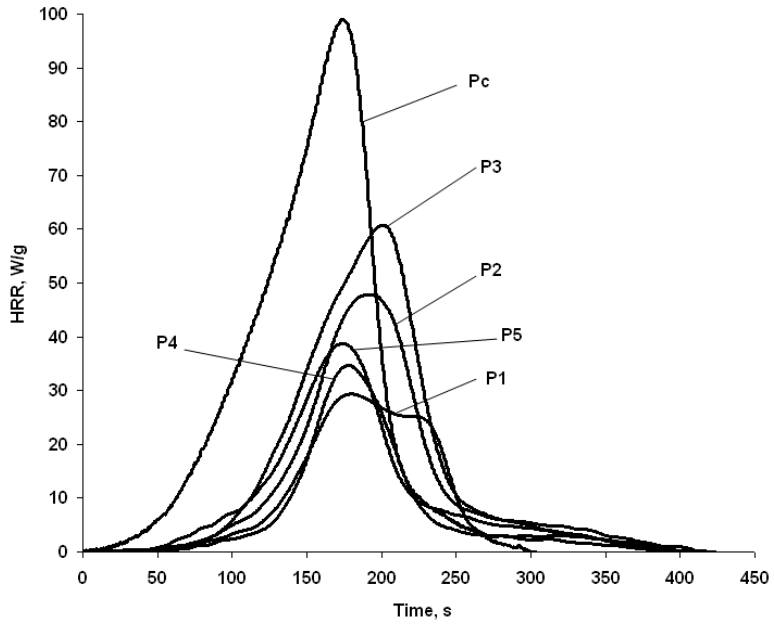

Figure 3. Time-dependent *HRR* curve representation for the obtained pellets.

Table 4

Microscale combustion calorimetry results for the obtained pellets.

Pellets	*Mass, mg*	*THR, kJ/g*	*PHRR, W/g*	T_{PHRR}, *°C*	*HRC, J/gK*	*Residue, %*
P1	5.12	3.28	29.34	328.46	29.96	14.84
P2	5.15	4.67	47.86	336.06	49.22	22.71
P3	4.11	5.77	60.78	355.34	61.03	20.19
P4	4.60	2.78	34.65	324.80	35.37	20.21
P5	4.40	3.72	38.72	329.93	38.78	24.09
Pc	4.30	8.42	99.07	375.59	122.64	17.67

P1 generated the smallest amount of residue. All mini-pellets obtained from plant wastes produce heat for about 350 seconds, according to time-dependent HRR curve (Figure 3). The results show that the latter had a higher *HRC* than our mini-pellets and also a higher heat release rate peak temperature. Pellets available on the market, marked Pc in the diagram in Figure 3, produce heat for about 275 seconds. Based on the results achieved in this study, it was shown that *HRC* is lower for mini-pellets than for commercial wood pellets, however, the duration of the combustion process is greater in their case, and the amount of ash obtained is comparable. Nonetheless, it can be concluded that mini-pellets made from agricultural waste can be used together with wood pellets to maintain combustion in heating systems based on pellets boilers.

Conclusions

This paper is devoted to the evaluation of the combustion heat of specific agricultural wastes, dried walnut shells, green walnut shell, cherry pits, sunflower seed shells, pumpkin seeds shells and sawdust, which may be used for pellets production. Their thermal decomposition in an air atmosphere was analysed within the 25-700°C temperature range.

Combustion heat and thermal stability increase sequences for the analysed materials were thus established. Combustion heat values greater than 18000 J/g were obtained for: sunflower seed shells, pumpkin seeds shells and sawdust. A different behaviour was noted in the case of the thermal decomposition in air of pumpkin seed shells, which, at temperatures higher than 350°C, undergo a two-process transformation. At the end of the second stage, a series of stable intermediates are probably formed up to a temperature of 437°C. It has also been noted that the largest amount of residue at 700°C was produced by green walnut shells. At the end of the third decomposition stage, green walnut shells also formed a stable intermediate whose decomposition starts at a temperature greater than 580°C.

Five types of mini-pellets were made from different combinations of selected wastes and their thermal behaviour was analysed by the microscale combustion calorimetry method. The mini-pellet, marked P3, containing wheat flour, cherry pits, sunflower seed shells and ash has shown the best energy performances and the better flammability behaviour. In comparison to commercially available pellets, the five prepared mini-pellets have a longer combustion time.

Acknowledgments

This work was supported by a grant of the Romanian Ministry of Research and Innovation, CCCDI – UEFISCDI, project number PN-III-P1-1.2-PCCDI-2017-0350/02.03.2018 (Graphene4 Life), within PNCDI III.

Supplementary information

Supplementary data are available free of charge at http://cjm.asm.md as PDF file.

References

1. Holubcik, M.; Jandacka, J.; Durcansky, P. Energy properties of wood pellets made from the unusual woody plants. AIP Conference Proceedings, 2016, 1768(1), pp. 020013. DOI: https://doi.org/10.1063/1.4963035
2. Mythili, R.; Venkatachalam, P. Briquetting of agro-residue. Journal of Scientific & Industrial Research, 2013, 72(01), pp. 58-61. DOI: http://nopr.niscair.res.in/handle/123456789/15553
3. Wach, E.; Bastian, M. Final report on producers, traders and consumers of mixed biomass pellets. Gdansk: Baltic Energy Conservation Agency, 2009, 54 p.https://ec.europa.eu/energy/intelligent/projects/en/projects/pelletslas
4. Cocchi, M.; Nikolaisen, L.; Junginger, M.; Goh, C.S.; Heinimö, J.; Bradley, D.; Hess, R.; Jacobson, J.; Ovard, L.P.; Thrän, D.; Hennig, C.; Deutmeyer, M.; Schouwenberg, P.P.; Marchal, D. Global wood pellet industry market and trade study. Florence: IEA Bioenergy, 2011, 190 p. https://www.ieabioenergy.com/iea-publications/

5. Alatzas, S.; Moustakas, K.; Malamis, D.; Vakalis, S. Biomass potential from agricultural waste for energetic utilization in Greece. Energies, 2019, 12(6), 1095, pp.1–20. DOI: https://doi.org/10.3390/en12061095
6. Barbanera, M.; Lascaro, E.; Stanzione, V.; Esposito, A.; Altieri, R.; Bufacchi, M. Characterization of pellets from mixing olive pomace and olive tree pruning. Renewable Energy, 2016, 88, pp. 185–191. DOI: https://doi.org/10.1016/j.renene.2015.11.037
7. Brlek, T.; Pezo, L.; Voća, N.; Krička, T.; Vukmirovic, D.; Colovic R.; Bodroža-Solarov, M. Chemometric approach for assessing the quality of olive cake pellets. Fuel Processing Technology, 2013, 116, pp. 250–256. DOI: https://doi.org/10.1016/j.fuproc.2013.07.006
8. Marculescu, C.; Ciuta, S. Wine industry waste thermal processing for derived fuel properties improvement. Renewable Energy, 2013, 57, pp. 645–652. DOI: https://doi.org/10.1016/j.renene.2013.02.028
9. Rossini, G.; Toscano, G.; Duca, D.; Corinaldesi, F.; Pedretti, E.F.; Riva, G. Analysis of the characteristics of the tomato manufacturing residues finalized to the energy recovery. Biomass and Bioenergy, 2013, 51, pp. 177–182. DOI: https://doi.org/10.1016/j.biombioe.2013.01.018
10. González, J.F.; González-Garcia, C.M.; Ramiro, A.; Gañán, J.; Ayuso, A.; Turegano, J. Use of energy crops for domestic heating with a mural boiler. Fuel Processing Technology, 2006, 87(8), pp. 717–726. DOI: https://doi.org/10.1016/j.fuproc.2006.02.002
11. Ruiz Celma, A.; Cuadros, F.; López-Rodríguez, F. Characterization of pellets from industrial tomato residues. Food and Bioproducts Processing, 2012, 90(4), pp. 700–706. DOI: https://doi.org/10.1016/j.fbp.2012.01.007
12. Brunerová, A.; Malaťák, J.; Müller, M.; Valášek, P.; Roubík, H. Tropical waste biomass potential for solid biofuels production. Agronomy Research, 2017, 15(2), pp. 359–368. https://agronomy.emu.ee/category/volume-15-2017/number-2-volume-15-2017/
13. Brunerová, A.; Brožek, M.; Müller, M. Utilization of waste biomass from post–harvest lines in the form of briquettes for energy production. Agronomy Research, 2017, 15(2), pp. 344–358. https://agronomy.emu.ee/category/volume-15-2017/number-2-volume-15-2017/
14. Al-Rahbi, A.S.; Williams, P.T. Waste ashes as catalysts for the pyrolysis–catalytic steam reforming of biomass for hydrogen-rich gas production. Journal of Material Cycles and Waste Management, 2019, 21, pp. 1224–1231. DOI: https://doi.org/10.1007/s10163-019-00876-8
15. Nenitescu, C.D.; Ioan V. The manual of the chemical engineer. vol.1, Bucharest, Technical Publishing House, 1951, 1043 p. (in Romanian).
16. ASTM D7309-07, Standard test method for determining flammability characteristics of plastics and other solid materials using microscale combustion calorimetry. ASTM International, West Conshohocken, PA, 2007. DOI: 10.1520/D7309-07
17. Hamciuc, C.; Vlad-Bubulac, T.; Serbezeanu, D.; Carja, I.-D.; Hamciuc, E.; Anghel, I.; Enciu, V.; Şofran, I.-E.; Lisa, G. New fire-resistant epoxy thermosets: nonisothermal kinetic study and flammability behavior. Journal of Polymer Engineering, 2019, 40(1), pp. 21–29. DOI: https://doi.org/10.1515/polyeng-2019-0210
18. Yang, H.; Fu, Q.; Cheng, X.; Yuen, R.K.K.; Zhang, H. Investigation of the flammability of different cables using pyrolysis combustion flow calorimeter. Procedia Engineering, 2013, 62, pp. 778–785. DOI: https://doi.org/10.1016/j.proeng.2013.08.125
19. Varnero, C.S.; Urrutia, M.V. Power Form Agripellets. IntechOpen, 2017, pp. 465–481. DOI: https://doi.org/10.5772/66186
20. Xiang, Y.; Xiang, Y.; Wang, L. Kinetics of the thermal decomposition of poplar sawdust. Energy Sources, Part A: Recovery, Utilization, and Environmental Effects, 2017, 39(2), pp. 213–218. DOI: https://doi.org/10.1080/15567036.2016.1212291
21. Rivera-Tenorio, M.; Moya, R. Potential for pellet manufacturing with wood waste from construction in Costa Rica. Waste Management & Research, 2019, pp. 1–10. DOI: https://doi.org/10.1177/0734242X19893022
22. Gravalos, I.; Xyradakis, P.; Kateris, D.; Gialamas, T.; Bartzialis, D.; Giannoulis, K. An experimental determination of gross calorific value of different agroforestry species and bio-based industry residues. Natural Resources, 2016, 7(1), pp. 57–68. DOI: https://doi.org/10.4236/nr.2016.71006
23. Sugathapala, A.G.T., Technologies for converting waste agricultural biomass to energy. UNEP DTIE, International Environmental Technology Centre (IETC): Osaka, Japan, 2013, 229 p. https://www.unenvironment.org/ietc/
24. Ondro, T.; Vitázek, I.; Húlan, T.; Lawson, M.; Csáki, Š. Non-isothermal kinetic analysis of the thermal decomposition of spruce wood in air atmosphere. Research in Agricultural Engineering, 2018, 64(1), pp. 41–46. DOI: https://doi.org/10.17221/115/2016-RAE
25. Haykiri-Acma, H.; Yaman, S. Comparison of the combustion behaviors of agricultural wastes under dry air and oxygen. WIT Transactions on Ecology and the Environment, 2012, 163, pp. 145–151. DOI: https://doi.org/10.2495/WM120141
26. Allouch, D.; Popa, M.; Popa, V.I.; Lisa, G.; Puițel, A.C.; Nasri, H. Characterization of components isolated from Algerian apricot shells (*Prunus Armeniaca L.*). Cellulose Chemistry and Technology, 2019, 53(9-10) pp. 851–859. DOI: https://doi.org/10.35812/CelluloseChemTechnol.2019.53.82

27. Fan, F.; Li, H.; Xu, Y.; Liu, Y.; Zheng, Z.; Kan, H. Thermal behaviour of walnut shells by thermogravimetry with gas chromatography–mass spectrometry analysis. Royal Society Open Science, 2018, 5(9), 180331, pp. 1–9. DOI: https://doi.org/10.1098/rsos.180331
28. Petuhov, O. Application of Taguchi optimization method in the preparation of activated carbon by microwave treatment. Chemistry Journal of Moldova, 2015, 10(1), pp. 95–103. DOI: dx.doi.org/10.19261/cjm.2015.10(1).14
29. Tolan, I.; Vlase, G.; Grigorie, C.A.; Vlase, T.; Ceban, I. Thermal behavior of simulated flour under non-isothermal conditions. Annals of West University of Timisoara, Series Chemistry, 2012, 21(2), pp. 103–112.
30. Agarwal, G.; Liu, G.; Lattimer, B. Pyrolysis and combustion energetic characterization of coal-biomass fuel blends. Proceedings of the ASME Power Conference, Boston, Massachusetts, USA, 2013, vol. 1, pp. 1–10. DOI: https://doi.org/10.1115/POWER2013-98313

CHEMISTRY JOURNAL OF MOLDOVA. General, Industrial and Ecological Chemistry. 2020, 15(1), 67-74
ISSN (p) 1857-1727 ISSN (e) 2345-1688
http://cjm.asm.md
http://dx.doi.org/10.19261/cjm.2019.675

RE-REFINEMENT OF CRYSTAL STRUCTURE OF BIS(LIDOCAINE) DIAQUATETRATHIOCYANATONICKELATE(II)

Koba Amirkhanashvili [a*], Alexandre Sobolev [b], Nani Zhorzholiani [a], Vladimer Tsitsishvili [a]

[a]*Petre Melikishvili Institute of Physical and Organic Chemistry, Ivane Javakhishvili Tbilisi State University, 31, A. Politkovskaia str., Tbilisi 0186, Georgia*
[b]*University of Western Australia, 35, Stirling hwy., Perth 6009 WA, Australia*
[*]*email: amirhan@hotmail.com; phone: (+995) 577 42 00 62*

Abstract. This paper reports on the synthesis and structure re-refinement of bis(lidocaine) diaquatetrathiocyanatonickelate(II). The compound with the formula $(LidH)_2[Ni(NCS)_4(H_2O)_2]$, where Lid is (2-(diethylamino)-*N*-(2,6-dimethylphenyl)acetamide, crystallizes in the monoclinic space group $P2_1/c$ with a= 18.3509(5), b= 7.6532(2), c= 14.9585(4) Å, β= 109.964 (2)°, V= 1974.57 (9) $Å^3$, and Z= 2. Coordination of the Ni^{2+} ion with thiocyanate ions and water molecules generates the slightly distorted octahedral anion $[Ni(NCS)_4(H_2O)_2]^{2-}$ with *N*-bonded thiocyanate groups, while two protonated cations $LidH^+$ remain in an outer coordination field. The anion and cations are associated through hydrogen bonds formed by sulphur atoms with amido nitrogen atoms; water molecules and an amino nitrogen atom are involved in the formation of hydrogen bonds with sulphur atoms of neighbouring unit cells arranging alternating $[Ni(NCS)_4(H_2O)_2]^{2-}$ anions and $LidH^+$ cations into endless sheets lying in the *ac* plane.

Keywords: lidocaine complex, nickel(II), crystal structure, hydrogen bond.

Received: 23 December 2019/ Revised final: 02 April 2020/ Accepted: 07 April 2020

Introduction

Lidocaine or lignocaine (2-(diethylamino)-*N*-(2,6-dimethylphenyl)acetamide, Lid, see Figure 1) is a drug used as an anesthetic and for the treatment of chronic pain [1]. The lidocaine base is easily soluble in diethyl ether, but poorly soluble in water, and thus is used as its chlorohydrate salt $Lid{\cdot}HCl{\cdot}H_2O$, which is water soluble.

Analytical profiles of lidocaine and its salt are discussed in [2], and current data are given in [3,4]. Despite the fact that the molecular mechanism of action of local anesthetics upon the nervous system and contribution of the cell membrane to the process are still controversial [4], as was suggested about half a century ago [5], the ability to hydrogen bond donation is essential to the action of local anesthetics [5].

The crystal structure, hydrogen-bonding arrangement and conformation of the lidocaine molecule are significantly different for the free base, hydrochloride and other salts. Thus, the structure of lidocaine is characterized by the presence of two independent molecules in the asymmetric unit and by chains of hydrogen-bonded molecules in the crystal structure (space group: $P2_1/c$, a= 12.9590(3) Å, b= 13.8003(3) Å, c= 18.8288(5) Å, α= 90°, β= 122.340(3)°, γ= 90°). The intermolecular hydrogen bond is formed between the amido nitrogen and aceto oxygen atoms with N···O distance of 2.8746(17) Å and N–H–O angle of 140.9(18)° [6].

Lidocaine hydrochloride monohydrate crystals, $Lid{\cdot}HCl{\cdot}H_2O$, are monoclinic, $P2_1/c$, Z= 4; if not taking into account the alternative structure present at about 5% occupancy, then the predominant structure is fully hydrogen bonded, with adjacent lidocaine cations linked by water molecules into endless chains parallel to *b* axis. Adjacent chains related by the screw axes are joined in pairs by chlorine ions, which bind N^+H and H_2O groups in different chains [7,8].

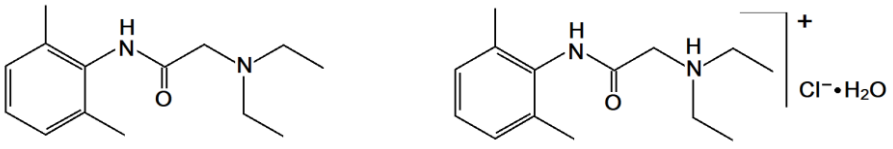

Figure 1. Lidocaine base (left) and lidocaine hydrochloride monohydrate (right).

The crystals of lidocaine hydrohexafluoroarsenate, $LidH{\cdot}AsF_6$, are monoclinic, *C*2/*c*, *Z*= 8; the lidocaine moiety was found to be in the biologically active cationic form, with the protonated amino nitrogen atom. This atom is strongly hydrogen-bonded to the oxygen atom of an adjacent cation and joins pairs of cations across the centers of symmetry, while the amido nitrogen atom is weakly hydrogen-bonded to a fluorine atom of the hexafluoroarsenate anion [9]. The lidocaine bis-*p*-nitrophenylphosphate, $[LidH]^+$ $[C_{12}H_8N_2O_4P]^-$, crystallizes in the monoclinic space group $P2_1/c$, *Z*= 4; both the amino and the amide hydrogen atoms participate in hydrogen bonds to the phosphate group, with N···O distances of 2.690 and 2.801 Å, respectively [10].

Lidocaine barbiturate, $[LidH]^+[C_4H_3N_2O_3]^-$, was synthesized and studied not for medical use, but as a nonlinear optical material. All nitrogen atoms participate in hydrogen bonding with N···O distances from 2.697(2) to 2.833(2) Å and N–H–O angles from 151 to 177°, forming tapes lying in the *bc* plane [11].

Bis(lidocaine) tetrathiocyanatocobaltate(II) hydrate crystals, $Lid_2[Co(NCS)_4](H_2O)$, are triclinic, space group no. 2, *Z*= 2; the packing shows a layered arrangement along *c* axis, lidocaine remains in the free base form and its layer is penetrated by the sulphur atom of one of the thiocyanate groups [12]. For crystals of lidocaine tetrachlorocobaltate(II) (monoclinic, space group $P2_1/c$, Z= 2), $Lid_4(CoCl_4)_2$ [13], and crystals of lidocaine tetrabromozincate(II) (orthorhombic, space group *P*bca, Z= 8), $Lid_4(ZnBr_4)_2$ [14], the asymmetric unit has four ligand molecules and two metal groups; the molecules are stacked and the metal and ligands do not form independent layers. In the cobalt(II) and nickel(II) complexes (Lid_2MX_2, where M is Co^{2+} or Ni^{2+}, X is dicyanamide $C_2N_3^-$ or thiocyanate SCN^-) lidocaine chelates metal ions through the amide and amino groups [15]. The tetrathiocyanatopalladate(II), $(LidH)_2[Pd(SCN)_4]$, crystallizes in the monoclinic space group $P2_1/n$, *Z*= 4; the palladium atom is in a square planar coordination, the coordination polyhedron is undistorted and it does not show any hydrogen bonding with protonated lidocaine, the packing of the molecules shows a strongly layered arrangement [16], same as in the crystal structures of bis(lidocaine) tetrabromocuprate(II) (monoclinic, $P2_1/c$, Z= 4), Lid_2CuBr_4 [17], and the lignocaine hydrochloride – nickel thiocyanate complex (monoclinic, $P2_1/a$, Z= 4) [18]. All of the listed lidocaine coordination compounds were obtained for medical use, but only for the cobalt(II) and nickel(II) complexes with lidocaine as a bidentate ligand, it was reported, that metal coordination enhanced the DNA binding activity, cleavage activity and cytotoxic properties of lidocaine [15].

The purpose of our work was to obtain new complexes of lidocaine and define their physico-chemical properties and structure; this contribution concerns bis(lidocaine) diaquatetrathiocyanatonickelate(II).

Experimental

Generalities

All solvents and reagents were obtained from commercial sources and were used as received without further purification.

Synthesis

Starting materials were lidocaine free base $C_{14}H_{22}N_2O$ (Lid), nickel chloride hexahydrate $NiCl_2{\cdot}6H_2O$, and anhydrous potassium thiocyanate KSCN. Nickel(II) complex of lidocaine was prepared in water-methanol solution (pH 5-6) with 1:2:4 molar ratio of the nickel chloride, lidocaine, and potassium thiocyanate. The prepared mixture was filtered, placed on a magnetic stirrer with heating for a while, and then left at room temperature for slow evaporation, details are given in [19]. Crystals suitable for X-ray measurements started to form after 2-3 days. The resulting crystals were washed with ether and dried in air. Isolated yield 67%. Elemental analyses data (wt.%) calculated for $C_{32}H_{50}N_8NiO_4S_4$: C 48.18; H 6.32; N 14.04; Ni 7.36; O 8.02; S 16.04; found: C 48.12; H 6.29; N 14.01; Ni 7.39; O 8.05; S 16.07.

Physical measurements

Fourier transform infrared spectra were recorded on a AgilentCary 630 FTIR spectrometer over the wavenumber range 4000–400 cm^{-1} using KBr pellets.

Elemental analysis was performed using a Labertherm CHN elemental analyser and a Perkin-Elmer atomic absorption spectrometer.

Melting point values have been measured on the Dynalon SMP_{10} device.

X-ray diffraction measurements were carried out with an Oxford Diffraction XCALIBUR E CCD diffractometer equipped with graphite-monochromated MoKα radiation. The data collection, cell refinement and data reduction were carried out with the CrysAlis^{PRO} package of Rigaku Oxford Diffraction [20]. The structure (Table 1) was solved by direct methods and refined against F^2 with full-matrix least-squares using the programs complex SHELXL-2014 [21].

Table 1

Crystal data and details of data collection for $(LidH)_2[Ni(NCS)_4(H_2O)_2]$.

Parameter	*Value*
Empirical formula	$C_{32}H_{50}N_8NiO_4S_4$
Fw	797.75
T, K	100(2)
Space group	$P2_1/c$ (No. 14)
a, Å	18.3509(5)
b, Å	7.6532(2)
c, Å	14.9585(4)
β, °	109.964(2)
V, Å^3	1974.57(9)
Z	2
ρ_{calc}, g·cm^{-3}	1.342
μ, mm^{-1}	0.748
Crystal size, mm	0.39x0.31x0.27
2Θ range, °	5.9 to 65.3
Reflections collected	41880
Independent reflections	6860 (R_{int}= 0.0338)
Data/restrains/parameters	5884/0/244
R_1 [a]	0.0314
wR_2 [b]	0.0755
GOF[ac]	1.000
$\|\Delta\rho\|_{max}$, e Å^{-3}	0.48(6)

[a] $R_1 = \Sigma||F_0| - |F_c||/\Sigma|F_0|$,
[b] $wR_2 = \{\Sigma[w(F_o^2-F_c^2)^2/\Sigma[w(F_o^2)^2]\}^{½}$,
[c] $GOF = \{\Sigma[w(F_o^2-F_c^2)^2]/(n-p)\}^{½}$, *where n is the number of reflections and p is the total number of parameters refined.*

CCDC 1859310 contains the supplementary crystallographic data for this contribution, and can be obtained free of charge *via https://www.ccdc.cam.ac.uk/conts/retrieving.html* (or from the Cambridge Crystallographic Data Centre, 12 Union Road, Cambridge CB2 1EZ, U.K; fax: (+44) 1223-336-033; or deposit@ccdc.cam.ac.uk).

Results and discussion

The reaction between nickel chloride, lidocaine, and potassium thiocyanate in methanol solution leads to the formation of a new complex; it crystallizes in a form of pale green prisms, has a melting point at 188°C, and is slightly soluble in water and readily soluble in ethanol and acetone. The results of elemental analysis [19] indicate the presence of two protonated lidocaine moieties, four thiocyanate groups, and two water molecules per nickel atom in the composition of the prepared complex, which differs from the composition of the known nickel(IV) thiocyanate complex having two unprotonated lidocaine molecules in its structure.

The IR spectrum of the lidocaine complex showed the same bands as for the lidocaine free base and its salts, including sharp absorption peaks at 3270 cm^{-1} (3250, 3172 and 3235 cm^{-1} for lidocaine free base, hydrochloride monohydrate and thiocyanide, respectively) due to amide N–H stretch, at 1690 cm^{-1} (1667, 1673 and 1660 cm^{-1}) due to amide C=O stretch, and at 1506 cm^{-1} due to aromatic C=C bending vibrations. The benzene ring in lidocaine molecule also gives the peak at about the 3030 cm^{-1} due to aromatic C–H stretch vibrations, other weak but resolved peaks are observed at 1590 cm^{-1} (1476, 1592 and 1546 cm^{-1}) and 1272 cm^{-1} (1292, 1272 and 1280 cm^{-1}) due to amide band II and III vibrations, as well as a peak in the fingerprint region at 780 cm^{-1} (765, 774 and 770 cm^{-1}) due to deformations of the 1,2,3-trisubstituted aromatic ring.

As in the long-standing work on the IR spectra of lidocaine salts [22] and other publications [2,3,14,17] no attempt was made to disentangle and assign the generally poorly resolved C–H stretching bands near 3000 cm^{-1} arising from the *N*-ethyl substituents ($\nu_{asym}(CH_2)$ near 2930±10 cm^{-1}, $\nu_{asym}(CH_3)$ near 2960±10 cm^{-1}, and $\nu_{sym}(CH_3)$ near 2870±10cm^{-1}) and the methyl substituents of the phenyl ring usually giving prominent bands near 2925 and 2865 cm^{-1} as well as variable intensity

bands near 2975 and 2945 cm^{-1}. Perhaps the band at 2800 cm^{-1} in the spectrum of lidocaine free base can be assigned to $\nu_{sym}(CH_2)$ for the methylene group at the nitrogen atom with a stretching frequency usually lowered from its value in hydrocarbons near 2850 cm^{-1}, but this effect is completely eliminated when nitrogen acquires a positive charge in amine salts.

The IR spectra of lidocaine salts and complexes show absorption peaks due to NH^+ stretching vibrations. In the IR spectrum of lidocaine hydrochloride monohydrate, all eight peaks and shoulders at 2640–2460 cm^{-1} are observed, but for complexes these peaks have higher frequencies, as is the case with salts of strong acids [22]. In addition, in complexes, NH^+ stretching peaks overlap with C–H stretching bands.

The IR spectrum of Lid·HCl·H_2O also shows two narrow peaks near 3460 and 3390 cm^{-1} due to O–H stretching vibrations in hydrogen-bonded water molecules, these peaks are also visible in the spectrum of lidocaine complex. It is believed that IR is a tool that allows identification of the formation of hydrogen bond interactions, by the shift of the bands of the functional groups involved in the formation of hydrogen bonds. However, this tool does not always lead to correct results. For example, according to the IR study of Neville, G.A. and Regnier, Z.R. [22], the lidocaine hydrohexafluoroarsenate is essentially free of hydrogen bonding, but the X-ray analysis [9] is in conflict with this conclusion.

The IR spectrum of the lidocaine thiocyanate, LidH·NCS, shows a very strong peak at 2068 cm^{-1} corresponding to the first fundamental frequency [23] of the thiocyanate C–N stretching, and weak peaks of the second (396 cm^{-1}) and third (770 cm^{-1}) fundamental frequencies. According to the data of Bertini, I. and Sabatini, A. [24], the IR spectra of substituted thiocyanate complexes showed the C–N stretching of characteristic forms and values: >2100 cm^{-1} and a sharp peak for *S*-bonded thiocyanates, and ≤2100 cm^{-1} and broad peaks for *N*-bonded ones. The second and third fundamental frequencies are also sensitive to the type of bonding: 450-490 and 760-880 cm^{-1} for *N*-bonded thiocyanates, 400-440 and ≈700 cm^{-1} for *S*-bonded thiocyanates. The IR spectrum of LidH NCS presents peaks at 2068, 496 and 790 cm^{-1} corresponding to *N*-bonding. However, for the obtained Ni(II) lidocaine thiocyanate complex, consideration of these IR bands does not allow us to unambiguously determine the type of bonding. So, in the spectrum of the complex the first fundamental frequency is observed at 2124 cm^{-1}, which indicates *S*-bonding, but the peak is rather narrow (<4 cm^{-1} at half height), as well as the second and third fundamental frequencies are registered at 480 and 810 cm^{-1}, respectively, and this indicates *N*-bonding.

According to the X-ray crystallography, the investigated compound has a molecular crystal structure of bis(lidocaine) diaquatetrathiocyanatonickelate(II), in which coordination of the Ni^{2+} ion with four thiocyanate (rhodanide) anions and two water molecules generates the slightly distorted octahedral anion $[Ni(NCS)_4(H_2O)_2]^{2-}$ with *N*-bonded thiocyanates, while two protonated cations $LidH^+$ remain in an outer coordination field (Figure 2).

The Ni(II) in the $[Ni(NCS)_4(H_2O)_2]^{2-}$ anion is in an octahedral NiN_4O_2 coordination geometry, being ligated by four nitrogen atoms from the monodentate thiocyanate groups and two trans-related aqua ligands. Oxygen atoms from water molecules are spaced from the central atom by the same distance of 2.0987(9) Å.

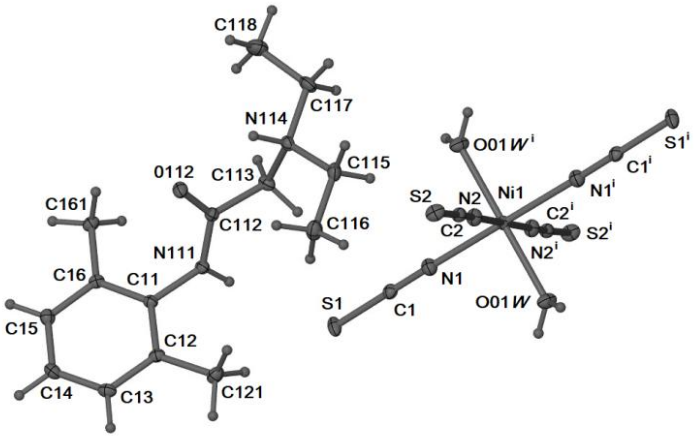

Figure 2. Cation and anion in the crystal structure of the $(LidH)_2[Ni(NCS)_4(H_2O)_2]$, showing the atom numbering scheme. Displacement ellipsoids are drawn at 50% of the probability level.

In the same anions of bis(4,4'-bipyridinium) diaquatetraisothiocyanato nickellate(II) dinitrate [25] and mixed ligand cationic–anionic nickel(II) complex containing 1,4-diazepane [26], this distance is somewhat smaller and amounts to 2.071(4) Å, but in the nickel thiocyanate complex described in a previous study this distance is larger and is 2.169(5) Å [18]. Nitrogen atoms in the NiN_4O_2 octahedron are located at different distances from the central nickel atom as shown in Figure 3, and the angles between the N–Ni–N bonds slightly deviate from 90° with a minimum of 87.89(4)° for angle $N1^{i}$–Ni–N2 and a maximum value of 92.11(4)° for angles N1–Ni–N2 and $N1^{i}$–Ni–$N2^{i}$ (Symmetry code: (i) *−x+1, −y+1, −z+1*). The Ni–N distances depend on the nature of the complex, in the cationic-anionic diazepane complex [26] they are the smallest, 1.905(4) and 1.918(3) Å, in the dipyridinium complex [25] they are comparable with our results, 2.055(3) and 2.107(4) Å, and in the thiocyanate complex [18] they are slightly larger, 2.13(2) and 2.18(3) Å.

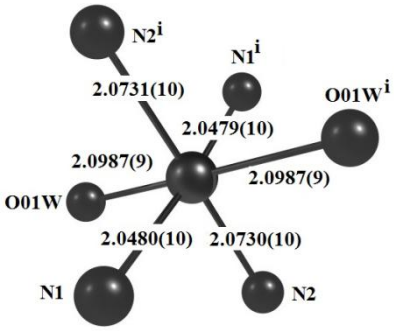

Figure 3. Length (Å) of Ni–O and Ni–N bonds in the $Ni[(NCS)_4(H_2O)_2]^{2-}$ ion.

The aromatic ring in $LidH^+$ is asymmetric, but the deviations of the C–C bond lengths (from 1.3887(16) to 1.4016(15) Å) and angles (from 117.79(10) to 122.37(10)°) from the standard ones are insignificant, the torsion angles are small (from -1.47(16) to 1.04(16)°), and the aromatic ring can conditionally be considered flat.

The C11–N111, N111–C112, C112–O112, and C112–C113 bond lengths are 1.4366(14), 1.3412(14), 1.2253(13), and 1.5281 Å, respectively, which is typical of crystalline carboxamides [27]. The amide group of Lid^+ is twisted out from the plane of the aromatic ring by 66.74(14)° (torsion angle C16–C11–N111–C112). The torsion angle C11–N111–C112–O112 is 3.93(18)°, so that the aromatic ring and the oxygen atom adopt a *synperiplanar* (*cis*) conformation with respect to the N111–C112 bond, while the aromatic ring and diethylamino chain adopt the *antiperiplanar* (*trans*) conformation (torsion angle C11–N111–C112–C113 is −174.10(10)°).

The nitrogen atoms N111 and N114 adopt an *antiperiplanar* conformation with respect to the N111–C112–C113–N114 torsion angle of −152.36(10)°. Such staggered conformation excludes the formation of an intramolecular hydrogen bond N111–H111···N114 noted in the lidocaine free base [6] and in the molecular complex of lidocaine with phloroglucinol, when the nitrogen atoms adopt a *synperiplanar* conformation [28]. On the contrary, the carbonyl oxygen atom and the nitrogen atom of the amino group adopt the *synperiplanar* conformation (torsion angle O112–C112–C113–N114 is 29.46(14)°), which leads to the formation of a strong intramolecular hydrogen bond N114–H114···O112 in $LidH^+$. In addition to the Coulomb attraction force, the anion $[Ni(NCS)_4(H_2O)_2]^{2-}$ and cations $LidH^+$ are associated by the N–H···S hydrogen bond between the amide nitrogen atoms N111 and sulphur atoms of the thiocyanate groups.

Hydrogen bonding also determines the nature of supramolecular structure through the interaction between neighbouring unit cells. In the water molecule, hydrogen atoms H01*A* and H01*B* are included in hydrogen bonding between the oxygen atom O01*W* and the sulphur atoms $S2^{ii}$ and $S2^{iii}$ of the neighbouring unit cells. The diethylamino-*N*-group is protonated, and corresponding hydrogen atom H114 forms a bifurcated hydrogen bond with the carbonyl oxygen atom O112 (intramolecular hydrogen bond described above) and the sulphur atom $S1^{iv}$ of the neighboring unit cell. Interatomic distances and valence angles for the intramolecular N–H···O and the intermolecular N–H···S, N–H···S, and O–H···S hydrogen bonds are given in Table 2.

The general picture of intermolecular hydrogen bonding in $(LidH)_2[Ni(NCS)_4(H_2O)_2]$ is shown in Figure 4, representing the unit cell and part of the crystal packing along the *b* crystallographic axis. Due to the O–H···S hydrogen bonds, anions $[Ni(NCS)_4(H_2O)_2]^{2-}$ form endless chains lying along the *c* axis, the $LidH^+$ ions are stacked with the anions by the N–H···S hydrogen bonds, the anions alternate with cations and together they form sheets lying in the *ac* plane.

Table 2

Hydrogen bonds geometry.

D–H···A	*D–H (Å)*	*H···A (Å)*	*D···A (Å)*	*D–H···A (°)*
N114–H114···O112	0.894 (16)	2.152 (16)	2.6824 (12)	117.3 (12)
N111–H111···S1	0.846 (19)	2.682 (19)	3.4942 (10)	161.4 (16)
O01*W*–H01*A*···S2^{ii}	0.85 (2)	2.45 (2)	3.2914 (10)	170.0 (18)
O01*W*–H01*B*···S2^{iii}	0.85 (2)	2.51 (2)	3.3110 (10)	158.5 (19)
N114–H114···S1^{iv}	0.894 (16)	2.499 (15)	3.2800 (10)	146.2 (13)

Symmetry codes: ^{ii} *−x+1, y+1/2, −z+1/2;* ^{iii} *x, y+1, z;* ^{iv} *x, y−*1, *z.*

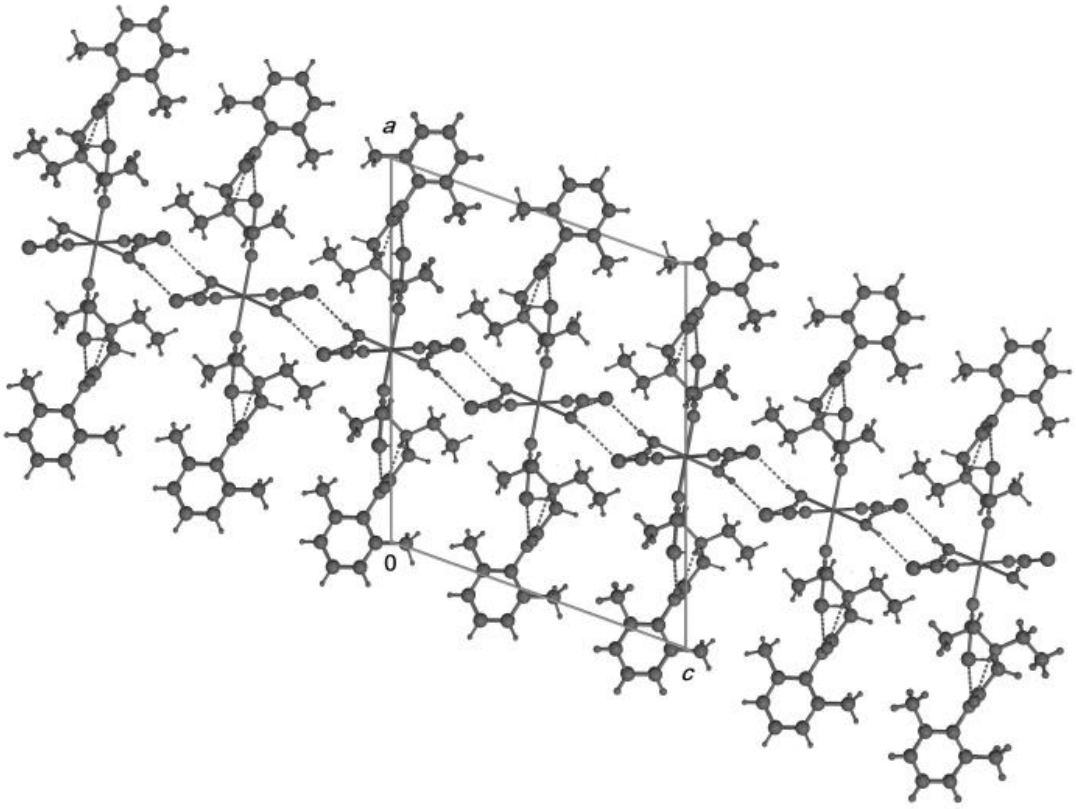

Figure 4. Unit cell of $(LidH)_2[Ni(NCS)_4(H_2O)_2]$ and partial crystal packing viewed along [010].

Conclusions

This work reports the synthesis and structure re-refinement of bis(lidocaine) diaquatetrathiocyanatonickelate(II). The synthesis of bis(lidocaine) diaquatetrathiocyanatonickelate(II) was carried out in water-methanol solution (pH=5-6) with 1:2:4 molar ratio of the nickel chloride, lidocaine, and potassium thiocyanate, resulting in pale green prismatic crystals.

The FTIR spectrum contains all the bands of corresponding functional groups, but the fundamental frequencies and the shape of the thiocyanate C–N stretching vibrations do not make it possible to unequivocally determine the nature of the bonding of thiocyanate to the nickel atom.

The single-crystal X-ray diffraction characterization shows that the complex crystallizes in the monoclinic space group $P2_1/c$ with a= 18.3509(5), b= 7.6532(2), c= 14.9585(4) Å, β= 109.964 (2)°, Z= 2, and consists of the $Ni[(NCS)_4(H_2O)_2]^{2-}$ slightly distorted octahedral anion with *N*-bonded thiocyanate groups and two protonated cations of lidocaine $LidH^+$ in an outer coordination field. Along with the Coulomb interaction, the anion and cations are associated by the N–H···S hydrogen bonds, while the N–H···S and O–H···S hydrogen bonds provide links with neighbouring unit cells, so the $[Ni(NCS)_4(H_2O)_2]^{2-}$ anions alternate with the $LidH^+$ cations and form endless sheets lying in the *ac* plane.

Acknowledgments

This research was initiated by Diabetic Children's Protection Association (DChPA), charitable organization for population with diabetes in Georgia, and was carried out with the financial support of the Shota Rustaveli National Science Foundation of Georgia (SRNSFG, project FR 18-3889).

The authors acknowledge access to the facilities at the Centre for Microscopy, Characterization and Analysis, University of Western Australia.

References

1. de Souza, M.F.; Kraychete, D.C. The analgesic effect of intravenous lidocaine in the treatment of chronic pain: A literature review. Revista Brasiliera de Reumatologia, 2014, 54(5), pp. 386–392. DOI: http://doi.org/10.1016/j.rbr.2014.01.010
2. Powell, M.F. Lidocaine and lidocaine hydrochloride. Elsevier: Amsterdam, 1986, 15, pp. 761–779. DOI: https://doi.org/10.1016/S0099-5428(08)60428-1
3. Badawi, H.M.; Förner, W.; Ali, S.A. The molecular structure and vibrational, ^{1}H and ^{13}C NMR spectra of lidocaine hydrochloride monohydrate. Spectrochimica Acta Part A: Molecular and Biomolecular Spectroscopy, 2016, 152, pp. 92–100. DOI: https://doi.org/10.1016/j.saa.2015.07.060
4. Jalili, S.; Saeedi, M. Study of procaine and tetracaine in the lipid bilayer using molecular dynamics simulation. European Biophysics Journal, 2017, 46, pp. 265–282. DOI: https://doi.org/10.1007/s00249-016-1164-8
5. Sax, M.; Pletcher, J. Local anesthetics: significance of hydrogen bonding in mechanism of action. Science, 1969, 166(3912), pp. 1546–1548. DOI: 10.1126/science.166.3912.1546
6. Bambagiotti-Alberti, M.; Bruni, B.; Di Vaira, M.; Giannellini, V.; Guerri, A. 2-(Diethylamino)-*N*-(2,6-dimethylphenyl)acetamide, a low-temperature redetermination. Acta Crystallographica Section E, 2007, E63, pp. o768–o770. DOI: https://doi.org/10.1107/S1600536807001523
7. Hanson, A.W.; Röhrl, M. The crystal structure of lidocaine hydrochloride monohydrate. Acta Crystallographica Section B, 1972, B28, pp. 3567–3571. DOI: https://doi.org/10.1107/S0567740872008350
8. Hamaed, H.; Pawlowski, J.M.; Cooper, B.F.T.; Fu, R.; Eichhorn, S.H.; Schurko, R.W. Application of solid-state ^{35}Cl NMR to the structural characterization of hydrochloride pharmaceuticals and their polymorphs. Journal of the American Chemical Society, 2008, 130(33), pp. 11056–11065. DOI: https://doi.org/10.1021/ja802486q
9. Hanson, A.W. The crystal structure of lidocaine hydrohexafluoroarsenate. Acta Crystallographica Section B, 1972, B28, pp. 672–679. DOI: https://doi.org/10.1107/S0567740872003000
10. Yoo, C.S.; Abola, E.; Wood, M.K.; Sax, M.; Pletcher, J. The crystal structure of lidocaine bis-*p*-nitrophenylphosphate. Acta Crystlographica Section B, 1975, B31, pp. 1354–1360. DOI: https://doi.org/10.1107/S0567740875005195
11. Gryl, M.; Koziel, M.; Stadnicka, K.; Matulkova, I.; Němec, I.; Tesařová, N.; Němec, P. Lidocaine barbiturate: a promising material for second harmonic generation. CrystEngComm, 2013, 15(17), pp. 3275–3278. DOI: 10.1039/C3CE00059A
12. Qayyas, N.N.A.; Sridhar, M.A.; Indira, A.; Shashidhara Prasad, J.; Abdoh, M.M.M. Crystal structure of bis(lignocainium) tetrathiocyanatocobaltate(II) hydrate, $(C_{14}H_{22}ON_2)_2$ $Co(NCS)_4$ (H_2O). Zeitschrift für Kristallographie–Crystalline Materials, 1994, 209(11), pp. 918–919. DOI: https://doi.org/10.1524/zkri.1994.209.11.918
13. Indira, A.; Babu, A.M.; Bellad, S.B.; Sridhar, M.A.; Shashidhara Prasad, J. Crystal structure of lignocaine tetrachlorocobaltate, $(C_{14}H_{22}N_2O)_2(CoCl_4)$. Zeitschrift für Kristallographie – Crystalline Materials, 1992, 202(1-4), pp. 286–289. DOI: https://doi.org/10.1524/zkri.1992.202.14.286
14. Sridhar, M.A.; Shashidhara Prasad, J.; Qayyas, N.N.A. Crystal structure of lignocaine tetrabromozincate, $(C_{14}H_{22}ON_2)_4(ZnBr_4)_2$. Zeitschrift für Kristallographie – Crystalline Materials, 1997, 212(5), pp. 391–392. DOI: https://doi.org/10.1524/zkri.1997.212.5.391
15. Tabrizi, L.; McArdle, P.; Erxleben, A.; Chiniforoshan, H. Nickel(II) and cobalt(II) complexes of lidocaine: Synthesis, structure and comparative *in vitro* evaluations of biological perspectives. European Journal of Medicinal Chemistry, 2015, 103, pp. 516–529. DOI: https://doi.org/10.1016/j.ejmech.2015.09.018
16. Sridhar, M.A.; Indira, A.; Shashidhara Prasad, J.; Cameron, T.S. Crystal structure of lignocaine hydrochloride – palladium thiocyanate complex. Zeitschrift für Kristallographie – Crystalline Materials, 1994, 209(5), pp. 437–439. DOI: https://doi.org/10.1524/zkri.1994.209.5.437
17. Qayyas, N.N.A.; Indira, A.; Sridhar, M.A.; Shashidhara Prasad, J.; Abdoh, M.M.M. Crystal structure of bis(lignocainium) tetrabromocuprate(II), $(C_{14}H_{22}ON_2)_2CuBr_4$. Zeitschrift für Kristallographie – Crystalline Materials, 1994, 209(11), pp. 920–921. DOI: https://doi.org/10.1524/zkri.1994.209.11.920
18. Indira, A.; Sridhar, M.A.; Shashidhara Prasad, J.; Cameron, T.S. Crystal structure of lignocaine hydrochloride – nickel thiocyanate complex. Zeitschrift für Kristallographie – Crystalline Materials, 1994, 209(5), pp. 440-442. DOI: https://doi.org/10.1524/zkri.1994.209.5.440
19. Zhorzholiani, N.B.; Amikhanashvili, K.D.; Lomtadze, O.G.; Tsitsishvili, V.G. Synthesis and biological potential of coordination compounds with anesthetic preparation. Modern Pharmacy – Science and Practice, Kutaisi (Georgia): Akaki

Tsereteli State University, 2017, pp. 77–80. http://dspace.nplg.gov.ge/handle/1234/250600?locale=en
20. CrysAlis PRO, version 1.171.38.46, Rigaku Oxford Diffraction, 2015. https://www.rigaku.com/en/products/smc/crysalis
21. Sheldrick, G.M. Crystal structure refinement with SHELXL. Acta Crystallographica Section C, 2015, C71, pp. 3–8. DOI: https://doi.org/10.1107/S2053229614024218
22. Neville, G.A.; Regnier, Z.R. Hydrogen bonding in lidocaine salts. I. The +NH stretching band and its dependence on the associated anion. Canadian Journal of Chemistry, 1969, 47(22), pp. 4229–4236. DOI: https://doi.org/10.1139/v69-698
23. Jones, L.H. Infrared spectrum and structure of the thiocyanate ion. The Journal of Chemical Physics, 1956, 25(5), pp. 1069–1072. DOI: https://doi.org/10.1063/1.1743101
24. Bertini, I.; Sabatini, A. Infrared spectra of substituted thiocyanate complexes. The effect of the substituent on bond type. Inorganic Chemistry, 1966, 5(6), pp. 1025–1028. DOI: https://doi.org/10.1021/ic50040a017
25. Chen, H.-J.; Tong, M.-L.; Chen, X.-M. `Chicken-coop' network assembled by hydrogen bonds with bridging nitrate ions. Crystal structure of bis(4,4'-bipyridinium)diaquatetraisothiocyanato nickellate(II) dinitrate. Inorganic Chemistry Communications, 2001, 4, pp. 76–78. DOI: https://doi.org/10.1016/S1387-7003(00)00210-0
26. Sain, S.; Saha, R.; Pilet, G.; Bandyopadhyay, D. Synthesis, crystal structure and characterization of a new mixed ligand cationic–anionic nickel(II) complex containing 1,4-diazepane. Journal of Molecular Structure, 2010, 984, pp. 350–353. DOI: https://doi.org/10.1016/j.molstruc.2010.10.002
27. Zabicky, J. The chemistry of amides. London, New York: Interscience, 1970, 927 p. DOI: 10.1002/9780470771235
28. Magaña-Vergara, N.E.; de la Cruz-Cruz, P.; Peraza-Campos, A.L.; Martinez-Martinez, F.J.; Gonzalez-Gonzalez. J.S. Mechanochemical synthesis and crystal structure of the lidocaine-phloroglucinol hydrate 1:1:1 complex. Crystals, 2018, 8(3), pp. 130–138. DOI: https://doi.org/10.3390/cryst8030130

CHEMISTRY JOURNAL OF MOLDOVA. General, Industrial and Ecological Chemistry. 2020, 15(1), 75-85
ISSN (p) 1857-1727 ISSN (e) 2345-1688
http://cjm.asm.md
http://dx.doi.org/10.19261/cjm.2019.657

DESIGN AND SYNTHESIS OF TWO BICYCLO[3.3.1]NONANE-STEROID DERIVATIVES

Lauro Figueroa [a*], Alejandra Garcimarero [b], Rolando Garcia [a], Francisco Diaz [c], Marcela Rosas [d], Virginia Mateu [d], Maria Lopez [a], Lenin Hau [a], Tomas Lopez [a], Abelardo Camacho [e], Yaritza Borges [a]

[a]*Faculty of Chemical-Biological Sciences, University Autonomous of Campeche, Agustín Melgar ave., Colonia Bellavista 24039, Campeche, Mexico*
[b]*Faculty of Medicine, University Veracruzana, Medicos and Odontologos str., Xalapa 91010, Veracruz, Mexico*
[c]*National School of Biological Sciences, National Polytechnic Institute, Prolacion Carpio and Plan de Ayala str., Colonia Santo Tomas 11340, Mexico*
[d]*Faculty of Nutrition, University Veracruzana, Medicos and Odontologos str., Xalapa 91010, Veracruz, México*
[e]*Faculty of Medicine and Nutrition, University Juarez of Durango State, Constitución str., Durango 34000, Mexico*
[*]*e-mail: lfiguero@uacam.mx*

Abstract. Several studies for the synthesis of bicyclo[3.3.1]nonane analogues have been reported, however, there is little information on the preparation of bicyclo[3.3.1]nonane-steroid derivatives. In this way, the aim of this study was to synthesize two steroid-bicyclo[3.3.1]nonane analogues (**11** or **12**) from either estradiol or estrone using some reactions such as etherification, addition, nucleophilic substitution and cyclization. The chemical structure was evaluated through NMR spectroscopic analysis. The results showed higher yield for **11** compared with **12**. It is noteworthy, that the reagents used in this investigation are not expensive and do not require special conditions for handling.

Keywords: bicyclo, steroid, estrone derivative, synthesis, NMR.

Received: 27 December 2019/ Revised final: 10 March 2020/ Accepted: 14 March 2020

Introduction

For several years, some derivatives of bicyclo[3.3.1]nonane have been prepared using different protocols; for example, the synthesis of a bicyclo[3.3.1]nonane derivative (garsubellin-A) from a silyl-enol ether and malonyl dichloride was reported [1]. Other report showed the preparation of some bicyclo[3.3.1]nonan-9-one analogues *via* cyclization of alkenyl-substituted *β*-di-carbonyls using selenium as catalyst [2]. In addition, a study showed the reaction of *N*-(l,4-cycloheptadienyl)morpholine with crotonyl chloride to form the 7-methylbicyclo[4.3.1]dec-3-ene-9,10-dione [3]. Furthermore, another study showed the synthesis of clusianone (bicyclo[3.3.1]nonane-2,4,9-trione derivative) through lithiation of some enol ether derivatives [4]. The compound tetramethoxycarbonylbicyclo[3.3.1]nonane was, also, prepared from dimethyl malonate, paraformaldehyde and piperidine [5]. Other data indicated the synthesis of a byciclo[3.3.1]nonan-3-one derivative by the reaction of cyclohexanediacetic acid with acetic anhydride [6]. The 3,3-dimethyl-2-bicyclo[3.3.l]nonanone was prepared from 2-bi-cyclo[3.3.1]nonanone and *t*-butoxide [7]. In addition, some bicyclo[3.3.1]nonane derivatives have been prepared *via* cyclization of cyclohexanol in the presence of *p*-toluensulphonic acid [8]. Other previous studies presented the synthesis of a byciclo[3.3.1]-nona-9-one *via* cyclization of 5-chlorocarbonylcyclooctene using aluminium trichloride as catalyst [9]. Recently, a bicyclo[3.2.2]nonane-steroid derivative (phomopsterone-A) from isocyathisterol has been prepared *via* some Wagner-Meervein rearrangement/epoxidation reactions [10]. Also, a spiro[bicyclo[3.2.2]-nonane-2,1'-cyclohexane]-steroid derivative (spiroaspertrione-A) was developed from farnesyl pyrophosphate and 5,7-dihydroxy-4,6-dimethyl-3*H*-isobenzofuran-1-one [11]. All these data show different protocols for the preparation of several bicyclo[3.3.1]nonane derivatives, however, there are few data regarding the synthesis of bicyclo[3.2.2]nonane derivatives bound to steroid nucleus.

The aim of this research was to develop two bicyclo[3.2.1]nonano-steroid derivatives using a series of reaction such as etherification, aromatic nucleophilic substitution, [2+2] addition, acylation and an internal cyclization which do not require special conditions.

Experimental

Generalities

All reagents such as ninhydrin (**1**), 1-fluoro-2,4-dinitrobenzene (**2**) used in this investigation were acquired from Sigma-Aldrich Co., Ltd. The *melting point* values of the obtained compounds were determined on an Electrothermal apparatus (900 model). *Infrared spectra* (IR) were recorded using KBr pellets on a Perkin Elmer Lambda 40 spectrometer. *^{1}H and ^{13}C NMR spectra* were recorded on a Varian VXR300/5 FT NMR spectrometer at 300 MHz in $CDCl_3$ using TMS as internal standard. *Electron ionization mass spectrometry* (EI-MS) was obtained with a Finnigan Trace Gas Chromatography Polaris Q-Spectrometer. *Elemental analysis* data were acquired from a Perkin Elmer II CHNS/02400 elemental analyzer.

Synthesis of 8-fluoro-1',3'-dihydro-2,4-dioxaspiro[bicyclo[3.3.1]nonane-3,2'-indene]-1(9),5,7-triene (3)

A solution containing of **1** (100 mg, 0.56 mmol), **2** (100 μL, 0.79 mmol), potassium carbonate (60 mg, 0.43 mmol) in 5 mL of dimethyl sulphoxide were stirred under reflux (120°C) for 24 h, then, the solvent was removed under reduced pressure, the reaction progress was monitored by thin layer chromatography. Further, the product was purified by crystallization using the methanol:water:hexane (3:1:1) system; yielding 66% of product; m.p. 48-50°C; IR (ν_{max}, cm^{-1}) 1136 and 1112. ^{1}H NMR δ_H: 5.84-7.34 (m, 3H), 8.04-8.20 (m, 4H) ppm. ^{13}C NMR δ_C: 78.00, 98.40, 108.80, 114.81, 126.00, 135.26, 138.20, 142.92, 146.60, 149.64, 184.62, 186.54 ppm. EI-MS m/z: 270.03. Calc. for $C_{15}H_7FO_4$: C, 66.67; H, 2.61; F, 7.03. Found: C, 66.64; H, 2.60.

Synthesis of N-(2,4-dinitrophenyl)-N-(3-ethynylphenyl)amine (4)

A solution of **2** (100 μL, 0.79 mmol), 3-ethynylaniline (100 μL, 0.88 mmol), and acetonitrile (5 mL) were stirred under reflux for 24 h; then, the solvent was removed under reduced pressure. Afterwards, the product was purified by crystallization using the methanol:water (3:1) system; yielding 75% of product; m.p. 42-44°C; IR (ν_{max}, cm^{-1}) 3322, 2110 and 1622. ^{1}H NMR δ_H: 2.88 (s, 1H), 7.12-7.30 (m, 4H), 7.88-9.00 (m, 3H), 9.70 (broad, 1H) ppm. ^{13}C NMR δ_C: 78.20, 84.02, 106.52, 118.20, 120.72, 123.36, 124.24, 124.34, 125.50, 128.04, 131.57, 134.74, 136.22, 141.52 ppm. EI-MS m/z: 283.05. Calc. for $C_{14}H_9N_3O_4$: C, 59.37; H, 3.20; N, 14.84. Found: C, 59.34; H, 3.20; N, 14.82.

Synthesis of 8-[(3-ethynylphenyl)-amino]-2,4-dioxaspiro[bicyclo[3.3.1]nonane-3,2'-indene]-1(9),5,7-triene-1',3'-dione (6)

Method A: A solution of compound **3** (200 mg, 0.82 mmol), 3-ethynylaniline (100 μL, 0.88 mmol) and acetonitrile (5 mL) were stirred under reflux for 24 h; then, the solvent was removed under reduced pressure. Following, the product was purified by crystallization using the methanol:water (3:1) system, yielding 48% of product; m.p. 58-60°C; IR (ν_{max}, cm^{-1}) 3320, 2110, and 1136. ^{1}H NMR δ_H: 2.88 (s, 1H), 5.90 (m, 1H), 6.90 (broad, 1H), 6.96-7.25 (m, 6H), 8.04-8.20 (m, 4H) ppm. ^{13}C NMR δ_C: 74.58, 78.21, 84.00, 96.30, 108.64, 113.74, 118.00, 123.18, 123.20, 125.50, 125.96, 126.00, 130.52, 132.48, 134.76, 136.00, 138.21, 146.30, 184.62, 186.54 ppm. EI-MS m/z: 367.08. Calc. for $C_{23}H_{13}NO_4$: C, 75.20; H, 3.57; N, 3.81. Found: C, 81.38; H, 3.56; N, 3.80.

Method B: A solution of compound **4** (160 mg, 0.56 mmol), compound **1** (100 mg, 0.56 mmol), potassium carbonate (60 mg, 0.43 mmol) and 5 mL of dimethyl sulphoxide were stirred at room temperature for 48 h; then, the solvent was removed under reduced pressure. The obtained product was purified by crystallization using the methanol:water:hexane (3:1:1) system, yielding 58% of product; similar ^{1}H NMR and ^{13}C NMR data were obtained and compared with the method A product.

Synthesis of 8-[(3-{7,16-dihydroxy-17-methylpentacyclo[10.7.0.0^{2,9}.0^{3,6}.0^{13,17}]nonadeca-2(9),4,7-trien-4-yl}phenyl)-amino]-2,4-dioxaspiro[bicyclo[3.3.1]nonane-3,2'-indene]-1(9),5,7-triene-1',3'-dione (7)

A solution of compound **6** (200 mg, 0.59 mmol), 17*β*-estradiol (160 mg, 0.58 mmol), cupric chloride anhydrous (55 mg, 0.41 mmol) in 5 mL of methanol were stirred at room temperature for 48 h; then, the solvent was removed under reduced pressure. Following, the product was purified by crystallization using the methanol:water (3:1) system, yielding 45% of product; m.p. 78-80°C; IR (ν_{max}, cm^{-1}) 3400, 3320, and 1134. ^{1}H NMR δ_H: 0.80 (s, 3H), 1.32-2.18 (m, 15H), 3.18-5.10 (m, 4H), 5.92 (m, 1H), 6.34 (d, 1H, *J*= 0.80 Hz), 6.96 (m, 1H), 6.97 (m, 1H), 7.08-7.40 (m, 4H), 8.06 (m, 2H), 8.08 (broad, 3H), 8.20 (m, 2H) ppm. ^{13}C NMR δ_C: 15.80, 22.22, 23.84, 28.14, 30.44, 32.78, 36.30,

36.82, 39.54, 42.10, 44.32, 45.26, 50.73, 74.61, 82.46, 96.30, 99.76, 108.62, 108.98, 111.84, 113.80, 120.34, 121.54, 126.00, 128.97, 132.69, 133.66, 136.06, 137.10, 137.90, 138.20, 140.32, 142.04, 146.34, 148.90, 155.16, 184.62, 186.54 ppm. EI-MS m/z: 639.26. Calc. for $C_{41}H_{37}NO_6$: C, 76.98; H, 5.83; N, 2.19. Found: C, 76.96; H, 5.80; N, 2.18.

Synthesis of 8-({3-[(17S)-7-hydroxy-17-methyl-16-oxopentacyclo[10.7.0.0^{2,9}.0^{3,6}.0^{13,17}]nonadeca-2(9),4,7-trien-4-yl]phenyl}-amino)-2,4-dioxaspiro[bicyclo[3.3.1]nonane-3,2'-indene]-1(9),5,7-triene-1',3'-dione (8)

A solution of compound **6** (200 mg, 0.58 mmol), estrone (160 mg, 0.59 mmol), cupric chloride anhydrous (55 mg, 0.41 mmol) in 5 mL of methanol were stirred at room temperature for 48 h; then, the solvent was removed under reduced pressure. The product was purified by crystallization using the methanol:water (3:1) system, yielding 48% of product; m.p. 110-112°C; IR (ν_{max}, cm^{-1}) 3400, 3322, 1706, and 1336. ^{1}H NMR δ_H: 0.90 (s, 3H), 1.40-2.00 (m, 10H), 2.12-5.10 (m, 8H), 5.92 (m, 1H), 6.36 (*d*, 1H, *J*= 0.80 Hz), 6.96-7.40 (m, 6H), 8.06-8.20 (m, 4H), 8.90 (broad, 2H) ppm. ^{13}C NMR δ_C: 13.82, 21.52, 22.22, 26.00, 28.72, 30.42, 35.70, 36.82, 39.50, 42.14, 47.32, 48.12, 51.90, 74.60, 96.30, 99.76, 108.66, 108.98, 111.84, 113.80, 120.30, 124.26, 126.00, 128.94, 132.70, 133.66, 136.06, 136.14, 137.10, 137.90, 138.20, 142.04, 146.34, 148.90, 155.20, 184.62, 186.54, 220.14 ppm. EI-MS m/z: 637.24. Calc. for $C_{41}H_{35}NO_6$: C, 77.22; H, 5.53; N, 2.20. Found: C, 77.20; H, 5.50; N, 2.18.

Synthesis of (17S)-16-[(2-chloroacetyl)oxy]-4-(3-{1',3'-dioxo-2,4-dioxaspiro[bicyclo[3.3.1] nonane-3,2'-indene]-1(9),5,7-trien-8-ylamino} phenyl)-17-methylpentacyclo [10.7.0.0^{2,9}.0^{3,6}.0^{13,17}]nonadeca-2(9),4,7-trien-7-yl 2-chloro-acetate (9)

A solution of compound **7** (200 mg, 0.32 mmol), chloroacetyl chloride (70 µL, 0.87 mmol), triethylamine (70 µL, 0.50 mmol) in 5 mL of dimethyl sulphoxide were stirred at room temperature for 24 h; then, the solvent was removed under reduced pressure. The product was purified by crystallization using the methanol:water:hexane (3:1:1) system; yielding 48% of product; m.p. 132-134°C; IR (ν_{max}, cm^{-1}) 3320, 1722, and 1332. ^{1}H NMR δ_H: 0.80 (s, 3H), 1.30-400 (m, 17H), 4.10-4.26 (m, 4H), 4.80-5.84 (m, 2H), 5.92 (m, 1H), 6.28 (broad, 1H), 6.34 (d, 1H, *J*= 0.80 Hz), 6.96-7.40 (m, 6H), 8.06-8.20 (m, 4H) ppm. ^{13}C NMR δ_C: 14.40, 22.22, 24.27, 28.00, 30.00, 30.44, 36.20, 36.80, 37.56, 40.80, 41.00, 42.12, 44.02, 45.28, 50.90, 74.60, 84.62, 96.30, 108.62, 109.74, 111.82, 113.82, 115.62, 121.06, 125.66, 126.00, 128.96, 130.90, 132.70, 136.02, 137.12, 138.04, 138.20, 142.04, 146.34, 146.84, 148.40, 150.66, 163.79, 168.00, 184.62, 186.54 ppm. EI-MS m/z: 791.20. Calc. for $C_{45}H_{39}Cl_2NO_8$: C, 68.18; H, 4.96; Cl, 8.94; N, 1.77. Found: C, 68.15; H, 4.94; N, 1.76.

Synthesis of (17S)-4-(3-{1',3'-dioxo-2,4-dioxaspiro[bicyclo[3.3.1]nonane-3,2'-indene]-1(9),5,7-trien-8-ylamino}phenyl)-17-methyl-16-oxopentacyclo[10.7.0.0^{2,9}.0^{3,6}.0^{13,17}]nonadeca-2(9),4,7-trien-7-yl 2-chloroacetate (10)

A solution of compound **8** (200 mg, 0.32 mmol), chloroacetyl chloride (50 µL, 0.62 mmol), triethylamine (70 µL, 0.50 mmol) in 5 mL of dimethyl sulphoxide was stirred at room temperature for 24 h; then, the solvent was removed under reduced pressure. The obtained product was purified by crystallization using the methanol:water:hexane (3:1:1) system; yielding 48% of product; m.p. 158-160°C; IR (ν_{max}, cm^{-1}) 3320, 1722, 1706 and 1330. ^{1}H NMR δ_H: 0.90 (s, 3H), 1.40-2.46 (m, 15H), 3.70-4.00 (m, 2H), 4.24-4.26 (m, 2H), 5.82 (m, 1H), 5.92 (m, 1H), 6.30 (broad, 1H), 6.33 (d, 1H, *J*= 5.32 Hz), 6.96-7.40 (m, 6H), 8.06-8.20 (m, 4H) ppm. ^{13}C NMR δ_C: 13.82, 21.52, 22.22, 26.00, 28.72, 30.42, 35.70, 36.78, 37.52, 41.00, 42.12, 47.34, 48.12, 51.90, 74.62, 96.28, 108.64, 109.74, 111.84, 113.80, 115.66, 121.10, 126.00, 128.34, 128.94, 130.96, 132.69, 136.02, 137.12, 138.04, 138.20, 142.06, 142.64, 146.30, 148.42, 150.64, 163.74, 184.62, 186.54, 220.20 ppm. EI-MS m/z: 713.21. Calc. for $C_{43}H_{36}ClNO_7$: C, 72.31; H, 5.08; Cl, 4.96; N, 1.96. Found: C, 72.30; H, 5.04; N, 1.94.

Synthesis of (5S)-21-(3-{1',3'-dihydro-2,4-dioxaspiro[bicyclo[3.3.1]nonane-3,2'-indene]-1(9),5,7-trien-8-ylamino}-phenyl)-5-methyl-16-oxo-17-oxahexacyclo[11.9.0.0^{2,10}.0^{5,9}.0^{14,18}.0^{19,22}] docosa-1(13),20-dien-6-yl-2-chloroacetate (11)

A solution of compound **9** (200 mg, 0.26 mmol), sodium hydroxide (25 mg, 0.62 mmol) in dimethyl sulphoxide (5 mL) was stirred under reflux for 48 h; then, the solvent was removed under reduced pressure. The obtained product was purified by crystallization using the methanol:water:hexane (3:1:1) system; yielding 66% of product; m.p. 120-122°C; IR (V_{max}, cm^{-1}) 3322, 1722, and 1332. ^{1}H NMR δ_H: 0.80 (s, 3H), 1.32-2.02 (m, 12H), 2.20-2.24 (m, 3H), 2.26 (m, 1H), 2.50 (m, 1H), 2.94-3.10 (m, 2H), 3.76 (m, 1H), 4.10 (m, 2H), 4.57-4.82 (m, 2H), 5.92 (m, 1H), 6.28 (d, 1H, *J*= 5.32 Hz), 6.30 (broad, 1H), 6.98-7.36 (m, 6H), 8.06-8.20 (m, 4H) ppm.

^{13}C NMR δ_C: 14.40, 24.26, 25.68, 26.04, 28.66, 30.00, 33.60, 35.64, 36.22, 40.00, 40.82, 40.90, 42.20, 43.38, 44.00, 50.90, 74.62, 84.62, 86.22, 96.24, 108.60, 108.76, 111.82, 113.82, 120.12, 126.00, 128.96, 129.76, 132.67, 132.80, 135.06, 136.02, 13710, 137.12, 138.20, 142.02, 146.34, 151.14, 168.00, 175.70, 184.62, 186.54, ppm. EI-MS m/z: 757.24. Calc. for $C_{45}H_{40}ClNO_8$: C, 71.28; H, 5.32; Cl, 4.68; N, 1.85. Found: C, 71.25; H, 5.32; N, 1.84.

Synthesis of (5S)-21-(3-{1',3'-dihydro-2,4-dioxaspiro[bicyclo[3.3.1]nonane-3,2'-indene]-1(9),5,7-trien-8-ylamino}-phenyl)-5-methyl-17-oxahexacyclo[11.9.0.0^{2,10}.0^{5,9}.0^{14,18}.0^{19,22}]docosa-1(13),20-diene-6,16-dione (12)

A solution of compound **10** (200 mg, 0.29 mmol), sodium hydroxide (25 mg, 0.62 mmol) in dimethyl sulphoxide (5 mL) was stirred under reflux for 48 h; then, the solvent was removed under reduced pressure. Following, the product was purified by crystallization using the methanol:water:hexane (3:1:1) system; yielding 45% of product; m.p. 208-210°C; IR (V_{max}, cm^{-1}) 3320, 1720, 1706 and 1330. ^{1}H NMR δ_H: 0.90 (s, 3H), 1.40-2.22 (m, 13H), 2.24 (m, 1H), 2.28-2.50 (m, 3H), 2.94-3.10 (m, 2H), 3.76-4.56 (m, 2H), 5.92 (m, 1H), 6.28 (d, 1H, *J*= 0.80 Hz), 6.30 (broad, 1H), 6.96-7.36 (m, 6H), 8.06-8.20 (m, 4H) ppm. ^{13}C NMR δ_C: 13.82, 21.52, 25.70, 26.76, 28.67, 33.02, 33.60, 35.64, 35.70, 40.92, 42.16, 42.86, 43.36, 47.32, 51.92, 74.62, 86.22, 96.24, 108.60, 108.79, 111.82, 113.82, 120.12, 126.00, 128.94, 129.79, 132.66, 132.83, 135.04, 136.02, 137.06, 137.12, 138.20, 142.02, 146.32, 151.16, 175.70, 184.62, 186.54, 220.20 ppm. EI-MS m/z: 679.25. Calc. for $C_{43}H_{37}NO_7$: C, 75.98; H, 5.49; N, 2.06. Found: C, 75.94; H, 5.46; N, 2.04.

Results and discussion

Synthesis and characterization

Several bicyclo-derivatives have been developed using different methods which involve some reagents that could be dangerous and require specific conditions [1-11]. In this study, two steroid-bicyclo[3.3.1]nonane derivatives were prepared using alternative chemical strategies: etherification and nucleophilic substitution.

Etherification

It is important to mention that ether derivatives have been prepared through the displacement of nitro groups using several reagents such as hexamethylphosphoramide [12], [^{18}F]fluoride [13], nitro-cyclohexanone [14], sodium phenoxide [15], dimethyl sulphoxide (DMSO) [16,17], and others. In this investigation, an ether derivative **3** was prepared from ninhydrin and 1-fluoro-2,4-dinitrobenzene using mild reaction conditions (Scheme 1 and 2).

The NMR results showed several signals present in the ^{1}H spectrum for compound **3** at 5.84-7.32 ppm for phenyl group bound to both ether groups; at 8.04-8.20 ppm for the indan fragment. The ^{13}C spectrum displayed chemical shifts at 78.00, 126.00-138.20 ppm for the indan fragment; at 98.40-114.81 and 142.92-149.64 ppm for phenyl bound to both ether groups; at 184.62-186.54 ppm for ketone groups. Additionally, the mass spectrum signal (m/z) from compound **3** was found at 270.02.

Nucleophilic substitution

There are several reports which show different aromatic nucleophilic substitution reactions; however, some of these reactions require special conditions thus greatly limiting the possibility of their application [18-22]. It is important to mention that a study indicates that there is no nucleophilic substitution of a 4-nitrofluorobenzene in liquid ammonia and only 4-nitroaniline is formed [23]. Based on that, the compound *N*-(3-ethynylphenyl)-2,4-dinitroaniline (**4**) was prepared in this study from 1-fluoro-2,4-dinitrobenzene and 3-ethynylaniline in the presence of acetonitrile in mild conditions (Scheme 3); here it is noteworthy that the formation of compound **5** (*N,N'*-bis-(3-ethynyl-phenyl)-4,6-dinitro-benzene-1,3-diamine) was not observed.

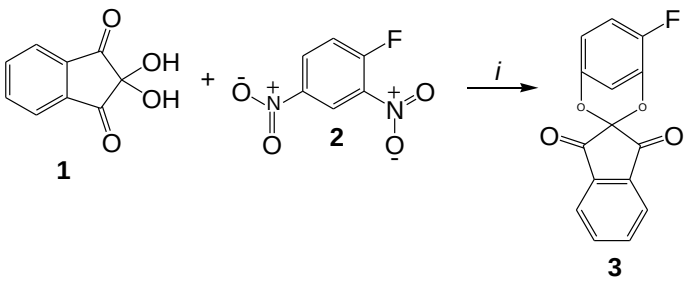

Reagents and conditions: i. K_2CO_3, DMSO, reflux, 24 h, 66%.

Scheme 1. Synthesis of 8-fluoro-1',3'-dihydro-2,4-dioxaspiro[bicyclo[3.3.1]nonane-3,2'-indene]--1(9),5,7-triene (3).

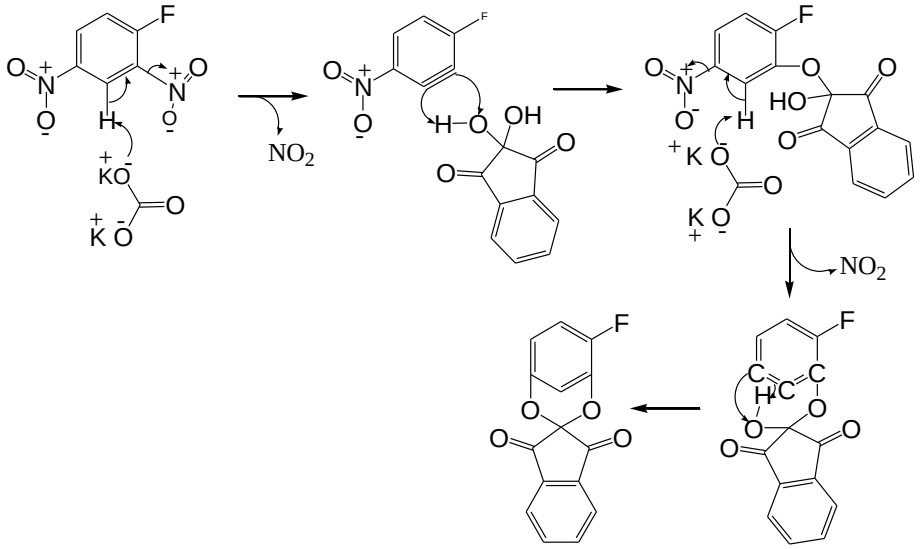

Scheme 2. Reaction mechanism involved in the synthesis of compound 3.

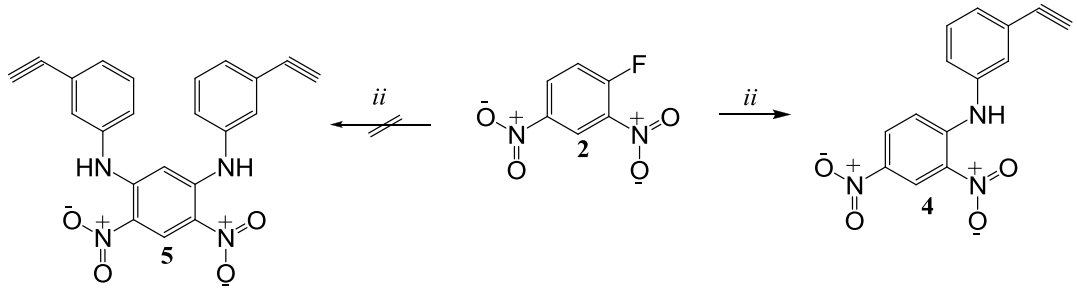

Reagents and conditions: ii. 3-ethynylaniline, acetonitrile, reflux, 24 h, 75%.
Scheme 3. Synthesis of *N*-(3-ethynylphenyl)-2,4-dinitroaniline (4).

The signals observed in the ^{1}H NMR spectrum for compound **4** displayed at 2.88 ppm for alkyne group, at 7.14-9.00 ppm for phenyl groups, and at 9.70 ppm for amino groups. In addition, the ^{13}C NMR spectrum showed bands at 78.20-84.02 ppm for alkyne group and at 106.52-141.52 ppm for phenyl groups. Additionally, the compound **4** was found at 283.05 in the mass spectrum.

Synthesis of N-(3-ethynylphenyl)-1',3'-dihydro-2,4-dio-xaspiro[bicyclo[3.3.1]nonane-3,2'-indene]-1(9),5,7-trien-8-amine (6)

Compound **6** was prepared using two methods: method A - *via* reaction of **3** with 3-ethynylaniline in the presence of acetonitrile in mild conditions (Scheme 4); method B - from compound **4** and ninhydrin. It is noteworthy, that there was a higher yield with method B in comparison to method A; this difference was attributed to the reaction conditions in each method. Several signals in the ^{1}H NMR spectrum for compound **6** were shown at 2.88 for alkyne group; 5.90 and 6.96-7.26 ppm for phenyl groups; at 6.90 ppm for amino group; at 8.04-8.20 ppm for indan fragment. Moreover, signals were registered in the ^{13}C NMR spectrum for compound **6** at 74.58, 126.00-130.52 and 136.00-138.21 ppm for the indan fragment; at 78.21-84.00 ppm for the alkyne group. Finally, the mass spectrum signal (m/z) from compound **6** was found at 376.05.

[2+2] addition reaction

Several cyclobutene have been prepared using reagents such as organolithium derivative [24], rhodium [25], palladium [26], nickel [27], cobalt complexes [28], copper(I) [29]. In this study, a cyclobutene derivative (compound **7**) was prepared *via* [2+2] addition of an alkyne derivative (compound **6**) to estradiol or estrone using copper(II) as catalyst (Scheme 5). Signals in the ^{1}H NMR spectrum for compound **7** were found at 0.80 for methyl linked to steroid nucleus; at 6.34 ppm for cyclobutene fragment; at 8.08 ppm for both hydroxyl and amino groups.

Other signals from the ^{13}C NMR spectrum were found at 15.80 ppm for methyl group; at 74.61, 126.00, 136.08 and 138.20 ppm for the indan fragment; at 133.66 and 148.90 ppm for cyclobutene ring; at 184.62 and 186.54 ppm for ketone groups. In addition, the mass spectrum signal (m/z) from compound **7** was found at 639.26.

Signals in the ^{1}H NMR spectrum for compound **8** were found at 0.90 ppm for methyl linked to steroid nucleus; at 8.06-8.20 ppm for the indan fragment; at 6.36 ppm for the cyclobutene fragment; at 8.90 ppm for both amino and hydroxyl groups. Other signals, from the ^{13}C NMR spectrum were found at 13.82 ppm for the methyl group; at 74.60, 126.00, 136.06 and 138.20 ppm for the indan fragment; at 133.66 and 148.90 ppm for the cyclobutene fragment; at 184.62-220.14 ppm for ketone groups. In addition, the mass spectrum (m/z) from compound **8** was found at 637.24.

Acylation of compounds 9 or 10

Some reports have shown the acylation of alcohol groups using several reagents such as cobalt(II) chloride [30], bismuth(III) trifluoromethanesulphonate [31], di-stannoxane [32], scandium trifluoro-methane sulphonate [33], tantalum(V) chloride [34] and others. However, some of the reagents require special conditions. Analysing these data, in this investigation the compounds **7** or **8** were acylated with chloroacetyl chloride in the presence of triethylamine to form the compounds **9** or **10** (Scheme 6). It is noteworthy, that the ^{1}H NMR spectrum for compound **9** showed signals at 0.80 ppm for the methyl group linked to the steroid nucleus, at 8.06-8.20 ppm for the indan fragment, at 6.34 ppm for the cyclobutene fragment, at 6.28 ppm for the amino group linked to phenyl and at 4.10-4.26 ppm for methylene bound to both ester group and chloride atom.

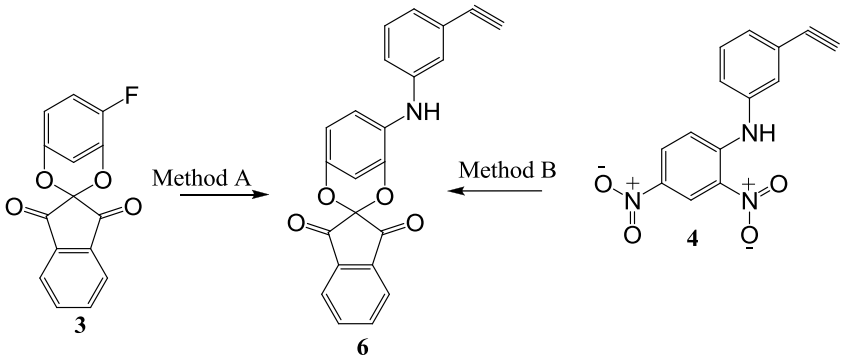

Reagents and conditions: Method A. 3-ethynylaniline, acetonitrile, reflux, 24 h, 48%;
Method B. ninhydrin, K_2CO_3, DMSO, rt, 48 h, 58%.

Scheme 4. Synthesis of *N*-(3-ethynylphenyl)-1',3'-dihydro-2,4-dioxaspiro[bicyclo[3.3.1]-nonane-3,2'-indene]-1(9),5,7-trien-8-amine (6).

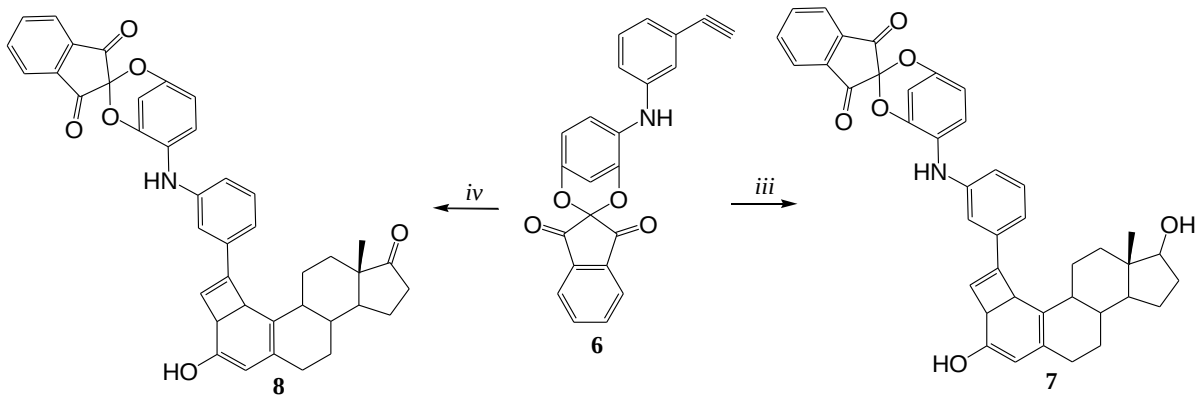

Reagents and conditions: iii. 17*β*-estradiol, cupric chloride, MeOH, rt, 48 h, 45%;
iv. estrone, cupric chloride, MeOH, rt, 48 h, 48%.

Scheme 5. Synthesis of two bicyclo[3.3.1]nonane-steroid derivatives (7 or 8).

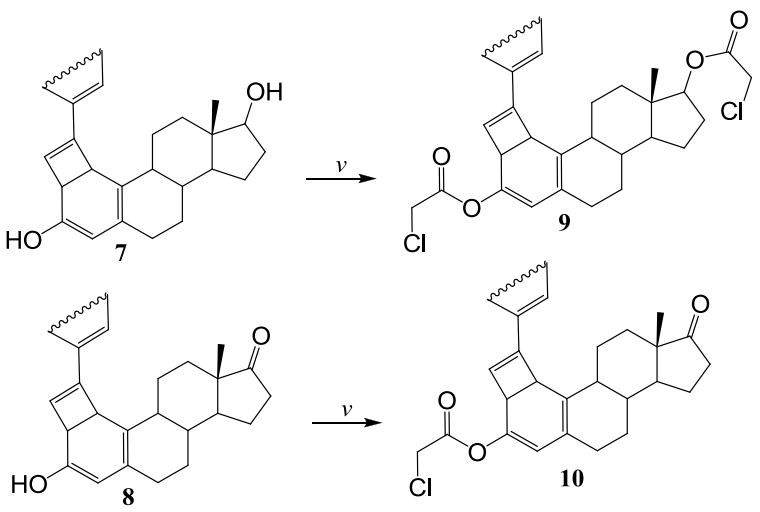

Reagents and conditions: v. chloroacetyl chloride, Et_3N, DMSO, rt, 24, 48%;
Scheme 6. Synthesis of two bicyclo[3.3.1]nonane-steroid chloroacetate derivatives (9 or 10).

In addition, several signals were found in the ^{13}C NMR spectrum, at 14.40 ppm for the methyl group; at 74.60, 126.00, 136.02 and 138.20 ppm for the indan fragment; at 130.90 and 150.66 ppm for the cyclobutene fragment; at 163.79-168.00 for both ester groups; at 184.62 and 186.54 ppm for both ketone groups. The mass spectrum signal (m/z) from compound **9** was found at 791.20.

The ^{1}H NMR spectrum for compound **10** showed several signals at 0.90 ppm for the methyl group linked to steroid nucleus; at 8.06-8.20 ppm for the indan fragment; at 6.33 ppm for the cyclobutene ring; at 6.30 for amino group linked to the phenyl group. The ^{13}C NMR spectrum for the compound **10** showed signals at 13.82 ppm for the methyl group; at 74.62, 126.00, 136.02 and 138.20 ppm for the indan fragment; at 130.96 and 150.64 ppm for the cyclobutene ring; at 184.62-220.20 ppm for ketone groups. In addition, the mass spectrum (m/z) from compound **10** was found at 713.21.

Internal cyclization reaction

There are studies which show the cyclization of halide derivatives with internal double bound using reagents such as $Pd(PPh_3)_4$ [35], $Pd(OAc)_2$ [36], $Bi(OTf)_3$ [37], $CoCl_2$ [38], copper(I) [39] and others. Based on these data, in this study, a dihydro-furan-2-one ring was involved in the chemical structure of **11** or **12** formed *via* internal reaction of chloride with double bond in basic medium (Schemes 7 and 8).

It is noteworthy that the ^{1}H NMR spectrum for compound **11** (Figure 1) showed several signals at 0.80 ppm for methyl linked to steroid nucleus; at 2.26 and 2.94-3.10 for the dihydro-furan-2-one ring; at 8.06-8.20 ppm for the indane fragment; 6.28 ppm for the cyclobutene ring; at 6.30 for the amino group; at 4.10 ppm for methylene bound to ester group; at 6.28 ppm for cyclobutene ring. Moreover, other signals of the ^{13}C NMR spectrum for compound **11** were found at 14.40 for the methyl group; at 76.62, 126.00, 136.02 and 138.20 ppm for the indan fragment; at 40.82 ppm for methylene bound to ester group; at 33.60 and 86.22 ppm for the dihydro-furan-2-one ring; at 132.80 and 151.14 ppm for the cyclobutene ring; at 168.00 ppm for the ester group; at 175.70-186.54 ppm for ketone groups. Additionally, the mass spectrum signal (m/z) from compound **11** was found at 757.24.

On the other hand, the ^{1}H NMR spectrum for compound **12** (Figure 2) displayed signals at 0.90 for methyl linked to steroid nucleus; at 2.26 and 2.94-3.10 ppm for the dihydro-furan-2-one ring; 8.06-8.20 ppm for indan; at 6.28 ppm for the cyclobutene ring; at 6.30 ppm for the amino group. It should be mentioned that several signals, in the ^{13}C NMR spectrum, were found at 13.82 for the methyl group; at 33.60 and 42.16 ppm for the dihydro-furan-2-one ring; at 74.62, 126.00, 136.02 and 138.20 ppm for the indan fragment; at 132.83 and 151.16 ppm for the cyclobutene ring; at 175.70-220.20 ppm for ketone groups. In addition, the mass spectrum (m/z) from compound **12** was found at 679.25

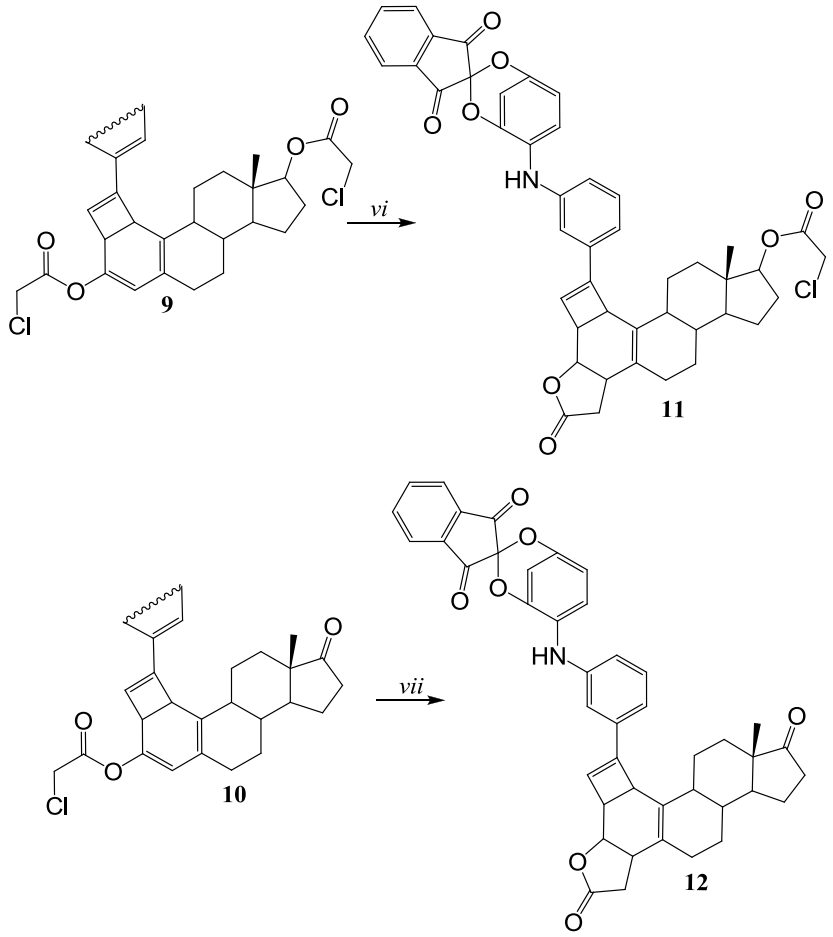

Reagents and conditions: vi. NaOH, DMSO, reflux, 48 h, 66%; *vii*. NaOH, DMSO, reflux, 48 h, 45%.

Scheme 7. Synthesis of two bicyclo[3.3.1]docosa-steroids derivatives (11 or 12).

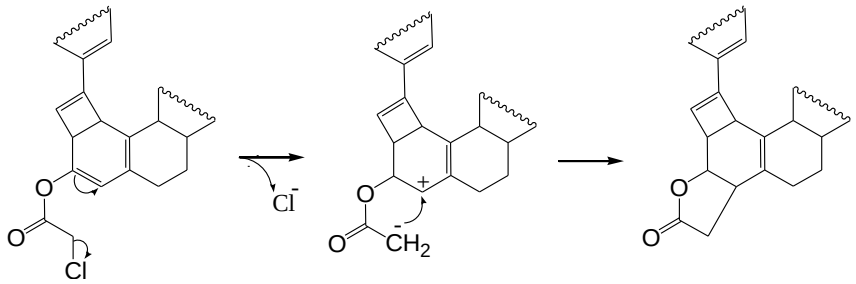

Scheme 8. Reaction mechanism involved in the synthesis of bicyclo[3.3.1]docosa-steroid derivatives.

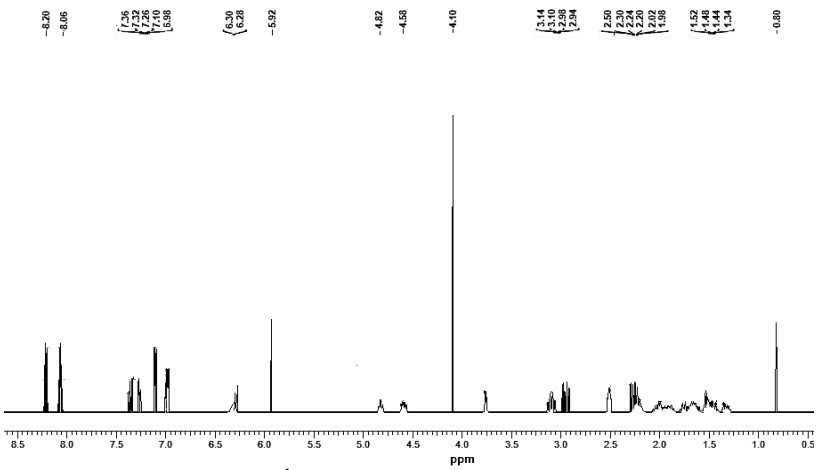

Figure 1. The ^{1}H NMR spectrum of compound 11.

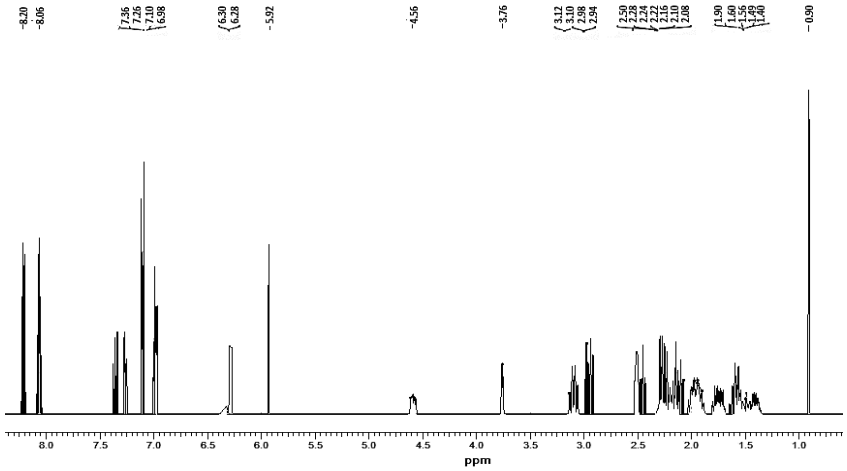

Figure 2. The ^{1}H NMR spectrum of compound 12.

Conclusions

In this study, the synthesis of two bicyclo[3.2.1]nonane-steroid derivatives was achieved from either estradiol or estrone using a series of reactions which involve etherification, nucleophilic aromatic substitution, [2+2] addition, acylation and an internal cyclization. It is noteworthy that the used reagents are easy to handle and do not require specific conditions. The presence of functional groups involved in their chemical structure was confirmed using both ^{1}H and ^{13}C NMR.

The yield of compound **11** ((5S)-21-(3-{1',3'-dihydro-2,4-dioxaspiro[bicyclo[3.3.1] nonane-3,2'-indene]-1(9),5,7-trien-8-ylamino}-phenyl)-5-methyl-16-oxo-17-oxahexacyclo[11.9.0.0^{2,10}.0^{5,9}. 0^{14,18}.0^{19,22}]docosa-1(13),20-dien-6-yl-2-chloroacetate) was higher compared to **12** ((5S)-21-(3-{1',3'-dihydro-2,4-dioxaspiro[bicyclo[3.3.1]nonane-3,2'-indene]-1(9),5,7-trien-8-ylamino}-phenyl)-5-methyl-17-oxahexacyclo[11.9.0. 0^{2,10}.0^{5,9}.0^{14,18}.0^{19,22}]docosa-13),20-diene-6,16-dione); this difference could be due to higher reactivity of compound **9** compared with **10** to form **11** or **12**.

References

1. Spessard, S.J.; Stoltz, B.M. Progress toward the synthesis of Garsubellin A and related phloroglucins: the direct diastereoselective synthesis of the bicyclo[3.3.1]nonane core. Organic Letters, 2002, 4(11), pp. 1943-1946. DOI: https://doi.org/10.1021/ol025968+
2. Nicolaou, K.C.; Pfefferkorn, J.A.; Cao, G.-Q.; Kim, S.; Kessabi, J. A facile method for the solution and solid-phase synthesis of substituted [3.3.1]bicycles. Organic letters, 1999, 1(5), pp. 807-810. DOI: https://doi.org/10.1021/ol990791d
3. Harding, K.E.; Clement, B.A.; Moreno, L.; Peter-Katalinic, J. Synthesis of some polyfunctionalized bicyclo[3.3.1] nonane-2,9-diones and bicyclo[4.3.1]decane-2,10-diones. The Journal of Organic Chemistry, 1981, 46(5), pp. 940-948. DOI: https://doi.org/10.1021/jo00318a020
4. Rodeschini, V.; Ahmad, N.M.; Simpkins, N.S. Synthesis of (+/−)-Clusianone: high-yielding bridgehead and diketone substitutions by regioselective lithiation of enol ether derivatives of bicyclo[3.3.1]nonane-2,4,9-triones. Organic Letters, 2006, 8(23), pp. 5283-5285. DOI: https://doi.org/10.1021/ol0620592
5. Schaefer, J.P.; Honig, L.M. Bicyclo[3.3.1]nonanes. IV. Dehydration of the bicyclo[3.3.1]nonane-2,6-diols. The Journal of Organic Chemistry, 1968, 33(7), pp. 2655-2659. DOI: https://doi.org/10.1021/jo01271a008
6. Hall Jr., H.K. Synthesis and polymerization of 3-azabicyclo-[4.3. 1]decan-4-one and 7,7-dimethyl-2-azabicyclo[4.1.1]octan-3-one. The Journal of Organic Chemistry, 1963, 28(11), pp. 3213-3214. DOI: https://doi.org/10.1021/jo01046a508
7. Marvell, E.N.; Gleicher, G.J.; Sturmer, D.; Salisbury, K. Conformational equilibria and rates of bridgehead proton exchange for 3,3-dimethyl-2-bicyclo[3.3.1]nonanone and 3,3-dimethyl-7-bicyclo[3.3.1]nonen-2-one. The Journal of Organic Chemistry, 1968, 33(9), pp. 3393-3397. DOI: https://doi.org/10.1021/jo01273a007
8. Chakravarty, J.; Dasgupta, R.; Ray, J.K.; Ghatak, U.R. Condensed cyclic and bridged-ring systems. VII. Acid-catalysed cyclisation of methyl substituted benzylcyclohexanols. Factors influencing the nature of cyclisation products. Proceedings of the Indian Academy of Sciences-Section A, 1977, 86, pp. 317-325. DOI: 10.1007/BF03046846
9. Heumann, A.; Kraus, W. Intramolecular cyclization of cycloalkene carboxylic acid chlorides. Tetrahedron, 1978, 34(4), pp. 405-411. DOI: https://doi.org/10.1016/0040-4020(78)80023-4

10. Hu, Z.; Wu, Y.; Xie, S.; Sun, W.; Guo, Y.; Li, X.-N.; Liu, J.; Li, H.; Wang, J.; Luo, Z.; Xue, Y. Phomopsterones A and B, two functionalized ergostane-type steroids from the endophytic fungus *Phomopsis* sp. TJ507A. Organic Letters, 2017, 19(1), pp. 258-261. DOI: https://doi.org/10.1021/acs.orglett.6b03557
11. He, Y.; Hu, Z.; Sun, W.; Li, Q.; Li, X.-N.; Zhu, H.; Huang, J.; Liu, J.; Wang, J.; Xue, Y.; Zhang, Y. Spiroaspertrione A, a bridged spirocyclic meroterpenoid, as a potent potentiator of oxacillin against methicillin-resistant *Staphylococcus aureus* from *Aspergillus* sp. TJ23. The Journal of Organic Chemistry, 2017, 82(6), pp. 3125-3131. DOI: https://doi.org/10.1021/acs.joc.7b00056
12. Kornblum, N.; Cheng, L.; Kerber, R.C.; Kestner, M.M.; Newton, B.N.; Pinnick, H.W.; Smith, R.G.; Wade, P.A. Displacement of the nitro group of substituted nitrobenzenes-a synthetically useful process. The Journal of Organic Chemistry, 1976, 41(9), pp. 1560-1564. DOI: https://doi.org/10.1021/jo00871a016
13. Attiná, M.; Cacace, F.; Wolf, A.P. Displacement of a nitro-group by [18 F] fluoride ion. A new route to aryl flurides of high specific activity. Journal of the Chemical Society, Chemical Communications, 1983, 0(3), pp. 108-109. DOI: 10.1039/C39830000108
14. Kornblum, N.; Boyd, S.D. Mechanism of displacement of a nitro group from .alpha.-nitro esters, ketones, and nitriles and from α,α-dinitro compounds by nitroparaffin salts. Journal of the American Chemical Society, 1970, 92(19), pp. 5784-5785. DOI: https://doi.org/10.1021/ja00722a067
15. Crossley, M.J.; King, L.G.; Simpson, J.L. Solvent-dependent ambident nucleophilicity of phenoxide ion towards nitroporphyrins: synthesis of 2-hydroxyaryl-and 2-aryloxy-5,10,15,20-tetraphenylporphyrins by displacement of a nitro group. Journal of the Chemical Society, Perkin Transactions 1, 1997, 0(20), pp. 3087-3096. DOI: 10.1039/A701673E
16. Beck, J.R. Nucleophilic displacement of aromatic nitro groups. Tetrahedron, 1978, 34(14), pp. 2057-2068. DOI: https://doi.org/10.1016/0040-4020(78)89004-8
17. Figueroa-Valverde, L.; Diaz-Cedillo, F.; Garcia-Cervera, E.; Pool-Gomes, E.; Lopez-Ramos, M.; Rosas-Nexticapa, M.; Hau-Heredia, L. Facile synthesis of two benzamidine-steroid derivatives. Letters in Organic Chemistry, 2014, 11(10), pp. 725-730. DOI: 10.2174/15701786116666140813210013
18. Ma, D.; Cai, Q. Copper/amino acid catalyzed cross-couplings of aryl and vinyl halides with nucleophiles. Accounts of chemical research, 2008, 41(11), pp. 1450-1460. DOI: https://doi.org/10.1021/ar8000298
19. Djukic, J.-P.; Rose-Munch, F.; Rose, E.; Simon, F.; Dromzee, Y. Nucleophilic aromatic substitutions: hydrodealkoxylation, hydrodehalogenation, and hydrodeamination of alkoxy, halogeno, and amino (.eta.6-arene)tricarbonylchromium complexes. Organometallics, 1995, 14(4), pp. 2027-2038. DOI: https://doi.org/10.1021/om00004a065
20. Bunnett, J.F.; Zahler, R.E. Aromatic nucleophilic substitution reactions. Chemical Reviews, 1951, 49(2), pp. 273-412. DOI: https://doi.org/10.1021/cr60153a002
21. Mutai, K.; Kobayashi, K. Photoinduced intramolecular aromatic nucleophilic substitution (the photo-smiles rearrangement) in amino ethers. Bulletin of the Chemical Society of Japan, 1981, 54(2), pp. 462-465. DOI: https://doi.org/10.1246/bcsj.54.462
22. Zoltewicz, J.A. New directions in aromatic nucleophilic substitution. Organic Syntheses, 1975, pp. 33-64. DOI: https://doi.org/10.1007/BFb0046186
23. Ji, P.; Atherton, J.H.; Page, M.I. The kinetics and mechanisms of aromatic nucleophilic substitution reactions in liquid ammonia. The Journal of Organic Chemistry, 2011, 76(9), pp. 3286-3295. DOI: https://doi.org/10.1021/jo200170z
24. Reed, M.W.; Pollart, D.J.; Perri, S.T.; Foland, L.D.; Moore, H.W. Synthesis of 4-substituted-3-alkoxy-3-cyclobutene-1,2-diones. The Journal of Organic Chemistry, 1988, 53(11), pp. 2477-2482. DOI: https://doi.org/10.1021/jo00246a016
25. Xu, H.; Zhang, W.; Shu, D.; Werness, J.B.; Tang, W. Synthesis of cyclobutenes by highly selective transition-metal-catalyzed ring expansion of cyclopropanes. Angewandte Chemie International Edition, 2008, 47(46), pp. 8933-8936. DOI: https://doi.org/10.1002/anie.200803910
26. Frébault, F.; Luparia, M.; Oliveira, M.T.; Goddard, R.; Maulide, N. A versatile and stereoselective synthesis of functionalized cyclobutenes. Angewandte Chemie International Edition, 2010, 49(33), pp. 5672-5676. DOI: https://doi.org/10.1002/anie.201000911
27. Huang, D.-J.; Rayabarapu, D.K.; Li, L.-P.; Sambaiah, T.; Cheng, C.-H. Nickel-catalyzed [2+2] cycloaddition of alkynes with activated cyclic alkenes: synthesis and novel ring expansion studies of cyclobutene products. Chemistry–A European Journal, 2000, 6(20), pp. 3706-3713. DOI: https://doi.org/10.1002/1521-3765(20001016)6:20<3706::AID-CHEM3706>3.0.CO;2-P
28. Chao, K.C.; Rayabarapu, D.K.; Wang, C.-C.; Cheng, C.-H. Cross [2+2] cycloaddition of bicyclic alkenes with alkynes mediated by cobalt complexes: A facile synthesis of cyclobutene derivatives. The Journal of Organic Chemistry, 2001, 66(26), pp. 8804-8810. DOI: https://doi.org/10.1021/jo010609y
29. Barluenga, J.; Riesgo, L.; López, L.A.; Rubio, E.; Tomas, M. Discrimination of diazo compounds toward carbenoids: copper(I)-catalyzed synthesis of substituted cyclobutenes. Angewandte Chemie International Edition, 2009, 48(41), pp. 7569-7572. DOI: https://doi.org/10.1002/anie.200903902

30. Iqbal, J.; Srivastava, R.R. Cobalt(II) chloride catalyzed acylation of alcohols with acetic anhydride: scope and mechanism. The Journal of Organic Chemistry, 1992, 57(7), pp. 2001-2007. DOI: https://doi.org/10.1021/jo00033a020
31. Orita, A.; Tanahashi, C.; Kakuda, A.; Otera, J. Highly efficient and versatile acylation of alcohols with $Bi(OTf)_3$ as catalyst. Angewandte Chemie International Edition, 2000, 39(16), pp. 2877-2879. DOI: https://doi.org/10.1002/1521-3773(20000818)39:16<2877::AID-ANIE2877>3.0.CO;2-V
32. Orita, A.; Mitsutome, A.; Otera, J. Distannoxane-catalyzed highly selective acylation of alcohols. The Journal of Organic Chemistry, 1998, 63(8), pp. 2420-2421. DOI: https://doi.org/10.1021/jo9800412
33. Ishihara, K.; Kubota, M.; Kurihara, H.; Yamamoto, H. Scandium trifluoromethanesulfonate as an extremely active lewis acid catalyst in acylation of alcohols with acid anhydrides and mixed anhydrides. The Journal of Organic Chemistry, 1996, 61(14), pp. 4560-4567. DOI: https://doi.org/10.1021/jo952237x
34. Chandrasekhar, S.; Ramachander, T.; Takhi, M. Acylation of alcohols with acetic anhydride catalyzed by TaCl5: Some implications in kinetic resolution. Tetrahedron Letters, 1998, 39(20), pp. 3263-3266. DOI: https://doi.org/10.1016/S0040-4039(98)00465-1
35. Mori, M.; Oda, I.; Ban, Y. Cyclization of α-haloamide with internal double bond by use of the low-valent metal complex. Tetrahedron Letters, 1982, 23(50), pp. 5315-5318. DOI: https://doi.org/10.1016/S0040-4039(00)85827-X
36. Zeni, G.; Larock, R.C. Synthesis of heterocycles *via* palladium-catalyzed oxidative addition. Chemical Reviews, 2006, 106(11), pp. 4644-4680. DOI: https://doi.org/10.1021/cr0683966
37. Hayashi, R.; Cook G.R. Bi(OTf)3-catalyzed 5-exo-trig cyclization via halide activation. Tetrahedron Letters, 2008, 49(24), pp. 3888-3890. DOI: https://doi.org/10.1016/j.tetlet.2008.04.067
38. Ohmiya, H.; Wakabayashi, K.; Yorimitsu, H.; Oshima, K. Cobalt-catalyzed cross-coupling reactions of alkyl halides with aryl Grignard reagents and their application to sequential radical cyclization/cross-coupling reactions. Tetrahedron, 2006, 62(10), pp. 2207-2213. DOI: https://doi.org/10.1016/j.tet.2005.12.013
39. Iwamoto, H.; Akiyama, S.; Hayama, K.; Ito, H. Copper(I)-catalyzed stereo- and chemoselective borylative radical cyclization of alkyl halides bearing an alkene moiety. Organic Letters, 2017, 19(10), pp. 2614-2617. DOI: https://doi.org/10.1021/acs.orglett.7b00940

CHEMISTRY JOURNAL OF MOLDOVA. General, Industrial and Ecological Chemistry. 2020, 15(1), 86-94
ISSN (p) 1857-1727 ISSN (e) 2345-1688
http://cjm.asm.md
http://dx.doi.org/10.19261/cjm.2019.647

NOVEL *β*-LACTAMS AND THIAZOLIDINONE DERIVATIVES FROM 1,4-DIHYDROQUINOXALINE SCHIFF'S BASE: SYNTHESIS, ANTIMICROBIAL ACTIVITY AND MOLECULAR DOCKING STUDIES

Hajer Hrichi [a,c*], Nadia Ali Ahmed Elkanzi [a,b], Rania Badawy Bakr [d,e]

[a]*Chemistry Department, College of Science, Jouf University, Sakaka 2014, Saudi Arabia*
[b]*Chemistry Department, Faculty of Science, Aswan University, Aswan 81528, Egypt*
[c]*National Institute of Applied Sciences and Technology, Carthage University, Centre Urbain Nord, Tunis Cedex 1080, Tunisia*
[d]*Department of Pharmaceutical Chemistry, College of Pharmacy, Jouf University, Sakaka, Aljouf 2014 Saudi Arabia*
[e]*Department of Pharmaceutical Organic Chemistry, Faculty of Pharmacy, Beni-Suef University, Beni-Suef 62514, Egypt*
[*]*e-mail: hahrichi@ju.edu.sa*

Abstract. A series of novel isolated *β*-lactams **3a-c** and thiazolidinone derivatives **4a-c** were successfully synthesized from reactions of new Schiff's bases **2a-c** with chloroacetyl chloride and thioglycolic acid. The chemical structures of the new compounds were confirmed through different spectroscopic techniques including IR, ^{1}H and ^{13}C NMR, mass spectrometry and elemental analysis. The antimicrobial activity of the obtained compounds was assessed *in vitro* against gram-positive *Staphylococcus aureus* and gram-negative *Escherichia coli* bacteria and *Aspergillus flavus* and *Candida albicans* fungi. All compounds exhibited good to excellent antimicrobial activity against the tested strains. Furthermore, a molecular docking study was carried out for the synthesized compounds and the results indicated that compounds **3b** and **4b** display comparable binding affinity scores as that of glutamate. These two compounds are promising candidates as antibacterial and antifungal agents that would deserve further investigations.

Keywords: heterocycle, *β*-lactam, quinoxaline, antimicrobial activity, molecular docking.

Received: 16 October 2020/ Revised final: 28 February 2020/ Accepted: 02 March 2020

Introduction

The *β*-lactam skeleton has attracted much attention from medicinal chemists for the past 60 years due to its numerous biological activities and the mechanism of action of its derivatives has been broadly reviewed [1-3]. As a class of organic molecules, *β*-lactams constitute more than 65% of the world antibiotics market in both human and veterinary medicine [4,5]. Since the discovery of penicillin, efforts have been devoted to synthesize various *β*-lactam derivatives bearing important biological activities [6]. Besides their antibacterial activity, *β*-lactam derivatives have shown antitumor [7,8], antiviral [9], antihyperglycemic [10], antitubercular [11], antileishmanial and other potent biological activities [12]. However, the evolution of antibiotic-resistant bacteria represents the main obstacle to broad the clinical application of *β*-lactams despite the exhaustive medicinal chemistry campaigns aiming to vary *β*-lactam antibiotics. Consequently, the need for new derivatives with efficient biological activities has increased.

During the past years, substituted quinoxaline derivatives have gained attention and have been progressively explored as a result of their broad spectrum of pharmacological properties [13-15]. Therefore, a wide variety of synthetic routes for the design of functionalized quinoxalines has been intensively studied. Quinoxaline derivatives display versatile biological activities such as antiviral [16,17], antimicrobial [18,19], anti-inflammatory [20], antitumor [21] anti-tuberculosis [22], *etc*. Diverse recent approaches were carried out to the existing drugs to minimize the microbial resistance. These, for the most part, necessitate structural modification of actual antimicrobial agents to improve the microbial intracellular concentration of the drug, and thereby to boost the antimicrobial activity. The throughout literature surveys indicate that some substituents,

particularly chlorine atoms, of structure of the bioactive organic compounds regarded as potential drug, have a promising effect on their specific biological activity. Several previous studies have pointed out that *β*-lactam derivatives possessing chlorine atoms were endued with significant biological activities [23-26]. The search for novel synthetic pathways for the design of heterocycles based on the *β*-lactam skeleton with improved biological derivatives is being actively pursued in our laboratory [27,28].

The aim of this study was to synthesize novel *β*-lactams **3a-c** and thiazolidinone derivatives **4a-c** and to evaluate *in vitro* their antibacterial and antifungal activity against several strains. Molecular docking studies were carried out to estimate the binding affinities of most active synthesized compounds on a molecular level.

Experimental

Generalities

Unless otherwise mentioned, reagents were purchased from Sigma Aldrich (Bayouni Trading Co. Ltd., Al-Khobar, Saudi Arabia) with high grade of purity and used without further purification. Reaction progress was monitored using *thin-layer chromatography* on silica gel pre-coated F254Merck plates (Darmstadt, Germany) and spots were visualized by ultraviolet irradiation. *Melting point* values of the synthesized compounds were determined using a Gallenkamp electro thermal melting point apparatus. *IR spectra* were measured as KBr pellets on a Pye-Unicam sp 1000 spectrophotometer. *^{1}H NMR spectra* were recorded in [$^2H_6$] dimethyl sulphoxide (DMSO) solution at 200 MHz on a Varian Gemini NMR spectrometer using tetramethylsilan as internal reference. *^{13}C NMR spectra* were measured on a Varian MercuryVXR-300 NMR spectrometer (Palo Alto, CA) at 400 and 125 MHz using DMSO-d_6 as solvents. *Mass spectra* were obtained on a Shimadzu GCMS-QP 1000EX mass spectrometer at 70 eV. *Elemental analysis* was carried out on CE 440 Elemental Analyzer-Automatic Injector (Exeter Analytical, Inc., USA) at the Micro analytical Center of Cairo University.

General procedure for the synthesis of compounds (2a-c)

Compound **1** was prepared according to the reported method [15]. Briefly, compound **1** (0.01 mol) was treated with different aromatic aldehydes in equivalent amount in ethanol 30 mL and the reaction mixture was refluxed for 4 h. Then, the formed solid product was filtered and recrystallized from ethanol to afford the corresponding compounds **2a-c**.

Ethyl 3-(benzylideneamino)-1,4-dihydroquinoxaline-2-carboxylate ***2a***, orange crystals in 79% yield, m.p. 120-122°C. IR (KBr, cm^{-1}): 1565 (CH=N), 1730 (CO ester), 3100-3400 (NH). ^{1}H NMR: δ 1.21 (t, 3H, J= 7.52 Hz, CH_2CH_3), 4.15 (q, 2H, J= 7.51 Hz, CH_2CH_3), 7.10–8.01 (m, 9H, Ar-H), 8.3 (s, 1H, C*H*=N), 12.35 (s, 1H, N-H$_{quinox}$), 12.62 (s, 1H, N-H). ^{13}C NMR: δ 14.21 (CH_3), 61.53 (CH_2), 87.15, 119.44, 119.83, 120.35, 131.42, 137.65 (C=C), 164.24, 165.43 (*C*H=N) and (CO ester). MS (m/z, %): 307.0 (M^+, 55). Calc. for $C_{18}H_{17}N_3O_2$ (307.35): C, 70.34; H, 5.58; N, 13.67%. Found: C, 70.22; H, 5.43; N, 13.23%.

Ethyl 3-((4-chlorobenzylidene) amino)-1,4-dihydroquinoxaline-2-carboxylate ***2b***, yellow white crystals in 84% yield; m.p. 110-112°C. IR (KBr, cm^{-1}): 1568 (CH=N), 1735 (CO ester), 3100-3400 (NH). ^{1}H NMR: δ 1.25 (t, 3H, J= 7.53 Hz, CH_2CH_3), 4.18 (q, 2H, J= 7.53 Hz, CH_2CH_3), 7.10-8.01 (m, 8H, Ar-H), 8.5 (s, 1H, C*H*=N), 12.37 (s, 1H, N-H$_{quinox}$), 12.65 (s, 1H, N-H). ^{13}C NMR: δ 14.25 (CH_3), 61.57 (CH_2), 87.17, 119.44, 119.86, 120.33, 131.41, 137.64 (C=C), 164.23, 165.45 (*C*H=N) and (CO ester). MS (m/z, %): 341.0 (M^+, 45). Calc. for $C_{18}H_{16}ClN_3O_2$ (341.79): C, 63.25; H, 4.72; Cl, 10.37; N, 12.29%. Found: C, 63.17; H, 4.55; Cl, 10.40; N, 12.18%.

Ethyl 3-((4-methoxybenzylidene) amino)-1,4-dihydroquinoxaline-2-carboxylate ***2c***, red crystals in 65% yield; m.p. 135-137°C. IR (KBr, cm^{-1}): 1563 (CH=N), 1730 (CO ester), 3100-3400 (NH). ^{1}H NMR: δ 1.21 (t, 3H, J= 7.52 Hz, CH_2CH_3), 3.56 (s, 3H, OCH_3), 4.15 (q, 2H, J= 7.52 Hz, CH_2CH_3), 7.10-8.01 (m, 8H, Ar-H), 8.3 (s, 1H, C*H*=N), 12.35 (s, 1H, N-H$_{quinox}$), 12.63 (s, 1H, N-H). ^{13}C NMR: δ 14.14 (CH_3), 61.16 (CH_2), 87.15, 119.42, 119.85, 120.37, 131.44, 137.66 (C=C), 164.19, 165.28 (*C*H=N) and (CO ester). MS (m/z, %): 337.37 (M^+, 38). Calc. for $C_{19}H_{19}N_3O_3$ (337.37): C, 67.64; H, 5.68; N, 12.46%. Found: C, 67.64; H, 5.68; N, 12.46%.

General procedure for the synthesis of ethyl 3-(3-chloro-2-oxo-4-phenylsubstituted azetidin-1-yl)-1,4-dihydroquinoxaline-2-carboxylate (3a-c)

To a solution of compounds **2a-c** (0.01 mol) in 1,4-dioxane (15 mL), chloroacetyl chloride (1.99 mL, 0.025 mol) was added drop-wise at 5-100°C in the presence of trimethylamine (3.49 mL, 0.025 mol). The mixture was stirred for 8 h, and then poured into an ice water. The obtained solid was separated by filtration and recrystallized from ethanol.

Ethyl 3-(3-chloro-2-oxo-4-phenylazetidin-1-yl)-1, 4-dihydroquinoxaline-2-carboxylate ***3a***, reddish brown crystals in 67% yield; m.p. 150-152°C. IR (KBr, cm^{-1}): 1685 (cyclic CO), 1730 (CO ester), 3100-3400 (NH). ^{1}H NMR: δ 1.21 (t, 3H, J= 7.52 Hz, CH_2CH_3), 4.15 (q, 2H, J= 7.52 Hz, CH_2CH_3), 7.10–8.01 (m, 9H, Ar-H), 5.2 (d, 1H, J= 5.59 Hz, CH-N), 5.47 (d, 1H, J= 5.78 Hz, CHCl), 12.35 (s, 1H, N-H_{quinox}) and 12.62 (s, 1H, N-H). ^{13}C NMR: δ 14.26 (CH_3), 60.73 (CH-N), 61.5 (CH_2), 64.25 (CH-Cl), 87.14, 119.41, 119.86, 120.37, 131.45, 137.62 (C=C), 161.1(CO cyclic), 165.4 (CO ester). MS (m/z, %): 383.0 (M^+, 30). Calc. for $C_{20}H_{18}ClN_3O_3$ (383.83): C, 62.58; H, 4.73; Cl, 9.24; N, 10.95%. Found: C, 62.53; H, 4.65; Cl, 9.17; N, 10.79%.

Ethyl 3-(3-chloro-2-(4-chlorophenyl)-4-oxoazetidin-1-yl)-1,4-dihydroquinoxaline-2-carboxylate ***3b***, green white crystals in 70% yield; m.p. 180-182°C. IR (KBr, cm^{-1}): 1690 (cyclic CO), 1732 (CO ester), 3100-3400 (NH). ^{1}H NMR: δ 1.21 (t, 3H, J= 7.53 Hz, CH_2CH_3), 4.15 (q, 2H, J= 7.53 Hz, CH_2CH_3), 7.10–8.01 (m, 8H, Ar-H), 5.2 (d, 1H, J= 5.61 Hz, CH-N), 5.47 (d, 1H, J= 5.83 Hz, CHCl), 12.35 (s, 1H, N-H_{quinox}), 12.62 (s, 1H, N-H). ^{13}C NMR: δ 14.24 (CH_3), 60.71 (CH-N), 61.55 (CH_2), 64.23 (CH-Cl), 87.16, 119.43, 119.84, 120.32, 131.45, 137.63 (C=C), 161.15 (cyclic CO), 165.46 (CO ester). MS (m/z, %): 418.0 (M^+, 42). Calc. for $C_{20}H_{17}Cl_2N_3O_3$ (418.27): C, 57.43; H, 4.10; Cl, 16.95; N, 10.05%. Found: C, 57.35; H, 4.02; Cl, 16.84; N, 10.01%.

Ethyl 3-(3-chloro-2-(4-methoxyphenyl)-4-oxoazetidin-1-yl)-1,4-dihydroquinoxaline-2-carboxylate ***3c***, violet crystals in 60% yield; m.p. 160-162°C. IR (KBr, cm^{-1}): 1685 (cyclic CO), 1732 (CO ester), 3100-3400 (NH). ^{1}H NMR: δ 1.21 (t, 3H, J= 7.52 Hz, CH_2CH_3), 3.56 (s, 3H, OCH_3), 4.15 (q, 2H, J= 7.52 Hz, CH_2CH_3), 7.10-8.01 (m, 8H, Ar-H), 5.2 (d, 1H, J= 5.59 Hz, CH-N), 5.47 (d, 1H, J= 5.78 Hz, CHCl), 12.35 (s, 1H, N-H_{quinox}), 12.62 (s, 1H, N-H). ^{13}C NMR: δ 14.25 (CH_3), 60.77 (CH-N), 61.54 (CH_2), 64.28 (CH-Cl), 87.16, 119.44, 119.86, 120.39, 131.44, 137.6 (C=C), 161.14 (CO cyclic), 165.47 (CO ester). MS (m/z, %): 413.0 (M^+, 25). Calc. for $C_{21}H_{20}ClN_3O_4$ (413.85): C, 60.95; H, 4.87; Cl, 8.57; N, 10.15%. Found: C, 60.90; H, 4.72; Cl, 8.53; N, 10.12%.

General procedure for the synthesis of ethyl 3-(4-oxo-3-phenyl substituted 1,2,3-thiadiazolidin-2-yl)-1,4-dihydroquinoxaline-2-carboxylate (4a-c)

Thioglycolic acid (0.02 mol) was added to compounds **2a-c** (0.01 mol) and zinc chloride. The reaction mixture was heated and refluxed for 12 h. The solid product was collected and recrystallized from diethyl ether to give compounds **4a-c**.

Ethyl 3-(4-oxo-2-phenylthiazolidin-3-yl)-1,4-dihydroquinoxaline-2-carboxylate ***4a***, brown crystals in 62% yield; m.p. 215-217°C. IR (KBr, cm^{-1}): 1730 (CO ester), 1760 (CO thiazolidinone), 3100-3400 (NH). ^{1}H NMR: δ 1.21 (t, 3H, J= 7.52 Hz, CH_2CH_3), 3.96 (s, 2H, CH_2), 4.15 (q, 2H, J= 7.52 Hz, CH_2CH_3), 4.93 (s, 1H, CH), 7.10–8.01 (m, 9H, Ar-H), 8.3 (s, 1H, C*H*=N), 12.35 (s, 1H, N-H_{quinox}), 12.62 (s, 1H, N-H). ^{13}C NMR: δ 14.23 (CH_3), 61.57 (CH_2), 87.15, 119.48, 119.86, 120.37, 131.45, 137.68 (C=C), 165.45 (CO ester); MS (m/z, %): 381.0 (M^+, 55). Calc. for $C_{20}H_{19}N_3O_3S$ (381.45): C, 62.97; H, 5.02; N, 11.02; S, 8.41%. Found: C, 62.92; H, 5.00; N, 10.99; S, 8.33%.

Ethyl 3-(2-(4-chlorophenyl)-4-oxothiazolidin-3-yl)-1,4-dihydroquinoxaline-2-carboxylate ***4b***, brown crystals in 62% yield; m.p. 215-217°C. IR (KBr, cm^{-1}): 1730 (CO ester), 1766 (CO thiazolidinone), 3100-3400 (NH). ^{1}H NMR: δ 1.21 (t, 3H, J= 7.53 Hz, CH_2CH_3), 4.1 (s, 2H, CH_2), 4.15 (q, 2H, J= 7.53 Hz, CH_2CH_3), 4.98 (s, 1H, CH) 7.10-8.01 (m, 8H, Ar-H), 8.3 (s, 1H, C*H*=N), 12.35 (s, 1H, N-H_{quinox}), 12.62 (s, 1H, N-H). ^{13}C NMR: δ 14.22 (CH_3), 61.51 (CH_2), 87.15, 119.43, 119.86, 120.37, 131.45, 137.66 (C=C), 165.46 (CO ester). MS (m/z, %): 415.0 (M^+, 16). Calc. for $C_{20}H_{18}ClN_3O_3S$ (415.89): C, 57.76; H, 4.36; Cl, 8.52; N, 10.10; S, 7.71%. Found: C, 57.70; H, 4.23; Cl, 8.44; N, 10.5; S, 7.63%.

Ethyl 3-(2-(4-methoxyphenyl)-4-oxothiazolidin-3-yl)-1,4-dihydroquinoxaline-2-carboxylate ***4c***, deep red crystals in 55% yield; m.p. 230-232°C. IR (KBr, cm^{-1}): 1730 (CO ester), 1762 (CO thiazolidinone), 3100-3400 (NH). ^{1}H NMR: δ 1.21 (t, 3H, J= 7.52 Hz ,CH_2CH_3), 3.94 (s, 2H, CH_2), 4.15 (q, 2H, J= 7.52 Hz, CH_2CH_3), 4.90 (s, 1H, CH), 7.10–8.01 (m, 8H, Ar-H), 8.3 (s, 1H, C*H*=N), 12.35 (s, 1H, N-H_{quinox}), 12.62 (s, 1H, N-H). ^{13}C NMR: 14.25 (CH_3), 61.58 (CH_2), 87.14, 119.46, 119.83, 120.37, 131.45, 137.67 (C=C), 165.45 (CO ester); MS (m/z, %): 411.0 (M^+, 27). Calc. for $C_{21}H_{21}N_3O_4S$ (411.47): C, 61.30; H, 5.14; N, 10.21; S, 7.79%. Found: C, 61.30; H, 5.14; N, 10.21; S, 7.79%.

Antimicrobial activity

Antimicrobial activity (antibacterial and antifungal) of the tested samples was assessed following a modified Kirby–Bauer disk diffusion method [29]. Plates impregnated with filamentous fungi like *Aspergillus flavus* at 25°C for 48 h;

gram-positive bacteria as *Staphylococcus aureus*; gram-negative bacteria as *Escherichia coli*, were incubated at 35-37°C for 24-48 h and *Candida albicans* and *Aspergillus flavus* fungi were incubated at 30°C for a period varying between 24 and 48 h. The standard disks of ampicillin (an antibacterial agent) and amphotericin B (an antifungal agent) served as positive control for antimicrobial activity and filter disks impregnated with 10 µL of solvent (distilled water, chloroform and DMSO) were used as negative controls. All experiments were repeated and carried out in triplicate in the case of a significant difference in the results and the average inhibition diameters were measured in mm/mg sample.

Molecular docking

In this study, molecular simulation and modelling were performed using Molecular Operating Environment software (MOE, Version 2010.08, Canada). Glucosamine-6-phosphate synthase enzyme (GlcN-6-P) (PDB: ID 1gdo) was downloaded from RCSB Protein Data Bank [30]. The novel synthesized compounds **3a-c** and **4a-c** were subjected to molecular docking *via* their 2D and 3D structures. Before docking, adequate steps were performed including running conformational analysis using systemic search, 2D protonation of the structures, selecting the least energetic conformer and applying the protocol.

Results and discussion

Synthesis and characterization

The chemical synthesis of the compounds is illustrated in Scheme 1. The synthesis of new Schiff's bases derived from ethyl 3-amino-1,4-dihydroquinoxaline-2-carboxylate **1** is the fundamental key in the synthesis of the conforming isolated *β*-lactams **3a-c** and thiazolidinone **4a-c** derivatives. Thus, the reaction of compound **1** with different aromatic aldehydes in ethanol (30 mL) under reflux for about 4 h [27,31-33] led to the formation of the corresponding Schiff's bases **2a-c** in 65-84% yield.

Subsequent cyclocondensation of Schiff's bases **2a-c** with chloroacetyl chloride in 1,4-dioxane and trimethylamine [27,31-33] afforded the corresponding *β*-lactam derivatives **3a-c** respectively in 60-70% yield. Similarly, cyclization of Schiff's bases with thioglycolic acid and 1,4-dioxane solvents [27,31-33] gave the corresponding thiazolidinones derivatives **4a-c** in 55-62% yield. The chemical structures of products **3a-c** and **4a-c** were determined based on ^{1}H and ^{13}C NMR, IR spectroscopy as well as mass spectrometry data.

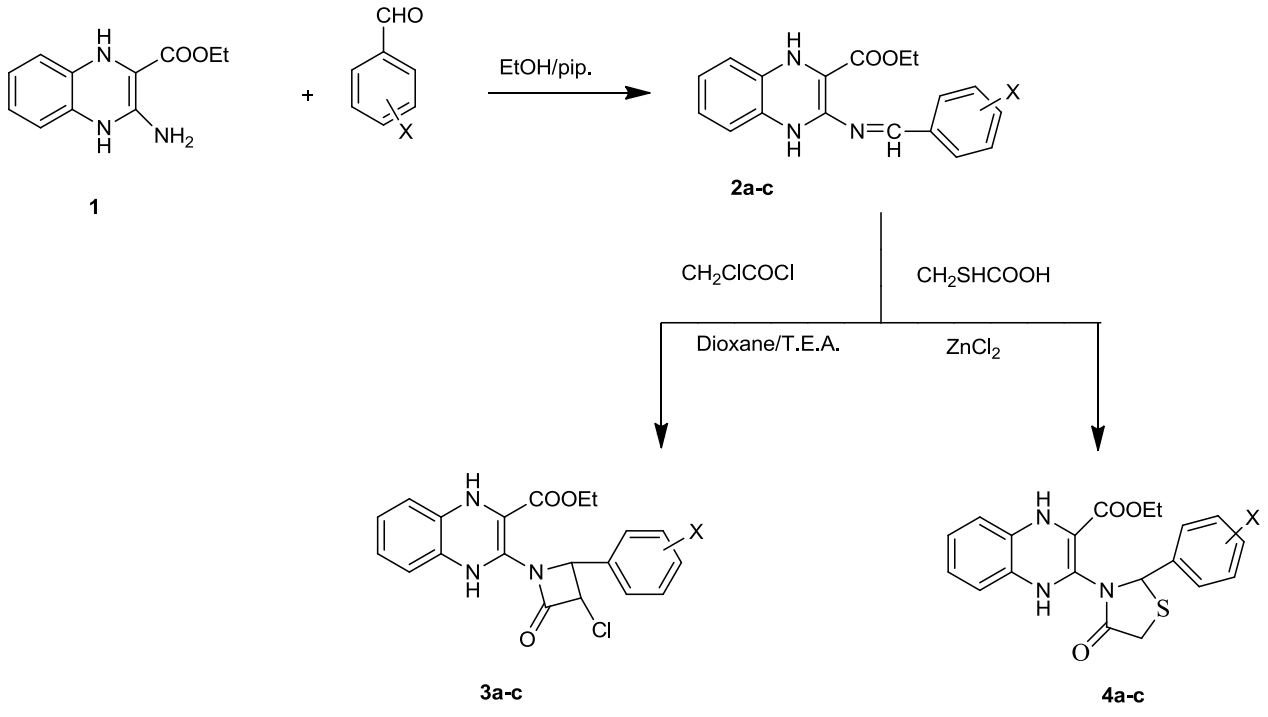

Scheme 1. Synthesis of the novel *β*-lactams (3a-c) and thiazolidinone derivatives (4a-c).

The IR spectra of compounds **3a-c** revealed a N-H stretching band at about 3100-3400 cm^{-1} and absorption bands at 1685-1690 cm^{-1} and 1730-1732 cm^{-1} corresponding to cyclic CO and CO ester, respectively. On the other hand, the IR spectrum of compounds **4a-c** exhibited absorption bands at 1760-1766 cm^{-1} corresponding to CO related to thiazolidinones. The ^1H NMR spectrum of compounds **3a-c** displayed a singlet resonate at 12.35 ppm assignable to N-H quinoxaline; the spectrum of compound **3c** showed a singlet at 3.56 ppm corresponding to (3H, for OCH_3). Moreover, the ^1H NMR spectrum of compounds **3a-c** exhibited a doublet at 5.2 ppm corresponding to -CH-N.

Antimicrobial activity

The synthesized compounds (**1**, **2a-c**, **3a-c** and **4a-c**) were evaluated for their antimicrobial activity against strains of gram-positive *Staphylococcus aureus*, gram-negative *Escherichia coli*, *Aspergillus flavus* and *Candida albicans* fungi. The initial screening results of *in vitro* antibacterial and antifungal activity are presented in Table 1. All tested compounds showed a comparatively promising activity towards gram-negative bacteria than gram-positive bacteria. Moreover, the highest activity of the designed compounds was recorded against the *Candia albicans* fungi. Thus, the obtained results show that compound **3b** exhibited the highest activity against *Escherichia coli* and *Staphylococcus aureus* bacteria. By comparing the *β*-lactam derivatives **3a-c** to their corresponding Schiff bases **2a-c**, the *β*-lactam derivatives exhibited better activity and higher growth inhibition for the tested strains including bacteria and fungi.

Structure-activity relationship studies were carried out to better understand the effect of benzene substitution operation on antimicrobial activity. Considering gram-negative bacteria (*Escherichia coli*) testing results, it is obvious that Schiff base **2b** and *β*-lactam derivative **3b** with electron-withdrawing chlorine atoms showed better antibacterial activity than all other tested compounds. Schiff base derivative **2a** without substituent on the benzene ring showed good antibacterial activity against *Escherichia coli*. It is worth noting that all thiazolidinones derivatives exhibited low activity against *Escherichia coli* compared to the Schiff base parents **2a-c**.

Besides, all compounds displaying an electron donating methoxy group on the benzene ring showed the lowest activity against gram-positive and gram-negative bacteria. It can be initially concluded that the presence of chlorine atom as a substituent on the benzene moiety withdraw electrons by induction and give electrons by resonance convey higher antibacterial and antifungal activity to Schiff's base **2b**, *β*-lactam **3b** and thiazolidinones derivatives **4b**. Whereas, the presence of the methoxy group as a substituent on the benzene ring (**2c**, **3c**, and **4c)** donates electrons by induction and reduces the antimicrobial activity of the synthesized compounds against the tested bacterial strains.

Molecular docking study

The most biologically active derivatives **3a-c** and **4a-c** were subjected to molecular docking study to predict their binding modes on a molecular level. Glucosamine-6-phosphate synthase enzyme (GlcN-6-P), a potential target for antibacterial and antifungal agents, was the enzyme of choice for performing the docking study.

Table 1

Antimicrobial evaluation of the new synthesized compounds[*].

Compound no.	*Bacteria*		*Fungi*	
	Staphylococcus aureus	*Escherichia coli*	*Aspergillus flavus*	*Candida albicans*
Control (DMSO)	0	0	0	0
Ampicillin	23	28	-	-
Amphotericin B	-	-	14	20
1	19	21	8	12
2a	20	23	9	13
2b	22	24	10	14
2c	18	20	8	11
3a	21	24	13	17
3b	25	26	15	22
3c	20	20	12	15
4a	19	17	11	12
4b	24	19	13	13
4c	18	16	11	10

[*]*Mean inhibition zone diameter (mm/mg sample) (n=3).*

The target derivatives were re-docked into the binding site of GlcN-6-P enzyme (PDB: ID 1gdo). To do so, first, glutamate was re-docked into GlcN-6-P with a root mean standard deviation (RMSD) of 1.25, the ligand showed score binding energy (S) of -15.11 kcal/mol and hydrogen bonding with Gly99, Trp74, Cys1, His86, Arg73, Thr76, Asp123 (Figure 1). The data of this study including the energy associated with intermolecular interactions (affinity in kcal/mol) of the target compounds **3a-c** and **4a-c** and hydrogen bonding interactions are presented in Table 2.

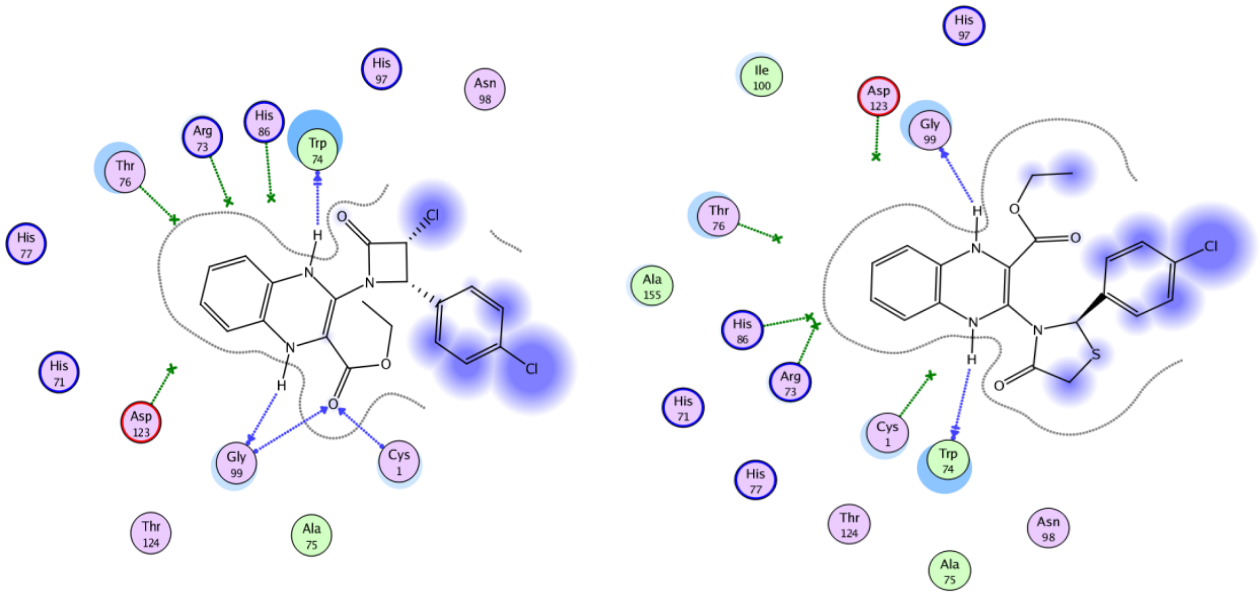

(a) *(b)*

Figure 1. The 2D predicted binding mode from docking simulation of compound 3b *(a)* and compound 4b *(b)* into the active site of GlcN-6-P synthase.

Table 2

Molecular modeling data for compounds 3a-c and 4a-c in the active site of glucosamine-6-phosphate synthase enzyme (PDB: ID 1gdo).

Compound	*Affinity, Kcal/mol*	*Number of hydrogen bonds*	*Distance from main residue, Å*		*Functional group*
3a	-16.67	4	Trp74	2.93	NH
			Gly99	2.12	NH
			Gly99	2.93	C=O
			Cys1	3.11	C=O
3b	-18.95	4	Trp74	2.95	NH
			Gly99	2.00	NH
			Gly99	2.89	C=O
			Cys1	3.16	C=O
3c	-16.00	4	Thr124	2.23	OCH_3
			Arg73	2.15	OCH_3
			His86	3.19	OCH_3
			Ser176	2.64	C=O
4a	-15.50	2	Thr76	2.99	NH
			Cys1	2.67	C=O
4b	-18.50	2	Thr76	3.12	NH
			Trp74	2.98	NH
4c	-13.22	1	Cys1	2.79	OCH_3

Continuation of Table 2

Compound	*Affinity, Kcal/mol*	*Number of hydrogen bonds*	*Distance from main residue, Å*		*Functional group*
Glutamate	-15.11	10	Gly99	2.02	C=O
			Trp74	2.06	CO-
			Cys1	2.54	CO-
			His86	1.77	CO-
			Arg73	2.70	CO-
			Arg73	3.05	C=O
			Thr76	2.70	C=O
			Asp123	3.05	NH
			Thr76	2.70	NH
			Gly99	3.07	NH

Docking results on the compounds **3a-c** and **4a-c** revealed moderate to strong binding affinity varying from -13.22 to -18.75 kJ/mol compared to -15.11 kJ/mol for the reference drug glutamate, which exhibited ten hydrogen-bonding interactions with the amino acid series Gly99, Trp74, Cys1, His86, Arg73, Thr76, Asp123, respectively (Table 2). Compound **3a** recorded the energy docking of -16.67 kcal/mol, and it showed four bonding as following: i) Trp74 with NH, ii) Gly99 with NH, iii) Gly99 with C=O, iv) Cys1 with C=O. Besides, compound **3b** registered a docking energy value of -18.95 kcal/mole and was found to perform four hydrogen-bonding interactions: i) Trp74 with NH, ii) Gly99 with NH, iii) Gly99 with C=O, iv) Cys1 with C=O. Moreover, the candidate **3c** recorded a docking energy value of -16.00 kcal/mol and four hydrogen-bonding interactions: i) Thr124 with OCH3, ii) Arg73 with OCH3, iii) His86 with OCH3, and iv) Ser176 with C=O. In addition, the target compound **4a** displayed two hydrogen bonds with Thr76 and Cys1 *via* binding with NH and C=O groups. On the other hand, the candidate **4b** showed a high docking energy value of -18.50 kcal/mol and two hydrogen-bonding interactions with Thr76 and Trp74. Finally, compound **4c** demonstrated the least docking energy score of -13.22 kcal/mol with only one hydrogen bonding interaction with Cys1 amino acid.

It can be concluded that the most active compounds are **3b** and **4b** since they showed comparable binding affinity scores as that of glutamate. These results are considered in agreement with the experimental results.

Conclusions

Substituted *β*-lactams **3a-c** and thiazolidinone derivatives **4a-c** were successfully synthesized from the reaction of new Schiff's bases **2a-c** with chloroacetyl chloride and thioglycolic acid. All reactions were prepared with satisfactory yields and spectral data (IR, ^{1}H and ^{13}C NMR) of the obtained compounds (**3a-c**, **4a-c**) were in full agreement with the proposed structures.

All newly synthesized compounds were evaluated *in vitro* for their antimicrobial activity against gram-positive and gram-negative bacteria and fungi. All compounds displayed moderate to excellent antimicrobial activity against the tested strains. The biological screening proved compound **3b** to be the most active compound against all tested bacteria and fungi. Furthermore, compound **4b** showed good antibacterial activity when tested against *Staphylococcus aureus* bacteria. This behaviour was ascribed to the presence of chlorine withdrawing atom as a substituent on the benzene moiety.

It was found that all compounds carrying an electrodonating methoxy group as a substituent on the benzene ring displayed the least biological activity. Furthermore, the results from the biological testing were in agreement with the molecular docking studies. Therefore, compounds **3b** and **4b** represent promising candidates as antibacterial and antifungal agents that would deserve further investigations.

References

1. Aranda, M.T.; Perez-Faginas, P.; Gonzalez-Muniz, R. An update on the synthesis of *β*-lactams. Current Organic Synthesis, 2009, 6(3), pp. 325-341. DOI: 10.2174/157017909788921899
2. Abraham, D.J. Burger's medicinal chemistry and drug discovery. 6th ed. Richmond: Wiley-Interscience, John Wiley and Sons, 2003, 6416 p. DOI: 10.1002/0471266949
3. Coleman, K. Diazabicyclooctanes (DBOs): a potent new class of non-*β*-lactam *β*-lactamase inhibitors. Current Opinion in Microbiology, 2011, 14(5), pp. 550-555. DOI: https://doi.org/10.1016/j.mib.2011.07.026
4. Tipper, D.J; Strominger, J.L. Mechanism of action of penicillins: a proposal based on their structural

similarity to acyl-D-alanyl-D-alanine. PNAS (Proceedings of the National Academy of Sciences of the United States of America), 1965, 54(4), pp. 1133-1141.
DOI: https://doi.org/10.1073/pnas.54.4.1133

5. Worthington, R.J; Melander, C. Overcoming resistance to *β*-lactam antibiotics. The Journal of Organic Chemistry, 2013, 78(9), pp. 4207-4213. DOI: https://doi.org/10.1021/jo400236f
6. Lee, M.; Hesek, D.; Blázquez, B.; Lastochkin, E.; Boggess, B.; Fisher, J.F.; Mobashery, S. Catalytic spectrum of the penicillin-binding protein 4 of *Pseudomonas aeruginosa*, a nexus for the induction of *β*-lactam antibiotic resistance. Journal of the American Chemical Society, 2015, 137(1), pp. 190-200.
DOI: https://doi.org/10.1021/ja5111706
7. Geesala, R.; Gangasani, J.K.; Budde, M.; Balasubramanian, S.; Vaidya, J.R.; Das, A. 2-Azetidinones: Synthesis and biological evaluation as potential anti-breast cancer agents. European Journal of Medicinal Chemistry, 2016, 124, pp. 544-558.
DOI: https://doi.org/10.1016/j.ejmech.2016.08.041
8. Galletti, P.; Soldati, R.; Pori, M.; Durso, M.; Tolomelli, A.; Gentilucci, L.; Dattoli, S.D.; Baiula, M.; Spampinato, S.; Giacomini, D. Targeting integrins $\alpha_v\beta_3$ and $\alpha_5\beta_1$ with new *β*-lactam derivatives. European Journal of Medicinal Chemistry, 2014, 83, pp. 284-293.
DOI: https://doi.org/10.1016/j.ejmech.2014.06.041
9. D'hooghe, M.; Mollet, K.; De Vreese, R.; Jonckers, T.H.M.; Dams, G.; De Kimpe, N. Design, synthesis, and antiviral evaluation of purine-*β*-lactam and purine-aminopropanol hybrids. Journal of Medicinal Chemistry, 2012, 55(11), pp. 5637-5641.
DOI: https://doi.org/10.1021/jm300383k
10. Hites, M.; Taccone, F.S.; Wolff, F.; Maillart, E.; Beumier, M.; Surin, R.; Cotton, F.; Jacobs, F. Broad-spectrum β-lactams in obese non-critically ill patients. Nutrition & diabetes, 2014, 4, e119, pp. 1-7.
DOI: https://doi.org/10.1038/nutd.2014.15
11. Luna-Herrera, J.; Lara-Ramirez, E.E.; Munoz-Duarte, A.R.; Olazaran, F.E.; Chan-Bacab, M.J.; Moo-Puc, R.; Perez-Vazquez, A.M.; Morales-Reyes, C.M.; Rivera, G. *In vitro* and *in silico* analysis of *β*-lactam derivatives as antimycobacterial agents. Letters in Drug Design & Discovery, 2017, 14(7), pp. 782-786.
DOI: 10.2174/1570180814666170106111316
12. Jarrahpour, A.; Shirvani, P.; Sinou, V.; Latour, C.; Brunel, J.M. Synthesis and biological evaluation of some new β-lactam-triazole hybrids. Medicinal Chemistry Research, 2016, 25(1), pp. 149-162. DOI: https://doi.org/10.1007/s00044-015-1474-x
13. Cogo, J.; Kaplum, V.; Sangi, D.P.; Ueda-Nakamura, T.; Correa, A.G.; Nakamura, C.V. Synthesis and biological evaluation of novel 2,3-disubstituted quinoxaline derivatives as antileishmanial and antitrypanosomal agents. European Journal of Medicinal Chemistry, 2015, 90, pp. 107-123.
DOI: https://doi.org/10.1016/j.ejmech.2014.11.018
14. Balsalobre, L.C.; Dropa, M.; Matté, M.H. An overview of antimicrobial resistance and its public health significance. Brazilian Journal of Microbiology, 2014, 45(1), pp. 1-5. DOI: https://doi.org/10.1590/S1517-83822014005000033
15. El Azab, I.H.; Elkanzi, N.A.A.; Gobouri, A.A. Design and synthesis of some new quinoxaline-based heterocycles. Journal of Heterocyclic Chemistry, 2018, 55(1), pp. 65-76.
DOI: 10.1002/jhet.2978
16. Tariq, S.; Somakala, K.; Amir, M. Quinoxaline: An insight into the recent pharmacological advances. European Journal of Medicinal Chemistry, 2018, 143, pp. 542-557.
DOI: https://doi.org/10.1016/j.ejmech.2017.11.064
17. El-Tombary, A.A.; El-Hawash, S.A.M. Synthesis, antioxidant, anticancer and antiviral activities of novel quinoxaline hydrazone derivatives and their acyclic C-nucleosides. Medicinal Chemistry, 2014, 10(5), pp. 521-532.
DOI: 10.2174/1573406411309666069
18. Singh, D.P.; Deivedi, S.K.; Hashim, S.R.; Singhal, R.G. Synthesis and antimicrobial activity of some new quinoxaline derivatives. Pharmaceuticals, 2010, 3(8), pp. 2416-2425.
DOI: https://doi.org/10.3390/ph3082416
19. Ishikawa, H.; Sugiyama, T.; Kurita, K.; Yokoyama, A. Synthesis and antimicrobial activity of 2,3-bis(bromomethyl)quinoxaline derivatives. Bioorganic Chemistry, 2012, 41-42, pp. 1-5.
DOI: https://doi.org/10.1016/j.bioorg.2011.12.002
20. Burguete, A.; Pontiki, E.; Hadjipavlou-Litina, D.; Ancizu, S.; Villar, R.; Solano, B.; Moreno, E.; Torres, E.; Pérez, S.; Aldana, I.; Monge, A. Synthesis and biological evaluation of new quinoxaline derivatives as antioxidant and anti-inflammatory agents. Chemical Biology & Drug Design, 2011, 77, pp. 255-267.
DOI: 10.1111/j.1747-0285.2011.01076.x
21. Pinheiro, A.C.; Mendonça Nogueira, T.C.; de Souza, M.V.N. Quinoxaline nucleus: a promising scaffold in anti-cancer drug discovery. Anti-Cancer Agents in Medicinal Chemistry, 2016, 16(10), pp. 1339-1352.
DOI: 10.2174/1871520616666160622090839
22. Wang, T.; Tang, Y.; Yang, Y.; An, Q.; Sang, Z.; Yang, T.; Liu, P.; Zhang, T.; Deng, Y.; Luo, Y. Discovery of novel anti-tuberculosis agents with pyrrolo[1,2-a]quinoxaline-based scaffold. Bioorganic & Medicinal Chemistry Letters, 2018, 28(11), pp. 2084-2090.
DOI: https://doi.org/10.1016/j.bmcl.2018.04.043
23. Bush, K.; Jacoby, G.A. Updated functional classification of *β*-lactamases. Antimicrobial Agents and Chemotherapy, 2010, 54(3), pp. 969-976.
DOI: 10.1128/AAC.01009-09
24. Hujer, A.M.; Kania, M.; Gerken, T.; Anderson, V.E.; Buynak, J.D.; Ge, X.; Caspers, P.;

Page, M.G.P.; Rice, L.B.; Bonomo, R.A. Structure-activity relationships of different *β*-lactam antibiotics against a soluble form of *Enterococcus faecium* pbp5, a type II bacterial transpeptidase. Antimicrobial Agents and Chemotherapy. 2005, 49(2), pp. 612-618. DOI: 10.1128/AAC.49.2.612-618.2005

25. Konaklieva, M.I. Molecular targets of *β*-lactam-based antimicrobials: Beyond the usual suspects. Antibiotics. 2014, 3(2), pp. 128-142. DOI: https://doi.org/10.3390/antibiotics3020128
26. Turan, B.; Şendil, K.; Şengül, E.; Gultekin, M.S.; Taslimi, P.; Gulcin, İ.; Supuran, C.T. The synthesis of some β-lactams and investigation of their metal-chelating activity, carbonic anhydrase and acetylcholinesterase inhibition profiles. Journal of Enzyme Inhibition and Medicinal Chemistry, 2016, 31(sup1), pp. 79-88. DOI: https://doi.org/10.3109/14756366.2016.1170014
27. Elkanzi, N.A.A. Synthesis of some new spiro *β*-lactams and thiazolidinones compounds containing sulfur incorporating quinon compounds. International Journal of Organic Chemistry, 2012, 2(4), pp. 352-361. DOI: 10.4236/ijoc.2012.24048
28. El-Kanzi, N.A.A.; Khalafallah, A.K.; Younis, M. Effect of iodine on the antimicrobial activity of new spiro and isolated *β*-lactam thiazolidinone derivatives. Phosphorus, Sulfur, and Silicon and the Related Elements, 2007, 182(5), pp. 1163-1181. DOI: https://doi.org/10.1080/10426500601149929
29. Komykhov, S.A.; Ostras, K.S.; Kostanyan, A.R.; Desenko, S.M.; Orlov, V.D.; Meier, H. The reaction of amino-imidazoles, -pyrazoles and -triazoles with *α*,*β*-unsaturated nitriles. Journal of Heterocyclic Chemistry, 2005, 42(6), pp. 1111-1116. DOI: https://doi.org/10.1002/jhet.5570420612
30. Isupov, M.N.; Obmolova, G.; Butterworth, S.; Badet-Denisot, M.A.; Badet, B.; Polikarpov, I.; Littlechild, J.A.; Teplyakov, A. Substrate binding is required for assembly of the active conformation of the catalytic site in Ntn amidotransferases: evidence from the 1.8 A crystal structure of the glutaminase domain of glucosamine 6-phosphate synthase. Structure, 1996, 4(7), pp. 801-810. DOI: https://doi.org/10.1016/s0969-2126(96)00087-1
31. Elkanzi, N.A.A. Synthesis of some new isolated/spiro *β*-lactam and thiazolidinone incorporating fused thieno pyrimidine derivatives. Journal of Applied Chemistry, 2012, 1(1), pp. 1-12. DOI: https://doi.org/10.9790/5736-0110112
32. Elkanzi, N.A.A. Synthesis of new class of (*β*-lactam, thiazolidinone) derivatives. Journal of Applied Chemistry, 2012, 1(1), pp. 18-30. DOI: https://doi.org/10.9790/5736-0111830
33. Patel, H.; Mishra, L.; Noolvi, M.; Karpoormath, R.; Cameotra, S.S. Synthesis, *in vitro* evaluation, and molecular docking studies of azetidinones and thiazolidinones of 2-amino-5-cyclopropyl-1,3,4-thiadiazole as antibacterial agents. Archiv der Pharmazie – Chemistry in Life Sciences, 2014, 347(9), pp. 668-684. DOI: https://doi.org/10.1002/ardp.201400140

CHEMISTRY JOURNAL OF MOLDOVA. General, Industrial and Ecological Chemistry. 2020, 15(1), 95-102
ISSN (p) 1857-1727 ISSN (e) 2345-1688
http://cjm.asm.md
http://dx.doi.org/10.19261/cjm.2019.694

CHROMATOGRAPHIC ANALYSIS OF ORCHID EXTRACTS AND QUANTUM CHEMICAL CALCULATIONS OF INDIVIDUAL COMPONENTS INTERACTION WITH SILICA

Olga Kazakova [a*], Roman Ivannikov [b], Iryna Laguta [a], Oksana Stavinskaya [a], Viktor Anishchenko [c], Olga Severinovska [a], Ludmila Buyun [b]

[a]*Chuiko Institute of Surface Chemistry of National Academy of Sciences of Ukraine, 17, General Naumov str., Kiev 03164, Ukraine*
[b]*M.M. Gryshko National Botanic Garden of National Academy of Sciences of Ukraine, 1, Timiryazevska str., Kiev 01014, Ukraine*
[c]*L.M. Litvinenko Institute of Physical-Organic Chemistry and Coal Chemistry of National Academy of Sciences of Ukraine, 50, Kharkivs'ke hwy., Kiev 02160, Ukraine*
[*]*e-mail: kazakova_olga@ukr.net*

Abstract. The aim of the work was to identify the main components of orchid extracts and to study their interaction with silica. Composition of sixteen orchid extracts was investigated by means of high performance liquid chromatography and laser desorption/ionization mass spectrometry; as it was shown in this study, flavonoids and phenolic acids were the main bioactive compounds available in the extracts. The interaction between various phenols and silica silanol groups was studied by quantum chemical method. Results show that the strength of interaction of phenols with silica increased in the following order: ferullic, feruloylquinic and fertaric acids< kaempferol, apingenin<< chlorogenic and caffeic acids, rhamnetin, quercetin, luteolin, epicatechin gallate. The common feature of compounds characterized by the strongest interaction with silanol groups is the presence of a phenol ring with two neighbouring hydroxyl groups. The hydrogen bonds formed between these groups and silanol groups are much shorter (about 0.17 nm) than those formed by other hydroxyl groups of phenols (up to 0.28 nm).

Keywords: orchid extract, phenolic compound, fumed silica, quantum chemical calculation.

Received: 22 April 2020/ Revised final: 23 May 2020/ Accepted: 27 May 2020

Introduction

The plants are known to be a valuable source of low-toxicity biologically active substances [1-3]. Among these substances, phenolic compounds possessing antioxidant or antimicrobial properties appear to be particularly attractive for practical application [4,5]. The orchid plants are used in traditional medicine of many countries and are known to contain high amounts of phenolic compounds [6-8]. It was reported that the content of phenols in orchids reached up to 12 mg of gallic acid equivalent per 1 g of dry weight, with the composition of the extracts being dependent on the climatic and external conditions of plants growing [9,10]. The majority of orchids were found to contain a significant amount of phenols such as hydroxybenzoic acids, hydroxycinnamic acids and flavonoids in the glycoside form [6].

Nowadays, half of all medical drugs, dietary supplements and herbal medicines are produced from natural sources, with phenols being the main active components of most of these drugs [11,12]. However, direct oral use of phenolic compounds has some disadvantages. Due to low solubility of phenols in water, as well as their poor gastrointestinal stability and absorbency, the compounds were shown to have low bioeffectiveness [13,14]. To improve the efficiency of plant-derived drugs, a number of drug delivery systems were developed [14-17], with fumed silica being one of the possible auxiliary ingredients used as carrier for plant extracts and plant-derived bioactive molecules [18,19]. Immobilization of biologically active substances on the silica surface offers the possibility of introducing hydrophobic compounds in aqueous solutions and hydrophilic substances in lipophilic media [20]. Inclusion of bioactive compounds in silica-based composites improves the compounds storage stability as compared to pure extracts/substances [19].

In some cases, the presence of silica can decelerate the release of the drug into solution, thus providing bioactive substances with elongated effect [18,20]. The properties of composites consisting of bioactive compounds and fumed silica apparently depend on the strength of interaction of compounds with silica.

The aim of this study was to identify the main components of the extracts from a number of orchid plants and to study their interaction with silica surface groups by using the quantum chemical method. The data on the interaction of various components from the orchids extracts with silica surface can be useful for preparation of the extracts - silica composites, possessing desirable properties.

Experimental

Materials

All reagents were obtained from commercial sources (Merck, Germany) and used without further purification.

Orchids of *Dendrobium* and *Anoectochilus* families were grown in M.M. Gryshko National Botanic Garden of National Academy of Sciences of Ukraine under greenhouse and *in vitro* conditions. In order to grow plants *in vitro*, sterilized seeds were placed in glass flasks containing Murashige and Skoog (MS) basal medium [21] and exposed to artificial light for 16 hours per day. The list of plants used for the extracts preparation is given in Table 1.

Table 1

The list of orchids used for extracts preparation.

The name of taxon	*Growing conditions*
Dendrobium chrysanthum Wall. Ex Lindl.	greenhouse, *in vitro*
Dendrobium draconis Rchb.f.	greenhouse, *in vitro*
Dendrobium henryi Schltr.	*in vitro*
Dendrobium linguella Rchb.f.	greenhouse, *in vitro*
Dendrobium lomatochilum Seidenf.	greenhouse, *in vitro*
Dendrobium moniliforme (L.) Sw.	greenhouse, *in vitro*
Dendrobium nobile Lindl.	greenhouse, *in vitro*
Dendrobium parishii Rchb.f.	greenhouse
Anoectochilus roxburghii (Wall.) Lindl.	*in vitro*
Anoectochilus formosanus Hayata	*in vitro*

Extracts preparation procedure: 100 mL of 70% ethanol were added to 1 g of finely chopped leaves, after that the mixtures were placed into steam bath for 30 min. After cooling, the extracts were adjusted to the initial volume and filtered.

Methods

High performance liquid chromatography (HPLC) was used for the identification and quantification of bioactive substances available in the extracts. The analysis was performed using a modular HPLC system, Agilent 1100 series (Germany) consisting of quaternary pump, autosampler, column thermostat, DAD detector. HPLC separations were achieved by using a reverse-phase Zorbax Eclipse PLUS C18 column 2.1×150 mm, 3.5 μm. Column temperature was controlled at 20°C.

Gradient elution was employed with a mobile phase consisting of 50 mM H_3PO_4 (solution A) and methanol (solution B) as follows: isocratic elution 89% A÷11% B with flow rate 0.2 mL/min, 0÷3 min; linear gradient from 89% A÷11% B to 34% A÷66% B with flow rate 0.2 mL/min, 3÷33 min; linear gradient from 34% A÷66% B to 0% A÷100% B with flow rate 0.2 mL/min, 33÷53 min; isocratic elution 0% A÷100% B with linear gradient of flow rate from 0.2 to 0.5 mL/min and column heating to 40°C, 53÷60 min; isocratic elution 0% A÷100% B with linear gradient of flow rate from 0.5 to 1.0 mL/min, 60÷70 min.

The analytical data were evaluated using the HP 3D Chem Station software. Wavelengths used for the identification of plant secondary metabolites, with the diode-array detector were set at 206 nm for hydroxybenzoic acids; 300 nm for hydroxycinnamic acids; 350 nm for flavonoids and their glycosides. For more reliable identification of the extracts components, their spectra and retention time were compared with those of the standard compounds: gallic, salicylic, vanillic, *p*-hydroxybenzoic, protocatechuic, syringic, *α*-resorcylic, *β*-resorcylic, *γ*-resorcylic, cinnamic, *p*-coumaric, *m*-coumaric, *o*-coumaric, caffeic, ferulic, sinapic, feruloylquinic, chlorogenic, fertaric acids, apingenin, myricetin, quercetin, quercetin 3-*O*-glucoside, kaempferol, kaempferol 3-*O*-arabinoside, kaempferol 3-*O*-glucoside. To estimate the quantity of compounds from various classes, the areas of appropriate signals were compared with those of reference substances (quercetin-3-arabinoside for flavonoids, caffeic acid for hydroxycinnamic acids and gallic acid for hydroxybenzoic acids).

Qualitative analysis of extracts composition was also performed by *laser desorption/ionization time-of-flight mass spectrometry (LDI-MS)*. Mass spectra were recorded in the positive and negative ion extraction mode on an Autoflex II mass

spectrometer (Bruker Daltonics Inc., Germany) equipped with a nitrogen laser (337 nm). The samples were ionized in the pulse mode: 3 ns pulse length, 20 Hz frequency, 65 mJ maximum energy. Spectra were recorded in the reflection mode using a delayed extraction of 20 ns and accelerating voltage 20 keV.

Quantum chemical calculations for individual components of the extracts and their complexes with silica clusters consisting of 12 $SiO_{4/2}$ tetrahedrons were carried out using density functional theory (DFT) method with hybrid functional ωB97X-D [22] (labelled as wB97XD in Gaussian 09) with the 6-31G (d,p) basis set and the Gaussian 09 program suit [23]. Geometry was optimized using the PM6 method. The solvation effects were analysed using the solvation method SMD [24] implemented in Gaussian 09.

Results and discussion

Chromatographic analysis

The chromatograms obtained by HPLC for several orchids plant extracts are presented in Figures 1-3; Table 2 gives the classes of the identified compounds. Results show that the most abundant phenol compounds in the extracts are the representatives of three classes: flavonoids and their derivatives; hydroxycinnamic acids and their derivatives; simple phenols, tannins, hydroxybenzoic acids and their derivatives.

The flavonoids are represented mainly by flavonol *O*-glycosides, flavones *O*-glycosides and flavones *C*-glycosides, although other flavonoids of non-identified structure are also available in the extracts. The total amount of flavonoids, hydroxycinnamic and hydroxybenzoic acids in various orchids was found to be in the range of 0.30÷2.30, 0.01÷0.30, 0.01÷0.10 mg per 1 g of dried leaves, respectively. In general, the plants grown under greenhouse condition are characterized by higher total phenol content than the plants grown *in vitro* [25]. Nevertheless, such plants as *Dendrobium parishii* Rchb.f., *Anoectochilus formosanus* Hayata, *Anoectochilus roxburghii* (Wall.) Lindl. were found to have very high phenol content (up to 1.60 mg/g) although being grown *in vitro*.

A more detailed study of the substances partitioned during the HPLC procedure and the comparison of their retention times and UV-Vis spectra with the standard compounds allowed us to conclude that the majority of the extracts contain feruloylquinic, chlorogenic, sinapic and fertaric acids. All the extracts were found to contain a number of flavones and flavonols in *O*- and *C*-glycoside form, with quercetin, kaempferol and apingenin being the most abundant aglycons. Several extracts appear to include also caffeic acid, epicatechin gallate, rhamnetin and/or the derivatives of these compounds. Orchids usually contain as well a significant amount of various hydroxybenzoic acids (*i.e.* gallic, protocatechuic, syringic, ellagic acids) [9,26]; the obtained HPLC data can confirm only the presence of hydroxybenzoic acids derivatives.

Table 2

Classes of compounds identified in the extracts by HPLC.

Legend	*Class of compounds*
Alk	Indole alkaloids
AC	Anthocyanins
AP	Anthracene and phenanthrene derivatives
B	Hydroxybenzoic acids and their derivatives, simple phenols and tannins
C	Hydroxycinnamic acids and their derivatives
Co	Coumarins
D	Catechins
F	Flavonoids of non-identified structure
F1	Flavonol *O*-glycosides
F2	Flavon *O*-glycosides
FC	Flavon *C*-glycosides
T	Terpenoids

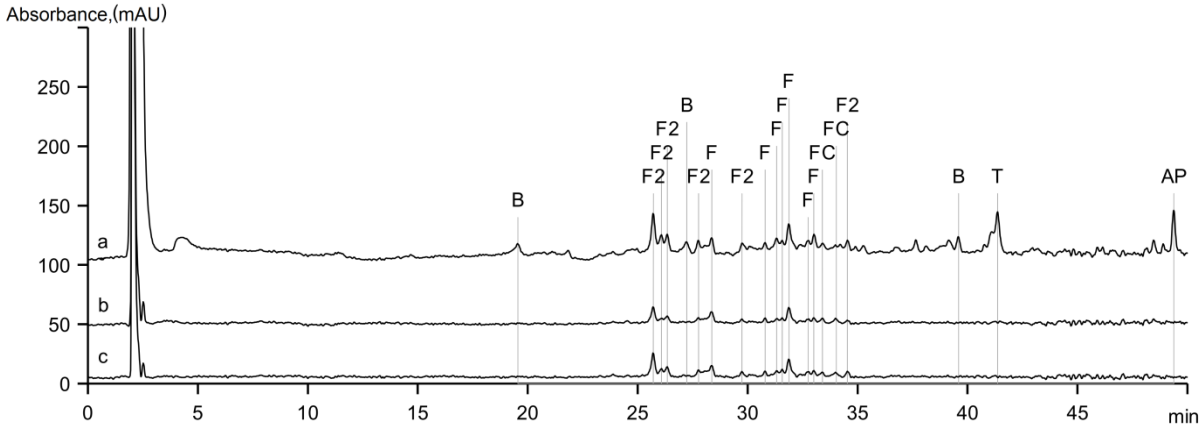

Figure 1. Chromatograms of the *Dendrobium nobile* Lindl. extract recorded at: 206 nm *(a)*, 300 nm *(b)*, 350 nm *(c)*.

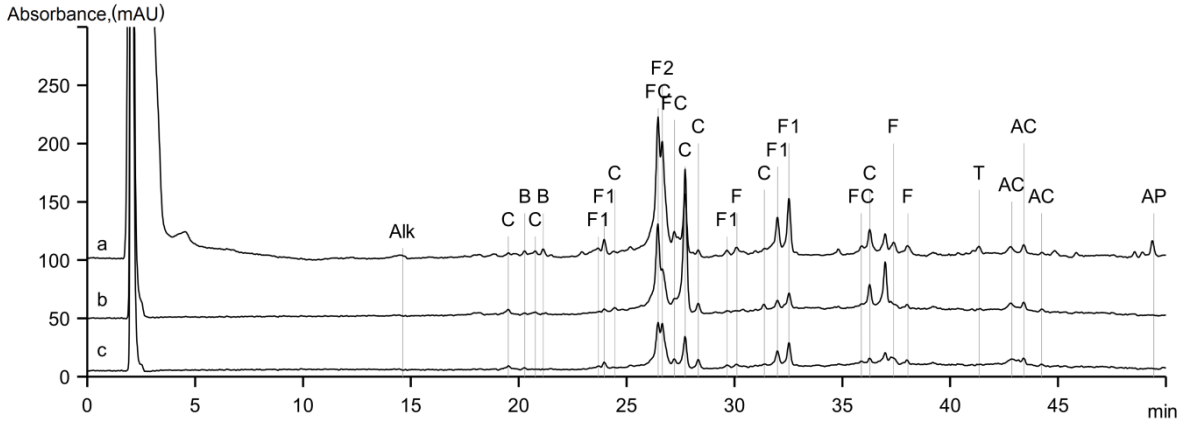

Figure 2. Chromatograms of the *Anoectochilus formosanus* Hayata extract recorded at: 206 nm *(a)*, 300 nm *(b)*, 350 nm *(c)*.

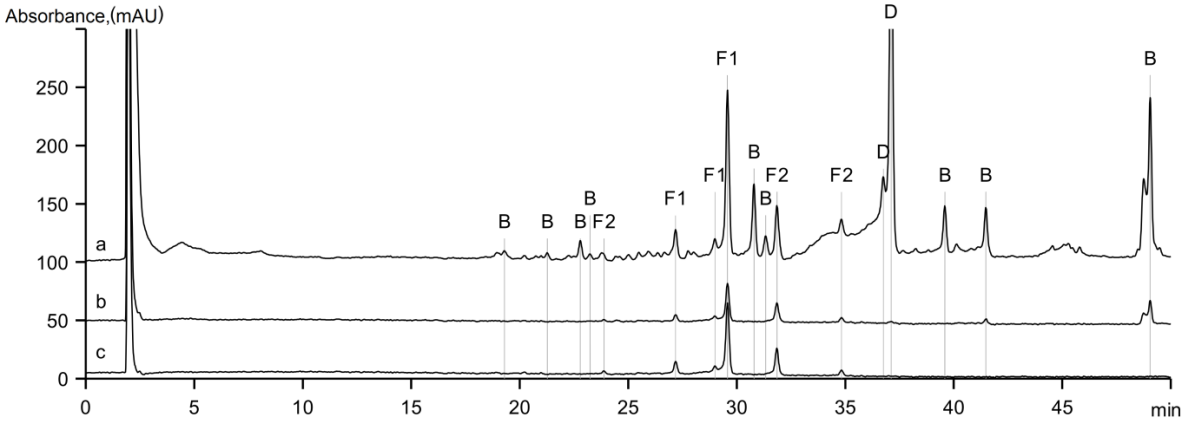

Figure 3. Chromatograms of the *Dendrobium chrysanthum* Wall. ex Lindl. extract recorded at: 206 nm *(a)*, 300 nm *(b)*, 350 nm *(c)*.

The mass spectroscopy data (Table 3) indicate that the extracts do contain hydroxybenzoic acids (confirmed by the signals at m/z 169 and 171 corresponding to $[M-H]^-$ and $[M+H]^+$ ions of gallic or phloroglucinic acids). The data also confirm the presence of hydrocinnamic acids or hydrocinnamic acids derivatives (the signals at m/z of 165, 225, 327, 339, 355 and 369 of $[M+H]^+$ molecular ions for coumaric, sinapic, fertaric, coumaroylquinic, chlorogenic and feruloylquinic acids). Several spectra showed peaks at m/z of 305 and 441 corresponding to $[M+H]^+$ ion of moscatilin and $[M-H]^-$ ion of epicatechin gallate, respectively. Spectra also included signals of a number of flavones or flavones derivatives (luteolin, nobiletin, apigenin and derivatives) and flavonols or flavonols derivatives (quercetin, rhamnetin, rhamnazin, kaempferol and derivatives).

Quantum chemical calculations

Taking into account these HPLC and LDI-MS results as well as the literature data on the orchids plants extracts composition [6], the following representatives of phenols were chosen as model compounds for the quantum-chemical study (Table 4).

All the studied compounds were found to interact with silica mainly due to the formation of hydrogen bonds between hydroxyl groups of the phenols and silanol groups of the surface. For each of the phenols, it was found that hydroxyl groups of the phenol ring formed more thermodynamically favourable complexes with silanols than others hydroxyl groups of the compounds. In the case of flavonoids, the hydroxyl groups of side B-ring form stronger complexes than hydroxyl groups of conjugated A- and C- rings. The optimized configurations of the H-bonded adsorption complexes on silica surface for various components of the extracts are given in Figure S1 (see Supplementary Material). The corresponding values of the Gibbs free energy of adsorption (ΔG) and the length of H-bonds ($R_{H\text{-}bond}$) are presented in Table 4.

Table 3

Main phenolic compounds identified in the extracts by LDI-MS.

Class of compounds	*Identified compound and its molecular mass, Da*	*Ions, m/z*
Hydroxybenzoic acids and their derivatives	Gallic/Phloroglucinic acid, 170	$[M+H]^+$, 171 $[M-H]^-$, 169
Hydrocinnamic acids and their derivatives	Coumaric acid, 164	$[M+H]^+$, 165
	Sinapic acid, 224	$[M+H]^+$, 225
	Fertaric acid, 326	$[M+H]^+$, 327
	Coumaroylquinic acid, 338	$[M+H]^+$, 339
	Chlorogenic acid, 354	$[M+H]^+$, 355; $[M-H]^-$, 353; $[M-H-\text{caffeoyl}-H_2O]^-$, 173
	Feruloylquinic acid, 368	$[M+H]^+$, 369; $[M+H-192]^+$, 177
Flavones and their derivatives	Flavon, 222	$[M+H]^+$, 223
	Luteolin, 286	$[M+H]^+$, 287; $[M+H-H_2O-2CO]^+$, 213
	Nobiletin, 402	$[M+H]^+$,403
	Apigenin-7-*O*-glucoside, 432	$[M-H]^-$, 431
Flavonols and their derivatives	Quercetin, 302	$[M+H]^+$, 303; $[M+H-H_2O-3CO]^+$, 201
	Rhamnetin / Isorhamnetin, 316	$[M-H]^-$, 315
	Rhamnazin, 330	$[M+H]^+$, 331
	8-Methoxyquercetin, 332	$[M+H]^+$, 333
	Kaempferol-3-*O*-rhamnoside, 432	$[M-H]^-$, 431
Other phenols	Moscatilin (dendrophenol), 304	$[M+H]^+$, 305
	Epicatechin gallate, 442	$[M-H]^-$, 441

Table 4

Chemical structure of the phenolic compounds, energetic and structural parameters of the most favourable adsorption complexes of the phenols on silica surface.

Class of compounds	*Compound*	*Chemical structure*	*-ΔG, kJ/mol*	$R_{H\text{-}bonds}$, *nm*
Hydroxybenzoic acids and their derivatives	Gallic acid	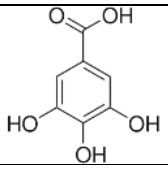	36	0.173, 0.186
Hydroxycinnamic acids and their derivatives	Caffeic acid	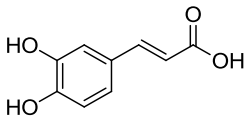	46	0.176, 0.177
	Sinapic acid	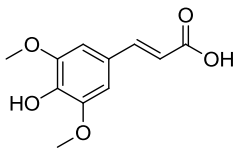	23	0.176
	Ferulic acid	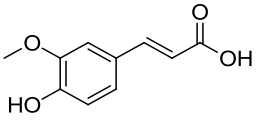	6	0.277
	Chlorogenic acid	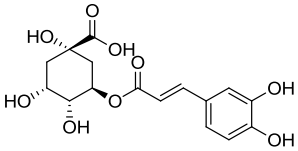	43	0.176, 0.176

Continuation of Table 4

Class of compounds	*Compound*	*Chemical structure*	*-ΔG, kJ/mol*	*$R_{H\text{-}bonds}$, nm*
Hydroxycinnamic acids and their derivatives	Feruloylquinic acid	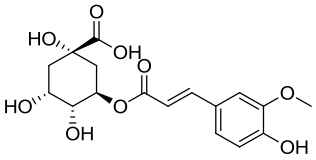	12	0.283
	Fertaric acid	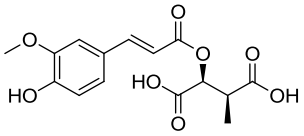	14	0.283
Flavones and their derivatives	Apigenin-8-*C*-glucoside	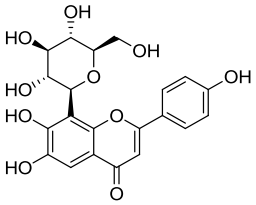	21	0.174, 0.261
	Luteolin	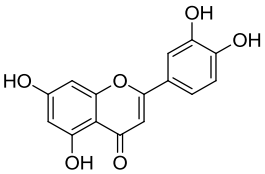	46	0.176, 0.177
Flavonols and their derivatives	Kaempferol-3-*O*-rhamnoside	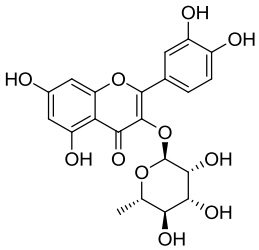	18	0.242, 0.242
	Quercetin	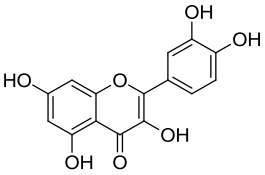	46	0.176, 0.177
	Quercetin-3-*O*-glucoside	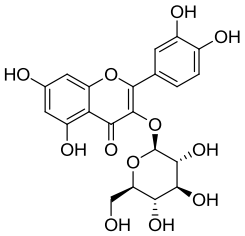	45	0.176, 0.176
	Rhamnetin	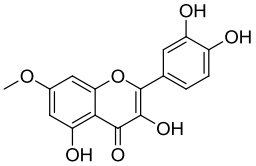	41	0.176, 0.177
Other phenols	Epicatechin gallate	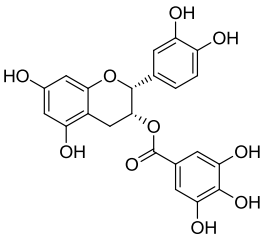	54	0.175, 0.204

Results of this study show that various phenols significantly differ from each other by their interaction with silica. The weakest interaction with silica surface is observed for ferullic, feruloylquinic and fertaric acids (Gibbs free energy ΔG= -6÷14 kJ/mol). These compounds form a single bond with surface silanols with the bond length of 0.277÷0.283 nm. Flavonoids apingenin and kaempferol interact with silica through two H-bonds and are characterized by the higher ΔG values (-18÷21 kJ/mol). Such compounds as caffeic and chlorogenic acids, quercetin, rhamnetin, luteolin, epicatechin gallate were found to have the strongest interaction with silanol groups, with ΔG and $R_{H\text{-}bond}$ values being in the range of -41÷54 kJ/mol and 0.176÷0.204 nm, respectively. The common feature of the structure of these compounds is the presence of two neighbouring hydroxyl groups in the phenol ring of hydroxycinnamic acids or in B-ring of flavonoids. Other hydroxyl groups of the phenols were found to form longer and weaker H-bonds.

For various phenols, the charges on O- and H-atoms participating in the formation of H-bonds with silanol groups did not significantly differ from each other. Thus, the steric effects seem to be the main factor affecting the interaction of various phenols with silica surface.

As it was mentioned above, flavonoids are usually available in plants in the glycoside form. The ΔG and $R_{H\text{-}bond}$ data for two variants of adsorption of kaempferol glycoside on silica surface (*via* aglycon and *via* glycoside) show that the silica-aglycon interaction is more favourable (ΔG= -18 kJ/mol) than the silica-glycoside interaction (ΔG= -4 kJ/mol). For adsorption of quercetin and quercetin-3-*O*-glucoside, the appropriate ΔG and $R_{H\text{-}bond}$ values are close to each other, that is, the presence of glycoside do not strongly affect the silica-aglycon interaction.

Conclusions

Composition of sixteen plant extracts from orchid leaves was investigated by means of high performance liquid chromatography and laser desorption / ionization mass spectrometry methods. Hydroxycinnamic and hydroxybenzoic acids, as well as flavonoids in *O*- and *C*- glycosides forms were found to be the main groups of bioactive compounds of the extracts. The most common substances found in the extracts included feruloylquinic, chlorogenic, sinapic and fertaric acids and quercetin, kaempferol and apingenin in the glycoside form, while several extracts also contained gallic, coumaric and caffeic acids, luteolin, nobiletin, moscatilin, rhamnetin, rhamnazin and epicatechin gallate.

The interactions between the extracts components and silica were studied using the quantum chemical method. The adsorption of phenolic compounds on silica surface was shown to occur mainly due to the formation of hydrogen bonds between hydroxyl groups of the phenols and silanol groups of the surface, with the strength of the interaction increasing in the following order: ferullic, feruloylquinic and fertaric acids (Gibbs free energy ΔG= -6÷14 kJ/mol) < kaempferol, apingenin (ΔG= -18÷21 kJ/mol) << chlorogenic and caffeic acids, rhamnetin, quercetin, luteolin, epicatechin gallate (ΔG= -41÷54 kJ/mol). The presence of two neighbouring hydroxyl groups in the phenol ring of the molecules was found to be a common feature in the structure of the compounds, which are characterized by the strongest interaction with silica silanol groups. These groups were shown to form the shortest hydrogen bonds lengths with silanol groups, providing the compounds with a strong interaction with silica surface.

Acknowledgements

The authors are grateful to the target complex multidisciplinary program of scientific researches of National Academy of Sciences of Ukraine “Molecular and cellular biotechnology for medicine, industry and agriculture” for financial support of this research.

Authors thank Prof. V.M. Gun’ko, Department of Amorphous and Structurally Ordered Oxides, Chuiko Institute of Surface Chemistry, National Academy of Sciences of Ukraine, for the use of the GAUSSIAN09 program suit.

Supplementary information

Supplementary data are available free of charge at http://cjm.asm.md as PDF file.

References

1. Kulciţki, V.; Vlad, P.F.; Duca, Gh.; Lupaşcu, T. Investigation of grape seed proanthocyanidins. Achievements and perspectives. Chemistry Journal of Moldova, 2007, 2(1), pp. 36–50. DOI: https://dx.doi.org/10.19261/cjm.2007.02(1).16
2. Pan, S.Y.; Zhou, S.F.; Gao, S.H.; Yu, Z.L.; Zhang, S.F.; Tang, M.K.; Sun, J.N.; Ma, D.L.; Han, Y.F.; Fong, W.F.; Ko, K.M. New perspectives on how to discover drugs from herbal medicines: CAM's outstanding contribution to modern therapeutics. Evidence-Based Complementary and Alternative Medicine, 2013, 25 p. DOI: https://doi.org/10.1155/2013/627375

3. Hintz, T.; Matthews, K.K.; Di, R. The use of plant antimicrobial compounds for food preservation. BioMed Research International, 2015, 12 p. DOI: https://doi.org/10.1155/2015/246264
4. Kumar, S.; Pandey, A.K. Chemistry and biological activities of flavonoids: an overview. The Scientific World Journal, 2013, 16 p. DOI: https://doi.org/10.1155/2013/162750
5. Proestos, C.; Chorianopoulos, N.; Nychas, G.-J.E.; Komaitis, M. RP-HPLC analysis of the phenolic compounds of plant extracts. Investigation of their antioxidant capacity and antimicrobial activity. Journal of Agricultural and Food Chemistry, 2005, 53(4), pp. 1190–1195. DOI: https://doi.org/10.1021/jf040083t
6. Williams, C.A. The leaf flavonoids of the orchidaceae. Phytochemistry, 1979, 18(5), pp. 803–813. DOI: https://doi.org/10.1016/0031-9422(79)80019-9
7. Kong, J.M.; Goh, N.K.; Chia, L.S.; Chia, T.F. Recent advances in traditional plant drugs and orchids. Acta Pharmacologica Sinica, 2003, 24(1), pp. 7–21. http://www.chinaphar.com/article/view/9014
8. Hossain, M.M. Therapeutic orchids: traditional uses and recent advances-an overview. Fitoterapia, 2011, 82(2), pp. 102–140. DOI: https://doi.org/10.1016/j.fitote.2010.09.007
9. Minh, T.N.; Khang, D.T.; Tuyen, P.T.; Minh, L.T.; Anh, L.H.; Quan, N.V.; Ha, P.T.T.; Quan, N.T.; Toan, N.P.; Elzaawely, A.A.; Xuan, T.D. Phenolic compounds and antioxidant activity of Phalaenopsis orchid hybrids. Antioxidants, 2016, 5(3), 31 p. DOI: https://doi.org/10.3390/antiox5030031
10. Ling, L.F.; Subramaniam, S. Biochemical analyses of *Phalaenopsis violacea* Orchids. Asian Journal of Biochemistry, 2007, 2(4), pp. 237–246. DOI: https://doi.org/10.3923/ajb.2007.237.246
11. Ferreira, V.F.; Pinto, A.C. Phytotherapy in the world today. Quimica Nova, 2010, 33(9), pp. 1829. (in Portuguese). DOI: http://doi.org/10.1590/S0100-40422010000900001
12. Kingston, D.G.I. Modern natural products drug discovery and its relevance to biodiversity conservation. Journal of Natural Products, 2011, 74(3), pp. 496–511. DOI: https://doi.org/10.1021/np100550t
13. De Souza, J.E.; Casanova, L.M.; Costa, S.S. Bioavailability of phenolic compounds: a major challenge for drug development? Revista Fitos, 2015, 9(1), pp. 1–72. DOI: https://doi.org/10.5935/2446-4775.20150006
14. Ajazuddin, S. Applications of novel drug delivery system for herbal formulations. Fitoterapia, 2010, 81(7), pp. 680–689. DOI: https://doi.org/10.1016/j.fitote.2010.05.001
15. De Jong, W.H.; Borm, P.J.A. Drug delivery and nanoparticles: Applications and hazards. International Journal of Nanomedicine, 2008, 3(2), pp. 133–149. DOI: https://doi.org/10.2147/ijn.s596
16. Shi, Z.G.; Guo, Q.Z.; Liu, Y.T.; Xiao, Y.X.; Xu, L. Drug delivery devices based on macroporous silica spheres. Materials Chemistry and Physics, 2011, 126(3), pp. 826–831. DOI: https://doi.org/10.1016/j.matchemphys.2010.12.035
17. Armendáriz-Barragán, B.; Zafar, N.; Badri, W.; Galindo-Rodríguez, S.A.; Kabbaj, D.; Fessi, H.; Elaissari, A. Plant extracts: from encapsulation to application. Expert Opinion on Drug Delivery, 2016, 13(8), pp. 1165–1175. DOI: https://doi.org/10.1080/17425247.2016.1182487
18. Chuiko, A.A. Medical chemistry and clinical application of silica. Naukova Dumka: Kyiv, 2003, 416 p. (in Russian). http://www.ndumka.kiev.ua/
19. Kuzema, P.O.; Laguta, I.V.; Stavinskaya, O.N.; Kazakova, O.A.; Borysenko, M.V.; Lupaşcu, T. Preparation and characterization of silica-enoxil nanobiocomposites. Nanoscale Research Letters, 2016, 11(68), 7 p. DOI: https:///doi.org/10.1186/s11671-016-1287-y
20. Laguta, I.V.; Kuzema, P.O.; Stavinskaya, O.N.; Kazakova, O.A. Supramolecular complex antioxidant consisting of vitamins C, E and hydrophilic-hydrophobic silica nanoparticles. Springer: Dordrecht, 2009, pp. 269–279. DOI: https://doi.org/10.1007/978-90-481-2309-4_22
21. Murashige, T.; Skoog, F. A revised medium for rapid growth and bio assays with tobacco tissue cultures. Physiologia Plantarum, 1962, 15(3), pp. 473–497. DOI: https://doi.org/10.1111/j.1399-3054.1962.tb08052.x
22. Chai, J.-D.; Head-Gordon, M. Long-range corrected hybrid density functionals with damped atom-atom dispersion corrections. Physical Chemistry Chemical Physics, 2008, 10(44), pp. 6615–6620. DOI: https://doi.org/10.1039/b810189b
23. Frisch, M.J.; Trucks, G.W.; Schlegel, H.B.; Scuseria, G.E.; Robb, M.A.; Cheeseman, J.R.; Scalmani, G.; Barone, V.; Mennucci, B.; Petersson, G.A.; et al. Gaussian 09, Revision D.01, 2013, Gaussian Inc, Wallingford CT. https://gaussian.com/
24. Marenich, A.V.; Cramer, C.J.; Truhlar, D.G. Universal solvation model based on solute electron density and on a continuum model of the solvent defined by the bulk dielectric constant and atomic surface tensions. The Journal of Physical Chemistry B, 2009, 113(18), pp. 6378-6396. DOI: https://doi.org/10.1021/jp810292n
25. Laguta, I.; Stavinskaya, O.; Kazakova, O.; Fesenko, T.; Brychka, S. Green synthesis of silver nanoparticles using *Stevia* leaves extracts. Applied Nanoscience, 2019, 9(5), pp. 755–765. DOI: https://doi.org/10.1007/s13204-018-0680-5
26. Singh, D.K.; Babbar, S.B. In vitro propagation and chemical profiling of *Herminium lanceum* (Thunb. ex Sw.) Vuijk, a medicinally important orchid, for therapeutically important phenolic acids. Plant Biotechnology, 2016, 33(3), pp. 153–160. DOI: https://doi.org/10.5511/plantbiotechnology.16.0523a